



UNIVERSITY OF  
LIVERPOOL

# Functional Materials, from Antimicrobial Surfaces to Complex Nanostructures for Renewable Energy

Thesis submitted in accordance with the requirements of the University of Liverpool  
for the degree of Doctor in Philosophy

**Gareth Peter Morris**

August 2019

**Supervisors**

Prof. Rasmita Raval

Dr. Frank Jaeckel

Dr. Yuri Diaz Fernandez

Open Innovation Hub for Antimicrobial Surfaces,  
Surface Science Research Centre

&

Stephenson Institute for Renewable Energy



# Table of Contents

<b>Acknowledgements .....</b>	<b>VII</b>
<b>Abstract.....</b>	<b>IX</b>
<b>Glossary .....</b>	<b>XI</b>
List of Symbols.....	XI
List of Abbreviations .....	XIII
<b>List of Figures.....</b>	<b>XVII</b>
<b>List of Tables .....</b>	<b>XXX</b>
<b>Chapter 1 Introduction .....</b>	<b>1</b>
1.1 Functional Materials .....	1
1.2 Functional Materials for Antimicrobial Applications.....	2
1.2.1 Antimicrobial Resistance .....	2
1.2.2 Biofilms.....	3
1.2.3 Antimicrobial Surfaces .....	7
1.2.4 Nature Inspired Antimicrobial Surfaces.....	8
1.3 Functional Materials for the Sustainable Production of Renewable Energy	13
1. 4 References.....	17
<b>Chapter 2 Experimental Techniques .....</b>	<b>29</b>
2.1 Introduction.....	29
2.2 Techniques for Physical Characterisation.....	30

2.2.1 Differential Scanning Calorimetry (DSC).....	30
2.2.2 Contact Angle.....	31
2.2.3 Ultraviolet-visible-near infrared (UV-Vis-NIR) Spectroscopy .....	34
2.3 Gas Chromatography Separation Techniques.....	37
2.4 Techniques for Chemical Characterisation .....	39
2.4.1 Vibrational Spectroscopy .....	39
2.4.2 X-ray Spectroscopy .....	47
2.5 Microscopy Techniques .....	58
2.5.1 Electron Microscopy .....	58
2.5.2 Fluorescence Microscopy .....	63
2. 6 References .....	72

**Chapter 3 Controlled Release and Antimicrobial Activity of Fatty Acid Impregnated Polydimethylsiloxane (PDMS) ..... 77**

3.1 Introduction.....	77
3.1.1 Polydimethylsiloxane .....	77
3.1.2 Modification of PDMS Towards Antimicrobial Activity.....	80
3.1.3 Fatty Acids .....	83
3.1.4 Antimicrobial Properties and Biocompatibility of Fatty Acids ...	88
3.2 Experimental Details.....	91
3.2.1 Chemicals .....	91
3.2.2 Fabrication of PDMS and Fatty Acid Functionalised PDMS (FAIP) Materials.....	91
3.2.3 Characterisation of PDMS and FAIP Materials .....	92

3.2.4 Characterisation of Fatty Acid Release from FAIP .....	95
3.2.5 Characterising the Antimicrobial Performance of FAIP Materials .....	96
3.3 Results and Discussion .....	100
3.3.1 Fabrication of PDMS and FAIP Materials.....	100
3.3.2 Characterisation of PDMS and FAIP Materials.....	101
3.3.3 Characterisation of Fatty Acid Release from FAIP Materials .	106
3.3.4 Characterising the Antimicrobial Performance of FAIP Materials .....	115
3.4 Conclusions.....	126
3.5 Future Work .....	129
3.6 References.....	131
3.7 Appendix.....	137

**Chapter 4 Combined Approach for the Photothermal Eradication of Bacteria and Photothermal Controlled Drug Release..... 141**

4.1 Introduction.....	141
4.1.1 Photothermal Materials .....	141
4.2 Experimental Details.....	148
4.2.1 Chemicals.....	148
4.2.2 Fabrication of Type I Material for Photothermal Eradication of Surface Attached Bacteria.....	148
4.2.3 Characterisation of Type I Materials.....	149
4.2.4 Photothermal Experiments.....	150

4.2.5 Heat Shock Experiments .....	155
4.2.6 Preparation of Type II materials for Photothermal Drug Delivery .....	157
4.2.7 Characterisation of Type II Materials .....	157
4.2.8 Characterising the Antimicrobial Performance of Type II Materials .....	159
4.3 Results and Discussion.....	161
4.3.1 Fabrication and Characterisation of Type I Materials .....	161
4.3.2 Photothermal Experiments .....	166
4.3.3 Assessing the Viability of Sessile and Planktonic Bacteria after Heat Shock Treatment .....	176
4.3.4 Comparative Discussion for the Photothermal and Heat Shock Experiments	185
4.3.5 Fabrication and Characterisation of Type II Materials .....	189
4.3.6 Characterising the Antimicrobial Performance of Type II Materials.....	192
4.4 Conclusions.....	199
4.5 Future Work .....	202
4.6 References.....	204
4.7 Appendix.....	209
4.7.1 Characterisation of Type I Materials.....	209
4.7.2 Investigating the Photothermal Effect of Type I Materials .....	211
4.7.3 Planktonic and Sessile Heat Shock Experiments.....	214
4.7.4 Fabrication and Characterisation of Type II Materials.....	215

<b>Chapter 5 Synthesis and Stability of Complex Nano-Hybrid Satellite Materials: Applications Towards Plasmonically Enhanced Evolution of Hydrogen from Water .....</b>	<b>217</b>
5.1 Introduction.....	217
5.1.1 Photocatalytic Evolution of Hydrogen from Water .....	217
5.1.2 Chalcogenide Based Quantum Dots (QDs).....	220
5.1.3 Self-Assembly of Nanomaterials .....	221
5.1.4 Plasmonic Nanomaterials.....	222
5.2 Experimental Details.....	228
5.2.1 Chemicals.....	228
5.2.2 Fabrication of Nanomaterials.....	229
5.2.2 Characterisation of Nanomaterials after Fabrication .....	232
5.2.3 Stability Testing of the Nano-Hybrid Satellite Material .....	234
5.2.4 Hydrogen Evolution Experiments.....	236
5.3 Results and Discussion .....	239
5.3.1 Fabrication and Characterisation of Nanomaterials.....	239
5.3.2 Investigating the Stability of the Nano-Hybrid Satellite Material under Active Working Conditions.....	248
5.3.3 Investigating the Mechanism Involved in the Stability of the Nano-Hybrid Satellite Material under Active Working Conditions.....	255
5.3.2 Hydrogen Evolution.....	261
5.4 Conclusions.....	265
5.5 Future Work.....	267

5.6 References .....	269
5.7 Appendix .....	276
5.7.1 Fabrication and Characterisation of Nanomaterials .....	276
5.7.2 Investigating the Stability of the Nano-Hybrid Satellite Material under Active Working Conditions .....	278
5.7.3 Investigating the Mechanism Involved in the Stability of the Nano-Hybrid Satellite Material under Active Working Conditions .....	281
5.7.4 Hydrogen Evolution .....	285

# Acknowledgements

I would like to thank my supervisors, Prof. Rasmita Raval and Dr. Frank Jaeckel for providing me with the opportunity to complete my PhD, as well as welcoming me to their research groups. I am also thankful to the Engineering and Physical Sciences Research Council (EPSRC) for providing me with the funding for my PhD. I would also like to express my gratitude to all my supervisors for their precious guidance and concise critique throughout the course of my PhD, with a special thanks to Dr. Yuri Diaz Fernandez, without whom a lot of this work would not be possible. His clear explanation of complex scientific problems and generous nature, not forgetting the odd pint or few of Guinness (“Elixir of the Gods”), have made a substantial impact on helping me throughout the course of the PhD and helped me to grow as a scientist and as person.

I would also like to thank everyone who was, in one way or another, involved in the research within this thesis: Dr. Sean Goodman, for his endless support, enthusiasm, can-do and caring attitude, as well as introducing me to the world of microbiology, proof reading and the odd pint or few; Dr. Fiona McBride, for her expert advice and experimental efforts in collecting and interpreting XPS and Auger data, as well as proof reading, her kind and caring nature, and support throughout the past few years; Dr. Ioritz Sorzabal Bellido, for his advice and support on tackling some spectroscopic and imaging issues, proof reading and being a friend from the start; Dr. Sam Haq, for his advice, adaptable working nature, and the endless stories, a true historian of surface science and the university; Dr Jon Lee, for teaching me how to synthesise quantum dots, as well his enthusiastic and energetic personality; Francesca Olgiati, for her time assisting in some experiments, your time and company was greatly appreciated; Alison Beckett of the electron microscopy unit, for providing me with the training and advice for TEM imaging and for always being there whenever help was needed; Dr. Matthew Bilton and

Dr. Karl Dawson of ICAL, for their time and support in high-resolution STEM imaging and EDS mapping, of which has been a significant help for this thesis; Our collaborators in Italy at the university of Pavia, particularly Prof. Chiara Milanese for the DSC measurements of several samples and also all the CCI staff, for their time and support in fluorescence imaging, especially Jen Adcott, whom never failed to smile and say hello.

I also want to thank all the incredible people that I have met or indirectly helped me during these years, especially my fellow PhD students and my friends near and far, with a special mention to: Andy McGowan (“Flamingo”), David Lucas (“Fruit Cup”), Luca Barbieri (“Bari”), Marcel Moritz (“Mr. Salsa”), Tiago Entradas (“The Bison”), Emile Durant (“Rubber Soul”) and Neil Potter (“Slappin da bass”), to name just a few, although there are many more. Their support and friendship have been important during this time, of which, this PhD would have been more difficult without you. I would also like to thank, Dr. Tapas Sen, whom was the first to spark my interest in research during my MChem degree. Last, but not least, I wish to thank my family, especially my parents, Terry and Denise Morris, my Auntie Maggi, and not forgetting my girlfriend, Etta, whose support, encouragement and love are invaluable.

# Abstract

The emergence of antimicrobial resistance and the need for clean and renewable energy are currently priority areas worldwide due to the ever-increasing world population and the depletion of natural resources. The vast spread of infection often caused by antimicrobial resistant bacteria adhered to surfaces (e.g. medical devices), can lead to life threatening illness posing a huge societal challenge. On the other hand, the increased demand in the world's energy supply, depletion in fossil fuels, along with the damage to the environment, are becoming critical issues, driving the need for alternative functional materials, that can deliver on demand antimicrobial activity and improve energy supply, using natural products or renewable energy sources. One of the main challenges in both areas of research, is finding materials that are effective, as well as being robust and inexpensive. In this thesis we discuss alternative strategies towards antimicrobial surfaces derived from natural and potentially renewable products. We also investigate a novel strategy to produce clean and sustainable fuels derived from solar energy.

Chapter 1 provides a general introduction into antimicrobial resistance and current strategies used for designing antimicrobial surfaces, including both synthetic materials and materials derived from natural products. This chapter also discusses the current situation on the worlds energy supply and proposes a potential avenue towards clean and renewable fuels derived from solar energy, with the future potential to expand into antimicrobial systems based on successful and well understood photocatalytic materials designed to produce clean and sustainable fuels.

Chapter 2 gives a general overview of the main characterisation techniques used throughout the thesis, allowing to unravel the physical and chemicals properties associated with the materials discussed in chapters 3-5. We also discuss the techniques used to examine the

antimicrobial performance of the materials discussed in chapters 3 and 4, as well as the tools used to characterise the photocatalytic activity of the materials discussed in chapter 5.

Chapter 3 describes a new approach to fabricate antimicrobial surfaces using products that can be derived from nature. By exploiting the properties associated with a polymer, commonly used for medical implants (i.e. polydimethylsiloxane (PDMS)), we incorporated fatty acids within the material, reporting a controlled biocidal response. The antimicrobial activity of these surfaces was tested against both Gram-negative (*E. coli*) and Gram-positive (*S. aureus*) bacterial species, displaying interesting results, both at the surface and in the planktonic state.

Chapter 4 follows a novel approach to fabricate a robust and cost effective photothermal material, by the incorporation of carbon nanopowder into PDMS, a potentially renewable material that can be produced by the pyrolysis of organic waste. This material displayed photoactive properties across a broad spectrum of light, including the NIR region, where water and living tissues are transparent and therefore, not susceptible to direct radiation damage. The material was used for the combined photothermal eradication of bacteria and photothermally controlled release of fatty acids, showing efficacy against both Gram-negative (*E. coli*) and Gram-positive (*S. aureus*) bacterial species.

Chapter 5 describes a novel wet chemical approach to produce nano-hybrid photocatalyst combining the properties of silver nanoparticles coupled with cadmium sulphide quantum dots functionalised with platinum to create photocatalytic satellite systems, for the enhanced photocatalytic production of hydrogen from water. This is a potential strategy to produce clean and sustainable energy using solar light. The photocatalytic activity and stability of these materials were investigated under active working conditions, sign posting key challenges to the future development of this technology.

# Glossary

## List of Symbols

K <sub>a</sub>	Acid dissociation constant
Å	Angstrom
~	Approximately
cm	Centimetre
ΔT	Change in Temperature
pH	Concentration of hydrogen ions, pH = -log <sub>10</sub> [H <sup>+</sup> ]
°	Degrees
°C	Degrees Celsius
g/ cm <sup>3</sup>	Density (Grams/ Cubic Centimetre)
eV	Electron Volt
ΔH	Enthalpy
g	Grams
g L <sup>-1</sup>	Grams per Litre
J	Joules
keV	Kiloelectron Volts
pK <sub>a</sub>	-log <sub>10</sub> K <sub>a</sub>
MΩ	Megaohm
μg	Micrograms
μl	Microlitres
μm	Micrometres
μmol	Micromole
mA	Milliamps
mg	Milligrams

mg/ml	Milligrams/ Millilitre
mm	Millimetre
mW	Milliwatts
nm	Nanometres
nmol	Nanomole
% (w/w)	Percentage (Weight/ Weight)
mW/ cm <sup>2</sup>	Power Density (Milliwatts/ Square Centimetre)
s	Seconds
cm <sup>2</sup>	Square Centimetres
μm <sup>2</sup>	Square Micrometres
σ	Standard Deviation
T	Temperature
T <sub>Max</sub>	Temperature of complete melting
T <sub>Onset</sub>	Temperature onset of melting
v/w	Volume/ Weight
W	Watts
λ	Wavelength
cm <sup>-1</sup>	Wavenumber (ATR-IR)/ Raman Shift (Raman)
wt.%	Weight Percentage
w/v	Weight/ Volume
w/w	Weight/ Weight

## List of Abbreviations

AgNP	Silver Nanoparticle
AgNP@SiO <sub>2</sub> -NH <sub>2</sub>	Silver Nanoparticle coated with Silica and Functionalised with (3-Aminopropyl)triethoxysilane
Approx.	Approximately
ATCC	American Type Culture Collection
APTES	(3-aminopropyl) triethoxysilane
ATM	Atmospheric Pressure
ATR-IR	Attenuated Total Reflection Infrared Spectroscopy
AuNP	Gold Nanoparticle
C <sub>10</sub>	Decanoic acid
C <sub>12</sub>	Dodecanoic acid
C <sub>14</sub>	Tetradecanoic Acid
CdS	Cadmium Sulphide
CdS@Pt	Cadmium Sulphide Functionalised with Platinum
CFM	Confocal Fluorescence Microscopy/ Confocal Fluorescence Microscope
CFU	Colony Forming Unit
CNP	Carbon Nanopowder
DCLS	Direct Classical Least Squares
DI	Deionised
DSC	Differential Scanning Calorimetry
<i>E. coli</i>	<i>Escherichia coli</i>
EDS	Energy Dispersive X-ray Spectroscopy
EMS	Electromagnetic Spectrum
EQE	External Quantum Efficiency

FAIP	Fatty Acid Impregnated Polydimethylsiloxane
GC	Gas Chromatograph
H <sub>2</sub>	Hydrogen
H <sub>2</sub> O	Water
Hr/ hr	Hour
LB	Lysogeny Broth
LSPR	Local Surface Plasmon Resonance
M	Molar
MES	2-(4-morpholinyl) ethanesulphonic acid hydrate
MIC	Minimum Inhibitory Concentration
Min/ min	Minutes
Na <sub>2</sub> SO <sub>3</sub>	Sodium Sulphite
NaCl	Sodium Chloride
NIR	Near Infrared
OD	Optical Density
PBS	Phosphate Buffer Saline
PDMS	Polydimethylsiloxane
PDMS C <sub>10</sub>	Polydimethylsiloxane impregnated with decanoic acid
PDMS C <sub>12</sub>	Polydimethylsiloxane impregnated with dodecanoic acid
PDMS C <sub>14</sub>	Polydimethylsiloxane impregnated with tetradecanoic acid
PI	Propidium Iodide
PPM	Parts Per Million
Pt	Platinum
QD	Quantum Dot
RCF	Relative Centrifugal Force
RPM	Revolutions Per Minute
RT	Room Temperature

<i>S. aureus</i>	<i>Staphylococcus aureus</i>
SiO <sub>2</sub>	Silica
STEM	Scanning Transmission Electron Microscopy
TEM	Transmission Electron Microscopy
TON	Turnover Number
Type I Material	Carbon Nanopowder Embedded in Polydimethylsiloxane
Type II Material	Type I material impregnated with dodecanoic acid
UV	Ultraviolet
UV-Vis	Ultraviolet- Visible
UV-Vis-NIR	Ultraviolet- Visible- Near Infrared
XPS	X-ray Photoelectron Spectroscopy

N.B. The symbols and abbreviations stated above only relate to the most common occurring symbols and abbreviations encountered throughout the thesis. Additional symbols and abbreviations have been described within the thesis content.



# List of Figures

## Chapter 1

<b>Figure 1. 1</b> SEM micrograph of a biofilm grown in the lumen of a Foley urinary catheter ...	3
<b>Figure 1. 2</b> Cell wall structure of Gram-negative and Gram-positive bacteria. ....	4
<b>Figure 1. 3</b> Representative chemical structure of teichoic acid from the wall of Gram-positive bacteria <i>S. aureus</i> .....	5
<b>Figure 1. 4</b> The five stages of biofilm formation. ....	6
<b>Figure 1. 5</b> SEM image of the rigid plate structure of shark-skin surface from <i>Carcharhinus brachyurous</i> (Copper Shark). ....	8
<b>Figure 1. 6</b> Chemical Structure of methylglyoxal, the active antimicrobial agent associated with Manuka Honey.....	10
<b>Figure 1. 7</b> Global energy consumption in 2016 and 2017 shown as a percentage (%). ....	13
<b>Figure 1. 8</b> Reaction scheme for the production of H <sub>2</sub> by the steam reforming process (A) and the water-gas shift reaction (B).....	14
<b>Figure 1. 9</b> General structure of chlorophyll pigment found in plants and other organisms, showing the structure of chlorophyll <i>a</i> and chlorophyll <i>b</i> .....	15

## Chapter 2

<b>Figure 2. 1</b> DSC profiles for different saturated fatty acids with increasing carbon chain length. ....	30
<b>Figure 2. 2</b> Illustration of contact angles formed by sessile liquid drops on a solid surface.	31
<b>Figure 2. 3</b> Droplet formation on a surface due to the unbalanced forces of liquid molecules. ....	32
<b>Figure 2. 4</b> Schematic showing general set-up of a telescope goniometer with camera used for static contact angle measurements. ....	33

<b>Figure 2. 5</b> UV-Vis spectrum of CdSe QDs functionalised with mercaptopropionic acid (MPA) dispersed in water (H <sub>2</sub> O).....	34
<b>Figure 2. 6</b> (A) Schematic showing the general configuration of gas chromatograph instrument with TCD. (B) Schematic showing the configuration of a TCD.....	37
<b>Figure 2. 7</b> Schematic representation of attenuated total reflectance (ATR) configuration in an ATR-IR instrument.....	40
<b>Figure 2. 8</b> ATR-IR spectrum of dodecanoic acid.....	41
<b>Figure 2. 9</b> Jablonski diagram of quantum energy transitions for Rayleigh (B) and Raman Scattering ((A) Anti-Stokes scattering and (C) Stokes scattering)). .....	42
<b>Figure 2. 10</b> Raman spectrum of dodecanoic acid.....	43
<b>Figure 2. 11</b> Illustration showing the signal to baseline mapping method. ....	45
<b>Figure 2. 12</b> Illustration showing general overview of the DCLS mapping method.....	46
<b>Figure 2. 13</b> Schematic showing the configuration of the Renishaw inVia confocal Raman microscope .....	47
<b>Figure 2. 14</b> Schematic showing the general configuration of an inductively coupled plasma optical emission spectroscopy (ICP-OES) instrument. ....	48
<b>Figure 2. 15</b> Schematic showing the XPS process. ....	50
<b>Figure 2. 16</b> Universal curve showing the escape depth of an electron from a solid as a function of kinetic energy (eV) with measured values for various elements .....	51
<b>Figure 2. 17</b> XPS spectra of the silver (Ag) 3d region for argon sputtered silver foil (Ag(0)) and silver nitrate (Ag(I)NO <sub>3</sub> ) showing a negative shift in binding energy for the oxidised silver species, AgNO <sub>3</sub> . ....	53
<b>Figure 2. 18</b> Schematic showing emission of an Auger electron. ....	54
<b>Figure 2. 19</b> Auger spectra of the silver (Ag(0)) MNN region for argon sputtered silver foil and silver nitrate (Ag(I)NO <sub>3</sub> ) showing a negative shift in kinetic energy for the oxidised silver species, AgNO <sub>3</sub> . ....	55
<b>Figure 2. 20</b> Schematic showing the EDS process. ....	57
<b>Figure 2. 21</b> Schematic showing the general configuration of a TEM.....	60

<b>Figure 2. 22</b> TEM image of gold nanostars (scale bar is 100 nm). .....	61
<b>Figure 2. 23</b> Schematic showing the general configuration of a combined STEM and TEM. .....	62
<b>Figure 2. 24</b> STEM bright-field (A) and dark-field (B) image of CdS QDs (scale bars are 10 nm). .....	63
<b>Figure 2. 25</b> Jablonski diagram showing the different fluorescence processes.....	64
<b>Figure 2. 26</b> Absorbance (green solid line) and emission (red dashed line) spectra of acridine orange. Insert shows the molecular structure of acridine orange.....	65
<b>Figure 2. 27</b> Jablonski diagram showing the mechanism of fluorescence resonance energy transfer (FRET) between a donor and acceptor fluorophore. ....	66
<b>Figure 2. 28</b> Schematic showing the optical pathway and general configuration of a confocal laser scanning microscope. ....	67
<b>Figure 2. 29</b> Absorbance and emission spectra of SYTO 9 green fluorescent stain (A) and propidium iodide red fluorescent stain.....	68
<b>Figure 2. 30</b> Representative merged CLSM image of <i>S. aureus</i> bacteria on PDMS, stained with SYTO 9 (green, live bacteria) and propidium iodide (red, dead bacteria) fluorescence dyes .....	69
<b>Figure 2. 31</b> Schematic showing a general overview of the image processing of CFM images using Fiji macro. ....	71

## Chapter 3

<b>Figure 3. 1</b> Proposed mechanism for the curing process of polydimethylsiloxane (PDMS) in the presence of platinum based Karstedt catalyst .....	78
<b>Figure 3. 2</b> Schematic representation of polydimethylsiloxane (PDMS) showing the unequal Si-O bond angles responsible for the high structured flexibility of the material .....	79
<b>Figure 3. 3</b> General overview for the surface modification of polydimethylsiloxane (PDMS) by plasma treatment. ....	81

<b>Figure 3. 4 (i)</b> Graphical illustration of polymer blends showing the interfacial adhesion between two polymers by hydrogen bonding and <b>(ii)</b> Graphical illustration showing the generic structure of a copolymer formed by reacting two different monomers. ....	82
<b>Figure 3. 5</b> General structure of fatty acids and derivatives.....	84
<b>Figure 3. 6</b> Schematic showing the acid base equilibria of fatty acids.....	86
<b>Figure 3. 7 (A)</b> Digestion of triglyceride by enzymatic hydrolysis with lipase to produce fatty acid and glycerol. <b>(B)</b> Base catalysed hydrolysis of triglyceride .....	87
<b>Figure 3. 8</b> Schematic showing the most abundant antimicrobial fatty acids found on human skin .....	89
<b>Figure 3. 9</b> Image showing an example of the Raman cross section experiment.....	94
<b>Figure 3. 10</b> Photographs of cured PDMS before <b>(A)</b> and after swelling with fatty acid <b>(B)</b> . PDMS C <sub>10</sub> showed as an example of FAIP.....	100
<b>Figure 3. 11</b> Raman spectra of pure starting materials prior to the functionalisation of PDMS .....	102
<b>Figure 3. 12</b> Raman spectra of PDMS and FAIP materials.....	103
<b>Figure 3. 13 (A)</b> Representative Raman spectra of PDMS (black) & PDMS C <sub>10</sub> (red), <b>(B)</b> distribution of decanoic acid across PDMS C <sub>10</sub> , <b>(C)</b> representative Raman spectra of PDMS (black) & PDMS C <sub>12</sub> (red), <b>(D)</b> distribution of dodecanoic acid across PDMS C <sub>12</sub> , <b>(E)</b> representative Raman spectra of PDMS (black) & PDMS C <sub>14</sub> (red), <b>(F)</b> distribution of tetradecanoic acid across PDMS C <sub>14</sub> . <b>(i)</b> Insert showing $\gamma$ CH <sub>2</sub> twist vibration of the respective fatty acids. ....	104
<b>Figure 3. 14 (A)</b> Normalised histogram showing the distribution of decanoic acid in PDMS C <sub>10</sub> , <b>(B)</b> normalised histogram showing the distribution of dodecanoic acid in PDMS C <sub>12</sub> , <b>(C)</b> normalised histogram showing the distribution of tetradecanoic acid in PDMS C <sub>14</sub> , <b>(D)</b> schematic representation of the experiment, where each green dot (●) represents the area of acquisition across the sample, at a depth of 500 $\mu$ m from the sample surface.....	105
<b>Figure 3. 15</b> Chart showing the release of fatty acids from the FAIP after 24 hrs. ....	108

<b>Figure 3. 16</b> Schematic representation showing the effect of pH on the carboxyl group in fatty acids .....	110
<b>Figure 3. 17</b> Representative Raman data for PDMS C <sub>12</sub> after each release condition .....	113
<b>Figure 3. 18</b> Contact angle measurements for PDMS and FAIP with pH 5 and pH 7 buffers at room temperature. ....	114
<b>Figure 3. 19</b> Planktonic MIC results for <i>E. coli</i> (ATCC 10798) against decanoic acid at different concentrations in LB media.....	116
<b>Figure 3. 20</b> Planktonic inhibition of <i>E. coli</i> (ATCC 10798) on PDMS C <sub>10</sub> . ....	117
<b>Figure 3. 21</b> Confocal fluorescence microscopy images of <i>E. coli</i> (ATCC 10798) on PDMS and PDMS C <sub>10</sub> , showing percentage of dead bacteria .....	118
<b>Figure 3. 22</b> Bar Chart showing summary of the CFM data with Live/ Dead staining for <i>E. coli</i> 10798 on PDMS (Control) and PDMS C <sub>10</sub> (Active) under different pH and temperature conditions.....	119
<b>Figure 3. 23</b> Planktonic MIC results for <i>S. aureus</i> (ATCC 6538P) against decanoic acid of different concentrations in LB media.....	120
<b>Figure 3. 24</b> Planktonic % growth of <i>S. aureus</i> (ATCC 6538P) in contact with PDMS C <sub>10</sub> in LB media.....	121
<b>Figure 3. 25</b> Confocal fluorescence microscopy images of <i>S. aureus</i> (ATCC 6538P) on PDMS and PDMS C <sub>10</sub> , showing percentage of dead bacteria .....	123
<b>Figure 3. 26</b> Bar Chart showing summary of the CFM data using Live/ Dead staining for <i>S. aureus</i> 6538P on PDMS (Control) and PDMS C <sub>10</sub> (Active) under different pH and temperature conditions.....	124
<b>Figure 3. 27</b> Mechanism of PDMS C <sub>10</sub> logic gate.....	125
<b>Figure A3. 1</b> Representative DSC profile for PDMS.....	137
<b>Figure A3. 2</b> Representative DSC profiles for Decanoic Acid and PDMS C <sub>10</sub> .....	137
<b>Figure A3. 3</b> Representative DSC profiles for Dodecanoic Acid and PDMS C <sub>12</sub> .....	138
<b>Figure A3. 4</b> Representative DSC profiles for Tetradecanoic Acid and PDMS C <sub>14</sub> .....	138

<b>Figure A3. 5</b> Representative Raman data for PDMS C <sub>10</sub> after each release condition.....	139
<b>Figure A3. 6</b> Representative Raman data for PDMS C <sub>14</sub> after each release condition.....	140

## Chapter 4

<b>Figure 4. 1</b> Schematic representation of a photothermal material .....	142
<b>Figure 4. 2</b> Illustration showing penetration depth of light at different wavelengths with human tissue.....	143
<b>Figure 4. 3</b> Absorbance spectrum of carbon nanopowder (CNP) dispersed in CHCl <sub>3</sub> (Conc. 0.025% w/v). .....	145
<b>Figure 4. 4</b> Images of <i>streptococcus</i> colonies on agar (control) and CNT/ agar composites irradiated with NIR light (800-1300 nm, $1.3 \times 10^4$ W/m <sup>2</sup> ).....	145
<b>Figure 4. 5</b> Schematic illustration for the preparation and release of the graphene based photothermal drug delivery system by Adeli <i>et al</i> .....	146
<b>Figure 4. 6</b> Schematic representation of type I and type II surface for photothermal eradication of surface attached bacteria ( <b>Type I</b> ) and controlled photothermal release antimicrobial agents ( <b>Type II</b> ). .....	147
<b>Figure 4. 7</b> Photograph of laser set up for photothermal experiments with type I and type II surfaces.....	151
<b>Figure 4. 8</b> Schematic of the laser set up for photothermal experiments with type I and type II surfaces.....	152
<b>Figure 4. 9</b> Schematic for the design of the sample well with thermocouple, for determining the temperature at the surface of the type I material during photothermal experiments .....	153
<b>Figure 4. 10</b> TEM image of carbon nanopowder.....	161
<b>Figure 4. 11</b> Absorbance spectrum of pristine PDMS and type I material.....	162
<b>Figure 4. 12</b> Raman spectra of raw materials used to fabricate type I materials .....	163
<b>Figure 4. 13</b> Raman spectra of raw materials and type I material. ....	164

<b>Figure 4. 14</b> (A) Representative Raman map for the distribution of CNP across the surface of type I material, (B) Raman spectrum of PDMS (Black) and averaged Raman spectrum of the type I material (Red), (C) Representative normalised histogram showing the distribution of CNP across the surface of the type I material. ....	165
<b>Figure 4. 15</b> Graph showing the density of water (H <sub>2</sub> O) as a function of temperature, in a range of 10°C to 100 °C at 1 ATM pressure.....	166
<b>Figure 4. 16</b> Graph showing laser power density (mW/ cm <sup>2</sup> ) as a function of current (mA) measured at the sample stage for the continuous wave laser set-up .....	167
<b>Figure 4. 17</b> Thermograms for the type I material during photothermal experiments, measured using a K type thermocouple. ....	168
<b>Figure 4. 18</b> Graph showing the linear relationship between power density (mW/ cm <sup>2</sup> ) and the temperature at stationary conditions ( $\Delta T_{\text{Max}}$ ) measured with the thermocouple during photothermal experiments with the type I material.....	170
<b>Figure 4. 19</b> Confocal fluorescence microscopy images of <i>E. coli</i> (ATCC 10798) on type I materials showing percentage of dead bacteria, after 5 mins irradiation under physiological conditions, at 808 nm wavelength using different laser power densities.....	172
<b>Figure 4. 20</b> Confocal fluorescence microscopy images of <i>S. aureus</i> (ATCC 6538P) on type I material showing percentage of dead bacteria, after 5 mins irradiation under physiological conditions at 808 nm wavelength using different laser power densities.....	173
<b>Figure 4. 21</b> Bar Chart showing summary of the CFM data with Live/ Dead staining for <i>E. coli</i> 10798 on non-irradiated and irradiated type I materials. ....	174
<b>Figure 4. 22</b> Bar Chart showing summary of the CFM data with Live/ Dead staining for <i>S. aureus</i> 6538P on non-irradiated and irradiated type I materials. ....	174
<b>Figure 4. 23</b> Confocal fluorescence microscopy images of <i>E. coli</i> (ATCC 10798) and <i>S. aureus</i> (ATCC 6538P) on transparent PDMS showing percentage of dead bacteria, after 5 mins irradiation under physiological conditions, at 808 nm wavelength with a laser power of 1651 mW/ cm <sup>2</sup> . Non-irradiated transparent PDMS shown as control .....	175

<b>Figure 4. 24</b> Bar Chart showing summary of the CFM data with Live/ Dead staining for <i>E. coli</i> 10798 and <i>S. aureus</i> 6538P on non-irradiated and 1651 mW/ cm <sup>2</sup> irradiated transparent PDMS. ....	176
<b>Figure 4. 25</b> Thermograms for the planktonic heat shock experiments, measured using a K type thermocouple. ....	177
<b>Figure 4. 26</b> Percentage (%) dead <i>E. coli</i> (ATCC 10798) and <i>S. aureus</i> (ATCC 6538P) bacteria compared to control, in planktonic heat shock experiments. ....	178
<b>Figure 4. 27</b> Thermograms for the type I material during sessile heat shock experiments, measured using a K type thermocouple. ....	179
<b>Figure 4. 28</b> Confocal fluorescence microscopy images of <i>E. coli</i> (ATCC 10798) on type I materials showing percentage of dead bacteria after 5 mins heat shock treatment under physiological conditions, at different nominal temperatures.....	182
<b>Figure 4. 29</b> Confocal fluorescence microscopy images of <i>S. aureus</i> (ATCC 6538P) on type I materials showing percentage of dead bacteria after 5 mins heat shock treatment under physiological conditions, at different nominal temperatures.....	183
<b>Figure 4. 30</b> Bar Chart showing summary of the CFM data with Live/ Dead staining for <i>E. coli</i> 10798 on type I materials after 5 minutes of heat shock treatment at different nominal temperatures. ....	184
<b>Figure 4. 31</b> Bar Chart showing summary of the CFM data with Live/ Dead staining for <i>S. aureus</i> 6538P on type I materials after 5 minutes of heat shock treatment at different nominal temperatures. ....	184
<b>Figure 4. 32</b> Summary of photothermal and heat shock experiments with <i>E. coli</i> and <i>S. aureus</i> bacteria showing % of dead bacteria vs temperature measured (according to thermograms) .....	188
<b>Figure 4. 33</b> ATR-IR spectroscopy data of type I material ( <b>Black</b> ), dodecanoic acid ( <b>Red</b> ) and type II material ( <b>Blue</b> ).....	190
<b>Figure 4. 34</b> ATR-IR spectroscopy data of type II material before (A) and after (B) irradiation at 881 mW/cm <sup>2</sup> for 5 mins. ....	191

<b>Figure 4. 35</b> Contact angle measurements for PDMS, type I materials and type II materials with 0.85% NaCl.....	192
<b>Figure 4. 36</b> Confocal fluorescence microscopy images of <i>E. coli</i> (ATCC 10798) on non-irradiated and irradiated, type I and type II materials, showing the percentage of dead bacteria. Samples were irradiated at a laser power density of 881 mW/cm <sup>2</sup> for 5 minutes using the photothermal set-up .....	194
<b>Figure 4. 37</b> Confocal fluorescence microscopy images of <i>S. aureus</i> (ATCC 6538P) on non-irradiated and irradiated, type I and type II materials, showing the percentage of dead bacteria. Samples were irradiated at a laser power density of 881 mW/cm <sup>2</sup> for 5 minutes using the photothermal set-up .....	195
<b>Figure 4. 38</b> Bar chart showing summary of CFM data with live/dead staining of <i>E. coli</i> 10798 on non-irradiated and 881 mW/cm <sup>2</sup> irradiated type I and type II materials.....	196
<b>Figure 4. 39</b> Bar chart showing summary of CFM data with live/dead staining of <i>S. aureus</i> 6538P on non-irradiated and 881 mW/cm <sup>2</sup> irradiated type I and type II materials.....	196
<b>Figure 4. 40</b> Percentage (%) viability of planktonic <i>E. coli</i> (ATCC 10798) and <i>S. aureus</i> (ATCC 6538P) bacteria with irradiated type I and type II materials, and non-irradiated type II materials. Samples irradiated with 881 mW/cm <sup>2</sup> using photothermal set-up. Control is non-irradiated type I material.....	198
<b>Figure A4. 1</b> Representative Raman map for the distribution of CNP across the surface of type I material showing a representative Raman spectrum for low (i) and high (ii) CNP content in the type I material. ....	209
<b>Figure A4. 2</b> Normalised histograms showing the distribution of CNP across the surface of 3 individual type I materials .....	210
<b>Figure A4. 3</b> ATR-IR spectroscopy data of PDMS (Black) and type I material (Red). ....	211
<b>Figure A4. 4</b> Schematic showing heat dissipation of the type I material under photothermal treatment, where a large % of heat may be dissipated into the bulk material.....	212

**Figure A4. 5** Graph used to determine  $\alpha$ , showing the linear relationship between power density in  $W/ m^2$  vs the temperature at stationary conditions ( $\Delta T_{max}$ ) measured with the thermocouple during photothermal experiments with the type I material.....212

## Chapter 5

**Figure 5. 1** Overall reaction scheme for evolution of  $H_2$  from  $H_2O$  ..... 218

**Figure 5. 2** Relationship between band structure of semiconductor and redox potentials for the evolution of  $H_2$  from  $H_2O$ ..... 219

**Figure 5. 3** Schematic representation for the photocatalytic evolution of  $H_2$  from  $H_2O$  using Pt (co-catalyst) decorated chalcogenide based QDs in the presence of hole scavenger  $Na_2SO_3$  ..... 220

**Figure 5. 4** Schematic showing the increase in the band gap energy levels of CdS QDs as the size of the QD decreases ..... 221

**Figure 5. 5** Schematic showing local surface plasmon resonance ..... 223

**Figure 5. 6** Examples of some plasmonic nanomaterials with different morphology and chemical composition..... 223

**Figure 5. 7** Schematic adapted from Torimoto *et al* showing the design of the plasmonic-semiconductor nano-hybrid material for plasmonically enhanced  $H_2$  evolution from  $H_2O$ . 225

**Figure 5. 8** Reaction scheme for the fabrication of the  $AgNP@SiO_2-CdS@Pt$  nano-hybrid satellite material. .... 229

**Figure 5. 9** Gas-tight glass reaction vessel used for the photocatalytic hydrogen evolution experiments ..... 236

**Figure 5. 10** Spectrum of filtered lamp light reaching the sample, used to illuminate the photocatalyst samples..... 237

**Figure 5. 11** AgNPs synthesised following adapted method from Bastus *et al* ..... 239

**Figure 5. 12** Combined  $SiO_2$  coating and APTES functionalisation of AgNPs ..... 240

<b>Figure 5. 13</b> Representative XPS data of the AgNP@SiO <sub>2</sub> -NH <sub>2</sub> material drop-cast on Al foil coated Si wafer.....	241
<b>Figure 5. 14</b> UV-Vis spectra of CdS QDs in chloroform (CHCl <sub>3</sub> ) (20 x dilution vs stock) showing the maximum of excitonic absorption at 415 nm. ....	242
<b>Figure 5. 15</b> Representative STEM images of CdS QDs .....	243
<b>Figure 5. 16</b> Normalised UV-Vis spectra of CdS QDs before and after phase transfer to H <sub>2</sub> O and after decorating the CdS QDs with Pt clusters. ....	244
<b>Figure 5. 17</b> (A) Representative normalised UV-Vis spectra of AgNP@SiO <sub>2</sub> -NH <sub>2</sub> (blue) and nano-hybrid satellite material (red), showing blue shift after fabrication of the nano-hybrid satellite material (B) Representative TEM image of the nano-hybrid satellite material after fabrication demonstrating the core shell structure, with plasmonic AgNP core unit coupled with CdS QDs, separated by an SiO <sub>2</sub> dielectric layer .....	245
<b>Figure 5. 18</b> Representative STEM images of the nano-hybrid satellite material after fabrication .....	246
<b>Figure 5. 19</b> Representative high resolution STEM image with EDS mapping of the nano-hybrid satellite material after fabrication .....	247
<b>Figure 5. 20</b> Representative XPS and Auger data of the nano-hybrid satellite material in DI H <sub>2</sub> O drop-cast on a silicon wafer .....	248
<b>Figure 5. 21</b> Representative TEM images of AgNPs@SiO <sub>2</sub> -NH <sub>2</sub> and the nano-hybrid satellite material dispersed in 20 mM Na <sub>2</sub> SO <sub>3</sub> . ....	250
<b>Figure 5. 22</b> Representative TEM images of the nano-hybrid satellite material dispersed in TEOA of different concentrations.....	251
<b>Figure 5. 23</b> Representative TEM images of AgNPs@SiO <sub>2</sub> -NH <sub>2</sub> and the nano-hybrid satellite material dispersed in 0.2 M oxalic acid .....	252
<b>Figure 5. 24</b> Representative TEM images of the nano-hybrid satellite material dispersed in L-ascorbic acid of different concentrations.....	253
<b>Figure 5. 25</b> Representative TEM images of the nano-hybrid satellite material dispersed in 50 mM MES buffer (pH 5.5). ....	254

<b>Figure 5. 26</b> Representative high resolution STEM image with EDS mapping of the nano-hybrid satellite material after 24 hrs dispersed in 20 mM Na <sub>2</sub> SO <sub>3</sub> .....	256
<b>Figure 5. 27</b> Representative high resolution STEM image with EDS mapping of the nano-hybrid satellite material after 24 hrs dispersed in 0.2 M L-ascorbic acid .....	257
<b>Figure 5. 28</b> Representative high resolution STEM image with EDS mapping of the nano-hybrid satellite material after 24 hrs dispersed in deionised H <sub>2</sub> O .....	258
<b>Figure 5. 29</b> Representative XPS and Auger data of the nano-hybrid satellite material dispersed in 20 mM Na <sub>2</sub> SO <sub>3</sub> drop-cast on a silicon wafer.....	259
<b>Figure 5. 30</b> Representative XPS and Auger data of the nano-hybrid satellite material dispersed in 0.2M L-ascorbic acid drop-cast on a silicon wafer .....	260
<b>Figure 5. 31</b> Representative TEM images of the nano-hybrid satellite materials after fabrication used in the photocatalytic hydrogen evolution reactions .....	263
<b>Figure A5. 1</b> EDS spectra of the nano-hybrid satellite material after fabrication, used for the EDS mapping. ....	276
<b>Figure A5. 2</b> XPS survey scan of AgNP@SiO <sub>2</sub> -NH <sub>2</sub> drop-cast on an aluminium coated silicon wafer.....	276
<b>Figure A5. 3</b> XPS survey scan of the nano-hybrid satellite material drop-cast on a silicon wafer.....	277
<b>Figure A5. 4</b> Representative XPS data of the nano-hybrid satellite material in DI H <sub>2</sub> O drop-cast on an aluminium coated silicon wafer.....	277
<b>Figure A5. 5</b> Representative TEM images of the nano-hybrid satellite material dispersed in 50 mM CAPS (pH 10).....	278
<b>Figure A5. 6</b> Representative TEM images of the nano-hybrid satellite material dispersed in 50 mM HEPES buffer (pH 7).....	278
<b>Figure A5. 7</b> Representative TEM images of the nano-hybrid satellite material dispersed in DI H <sub>2</sub> O.....	279

<b>Figure A5. 8</b> Monitoring the pH of the nano-hybrid satellite material dispersion over 3 days .....	281
<b>Figure A5. 9</b> EDS spectra of the nano-hybrid satellite material after 24 hrs dispersed in 20 mM Na <sub>2</sub> SO <sub>3</sub> , used for the EDS mapping. ....	282
<b>Figure A5. 10</b> EDS spectra of the nano-hybrid satellite material after 24 hrs dispersed in 0.2 M L-ascorbic acid, used for the EDS mapping. ....	282
<b>Figure A5. 11</b> EDS spectra of the nano-hybrid satellite material after 24 hrs dispersed in DI H <sub>2</sub> O, used for the EDS mapping. ....	283
<b>Figure A5. 12</b> XPS survey scan of the nano-hybrid satellite material after 24 hrs dispersed in 20 mM Na <sub>2</sub> SO <sub>3</sub> drop-cast on a silicon wafer. ....	283
<b>Figure A5. 13</b> XPS Survey scan of the nano-hybrid satellite material after 24 hrs dispersed in 0.2 M L-ascorbic acid drop-cast on a silicon wafer. ....	284

# List of Tables

## Chapter 2

<b>Table 2. 1</b> Different vibrational modes of molecules in infrared and Raman spectroscopy, with their assigned symbol in this thesis. ....	39
<b>Table 2. 2</b> Characteristic infrared vibrational frequencies for dodecanoic acid .....	41
<b>Table 2. 3</b> Characteristic Raman vibrational frequencies for dodecanoic acid.....	44
<b>Table 2. 4</b> Spin-orbit splitting $j$ values and peak intensity ratios.....	52

## Chapter 3

<b>Table 3. 1</b> Literature data for some common saturated fatty acids. ....	85
<b>Table 3. 2</b> Loading temperature's and average mass of each fatty acid loaded in PDMS...	101
<b>Table 3. 3</b> DSC melting transition data for pure fatty acids and FAIP. ....	106
<b>Table 3. 4</b> Release conditions for the fatty acid release experiments .....	107
<b>Table 3. 5</b> Acid dissociation constants and solubility of fatty acids.....	109

## Chapter 4

<b>Table 4. 1</b> Thermal Properties of carbon nanopowder, water and PDMS .....	187
<b>Table A4. 1</b> Temperatures measured by K type thermocouple at $T_0$ and $T_{5 \text{ Mins}}$ for the type I material during photothermal experiments at different laser powers. ....	211
<b>Table A4. 2</b> Temperatures measured by K type thermocouple at $T_0$ and $T_{5 \text{ Mins}}$ for the planktonic heat shock experiments at different nominal temperatures .....	214
<b>Table A4. 3</b> Temperatures measured by K type thermocouple at $T_0$ , $T_{5 \text{ Mins}}$ and $T_{10 \text{ Mins}}$ for the type I material during sessile heat shock experiments at different nominal temperatures. ...	214

**Table A4. 4** Table showing the mass of dodecanoic acid loaded in the type I material. .... 215

**Table A4. 5** Photothermal release data for the type II material, before and after irradiation at 881 mW/cm<sup>2</sup>. ..... 215

## Chapter 5

**Table 5. 1** Photocatalytic H<sub>2</sub> evolution results for batch 1 and 2 of the nano-hybrid satellite material and the CdS@Pt QDs, including the concentrations of Pt and CdS QDs in the reaction solution..... 264

**Table A5. 1** Summary of the results obtained from the TEM analysis of the nano-hybrid satellite material dispersed in different pH buffers and hole scavengers from literature..... 280

**Table A5. 2** Total concentration of Ag, Cd and Pt in the 7 ml photocatalytic reaction solutions in parts per million (PPM). ..... 285



# Chapter 1

## Introduction

### 1.1 Functional Materials

Functional materials, defined as those materials that perform specific functions, have always been of interest for humanity, with the everlasting quest for novel, tailored tools for the survival, development and prosperity of mankind.<sup>1</sup> Looking back through human history, mankind has achieved a dramatic advancement of technology, from the stone age, all the way up to the current age of advanced materials.<sup>2</sup> Since early times, materials have evolved from the use of inert structural components for the fabrication of objects, such as tools and weapons, to materials with tailored properties, with the intrinsic ability to respond to stimuli and environmental changes, activating specific functions on demand.<sup>3</sup>

Functional materials have become essential for the progression of modern society, in priority areas, such as energy storage, health care and environment protection.<sup>3</sup> Improvements and innovations in fundamental science and engineering have allowed for a better understanding of the properties of materials, resulting in the control over fabrication processes for new materials, tailored towards a wide spectrum of applications, such as photovoltaics, batteries, supercapacitors, biomaterials and tissue engineering, among others.<sup>3</sup> In this area of research, the design and fabrication of functional materials for medicinal applications (e.g. tackling antimicrobial resistance (section 1.2)), or for the production of clean and renewable energy (section 1.3) are currently of interest due to the ever-increasing world population, as well as the need for cleaner and alternative fuels for preserving the environment.

## 1.2 Functional Materials for Antimicrobial Applications

### 1.2.1 Antimicrobial Resistance

Bacterial infections are one of the main causes of death worldwide, with many infections often caused by antimicrobial resistant bacteria.<sup>4</sup> Since the discovery of antibiotics in the early 20<sup>th</sup> century by Alexander Fleming, they have been used for medicinal treatment of infections and played a key role in improving life expectancy.<sup>5,6</sup> However, due to the excessive or inappropriate use of antibiotics and other antimicrobial drugs (e.g. germicides) in health care, veterinary and agricultural settings, bacteria have developed a resistance to antimicrobial drugs through evolutionary pressure.<sup>5-7</sup>

Bacterial resistance to antimicrobial drugs can be primarily the consequence of a variety of phenomena, including metabolic alteration of the target drug, impermeability of the bacteria envelop to the antimicrobial drug, and genetically associated modifications.<sup>8</sup> Antimicrobial resistance can also emerge when bacteria attach to surfaces and form multicellular communities, known as a biofilm, protected by an extracellular polymeric matrix (Figure 1. 1). This is one of the mechanisms of resistance used by bacteria to survive in the presence of antimicrobial drugs.<sup>9-11</sup> In this state, bacteria may have an increased antimicrobial resistance to antimicrobial drugs<sup>12,13</sup> and external biocidal factors from the surrounding media (e.g. heat),<sup>14,15</sup> with respect to bacteria in the planktonic state (liquid media).

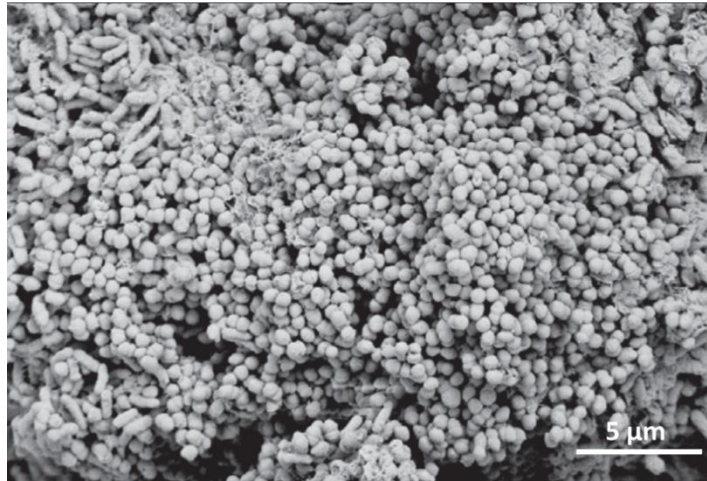


**Figure 1. 1** SEM micrograph of a biofilm grown in the lumen of a Foley urinary catheter removed from a patient admitted to the Fondazione Santa Lucia research hospital for neuromotor rehabilitation in Rome. The species identified by culture methods were *Klebsiella pneumoniae*, *Pseudomonas aeruginosa* and *Acinetobacter baumannii*. Figure adapted from reference 16.<sup>16</sup>

### 1.2.2 Biofilms

Biofilms are ubiquitous in nature, where they are often seen as layers of slime on rocks or other objects within water or water-air interfaces.<sup>17</sup> Biofilms can virtually form on any surface, such as the hulls of boats and ships, where they may cause corrosion, or on medical devices, such as wound dressings and heart valve, knee and hip replacements, which can often lead to life threatening illness and device failure.<sup>17,18</sup> Biofilms can be constituted by single or multiple species, including both Gram-negative and Gram-positive bacteria.<sup>19</sup> The terms Gram-negative and Gram-positive are used to define categories of bacterial cells with respect to their cell wall structure (Figure 1. 2).<sup>20</sup>

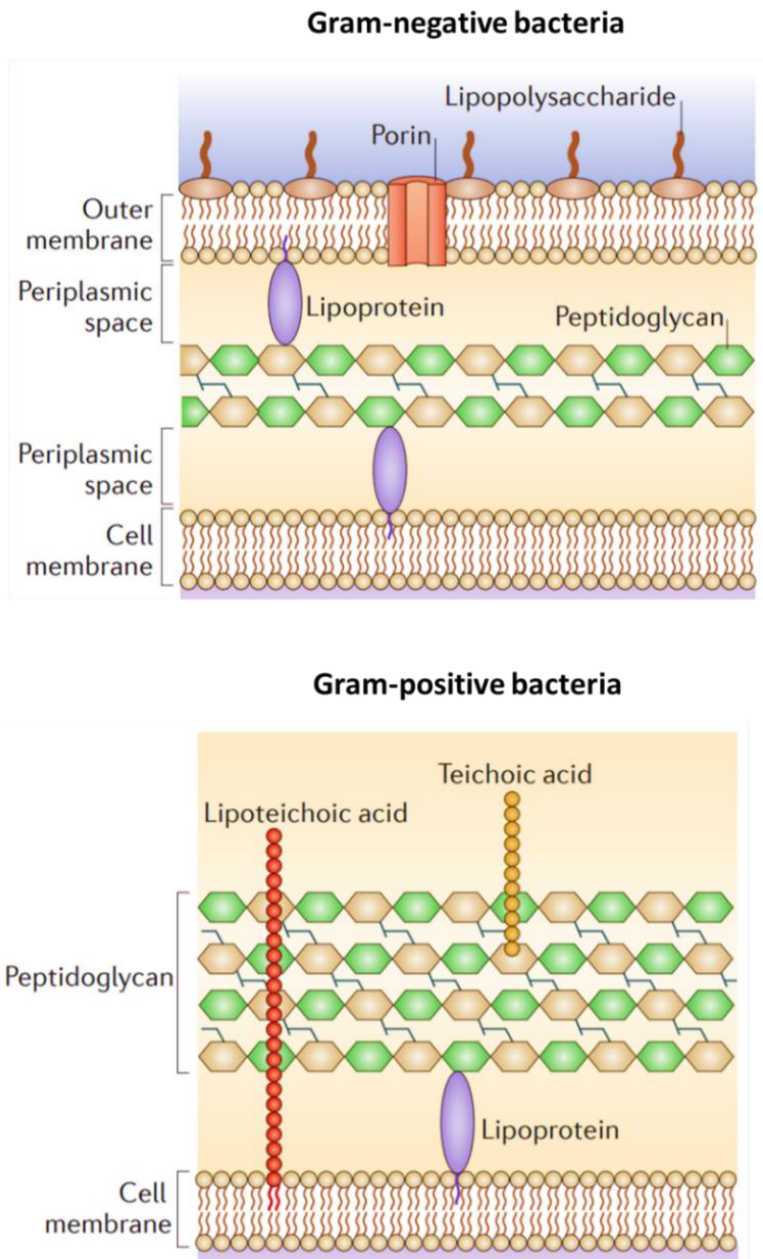


**Figure 1. 2** Cell wall structure of Gram-negative and Gram-positive bacteria. Figure adapted from reference 20.<sup>20</sup>

The cell wall of Gram-negative bacteria consists of a thin layer of peptidoglycan in the periplasmic space between the inner and outer lipid membranes. The lipid membranes are composed of phospholipids consisting of hydrophilic phosphate head groups attracted to aqueous extracellular and intracellular (periplasmic space) environments, with hydrophobic fatty acid carbon chains as tails, forming a lipid bilayer. The outer membrane also contains lipopolysaccharides on its outer leaflet to facilitate non-vesicle-mediated transport through channels such as porins.<sup>20,21</sup> Gram-positive species have a single lipid membrane surrounded

by a cell wall composed of a thick layer of peptidoglycan, interconnected by teichoic acids (Figure 1. 3).<sup>20</sup> Teichoic acids provide rigidity to the cell wall structure and can be freely bonded to the thick peptidoglycan layer or can be connected to both the peptidoglycan layer and phospholipid membrane via a lipid anchor, referred to as a lipoteichoic acid.<sup>22</sup>

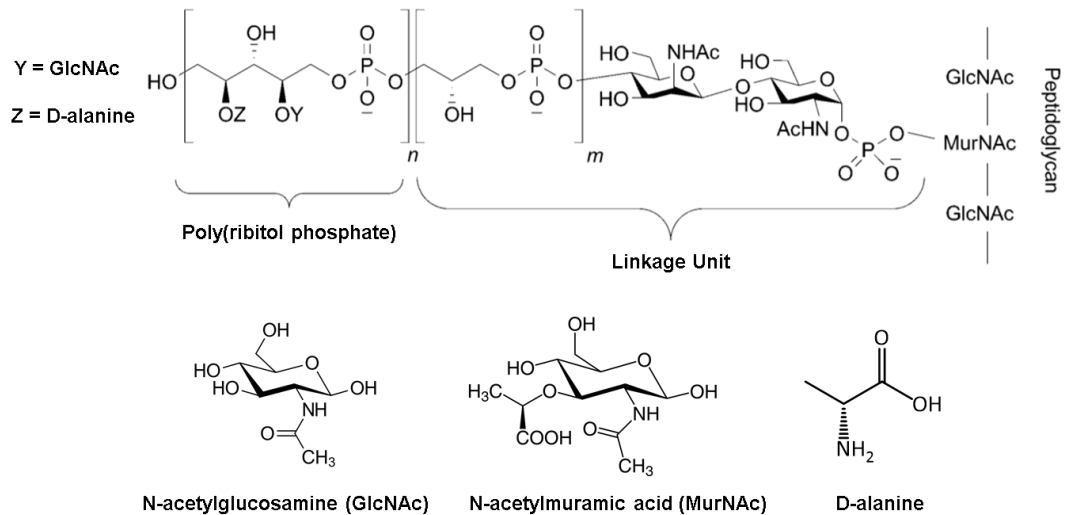


**Figure 1. 3** Representative chemical structure of teichoic acid from the wall of Gram-positive bacteria *S. aureus* ( $m=1-3$  and  $n=20-40$  repeat units). Figure adapted from reference 21.<sup>23</sup>

Although, the structural and chemical information of bacteria cell wall suggests different hydrophobic/ hydrophilic properties, the overall hydrophobic/ hydrophilic nature of the bacteria cell surface is strain specific and can vary depending on the surrounding conditions, such as the composition of the media.<sup>24-26</sup> For example, some strains of *Bacillus licheniformis* reduce the cell surface hydrophobicity in the presence of organic solvents and exhibit little affinity toward toxic organic compounds.<sup>27</sup>

### 1.2.2.1 Biofilm Formation

Biofilms initially start with the attachment of bacterial cells to a conditioned surface (Figure 1. 4 A), where the surface has been exposed to materials such as proteins and other molecules from the environment (e.g. medical implants in contact with biological fluids such as blood and urine).<sup>17,28–30</sup> The bacteria then adhere to the surface via physical forces (e.g. van der Waals interactions) or by bacterial appendages such as flagella.<sup>17,29–31</sup> After initial attachment, the bacteria can divide to form a monolayer of microcolonies and excrete extracellular polymeric (EPS) substances (Figure 1. 4 B) to form an extracellular polymeric matrix known as a biofilm (Figure 1. 4 C).<sup>17,29,30</sup> The matrix consists of extracellular polysaccharides, structural proteins, cell debris and nucleic acids.<sup>32</sup> The bacterial cells then proliferate, and the formed biofilm matures into a complex multi-layered structure (Figure 1. 4 D), providing protection against host defence mechanisms and antimicrobial drugs.<sup>19,30,31</sup> The biofilm then matures further, reaching a stationary phase of growth when the bacteria start to leave the biofilm and return to the planktonic state (Figure 1. 4 E).<sup>19,30</sup> These planktonic bacteria can then colonise another surface and the cycle repeats (Figure 1. 4 F), resulting in the spread of infection.<sup>19,30</sup> For this reason, there is an increased need for new solutions to prevent or control bacterial attachment to surfaces.

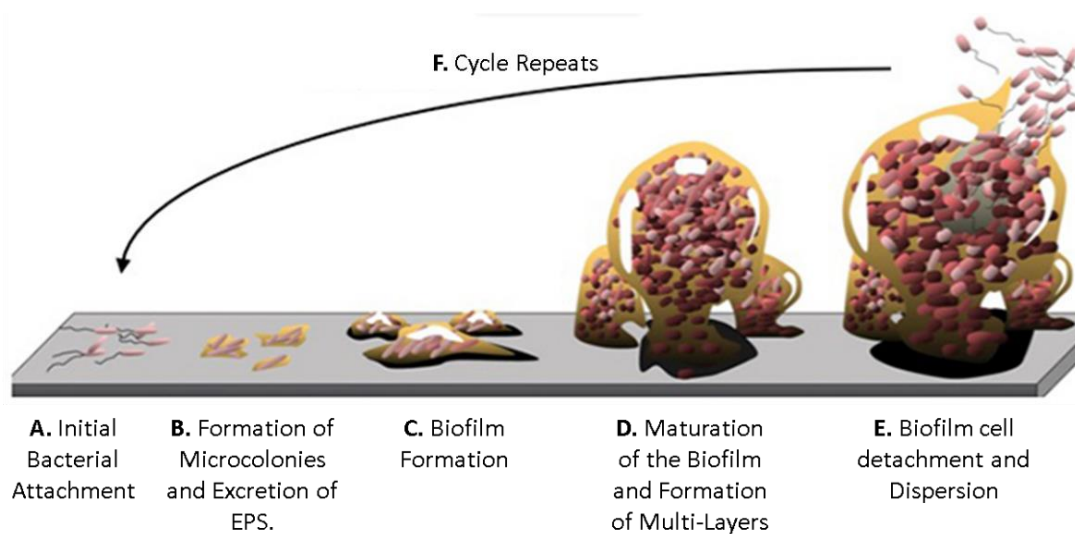


**Figure 1. 4** The five stages of biofilm formation. Figure adapted from reference 27.<sup>33</sup>

### 1.2.3 Antimicrobial Surfaces

Several strategies have been reported for repelling or killing surface attached bacteria, including anti-biofouling surfaces,<sup>34-38</sup> bactericidal surfaces<sup>39-42</sup> and photothermal treatment.<sup>43,44</sup> Anti-biofouling surfaces prevent or remove bacteria from the surface, due to unfavourable topography or chemical treatment, while bactericidal surfaces prevent the initial colonisation of bacteria by causing cell death.<sup>38</sup> Photothermal treatment can be different from these two strategies, considering that bacteria can freely colonise the surface, but are then killed by the generation of a photo-induced localised heat.<sup>43</sup> In some cases, however, the different antimicrobial surface mechanisms can be combined to form hybrid materials, displaying the properties of different antimicrobial surfaces, showing synergistic effects.<sup>45,46</sup> For example, Pallavicini *et al*<sup>45</sup> produced a surface functionalised with silica coated gold nanostars decorated with silver nanoparticles for the combined photothermal treatment and biocidal release.

Antimicrobial surfaces now encompass a broad and very attractive area of research, and many strategies can be found in literature regarding their fabrication and their associated antimicrobial mechanisms, using both synthetic and natural materials. However, in the context of this thesis, we will focus on the design and implementation of antimicrobial surfaces inspired by nature, with a particular attention to the incorporation of materials derived from natural and potentially renewable products to deliver antimicrobial functions.

## 1.2.4 Nature Inspired Antimicrobial Surfaces

Much of what we have learnt regarding antimicrobial surfaces has been inspired by nature. Nature provides an unexhausted source of inspiration for scientists, particularly in the field of biomimetics, where biological systems are fundamentally studied for biotechnological applications.<sup>38</sup> Natural surfaces of living animals and plants have evolved over time, developing the ability to resist or prevent bacterial colonisation.<sup>36,38,41,47,48</sup> For example, the rigid plate structures on shark skin (Figure 1. 5) are known to be a key factor in the prevention of biofouling.<sup>48-50</sup> The rigid plates are oriented parallel to the swimming direction, reducing drag, allowing the water layer next to the skin to move faster, preventing the settlement of microorganisms, such as bacteria. In addition, microorganisms are also deterred from settlement on the surface of the shark skin as they prefer particular groove widths and depths for settlement.<sup>51</sup> Reports also suggest that chemical modification of surfaces may be necessary to achieve the desired level of antifouling, as mucous found on the surface of shark skin also provides lubricating and antifouling benefits.<sup>52</sup>

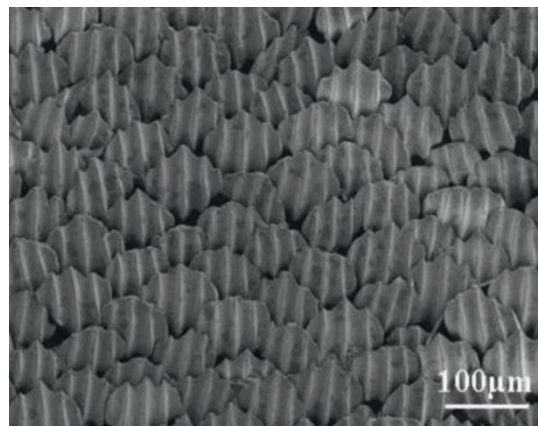


**Figure 1. 5** SEM image of the rigid plate structure of shark-skin surface from *Carcharhinus brachyurus* (Copper Shark). Figure adapted from reference 42.<sup>48</sup>

Chemical modifications of materials can confer new properties to surfaces preventing the initial attachment of bacteria or killing the bacteria after attachment to the surface.<sup>38</sup> Another example of this found in nature, is the production of the antimicrobial peptide cecropin A by insects, such as moths.<sup>53</sup> Cecropin A is one of the most extensively studied antimicrobial

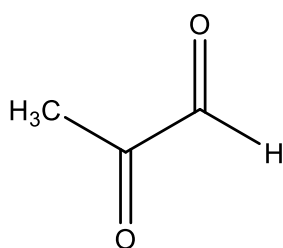
polypeptides produced by insects as components of their host defence systems against bacterial infection.<sup>53</sup> Many other animals and plants can also produce antimicrobial peptides as host defence mechanisms, and it is believed that most antimicrobial peptides act by disrupting the membrane bilayer of the bacteria through various mechanisms, including the formation of pores, disintegration of the membrane and attacking the cytoplasm and metabolic functions of the cells.<sup>54,55</sup> Several different antimicrobial peptides have been incorporated into materials to create antimicrobial surfaces.<sup>56-60</sup> For example, Yüksel and Karakeçili<sup>57</sup> reported the incorporation of antimicrobial peptide Magainin II (a 23-residue peptide extracted from the skin of *Xenopus laevis* (South African clawed frog))<sup>61</sup> on poly(lactic-co-glycolic acid) (PLGA)-electrospun nanofibres, exhibiting antimicrobial activity towards both *E. coli* and *S. aureus* bacteria. Unfortunately, antimicrobial peptides are currently prepared using processes which are often laborious, expensive and of low-yield, thus hindering large scale applications.<sup>62</sup> As a result, other natural products, such as antimicrobial agents derived from plants are now being sought as an alternative to antibiotics and antimicrobial peptides, with the incorporation of these natural products into new materials for potential applications in wound dressing and medical devices.<sup>6</sup>

#### 1.2.4.1 Antimicrobial Agents Derived from Plants for the Production of Antimicrobial Surfaces

Plant-derived antimicrobial agents, such as Manuka honey, propolis and essential oils (e.g. carvacrol) have been investigated recently for their antimicrobial activity and have been successfully incorporated into materials to create antimicrobial surfaces.<sup>54-67, 69-74</sup> Manuka honey is produced by honeybees ingesting nectar from the Manuka trees, processing it and storing the substance into honeycombs as food stocks.<sup>63</sup> Manuka honey has proven to be an effective antimicrobial towards a range of different bacterial species and has been reported to owe its antimicrobial activity to the production of hydrogen peroxide (H<sub>2</sub>O<sub>2</sub>) and the presence

of methylglyoxal (Figure 1. 6), a keto-aldehyde yellow liquid.<sup>64-74</sup> As a result, Manuka honey has been incorporated into a range of materials for antimicrobial applications.<sup>64,66,74,75</sup> For example, Carr *et al*<sup>64</sup> coated TENCEL<sup>®</sup>, a cellulose based fabric with Manuka honey for the potential as antimicrobial wound dressings. The coated fabric dressings exhibited an antimicrobial activity towards *S. aureus*, *K. pneumoniae* and *E. coli* bacteria.

Propolis is also a product of the honeybee and is derived from honey and the secretion glands of worker honeybees, to produce a resinous substance consisting of a complex mixture of flavonoid aglycones, phenolic acids and aldehydes, steroids, amino acids and natural pigments (e.g. chlorophyll and carotenoids) and is used by the honeybee as a sealant for unwanted open spaces in the hive.<sup>66-68</sup> Propolis has been reported to owe its antimicrobial activity to the phenolic compounds present in the resinous mixture and have been successfully incorporated into materials for applications as antimicrobial surfaces.<sup>76,77,79,80</sup> For example, Kim *et al*<sup>79</sup> successfully incorporated propolis into polyurethane nanofibres, exhibiting an inhibitory effect towards *E. coli* bacteria.



Methylglyoxal

**Figure 1. 6** Chemical Structure of methylglyoxal, the active antimicrobial agent associated with Manuka Honey.

Essential oils derived from plants have also demonstrated antimicrobial activity, attributed to hydrophobic terpenoid and phenolic compounds present in the essential oils. It is believed that these compounds permeate cell membranes and lead to depletion of protons, disruption of adenosine triphosphate (ATP) synthesis, and in some cases cause cell lysis.<sup>81</sup> Essential oils are

concentrated hydrophobic liquids containing volatile compounds extracted from plants, often with a specific aroma and have been incorporated into several different materials as potential antimicrobial surfaces.<sup>80-82</sup> For example, Liakos *et al*<sup>82</sup> incorporated essential oils of cinnamon, lemongrass and peppermint into a cellulose based fabric as a potential wound dressing, exhibiting an inhibitory effect towards *E. coli* bacteria.

Herein, we look at an alternative approach to the production of antimicrobial surfaces using products that can be derived from natural or cheap materials. We employ a polymer commonly used for the fabrication of medical implants, known as polydimethylsiloxane (PDMS)<sup>83-87</sup> and incorporate fatty acids as antimicrobial agents<sup>88-97</sup> for the controlled biocidal release (Chapter 3). Fatty acids are abundant biomolecules that naturally occur in most living organisms and are one of the main constituents of natural fats and oils (e.g. Palm Oil).<sup>98,99</sup> We also developed a novel approach to fabricate a photothermal material, by the incorporation of a carbon nanopowder into PDMS, that can be potentially produced by pyrolysis of organic waste,<sup>100</sup> for the combined photothermal eradication of bacteria and photothermally controlled release of fatty acids as antimicrobial agents (Chapter 4).

Another strategy to prevent bacterial infections is the photocatalytic generation of reactive oxygen species (ROS).<sup>101-103</sup> ROS have proven antimicrobial activity against a wide spectrum of pathogens of both Gram-positive and Gram-negative bacteria, including highly antimicrobial resistant strains.<sup>102-107</sup> The term ROS refers to reactive moieties containing oxygen(O<sub>2</sub>), including superoxide anion (O<sub>2</sub><sup>-</sup>), singlet oxygen (<sup>1</sup>O<sub>2</sub>), peroxide (O<sub>2</sub><sup>-2</sup>), hydrogen peroxide (H<sub>2</sub>O<sub>2</sub>), hydroxyl radicals (OH•), and hydroxyl (OH<sup>-</sup>) ions.<sup>106</sup> The antimicrobial mechanism of ROS is still the subject of much debate, although the current understanding is ROS induces oxidative stress, damaging virtually all types of organic biomolecules within the

bacteria cell, including carbohydrates, nucleic acids (RNA and DNA), lipids, proteins, and amino acids.<sup>107</sup>

ROS can be photocatalytically produced by metal oxide nanoparticles, such as the semiconductor titanium dioxide (TiO<sub>2</sub>).<sup>105,107</sup> TiO<sub>2</sub> is a naturally occurring oxide of titanium, with three natural crystallite forms of Rutile, Anatase and Brookite. These changes in the crystal structure of TiO<sub>2</sub> significantly impact the semi-conducting properties of the material, for example Rutile TiO<sub>2</sub> has a band gap energy of 3.02 eV, while the Anatase and Brookite crystallites have a band energy of 3.2 eV and 2.96 eV, respectively.<sup>108</sup>

TiO<sub>2</sub> has been employed as a catalyst in wide range of applications, for example: coatings for self-cleaning windows;<sup>109,110</sup> photocatalytic degradation of organic materials;<sup>111,112</sup> incorporated into sun cream providing a barrier against UV radiation<sup>113,114</sup> and the photocatalytic production of hydrogen from water.<sup>115-119</sup> However, more recently, research has led to the use of TiO<sub>2</sub> in medical applications, such as the treatment of cancer and bacterial infections, owing to its ability to produce ROS species. In this system, after initial photo excitation, excited electrons can catalyse the reduction of oxygen to produce O<sub>2</sub><sup>-</sup>, while the electron hole left behind as a result of electron excitation breaks down water to generate OH• through an oxidative process.<sup>105,107</sup> The design of a system that can enhance the catalytic process, increasing the generation of ROS with these types of materials is therefore of great interest. Similar systems, based on this idea, are currently also under intense study for the photocatalytic production of renewable energy.<sup>120-125</sup> The design and fabrication of antimicrobial surfaces based on photocatalysis, in the context of renewable energy can therefore provide further insights towards the development and enhancement of photocatalytic ROS generation.

## 1.3 Functional Materials for the Sustainable Production of Renewable Energy

Energy is an essential requirement for the development of modern society and is therefore one of the world's largest and most important markets, influencing economy in a myriad of ways, including the supply of electricity to our homes, fuel for our cars, enabling modern agriculture and more.<sup>126,127</sup> Although, the world's energy consumption is still primarily dependent on fossil fuels, including oil, coal and natural gas (Figure 1. 7), which have largely been depleted over the past century.<sup>126-128</sup> Fossil fuels are unsustainable and have a direct impact on the environment, including the release of harmful greenhouse gases (e.g. carbon dioxide (CO<sub>2</sub>)) as a result of combustion.<sup>127</sup> For these reasons, there has been an increasing interest in the production of alternative and renewable energy sources, with a low carbon footprint.

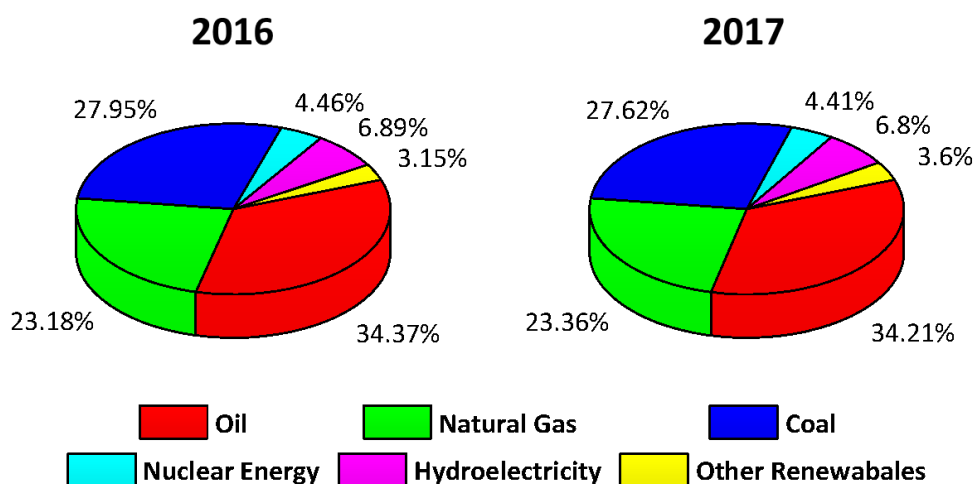


**Figure 1. 7** Global energy consumption in 2016 and 2017 shown as a percentage (%). Data taken from reference 109.<sup>128</sup>

Renewable and sustainable technologies are considered as clean sources of energy, with minimal or no environmental impact.<sup>129</sup> Hydrogen (H<sub>2</sub>) is a potential alternative fuel source that can replace fossil fuels and it is of particular interest considering its low environmental impact. H<sub>2</sub> produces a high energy yield (120 kJ g<sup>-1</sup>) and generates water (H<sub>2</sub>O) as the only by-product of H<sub>2</sub> combustion and is therefore considered a pollutant free technology.<sup>127</sup> However, to present day, the world's supply of hydrogen is still predominately derived from

fossil fuels, via the steam reforming of methane (CH<sub>4</sub>) (Figure 1. 8 A).<sup>130</sup> At high temperatures and in the presence of metal catalysts, such as Nickel or Iron, steam reacts with CH<sub>4</sub> to produce carbon monoxide (CO) and H<sub>2</sub>.<sup>131,132</sup> CO can then go on further to react with H<sub>2</sub>O via the water-gas shift reaction (Figure 1. 8 B), in the presence of a hot iron oxide or cobalt oxide catalyst, to produce additional H<sub>2</sub>.<sup>131,132</sup> As a result of this, CO<sub>2</sub> is also produced as a by-product, leaving a carbon footprint. This contradiction, together with the need of high temperatures and fossil fuels is energy inefficient and suboptimal in terms of alternative fuel technologies. As a result, new sustainable strategies to produce H<sub>2</sub> need to be considered, with a low carbon footprint, e.g. solar energy.

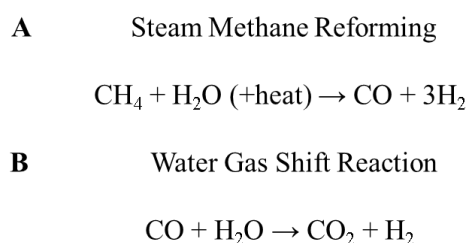


**Figure 1. 8** Reaction scheme for the production of H<sub>2</sub> by the steam reforming process (A) and the water-gas shift reaction (B).<sup>131</sup>

Solar energy is by far the largest exploitable and renewable resource. The sun delivers more energy to the earth in one hour than all the energy consumed by humans in an entire year.<sup>126</sup> Its potential as a renewable energy source to produce fuels (e.g. H<sub>2</sub>), termed solar fuels, is therefore of considerable interest. One avenue to produce solar fuel is the photosynthetic production of fuel by the conversion of light to chemical energy, such as mimicking the photosynthetic processes displayed in nature by plants and other organisms (e.g. algae).<sup>133</sup> In natural photosynthesis, chlorophyll (Figure 1. 9), a natural pigment found in plants and other organisms, absorbs light to excite an electron from a lower energy state to a higher energy state. The excited electron is then used to catalyse the transformation of H<sub>2</sub>O and CO<sub>2</sub> into carbohydrates (e.g. sugars) through enzymatic catalysis, with molecular oxygen (O<sub>2</sub>) generated as a by-product. The energy stored in the carbohydrates can then be released to fuel the metabolic activity of plants and other organisms.<sup>134</sup>

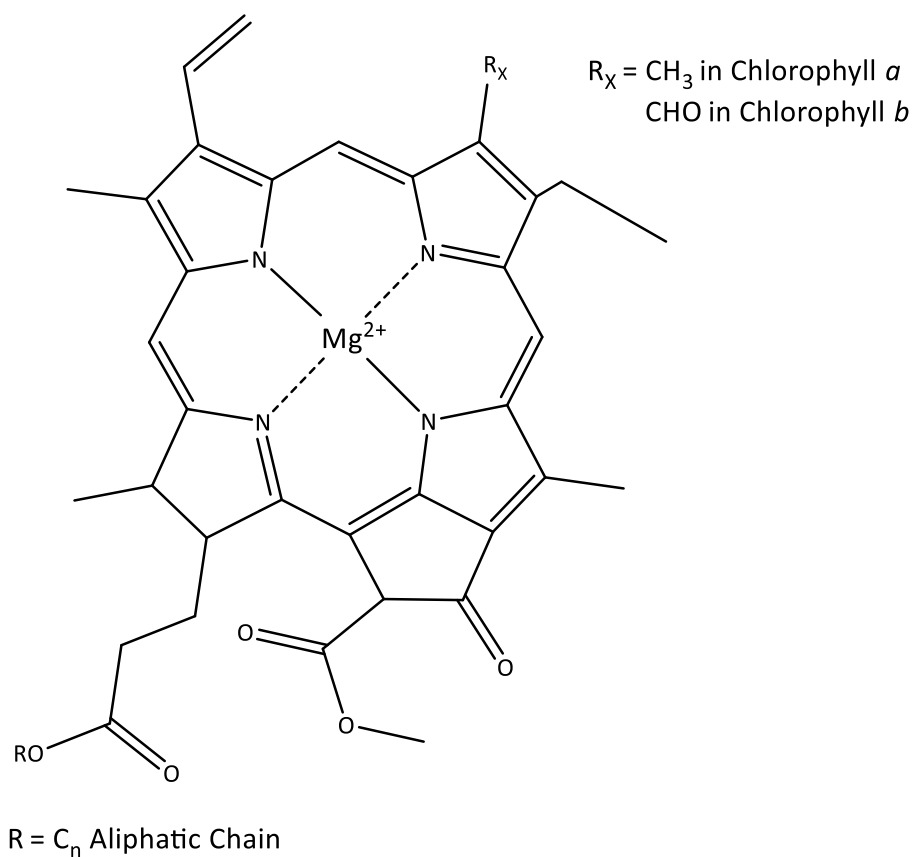


**Figure 1. 9** General structure of chlorophyll pigment found in plants and other organisms, showing the structure of chlorophyll *a* and chlorophyll *b*.<sup>19</sup>

The possibility of using solar energy to produce fuel by mimicking natural photosynthetic processes, often termed artificial photosynthesis, initially appeared unrealistic and intrigued scientists for more than a century.<sup>135</sup> However, thanks to the tremendous efforts of researchers, it is now becoming feasible, with the production of new functional materials to produce fuels through artificial photosynthesis, such as H<sub>2</sub>, by the decomposition of H<sub>2</sub>O.<sup>116,118,120,136</sup> However, current photocatalytic H<sub>2</sub> evolution systems are not sustainable.<sup>130</sup> As a result, new photocatalytic technologies to produce H<sub>2</sub> need to be considered, including the production of new photocatalysts for the sustainable photocatalytic evolution of H<sub>2</sub> from H<sub>2</sub>O. In addition to this, the photocatalysts also need to be both reusable and robust to remain cost effective.

Herein, we report a novel wet chemical approach to produce a plasmonically enhanced photocatalytically active nano-hybrid material, using silver nanoparticles (AgNPs) as a plasmonic core, coupled with cadmium sulphide quantum dots functionalised with platinum (CdS@Pt QDs), separated by a silica (SiO<sub>2</sub>) dielectric layer, for the potential photocatalytic production of H<sub>2</sub> from H<sub>2</sub>O. Plasmonic nanomaterials have been known for their photoactive properties for over 160 years<sup>137</sup> and are widely used for applications in several different fields,<sup>121,138–142</sup> with recent reports documenting a plasmonic enhanced catalysis towards H<sub>2</sub> evolution from H<sub>2</sub>O.<sup>121,123–125,143–146</sup> Most of this work has predominately used gold nanoparticles as plasmonic units and therefore little is known regarding the experimental effect of AgNPs in these photocatalytic systems. As a result, we have investigated both the photocatalytic activity and stability of these nanomaterials under active working conditions.

## 1.4 References

- 1 F. Liebner and T. Rosenau, *Functional Materials from Renewable Sources*, American Chemical Society, Washington, DC, 2012, vol. 1107.
- 2 H.-G. Woo and H. Li, *Advanced functional materials*, Zhejiang University Press, 1st Edition, 2011.
- 3 M. Leclerc and R. Gauvin, *Functional Materials: For Energy, Sustainable Development and Biomedical Sciences*, De Gruyter, 1st Edition, 2014.
- 4 M. A. Hayashi, F. C. Bizerra, P. I. Da Silva, *Front. Microbiol.*, 2013, **4**, 195.
- 5 J. Ali, Q. A. Rafiq and E. Ratcliffe, *Futur. Sci. OA*, 2018, **4**, 1–9.
- 6 J. Wang, W. Vermerris, J. Wang and W. Vermerris, *Materials (Basel)*, 2016, **9**, 255.
- 7 S. Bin Zaman, M. A. Hussain, R. Nye, V. Mehta, K. T. Mamun and N. Hossain, *Cureus*, 2017, **9**, 1403–1412.
- 8 V. Cepas, Y. López, E. Muñoz, D. Rolo, C. Ardanuy, S. Martí, M. Xercavins, J. P. Horcajada, J. Bosch and S. M. Soto, *Microb. Drug Resist.*, 2019, **25**, 72–79.
- 9 R. M. Donlan and J. W. Costerton, *Clin. Microbiol. Rev.*, 2002, **15**, 167–93.
- 10 H.-C. Flemming, J. Wingender, U. Szewzyk, P. Steinberg, S. A. Rice and S. Kjelleberg, *Nat. Rev. Microbiol.*, 2016, **14**, 563–75.
- 11 L. Hall-Stoodley, J. W. Costerton and P. Stoodley, *Nat. Rev. Microbiol.*, 2004, **2**, 95–108.
- 12 K. Lewis, in *Current Topics in Microbiology and Immunology*, T. Romeo, Springer, Berlin, Heidelberg, Berlin, 322nd Edition, 2008, 107–131.
- 13 D. Mack, P. Becker, I. Chatterjee, S. Dobinsky, J. K.-M. Knobloch, G. Peters, H. Rohde and M. Herrmann, *Int. J. Med. Microbiol.*, 2004, **294**, 203–212.

- 14 A. Almatroudi, S. Tahir, H. Hu, D. Chowdhury, I. B. Gosbell, S. O. Jensen, G. S. Whiteley, A. K. Deva, T. Glasbey and K. Vickery, *J. Hosp. Infect.*, 2018, **98**, 161–167.
- 15 M. Farhat, M. C. Trouilhé, E. Briand, M. Moletta-Denat, E. Robine and J. Frère, *J. Appl. Microbiol.*, 2010, **108**, 1073–1082.
- 16 F. Longo, C. Vuotto and G. Donelli, *New Microbiol.*, 2014, **37**, 119–27.
- 17 J. M. Willey, L. Sherwood, C. J. Woolverton and L. M. Prescott, *Prescott, Harley, and Klein's microbiology*, McGraw-Hill Higher Education, 7th Edition, 2008.
- 18 P.-Y. Litzler, L. Benard, N. Barbier-Frebourg, S. Vilain, T. Jouenne, E. Beucher, C. Bunel, J.-F. Lemeland and J.-P. Bessou, *J. Thorac. Cardiovasc. Surg.*, 2007, **134**, 1025–1032.
- 19 J. Slonczewski and J. W. Foster, *Microbiology : An Evolving Science*, W. W. Norton & Company, London, 4th Edition, 2017.
- 20 L. Brown, J. M. Wolf, R. Prados-Rosales and A. Casadevall, *Nat. Rev. Microbiol.*, 2015, **13**, 620–630.
- 21 I. Barák and K. Muchová, *Int. J. Mol. Sci.*, 2013, **14**, 4050–65.
- 22 D. van der Es, W. F. J. Hogendorf, H. S. Overkleeft, G. A. van der Marel and J. D. C. Codée, *Chem. Soc. Rev.*, 2017, **46**, 1464–1482.
- 23 J. G. Swoboda, J. Campbell, T. C. Meredith and S. Walker, *ChemBioChem*, 2010, **11**, 35–45.
- 24 A. Krasowska and K. Sigler, *Front. Cell. Infect. Microbiol.*, 2014, **4**, 112.
- 25 H. J. Heipieper, S. Cornelissen and M. Pepi, in *Handbook of Hydrocarbon and Lipid Microbiology*, K. N. Timmis, Springer Berlin Heidelberg, Berlin, Heidelberg, 1st Edition, 2010, pp. 1615–1624.
- 26 F. Hamadi, H. Latrache, H. Zahir, A. Elghmari, M. Timinouni and M. Ellouali, *Braz.*

- J. Microbiol.*, 2008, **39**, 10–5.
- 27 S. Torres, A. Pandey and G. R. Castro, *Biotechnol. Adv.*, 2011, **29**, 442–452.
- 28 M. W. Mittleman, in *Bacterial Adhesion: Molecular and Ecological Diversity*, Fletcher. M, Wiley, 1st Edition, 1996, 89–127.
- 29 T. R. Garrett, M. Bhakoo and Z. Zhang, *Prog. Nat. Sci.*, 2008, **18**, 1049–1056.
- 30 R. M. Donlan, *Emerg. Infect. Dis.*, 2002, **8**, 881–890.
- 31 M. Jamal, W. Ahmad, S. Andleeb, F. Jalil, M. Imran, M. A. Nawaz, T. Hussain, M. Ali, M. Rafiq and M. A. Kamil, *J. Chinese Med. Assoc.*, 2018, **81**, 7–11.
- 32 I. Dogsa, M. Kriechbaum, D. Stopar and P. Laggner, *Biophys. J.*, 2005, **89**, 2711–2720.
- 33 D. Monroe, *PLoS Biol.*, 2007, **5**, 2458–2461.
- 34 M. Michailidis, I. Sorzabal-Bellido, E. A. Adamidou, Y. A. Diaz-Fernandez, J. Aveyard, R. Wengier, D. Grigoriev, R. Raval, Y. Benayahu, R. A. D'Sa and D. Shchukin, *ACS Appl. Mater. Interfaces*, 2017, **9**, 38364–38372.
- 35 E. P. Ivanova, V. K. Truong, H. K. Webb, V. A. Baulin, J. Y. Wang, N. Mohammadi, F. Wang, C. Fluke and R. J. Crawford, *Sci. Rep.*, 2011, **1**, 165.
- 36 V. B. Damodaran and S. N. Murthy, *Biomater. Res.*, 2016, **20**, 1–11.
- 37 B. Mrabet, M. N. Nguyen, A. Majbri, S. Mahouche, M. Turmine, A. Bakhrouf and M. Chehimi, *Surf. Sci.*, 2009, **603**, 2422–2429.
- 38 J. Hasan, R. J. Crawford and E. P. Ivanova, *Trends Biotechnol.*, 2013, **31**, 295–304.
- 39 A. Taglietti, C. R. Arciola, A. D'Agostino, G. Dacarro, L. Montanaro, D. Campoccia, L. Cucca, M. Vercellino, A. Poggi, P. Pallavicini and L. Visai, *Biomaterials*, 2014, **35**, 1779–1788.
- 40 A. Susarrey-Arce, I. Sorzabal-Bellido, A. Oknianska, F. McBride, A. J. Beckett, J. G.

- E. Gardeniers, R. Raval, R. M. Tiggelaar and Y. A. Diaz Fernandez, *J. Mater. Chem. B*, 2016, **4**, 3104–3112.
- 41 C. D. Bandara, S. Singh, I. O. Afara, A. Wolff, T. Tesfamichael, K. Ostrikov and A. Oloyede, *ACS Appl. Mater. Interfaces*, 2017, **9**, 6746–6760.
- 42 G. S. Watson, D. W. Green, L. Schwarzkopf, X. Li, B. W. Cribb, S. Myhra and J. A. Watson, *Acta Biomater.*, 2015, **21**, 109–122.
- 43 P. Pallavicini, A. Donà, A. Taglietti, P. Minzioni, M. Patrini, G. Dacarro, G. Chirico, L. Sironi, N. Bloise, L. Visai and L. Scarabelli, *Chem. Commun.*, 2014, **50**, 1969–1971.
- 44 T. Akasaka, M. Matsuoka, T. Hashimoto, S. Abe, M. Uo and F. Watari, *Mater. Sci. Eng. B*, 2010, **173**, 187–190.
- 45 P. Pallavicini, B. Bassi, G. Chirico, M. Collini, G. Dacarro, E. Fratini, P. Grisoli, M. Patrini, L. Sironi, A. Taglietti, M. Moritz, I. Sorzabal-Bellido, A. Susarrey-Arce, E. Latter, A. J. Beckett, I. A. Prior, R. Raval and Y. A. Diaz Fernandez, *Sci. Rep.*, 2017, **7**, 5259.
- 46 Z. Cao, L. Mi, J. Mendiola, J. R. Ella-Menye, L. Zhang, H. Xue and S. Jiang, *Angew. Chemie - Int.*, 2012, **51**, 2602–2605.
- 47 E. P. Ivanova, J. Hasan, H. K. Webb, V. K. Truong, G. S. Watson, J. A. Watson, V. A. Baulin, S. Pogodin, J. Y. Wang, M. J. Tobin, C. Löbbe and R. J. Crawford, *Small*, 2012, **8**, 2489–2494.
- 48 X. Pu, G. Li and Y. Liu, *ChemBioEng Rev.*, 2016, **3**, 26–40.
- 49 S. Rigo, C. Cai, G. Gunkel-Grabole, L. Maurizi, X. Zhang, J. Xu and C. G. Palivan, *Adv. Sci.*, 2018, **5**, 1700892.
- 50 K. Efimenko, J. Finlay, M. E. Callow, J. A. Callow and J. Genzer, *ACS Appl. Mater. Interfaces*, 2009, **1**, 1031–1040.

- 51 G. D. Bixler and B. Bhushan, *Philos. Trans. R. Soc. A Math. Phys. Eng. Sci.*, 2012, **370**, 2381–2417.
- 52 G. D. Bixler and B. Bhushan, *Soft Matter*, 2012, **8**, 11271–11284.
- 53 L. Silvestro, J. N. Weiser and P. H. Axelsen, *Antimicrob. Agents Chemother.*, 2000, **44**, 602–607.
- 54 R. E. W. Hancock and H. G. Sahl, *Nat. Biotechnol.*, 2006, **24**, 1551–1557.
- 55 L. T. Nguyen, E. F. Haney and H. J. Vogel, *Trends Biotechnol.*, 2011, **29**, 464–472.
- 56 P. Cao, C. Yuan, J. Xiao, X. He and X. Bai, *Surf. Interface Anal.*, 2018, **50**, 516–521.
- 57 E. Yüksel and A. Karakeçili, *Mater. Sci. Eng. C*, 2014, **45**, 510–518.
- 58 J. He, J. Chen, G. Hu, L. Wang, J. Zheng, J. Zhan, Y. Zhu, C. Zhong, X. Shi, S. Liu, Y. Wang and L. Ren, *J. Mater. Chem. B*, 2017, **6**, 68–74.
- 59 S. Ghamrawi, J. P. Bouchara, O. Tarasyuk, S. Rogalsky, L. Lyoshina, O. Bulko and J. F. Bardeau, *Mater. Sci. Eng. C*, 2017, **75**, 969–979.
- 60 M. Mateescu, S. Baixe, T. Garnier, L. Jierry, V. Ball, Y. Haikel, M. H. Metz-Boutigue, M. Nardin, P. Schaaf, O. Etienne and P. Lavallo, *PLoS One*, 2015, **10**, 145143.
- 61 M. Zasloff, *Proc. Natl. Acad. Sci. U. S. A.*, 1987, **84**, 5449–53.
- 62 B. Sun, D. Wibowo, A. P. J. Middelberg and C. X. Zhao, *AMB Express*, 2018, **8**, 6.
- 63 D. T. Burns, A. Dillon, J. Warren and M. J. Walker, *Food Anal. Methods*, 2018, **11**, 1561–1567.
- 64 S. E. L. Bulman, G. Tronci, P. Goswami, C. Carr, S. J. Russell, S. E. L. Bulman, G. Tronci, P. Goswami, C. Carr and S. J. Russell, *Materials (Basel)*, 2017, **10**, 954.
- 65 S. E. Maddocks, M. S. Lopez, R. S. Rowlands and R. A. Cooper, *Microbiology*, 2012, **158**, 781–790.

- 66 G. Gethin and S. Cowman, *J. Wound Care*, 2008, **17**, 241–247.
- 67 O. Sherlock, A. Dolan, R. Athman, A. Power, G. Gethin, S. Cowman and H. Humphreys, *BMC Complement. Altern. Med.*, 2010, **10**, 47.
- 68 J. Majtan, J. Bohova, M. Horniackova, J. Klaudiny and V. Majtan, *Phyther. Res.*, 2014, **28**, 69–75.
- 69 R. Cooper, L. Jenkins and S. Hooper, *J. Wound Care*, 2014, **23**, 93–104.
- 70 A. F. Henriques, R. E. Jenkins, N. F. Burton and R. A. Cooper, *Eur. J. Clin. Microbiol. Infect. Dis.*, 2011, **30**, 167–171.
- 71 R. Jenkins, N. Burton and R. Cooper, *J. Antimicrob. Chemother.*, 2011, **66**, 2536–2542.
- 72 C. J. Adams, M. Manley-Harris and P. C. Molan, *Carbohydr. Res.*, 2009, **344**, 1050–1053.
- 73 E. Mavric, S. Wittmann, G. Barth and T. Henle, *Mol. Nutr. Food Res.*, 2008, **52**, 483–489.
- 74 P. U. Kadakia, E. A. Growney Kalaf, A. J. Dunn, L. P. Shornick and S. A. Sell, *J. Bioact. Compat. Polym.*, 2018, **33**, 79–94.
- 75 S. EL Bulman, P. Goswami, G. Tronci, S. J. Russell and C. Carr, *J. Biomater. Appl.*, 2015, **29**, 1193–1200.
- 76 E. C. E. Gebara, L. A. Lima and M. P. A. Mayer, *Brazilian J. Microbiol.*, 2002, **33**, 365–369.
- 77 S. Stepanović, N. Antić, I. Dakić and M. Švabić-Vlahović, *Microbiol. Res.*, 2003, **158**, 353–357.
- 78 M. Simone-Finstrom and M. Spivak, *Apidologie*, 2010, **41**, 295–311.
- 79 J. I. Kim, H. R. Pant, H. J. Sim, K. M. Lee and C. S. Kim, *Mater. Sci. Eng. C*, 2014,

- 44**, 52–57.
- 80 A. J. Silva, J. R. Silva, N. C. de Souza and P. C. S. Souto, *Mater. Lett.*, 2014, **116**, 235–238.
- 81 S. Burt, *Int. J. Food Microbiol.*, 2004, **94**, 223–253.
- 82 I. Liakos, L. Rizzello, H. Hajiali, V. Brunetti, R. Carzino, P. P. Pompa, A. Athanassiou and E. Mele, *J. Mater. Chem. B*, 2015, **3**, 1583–1589.
- 83 F. Abbasi, H. Mirzadeh and A. A. Katbab, *Polym. Int.*, 2001, **50**, 1279–1287.
- 84 M. K. Kwak, H. E. Jeong and K. Y. Suh, *Adv. Mater.*, 2011, **23**, 3949–3953.
- 85 S. Barr, E. W. Hill and A. Bayat, *Acta Biomater.*, 2017, **49**, 260–271.
- 86 R. K. Malcolm, K. L. Edwards, P. Kiser, J. Romano and T. J. Smith, *Antiviral Res.*, 2010, **88**, 30–39.
- 87 A. Kottmann, E. Mejía, T. Hémerly, J. Klein and U. Kragl, *Chem. - An Asian J.*, 2017, **12**, 1168–1179.
- 88 A. P. Desbois and V. J. Smith, *Appl. Microbiol. Biotechnol.*, 2010, **85**, 1629–1642.
- 89 M. Masuda, M. Era, T. Kawahara, T. Kanyama and H. Morita, *Biocontrol Sci.*, 2015, **20**, 209–213.
- 90 J. S. Choi, N. H. Park, S. Y. Hwang, J. H. Sohn, I. Kwak, K. K. Cho and I. S. Choi, *J. Environ. Biol.*, 2013, **34**, 673–676.
- 91 J. B. Parsons, J. Yao, M. W. Frank, P. Jackson and C. O. Rock, *J. Bacteriol.*, 2012, **194**, 5294–5304.
- 92 C. B. Huang, Y. Alimova, T. M. Myers and J. L. Ebersole, *Arch. Oral Biol.*, 2011, **56**, 650–654.
- 93 T. Kitahara, N. Koyama, J. Matsuda, Y. Aoyama, Y. Hirakata, S. Kamihira, S. Kohno,

- M. Nakashima and H. Sasaki, *Biol. Pharm. Bull.*, 2004, **27**, 1321–1326.
- 94 J. A. Jackman, B. K. Yoon, D. Li and N. J. Cho, *Molecules*, 2016, **21**, 1–19.
- 95 D. R. Drake, K. A. Brogden, D. V. Dawson and P. W. Wertz, *J. Lipid Res.*, 2008, **49**, 4–11.
- 96 J. J. Kabara, D. M. Swieczkowski, A. J. Conley and J. P. Truant, *Antimicrob. Agents Chemother.*, 1972, **2**, 23–28.
- 97 L. J. McGaw, A. K. Jäger and J. Van Staden, *South African J. Bot.*, 2002, **68**, 417–423.
- 98 L. Spitz and CRC Press., *SODEOPEC: soaps, detergents, oleochemicals, and personal care products*, AOCS Press, 1st Edition, 2004.
- 99 J. Orsavova, L. Misurcova, J. Vavra Ambrozova, R. Vicha and J. Mlcek, *Int. J. Mol. Sci.*, 2015, **16**, 12871–12890.
- 100 J. Deng, Y. You, V. Sahajwalla and R. K. Joshi, *Carbon N. Y.*, 2016, **96**, 105–115.
- 101 M. Dryden, *Int. J. Antimicrob. Agents*, 2018, **51**, 299–303.
- 102 B. Jalvo, M. Faraldos, A. Bahamonde and R. Rosal, *J. Hazard. Mater.*, 2017, **340**, 160–170.
- 103 Y. Feng, L. Liu, J. Zhang, H. Aslan and M. Dong, *J. Mater. Chem. B*, 2017, **5**, 8631–8652.
- 104 V. S. Khodade, M. Sharath Chandra, A. Banerjee, S. Lahiri, M. Pulipeta, R. Rangarajan and H. Chakrapani, *ACS Med. Chem. Lett.*, 2014, **5**, 777–781.
- 105 S. Parham, D. H. B. Wicaksono, S. Bagherbaigi, S. L. Lee and H. Nur, *J. Chinese Chem. Soc.*, 2016, **63**, 385–393.
- 106 M. Y. Memar, R. Ghotaslou, M. Samiei and K. Adibkia, *Infect. Drug Resist.*, 2018, **11**, 567–576.

- 107 L. Yang, Z. Wen, N. Junfeng and C. Yongsheng, *ACS Nano*, 2012, **6**, 5164–5173.
- 108 S. M. Gupta and M. Tripathi, *Chinese Sci. Bull.*, 2011, **56**, 1639–1657.
- 109 V. A. Ganesh, H. K. Raut, A. S. Nair and S. Ramakrishna, *J. Mater. Chem.*, 2011, **21**, 16304–16322.
- 110 E. I. Cedillo-González, R. Riccò, M. Montorsi, M. Montorsi, P. Falcaro and C. Siligardi, *Build. Environ.*, 2014, **71**, 7–14.
- 111 A. Ajmal, I. Majeed, R. N. Malik, H. Idriss and M. A. Nadeem, *RSC Adv.*, 2014, **4**, 37003–37026.
- 112 J. Yang, C. Chen, H. Ji, W. Ma and J. Zhao, *J. Phys. Chem. B*, 2005, **109**, 21900–21907.
- 113 J. F. Jacobs, I. van de Poel and P. Osseweijer, *Nanoethics*, 2010, **4**, 103–113.
- 114 M. Trivedi and J. Murase, in *Application of Titanium Dioxide*, M. Janus, InTech, London, 1st Edition, 2017, pp. 61–71.
- 115 E. P. Melián, O. G. Díaz, A. O. Méndez, C. R. López, M. N. Suárez, J. M. D. Rodríguez, J. A. Navío, D. F. Hevia and J. P. Peña, *Int. J. Hydrogen Energy*, 2013, **38**, 2144–2155.
- 116 M. Ashokkumar, *Int. J. Hydrogen Energy*, 1998, **23**, 427–438.
- 117 H. Ahmad, S. K. Kamarudin, L. J. Minggu and M. Kassim, *Renew. Sustain. Energy Rev.*, 2015, **43**, 599–610.
- 118 A. Fujishima and K. Honda, *Nature*, 1972, **238**, 37–38.
- 119 D. A. J. Rand and R. M. Dells, in *Hydrogen Energy: Challenges and Prospects*, Rand, D.A.J and Dell, R.M, RSC Publishing, Cambridge, 1st Edition, 2008 106–145.
- 120 N. Zhou, V. López-Puente, Q. Wang, L. Polavarapu, I. Pastoriza-Santos and Q. H. Xu, *RSC Adv.*, 2015, **5**, 29076–29097.

- 121 W. Hou and S. B. Cronin, *Adv. Funct. Mater.*, 2013, **23**, 1612–1619.
- 122 S. Zeng, X. Yu, W. C. Law, Y. Zhang, R. Hu, X. Q. Dinh, H. P. Ho and K. T. Yong, *Sensors Actuators, B Chem.*, 2013, **176**, 1128–1133.
- 123 C. Gomes Silva, R. Juárez, T. Marino, R. Molinari and H. García, *J. Am. Chem. Soc.*, 2011, **133**, 595–602.
- 124 T. Torimoto, H. Horibe, T. Kameyama, K. I. Okazaki, S. Ikeda, M. Matsumura, A. Ishikawa and H. Ishihara, *J. Phys. Chem. Lett.*, 2011, **2**, 2057–2062.
- 125 M. A. Khan, L. Sinatra, M. Oufi, O. M. Bakr and H. Idriss, *Catal. Letters*, 2017, **147**, 811–820.
- 126 C. S., Jones, S. P. and Mayfield, *Introduction to Renewable Energy and Biofuels*, University of California Press, Oakland, 1st Edition, 2016.
- 127 S. Dutta, *J. Ind. Eng. Chem.*, 2014, **20**, 1148–1156.
- 128 BP, *BP Statistical Review of World Energy, June 2018*, 2018.
- 129 N. L. Panwar, S. C. Kaushik and S. Kothari, *Renew. Sustain. Energy Rev.*, 2011, **15**, 1513–1524.
- 130 B. A. Pinaud, J. D. Benck, L. C. Seitz, A. J. Forman, Z. Chen, T. G. Deutsch, B. D. James, K. N. Baum, G. N. Baum, S. Ardo, H. Wang, E. Miller and T. F. Jaramillo, *Energy Environ. Sci.*, 2013, **6**, 1983–2002.
- 131 P. Basu, in *Biomass Gasification, Pyrolysis and Torrefaction*, P. Basu, Academic Press, 3rd Edition, 2018, 211–262.
- 132 A. Kudo and Y. Miseki, *Chem. Soc. Rev.*, 2009, **38**, 253–278.
- 133 S. Styring, *Faraday Discuss.*, 2012, **155**, 357–376.
- 134 N. Nelson and A. Ben-Shem, *Nat. Rev. Mol. Cell Biol.*, 2004, **5**, 971–982.

- 135 G. Ciamician, *Science*, 1912, **36**, 385–94.
- 136 F. E. Osterloh, *Chem. Soc. Rev.*, 2013, **42**, 2294–2320.
- 137 M. Faraday, *Philos. Trans. R. Soc. London*, 1857, **147**, 145–181.
- 138 K. A. Willets and R. P. Van Duyne, *Annu. Rev. Phys. Chem.*, 2006, **58**, 267–297.
- 139 P. C. Lee and D. Meisel, *J. Phys. Chem.*, 1982, **86**, 3391–3395.
- 140 P. Pallavicini, G. Chirico, M. Collini, G. Dacarro, A. Donà, L. D’Alfonso, A. Falqui, Y. Diaz-Fernandez, S. Freddi, B. Garofalo, A. Genovese, L. Sironi and A. Taglietti, *Chem. Commun.*, 2011, **47**, 1315–1317.
- 141 G. Chirico, P. Pallavicini and M. Collini, *Nanomedicine*, 2014, **9**, 1–3.
- 142 H. Yuan, C. G. Khoury, C. M. Wilson, G. A. Grant, A. J. Bennett and T. Vo-Dinh, *Nanomedicine Nanotechnology, Biol. Med.*, 2012, **8**, 1355–1363.
- 143 P. Zhang, T. Wang and J. Gong, *Adv. Mater.*, 2015, **27**, 5328–5342.
- 144 J. Li, G. Zhan, Y. Yu and L. Zhang, *Nat. Commun.*, 2016, **7**, 11480.
- 145 F. Su, T. Wang, R. Lv, J. Zhang, P. Zhang, J. Lu and J. Gong, *Nanoscale*, 2013, **5**, 9001–9009.
- 146 W. Hou, Z. Liu, P. Pavaskar, W. H. Hung and S. B. Cronin, *J. Catal.*, 2011, **277**, 149–153.



# Chapter 2

## Experimental Techniques

### 2.1 Introduction

The investigation of functional materials requires the use of complementary techniques able to unravel their physical and chemical properties. In this chapter, these experimental techniques, used to characterise the different materials discussed throughout the chapters of the thesis, are described. We also describe the gas chromatography technique used for the analysis of hydrogen ( $H_2$ ) produced from water ( $H_2O$ ) by the nanomaterials discussed in chapter 5. The microscopy techniques used to characterise the antimicrobial performance of the surfaces described in chapters 3 and 4, as well as the microscopy techniques used to study the morphology and stability of our nanomaterials described in chapter 5 are also discussed.

## 2.2 Techniques for Physical Characterisation

### 2.2.1 Differential Scanning Calorimetry (DSC)

DSC is an analytical technique used to measure the thermal properties of materials, by measuring the heat flow into or out of materials during a physical or chemical process. This heat flow, expressed as power (mW), can be measured as a function of temperature under controlled atmosphere conditions. As a result, transitions that occur within the material over a temperature range are revealed, such as melting and re-crystallisation, providing a direct route to calculate the enthalpy of change.<sup>1</sup>

Typical examples of heat flow DSC curves are displayed in figure 2. 1, showing the melting transitions for different saturated fatty acids, with increasing carbon chain length.

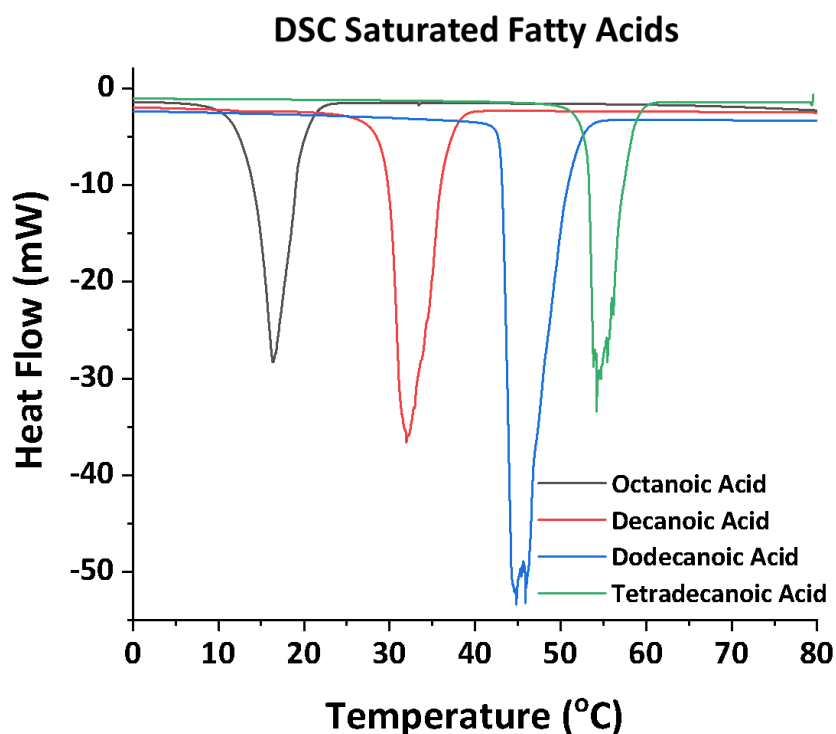


**Figure 2. 1** DSC profiles for different saturated fatty acids with increasing carbon chain length. Octanoic acid (C<sub>8</sub>, black), decanoic acid (C<sub>10</sub>, red), dodecanoic acid (C<sub>12</sub>, blue) and tetradecanoic acid (C<sub>14</sub>, green).

In a typical DSC experiment, a sample and a reference sample (e.g. an empty crucible) are simultaneously heated at the same rate. The difference in the input energy (mW) required to match the temperature of the reference sample is recorded as a peak in the DSC profile (Figure 2. 1) and refers to a transition in the material (e.g. melting point). The enthalpy ( $\Delta H$ ) of transition can then be calculated by integration of the peak area.<sup>1</sup>

In this thesis, DSC was used to characterise the melting transition temperature ( $T_{\text{onset}}$  and  $T_{\text{max}}$ ) and the enthalpy of phase change ( $\Delta H$ , J/g) for pure fatty acids used as starting materials and for the fatty acid impregnated in polydimethylsiloxane (FAIP) samples, discussed in chapter 3. DSC data was acquired in air using a TA Instruments Q2000 differential scanning calorimeter. Further details of experimental methods are presented in chapter 3.

### 2.2.2 Contact Angle

Contact angle measurements are used to investigate the wetting of materials. When a drop of liquid rests on a flat surface, i.e. a sessile drop, the contact angle can be defined as the angle formed by the intersection of the liquid-solid interface and the liquid-vapour interface (Figure 2. 2). This is often referred to as the three-phase contact line (Figure 2. 2). Small contact angles ( $< 90^\circ$ ) suggest the surface is susceptible to wetting, while larger contact angles ( $> 90^\circ$ ) suggest the surface is less susceptible to wetting (Figure 2. 2).<sup>2</sup>

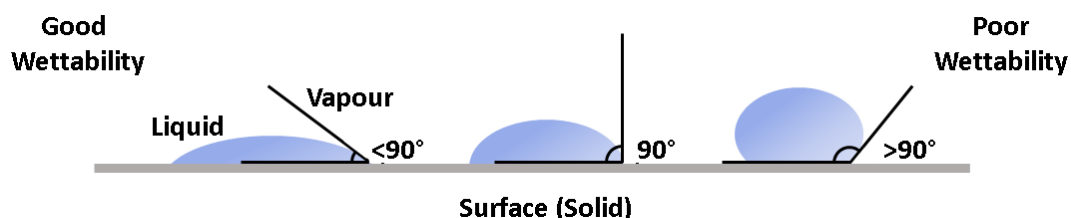


**Figure 2. 2** Illustration of contact angles formed by sessile liquid drops on a solid surface.

The shape of a liquid droplet is determined by the surface tension of the liquid (e.g. water is 72 dynes cm<sup>-1</sup>) and its interactions with the surface. In the bulk liquid, each molecule is pulled away in every direction by the surrounding liquid molecules, resulting in an average null force. However, the molecules that remain exposed at a surface do not have neighbouring liquid molecules in all directions to provide a balanced net force and are pulled inwards creating an internal pressure, that shapes the droplet, to maintain the lowest possible free energy (Figure 2. 3).<sup>2</sup>



**Figure 2. 3** Droplet formation on a surface due to the unbalanced forces of liquid molecules. Figure reproduced from reference 2.<sup>2</sup>

The equilibrium of interfacial tensions at the three-phase contact line dictates the contact angle under mechanical equilibrium and can be expressed according to Young's equation:<sup>3</sup>

$$\gamma_{lv} \cos \theta = \gamma_{sv} - \gamma_{sl}$$

**Equation 2. 1**

Where  $\theta$  is the contact angle and  $\gamma_{lv}$ ,  $\gamma_{sv}$  and  $\gamma_{sl}$  represent the liquid-vapour, solid-vapour and solid-liquid interfacial tensions, respectively.

Contact angles are most commonly measured using the telescope- goniometer technique (Figure 2. 4); this technique provides a direct measurement of the tangent angle at the three-phase contact line on a sessile drop profile (Figure 2. 2).<sup>2</sup> The general set-up for this type of instrument consists of a horizontal stage for mounting a sample, a micrometer syringe for accurate dispensing of a liquid, a light source and a telescope fitted with a protractor eye piece or camera (Figure 2. 4). The measurement can then be performed by aligning the tangent of the sessile drop profile at the contact point with the surface and reading the resultant angle using a protractor eyepiece<sup>2</sup> or determined using contact angle software (e.g. FTA 32 drop

shape analysis).<sup>4</sup> For software analysis, the contact angles can be measured using spherical or non-spherical models.<sup>4</sup> The spherical fit model fits a spherical curve to the sessile drop and determines an overall contact angle, while non-spherical analysis uses two separate tangents fitted on either side of the sessile drop to determine two individual contact angles. Non-spherical analysis is often preferred, as no presumption about the effect of gravity on the sessile drop is considered.<sup>4</sup>

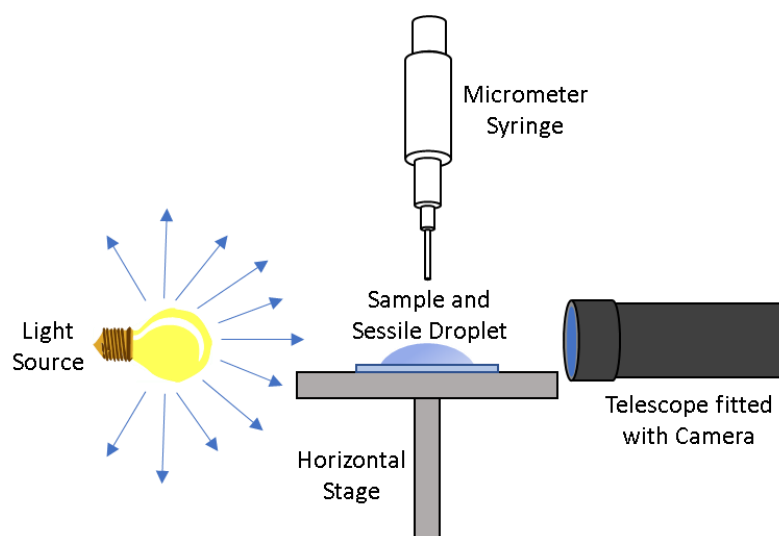


**Figure 2. 4** Schematic showing general set-up of a telescope goniometer with camera used for static contact angle measurements.

In this thesis, contact angle measurements were used to determine the wetting properties of the surfaces discussed in chapter 3 and 4, using different buffers. In chapter 3 different pH buffers were used to identify the wetting of the FAIP materials at different pH environments associated with the internal human body (pH 7) and human skin (pH 5),<sup>5</sup> while the buffer used in the experiments presented in chapter 4 mimicked physiological conditions associated with the natural pH of LB media (pH 7). All static contact angle measurements were performed using a First Ten Ångströms (FTA) 1000 instrument with a Gilmont GS-1201 micrometer dispenser syringe via the sessile drop method.

### 2.2.3 Ultraviolet-visible-near infrared (UV-Vis-NIR) Spectroscopy

UV-Vis-NIR spectroscopy refers to an extinction spectroscopy technique, which measures the intensity of light transmitted across a material in the wavelength range of 200 nm to 1100 nm. As a result of the measurement, a spectrum is obtained showing the values of extinction of a material at different wavelengths of light (Figure 2. 5).<sup>6</sup> In general, the extinction is equivalent to the absorption in the case of most molecular solutions, but scattering of light by materials, such as colloids, can also contribute the extinction value. For example, in molecules and small particles (e.g. quantum dots), the incident light is predominately absorbed, exciting electrons to a higher energy level. Whereas for larger particles, such as plasmonic nanomaterials, the light is predominately scattered. As a result, the extinction values will be the combination of the absorption and the scattering of light. For simplicity in this section, we will consider the case in which extinction is equal to absorbance.

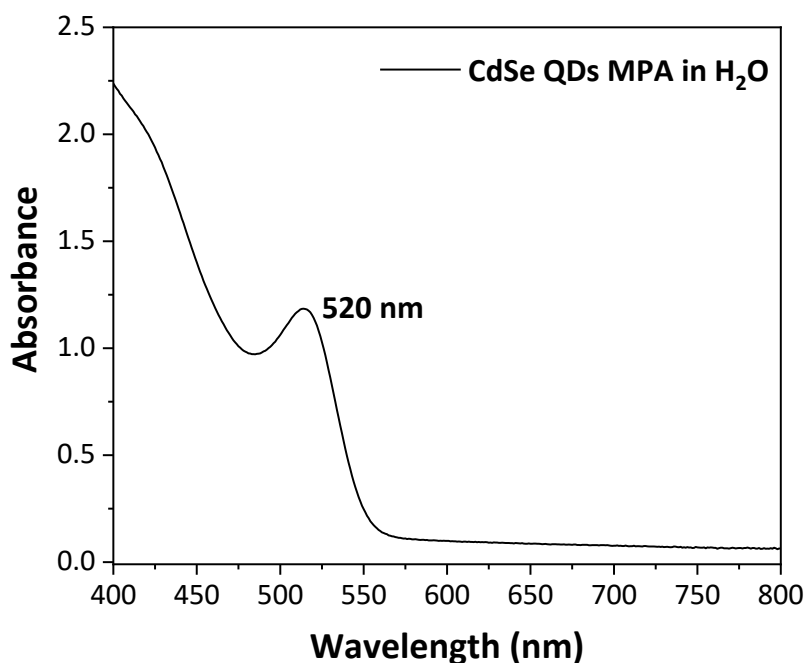


**Figure 2. 5** UV-Vis spectrum of CdSe QDs functionalised with mercaptopropionic acid (MPA) dispersed in water (H<sub>2</sub>O).

The transmittance ( $T$ ) is calculated from measuring the intensity of incident light ( $I_0$ ) transmitted by the sample ( $I$ ), which can be expressed as follows:<sup>6</sup>

$$T = \frac{I}{I_0}$$

**Equation 2. 2**

The absorbance is then calculated as a logarithmic function of transmittance:<sup>6</sup>

$$A = \text{Log}_{10} \frac{I_0}{I}$$

**Equation 2. 3**

Lambert stated that the amount of light absorbed by a material is dependent on how strongly a chemical species attenuates light at a given wavelength across a path length ( $l$ ), known as the extinction coefficient ( $\epsilon$ ), which changes depending on the material and can be expressed as:<sup>6</sup>

$$A = \epsilon l$$

**Equation 2. 4**

Later, Beer found that the amount of light absorbed by a material is also related to the concentration ( $c$ ) of the absorbent, changing  $\epsilon$  to the molar extinction coefficient and the equation can be further expressed as:<sup>6</sup>

$$A = \epsilon c l$$

**Equation 2. 5**

This equation is now commonly known as the *Beer-Lambert* law and is frequently used for calculating the concentration of absorbing materials, providing that a reference material of a known concentration or the molar extinction coefficient of an analyte material are available. The absorbance is also sometimes referred to optical density (OD), which is equal to the absorbance of a material across a path length ( $l$ ) of 1 cm.<sup>6</sup>

In this work, UV-Vis-NIR infrared spectroscopy was used for determining the absorbance of the materials discussed in chapters 4 and 5, at different wavelengths. The absorbance measurements collected for the materials discussed in chapter 5 were performed using a Shimadzu UV-2600 spectrophotometer, while a Shimadzu UV-1800 was used for the analysis of the materials discussed in chapter 4. For further experimental details see chapters 4 and 5.

## 2.3 Gas Chromatography Separation Techniques

Gas chromatography (GC) is a technique used for separation and quantification of components within mixtures.<sup>7</sup> In a typical instrument (Figure 2. 6 A) a liquid or gas sample is injected into the mobile phase (usually an inert carrier gas such as argon) of a heated separating column which separates the mixture, due to preferential interactions of the different components with the packing material inside the column, known as the stationary phase. The components are then eluted from the column at different times, known as retention times and subsequently detected. Commonly, flame ionisation detectors (FID) or thermal conductivity detectors (TCD) are used. FIDs detect ions formed during the combustion of organic compounds using a flame placed just before the detector, while TCDs are used for detection of gases via changes in thermal conductivity with respect to the reference gas (Figure 2. 6 B).<sup>7,8</sup>

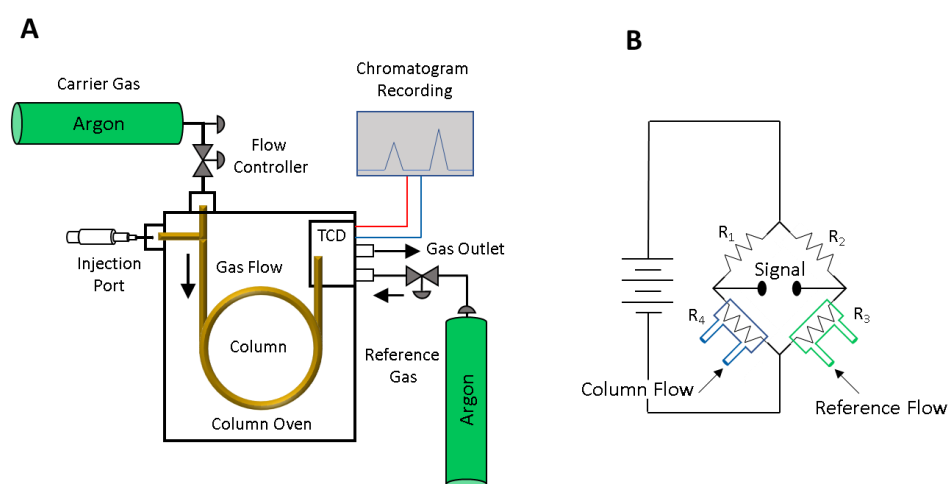


**Figure 2. 6 (A)** Schematic showing the general configuration of gas chromatograph instrument with TCD. **(B)** Schematic showing the configuration of a TCD.

A typical TCD design (Figure 2. 6 B) directs the carrier gas and the reference gas to two different temperature-controlled chambers, which are surrounded by one of four filaments in a Wheatstone bridge circuit. Electric current flowing through the circuit heats the filaments and the reference and carrier gas flow through each chamber removing the heat at a constant rate, creating a stable background temperature. When components within the carrier gas, with a relatively high or low conductivity with respect to the reference gas pass through the

chamber, they remove more/ less heat than the reference gas. The resultant temperature change alters the resistance of the filament and is detected as a potential difference with respect to the reference chamber. The time the difference in thermal conductivity was detected is then recorded by a computer as retention time displaying a peak.<sup>7,8</sup>

The area of the retention peak can be integrated and compared to a calibration standard to calculate the concentration of gas eluted.<sup>7,8</sup> In the case of the work conducted in this thesis, the retention peak generated from H<sub>2</sub> in the carrier gas was compared to a standard and subsequently re-calculated to determine the concentration of H<sub>2</sub> produced from H<sub>2</sub>O in hydrogen evolution experiments with the nanomaterials discussed in chapter 5. All GC measurements were performed using a Scion Instruments 436-GC fitted with a BRP 81025 column (Bruker) packed with 5 Å molecular sieves and a TCD. Argon was used as carrier/reference gas. For further experimental details see chapter 5.

## 2.4 Techniques for Chemical Characterisation

### 2.4.1 Vibrational Spectroscopy

Vibrational spectroscopy is a term commonly used to describe two main analytical techniques: infrared spectroscopy and Raman spectroscopy. Vibrational spectroscopy provides a way of identifying chemical species by measuring vibrational frequencies associated with specific vibrational modes (Table 2. 1) for chemical bonds and functional groups. In vibrational spectroscopy, molecules can be excited by incident light leading to changes in the oscillation frequency of chemical bonds, associated with specific vibrational modes (Table 2. 1), that can be described by harmonic oscillations. The frequency expressed in wavenumbers ( $\bar{\omega}$ ,  $\text{cm}^{-1}$ ) of the specific vibrational modes can be conveyed as follows:<sup>9-11</sup>

$$\bar{\omega} = \frac{1}{2\pi c} \sqrt{\frac{k}{\mu}}$$

**Equation 2. 6**

Where  $c$  is the velocity of light ( $3 \times 10^{10} \text{ cm s}^{-1}$ ),  $k$  is the force constant ( $\text{dynes cm}^{-1}$ ) associated with the strength of chemical bonds and  $\mu$  is the reduced mass (atomic mass units).<sup>9-11</sup>

**Table 2. 1** Different vibrational modes of molecules in infrared and Raman spectroscopy, with their assigned symbol in this thesis.

Vibrational Mode	Assigned Symbol
Stretch	$\nu$
Bend	$\delta$
Wagging	$\alpha$
Scissoring	$\beta$
Twist	$\gamma$
Rocking	$\rho$

### 2.4.1.1 Attenuated Total Reflection- Infrared Spectroscopy

Infrared spectroscopy involves the absorption of light in the infrared region of the electromagnetic spectrum (EMS), in a wavelength range of 2.5  $\mu\text{m}$  to 25  $\mu\text{m}$ . Light in this spectral range is absorbed by a molecule when the oscillation frequency of the incident radiation matches the frequency of a specific vibrational mode. However, for a molecule to be infrared active it must possess a dipole moment, which changes upon interaction with infrared light.<sup>9,10</sup> In an attenuated total reflection infrared spectroscopy (ATR-IR) instrument, infrared light passes through a prism (ATR crystal) with a high refractive index (e.g. diamond or zinc selenide), at an angle of incidence above the critical angle ( $\theta$ ).<sup>10-12</sup> The critical angle is a result of the difference in the refractive index of the ATR crystal ( $n_1$ ) and the sample ( $n_2$ ) and can be shown as follows:<sup>12</sup>

$$\theta = \arcsin \frac{n_2}{n_1}$$

**Equation 2. 7**

Due to higher refractive index of the ATR prism than the sample, the infrared light is reflected at the interface between the prism and the sample producing an evanescent wave that can be absorbed by the molecules located within 5  $\mu\text{m}$  of the surface of the prism (Figure 2. 7).<sup>10-12</sup> The absorption of the evanescent wave by the molecules in the sample is measured by a detector and the signal is processed using a Fourier transformation, producing a plot of intensity as a function of wavelength (often conveyed as wavenumber ( $\text{cm}^{-1}$ )) (Figure 2. 8).

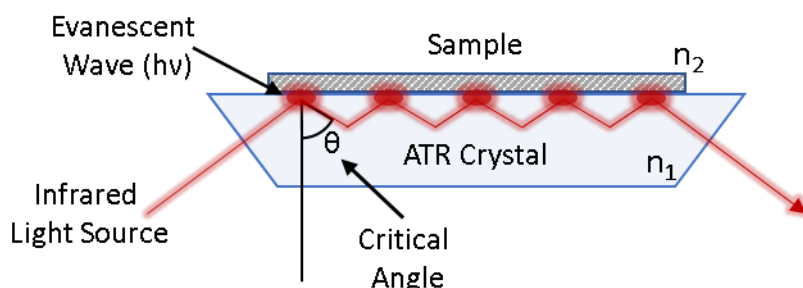


**Figure 2. 7** Schematic representation of attenuated total reflectance (ATR) configuration in an ATR-IR instrument.  $\theta$  is the critical angle and  $n_1$  and  $n_2$  represent the refractive index of the ATR crystal and a sample, respectively.

The infrared spectrum produced as a result of ATR-IR analysis can be used to probe the molecular structure of the chemical species in a sample, owing to the specific vibrations of chemical bonds and functional groups, known as fingerprints,<sup>13</sup> such as the characteristic infrared vibrational frequencies presented in table 2. 2 for dodecanoic acid.<sup>14</sup>

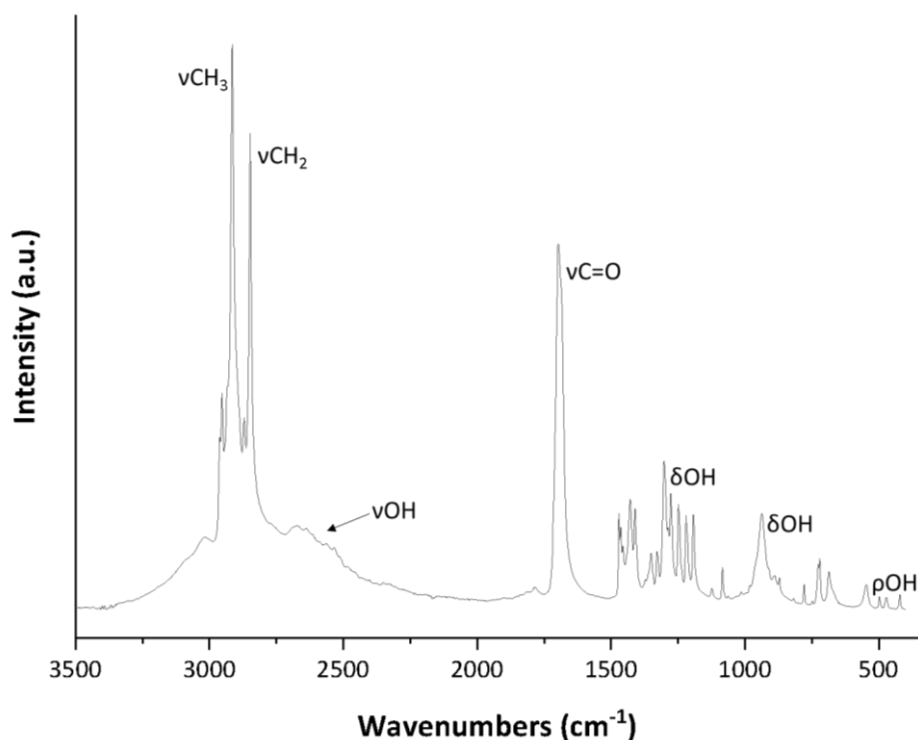


**Figure 2. 8** ATR-IR spectrum of dodecanoic acid

**Table 2. 2** Characteristic infrared vibrational frequencies for dodecanoic acid.<sup>14</sup>

Wavenumber (cm <sup>-1</sup> )	Assignment	Wavenumber (cm <sup>-1</sup> )	Assignment
2500 – 3000 (broad)	OH stretch	1700	C=O, carbonyl stretch
2953	Asymmetric CH <sub>3</sub> stretch	1303	In-plane OH bend
2915	Symmetric CH <sub>3</sub> stretch	938	Out-of-plane OH bend
2871	Asymmetric CH <sub>2</sub> stretch	721	In-plane OH rocking
2848	Symmetric CH <sub>2</sub> stretch		

In this work, ATR-IR was used to characterise materials discussed in chapter 4. All infrared spectroscopic data were collected using a Bruker Tensor II FT-IR with platinum ATR module. For further experimental details see chapter 4.

### 2.4.1.2 Raman Spectroscopy

Raman spectroscopy is a vibrational spectroscopic technique complementary to infrared spectroscopy, that measures the inelastic scattering of light by molecules.<sup>15,16</sup> When light is incident on a sample, most of the light is elastically scattered, known as Rayleigh scattering, where the incident light and the scattered light have the same energy and therefore the same wavelength (Figure 2. 9 B). However, during this interaction, part of the incident photon energy may be transferred to a molecule, leading to scattered light of lower energy and higher wavelengths, known as Stokes scattering (Figure 2. 9 C). The opposite can also occur, where energy is transferred from a molecule in an excited vibrational state to the incident photon, resulting in scattered light of higher energy and lower wavelengths, known as anti-Stokes scattering (Figure 2. 9 A).<sup>15,16</sup>

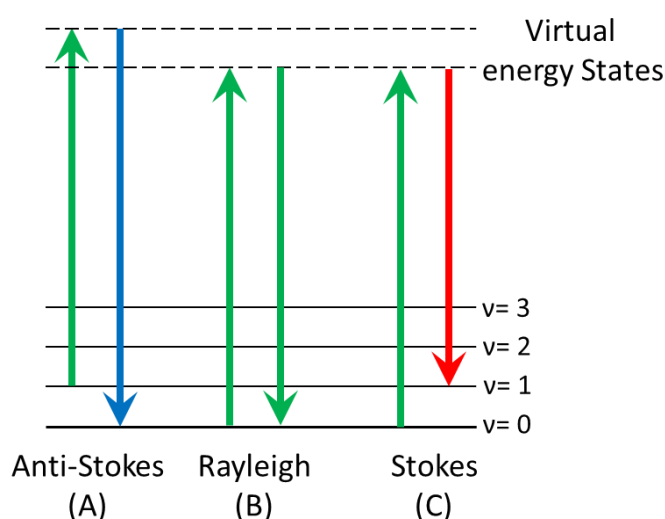


**Figure 2. 9** Jablonski diagram of quantum energy transitions for Rayleigh (B) and Raman Scattering ((A) Anti-Stokes scattering and (C) Stokes scattering)).

In the Raman scattering process, a vibrational transition will be Raman active if it induces a change in the polarizability of the molecule. As a result, Raman measurements will only show vibrational transitions that follow this selection rule.<sup>15,16</sup> The polarizability measures the ability of the electron cloud around a molecule to be distorted by an external electromagnetic field. The induced dipole scatters light at frequencies related to specific vibrational modes, which are then detected.<sup>16</sup> The vibrational frequency for a specific vibration mode that is both infrared and Raman active may differ due to the different selection rules,<sup>10,13,15,16</sup> such as the characteristic Raman peaks for dodecanoic acid<sup>17-19</sup> shown in figure 2. 10 and table 2. 3, making Raman spectroscopy a complementary technique to infrared spectroscopy, for probing the molecular structure of the chemical species present in a sample.

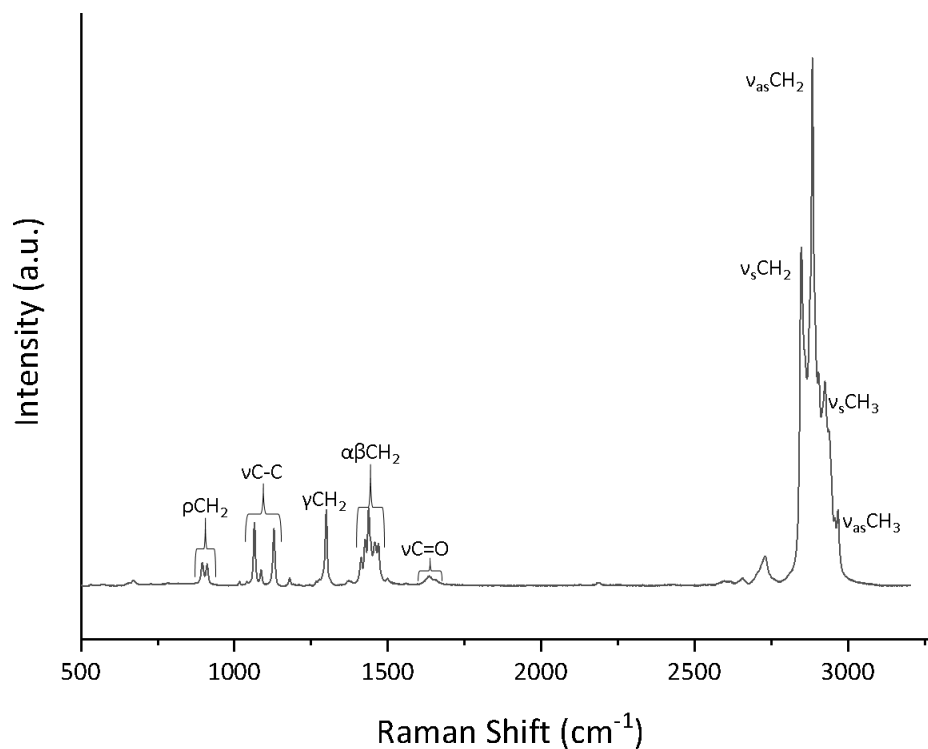


**Figure 2. 10** Raman spectrum of dodecanoic acid.

**Table 2. 3** Characteristic Raman vibrational frequencies for dodecanoic acid.<sup>17-19</sup>

Wavenumber (cm <sup>-1</sup> )	Assignment	Wavenumber (cm <sup>-1</sup> )	Assignment
2965	Asymmetric CH <sub>3</sub> stretch	1400- 1500	CH <sub>2</sub> wagging and scissoring
2930	Symmetric CH <sub>3</sub> stretch	1295	CH <sub>2</sub> twist
2880	Asymmetric CH <sub>2</sub> stretch	1075- 1100	C-C stretches
2850	Symmetric CH <sub>2</sub> stretch	894- 910	CH <sub>2</sub> rocking
1640	C=O, carbonyl stretch		

#### 2.4.1.2.1 Raman Mapping

Depending on the configuration of the instrument, Raman spectroscopy can be also used for mapping the chemical components of a sample, by scanning across a selected area or volume of the sample and processing the spectra obtained at each point. In this thesis, we used two different processing methods for mapping chemical components within a sample: signal to baseline mapping and direct classical least squares (DCLS) component fit analysis.

**Signal to baseline mapping:** Signal to baseline mapping mode integrates the area of a collected Raman signal between a selected range and the baseline of a Raman spectra obtained at each point of the measurement (Figure 2. 11).

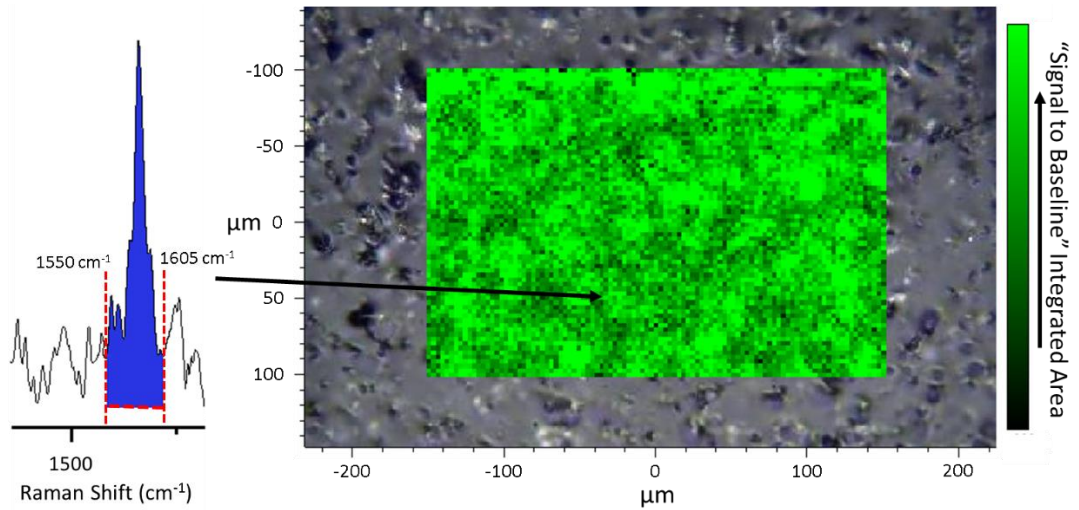


**Figure 2. 11** Illustration showing the signal to baseline mapping method. Increase in the green intensity represents increasing peak area of the integrated Raman signal. Raman signal between  $1550\text{ cm}^{-1}$  and  $1605\text{ cm}^{-1}$  of the G band vibrational mode associated with carbon nanopowder embedded in PDMS displayed as the example.

**DCLS component fit analysis:** DCLS component fit analysis is a correlative analytical method, where each spectrum in a data set collected across a selected area of a sample is compared to reference spectra using a least squares algorithm, to identify the pure components contained within a sample. However, this method has strict requirements: all reference spectra need to be available for the algorithm to reliably compare with the spectra of a sample and the Raman peaks in the sample spectra need appear at the same Raman shift as those in the reference spectra (Figure 2. 12).<sup>20,21</sup>

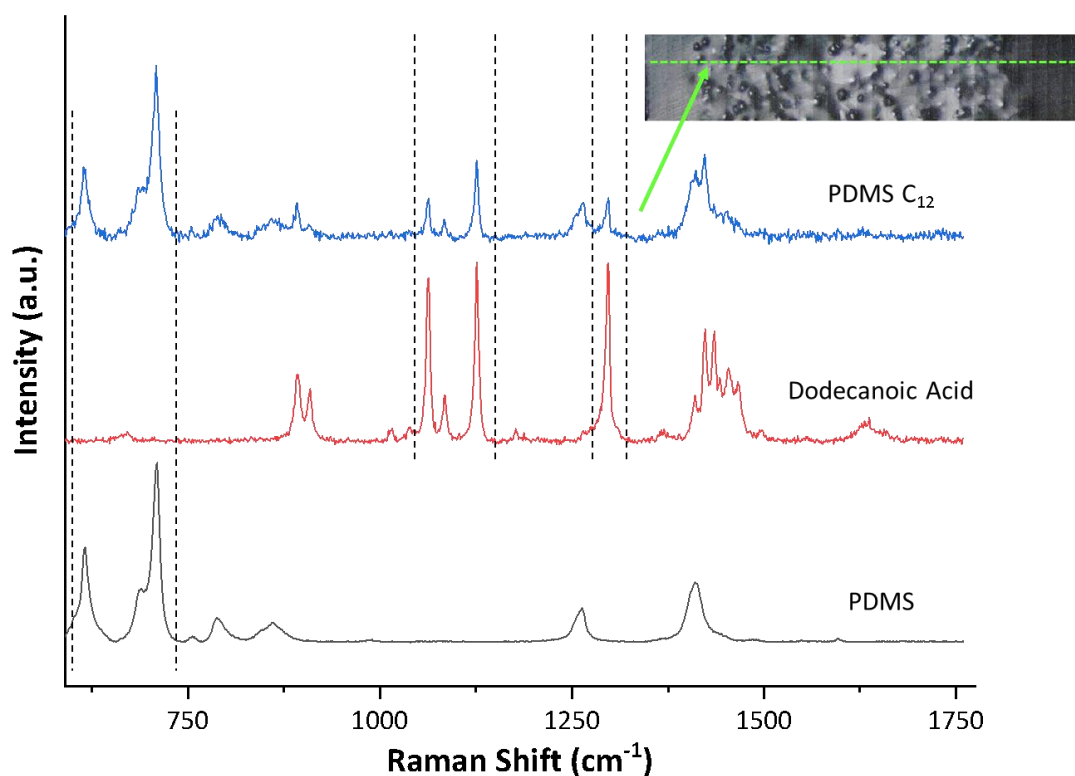


**Figure 2. 12** Illustration showing general overview of the DCLS mapping method. Black dashed lines represent some, but not all correlations between Raman signals of the raw materials (PDMS and dodecanoic acid(C<sub>12</sub>)) and the composite material (PDMS C<sub>12</sub>). Insert shows an example of Raman mapping across the depth of a material (PDMS C<sub>12</sub>), with green dashed lines representing the scanning area. Example of Raman spectrum PDMS C<sub>12</sub> is taken from an area with high concentrations of dodecanoic acid in the PDMS, represented by the green arrow.

Raman spectroscopy in combination with Raman mapping was used for the characterisation of materials discussed in chapters 3 and 4. All Raman spectroscopic data were collected using a Renishaw inVia confocal Raman microscope (Figure 2. 13). The confocality feature defines the sample volume from which the spectroscopic signal is collected. Using the high confocality option in this instrument, the sampling volume is decreased, and the spatial resolution is increased. However, this also reduces the total intensity of the Raman signal. For further experimental details see chapters 3 and 4.

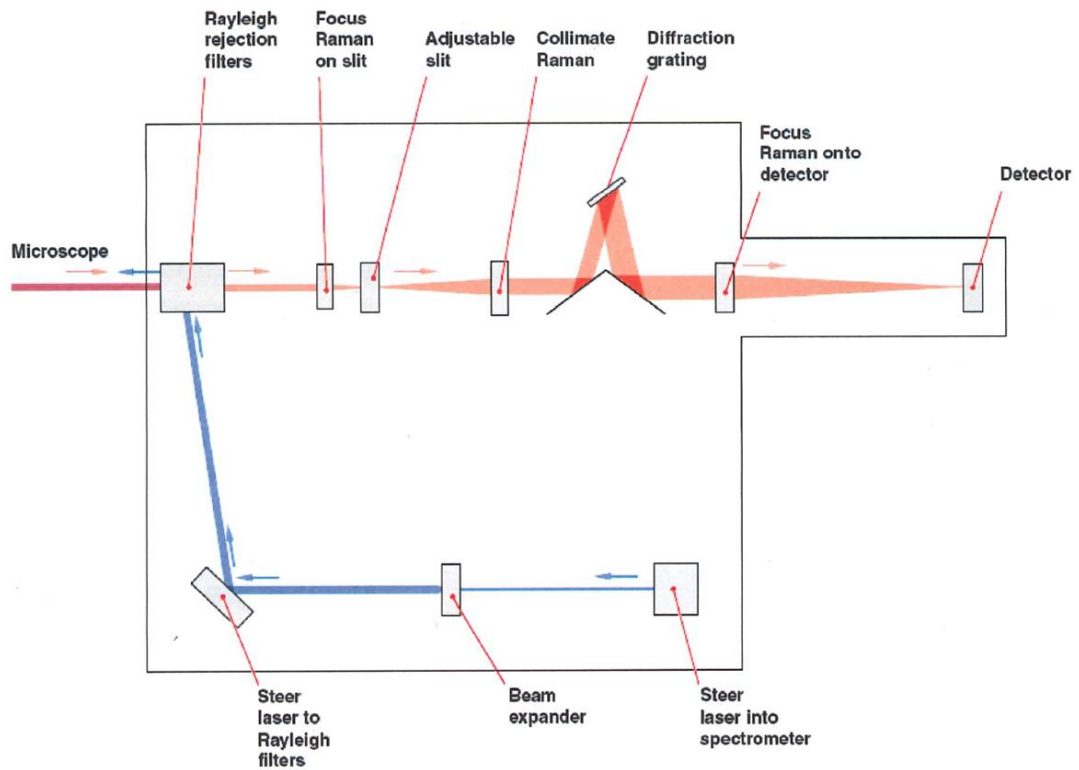


**Figure 2. 13** Schematic showing the configuration of the Renishaw inVia confocal Raman microscope. (Courtesy of Renishaw). The configuration of the instrument consists of a microscope coupled with a laser for illumination of a sample. The light scattered by sample is then directed through a Rayleigh reflection filter, and a set of slits to remove out of focus light. A diffraction grating is then used to split the Raman scattered light into the component wavelengths, which are then detected.

## 2.4.2 Inductively Coupled Plasma Optical Emission Spectroscopy (ICP-OES)

ICP-OES is a technique used to quantify the concentration of elements in a solution. In this process a solution is injected into a nebuliser, which mixes with a gas (usually Argon) to form an aerosol (Figure 2. 14). The aerosol then passes through a flame, causing the solvent to evaporate and the remaining molecules then breakdown into their component atoms. The component atoms then react with an inductively coupled plasma.<sup>22</sup>

The plasma in ICP is formed by passing a gas (usually Argon) through an intense, high frequency radio signal produced by a radiofrequency (RF) coil and applying a spark to initiate the ionisation process (Figure 2. 14). The ionised gas and free electrons are then accelerated by an alternating magnetic field created by the radio signal. As the magnetic field alternates, collisions between charged particles and neutral Argon atoms occurs, causing the neutral atoms to ionise. The free electrons and ions can then recombine, and the process continues. When the rate of ionisation equals the rate at which the free electrons and ions recombine a stable plasma flame is generated. As the component atoms of the sample are injected into the plasma, they also undergo ionisation and recombination. As a result of recombination, radiation in form of light of a specific frequency associated with the components atoms is emitted. The emitted light is then filtered by a monochromator and detected using a charge couple device detector (CCD) (Figure 2. 14). The concentration of the elements within the sample are then quantified depending on the intensity of the signal.<sup>22</sup>

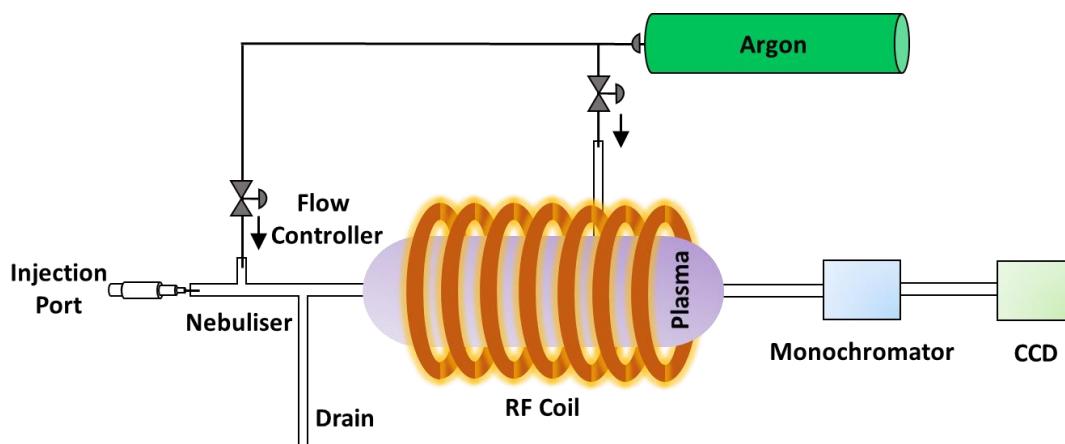


**Figure 2. 14** Schematic showing the general configuration of an inductively coupled plasma optical emission spectroscopy (ICP-OES) instrument.

### 2.4.3 X-ray Spectroscopy

X-ray spectroscopy is a term that can refer to several techniques used to probe the electronic structure and elemental composition of a chemical species, by the direct (i.e. excitation) or indirect (i.e. emission) use of x-rays. These techniques include x-ray photoelectron spectroscopy (XPS), Auger electron Spectroscopy and energy dispersive spectroscopy (EDS).<sup>23-26</sup>

#### 2.4.3.1 X-ray Photoelectron Spectroscopy (XPS)

XPS is a surface sensitive spectroscopic technique used to probe the occupied electronic states of a material, by measuring the kinetic energy of electrons emitted from a solid sample, due to the bombardment of incident x-ray photons. This technique can be used to identify and quantify the elemental composition of a material. In XPS, X-ray photons of an energy  $h\nu$  are used to excite the electrons from core levels of atoms into vacuum (Figure 2. 15). The specific kinetic energy ( $E_{kin}$ ) of these electrons can then be detected, making this technique element specific.<sup>24,27</sup> The energy required to remove an electron from a core level of an atom is known as the binding energy ( $E_B$ ), measured with respect to the fermi level (i.e. highest occupied level in the solid) and be calculated according to equation 2.8.

$$E_B = h\nu - E_{kin} - \Phi$$

**Equation 2. 8**

Where  $h\nu$  is the x-ray photon energy and  $\Phi$  is the work function (i.e. the minimum energy required to remove an electron from the highest occupied level in the solid, the Fermi level, to the vacuum level).<sup>24,27</sup>

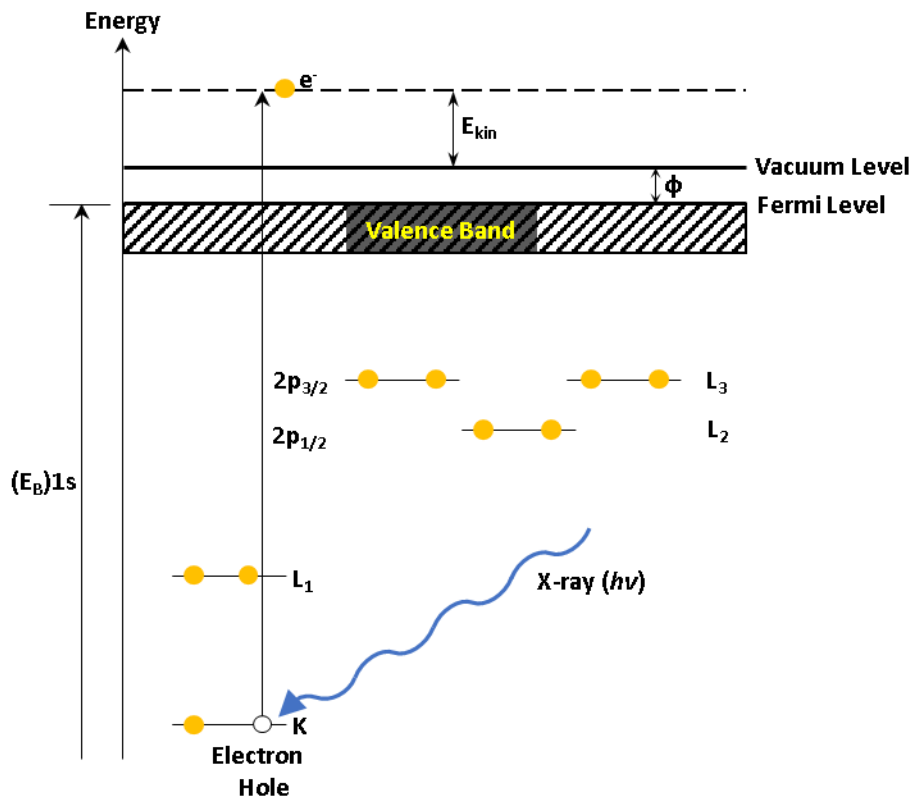


**Figure 2. 15** Schematic showing the XPS process.

When a sample is irradiated with x-rays, only a fraction of electrons from the sample are emitted into vacuum, due to inelastic scattering events, resulting in the loss of kinetic energy. The loss in kinetic energy can be associated with the inelastic mean free path (IMFP) of the electrons. The IMFP is defined as the distance an electron can travel through a solid before losing energy and is independent on the chemical species of material, generating a universal curve (Figure 2. 16). The universal curve describes the IMFP of approximately only a few nm for electrons in the kinetic energy range of 2 to 2000 eV (Figure 2. 16). This means only electrons emitted from the top few nm of a material will be able to reach the detector, making XPS a surface sensitive technique.<sup>23,24,27</sup>

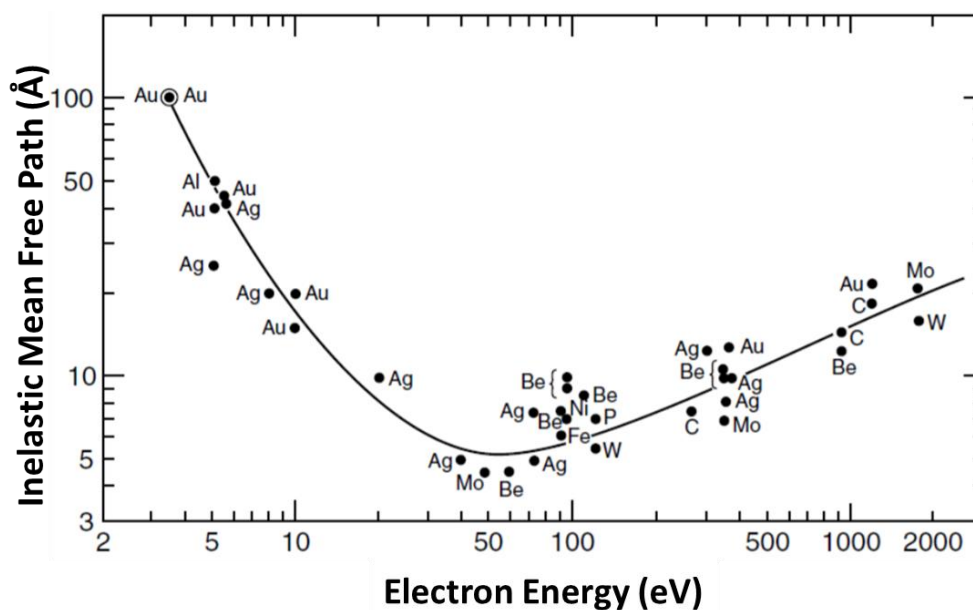


**Figure 2. 16** Universal curve showing the escape depth of an electron from a solid as a function of kinetic energy (eV) with measured values for various elements. Figure adapted from reference 27.<sup>28</sup>

The number of peaks observed in the XPS spectra for a specific element varies depending on the excited energy levels of an element and the chemical environment (Figure 2. 17). Emission from p, d and f energy levels of an atom will give rise to doublets due to spin-orbit coupling (Figure 2. 17). This can be explained because the electrons have different total angular momenta ( $l \pm 1/2$ ) (Table 2. 4). The peaks will also have specific intensity ratios based on the degeneracy of each spin state (i.e. the number of different spin combinations that can give rise to the total  $j$ ) (Table 2. 4).<sup>23,24,27</sup> For example, for the 3d spectra of silver (Ag) (Figure 2. 17), where  $n$  (principal quantum number) is 3 and  $l$  is 2,  $j$  will be  $3/2$  and  $5/2$ . The intensity ratio for the two spin orbit peaks ( $3d_{3/2}:3d_{5/2}$ ) will be 2:3 corresponding to 4 electrons in the  $3d_{3/2}$  level and 6 electrons in the  $3d_{5/2}$  level.

**Table 2. 4** Spin-orbit splitting  $j$  values and peak intensity ratios.

<b>Electron Energy Level</b>	<b><math>j</math> Value</b>		<b>Intensity Ratio</b>
s ( $l=0$ )	1/2		n/a
p ( $l=1$ )	1/2	3/2	1:2
d ( $l=2$ )	3/2	5/2	2:3
f ( $l=3$ )	5/2	7/2	3:4

Changes in the chemical environment of an element can also be observed in XPS by a shift in binding energy. This is associated with variations in electron density as a result of electrostatic interactions with the positively charged nucleus of the atom, and the electrons in different orbitals. For example, cationic species tend to have a higher binding energy, due a low electron density around the atom, whereas the opposite occurs for anionic species, due to an increased electron density.<sup>23,24,27</sup> Changes in the binding energy of an element can therefore allow for determination of the oxidation state of an element. Interestingly, however, oxidation of materials does not always lead to a positive shift in the binding energy e.g. oxidised silver exhibits a negative shift in binding energy (Figure 2. 17).<sup>29,30</sup> In addition, oxidised materials, such as silver do not always exhibit significant shifts in binding energy and therefore the shape of the 3d binding energy peaks (e.g. oxidised silver has broader 3d peaks than metallic silver) and the Auger peaks (see below) are considered more reliable for interpretation of data.<sup>29,30</sup>

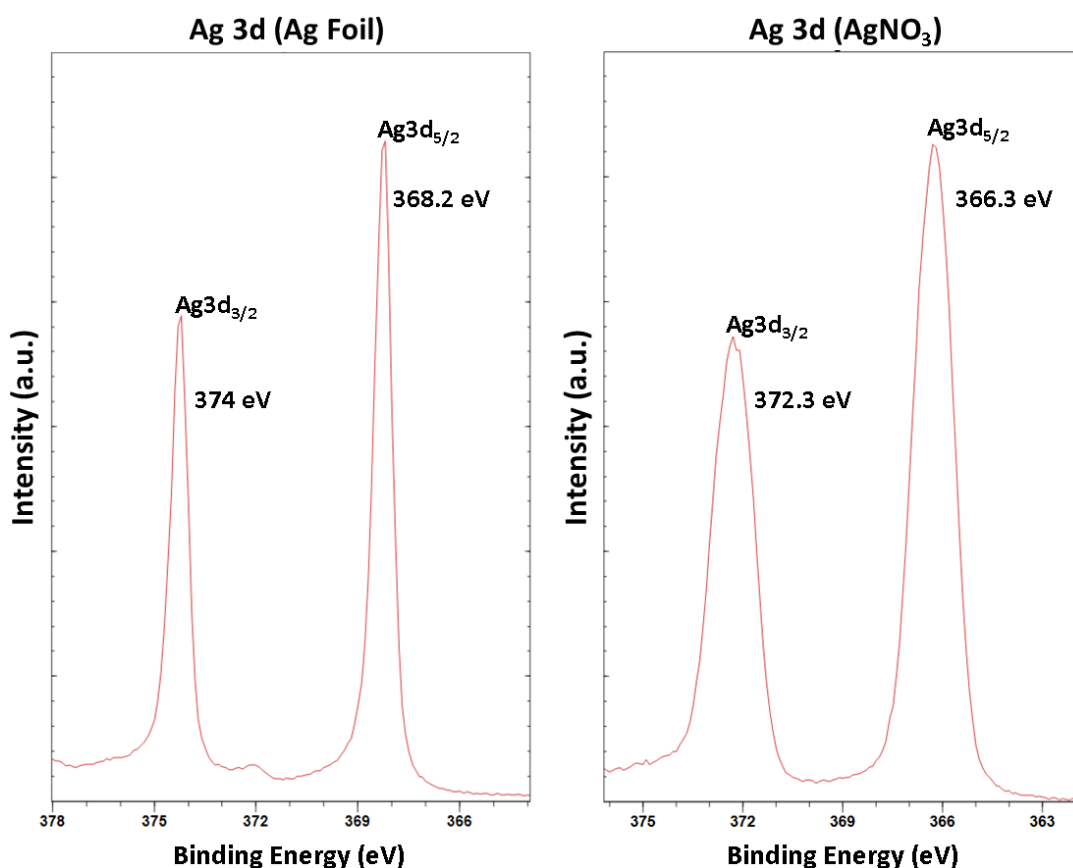


**Figure 2. 17** XPS spectra of the silver (Ag) 3d region for argon sputtered silver foil (Ag(0)) and silver nitrate (Ag(I)NO<sub>3</sub>) showing a negative shift in binding energy for the oxidised silver species, AgNO<sub>3</sub>.

Other factors can also contribute to shifts in the binding energy, such as bond strength in covalent molecules and changes in electronegativity. In general, longer bond lengths lead to smaller binding energy shifts due to the lower electron density transferred between atoms, whereas increases in electronegativity differences lead to larger binding energy shifts.<sup>23,24,27</sup>

In order to identify the chemical composition and oxidation state of the nanomaterials discussed in chapter 5, XPS was employed as an analytical technique, along with Auger electron spectroscopy (see below). All XPS measurements were performed using a Kratos Axis Supra instrument, equipped with a monochromatic Al K $\alpha$  radiation source. Argon sputtering was employed for XPS analysis of the silver foil displayed above (Figure 2. 17), for the removal of potential contamination or natural oxidation at the surface. Further experimental details can be found in chapter 5.

### 2.4.3.2 Auger Electron Spectroscopy

Auger electron spectroscopy is a surface sensitive technique complementary to XPS, that involves the emission of a second electron as a result of electron excitation, typically by incident photons. After electron excitation, an electron hole is left behind, which is then filled by an electron from a higher energy level, known as the down electron, resulting in the release of energy. The energy released can either be emitted as an x-ray photon into vacuum or it can be transferred to another electron, which is then excited into the vacuum, known as the Auger electron (Figure 2. 18).<sup>23,24,27</sup>

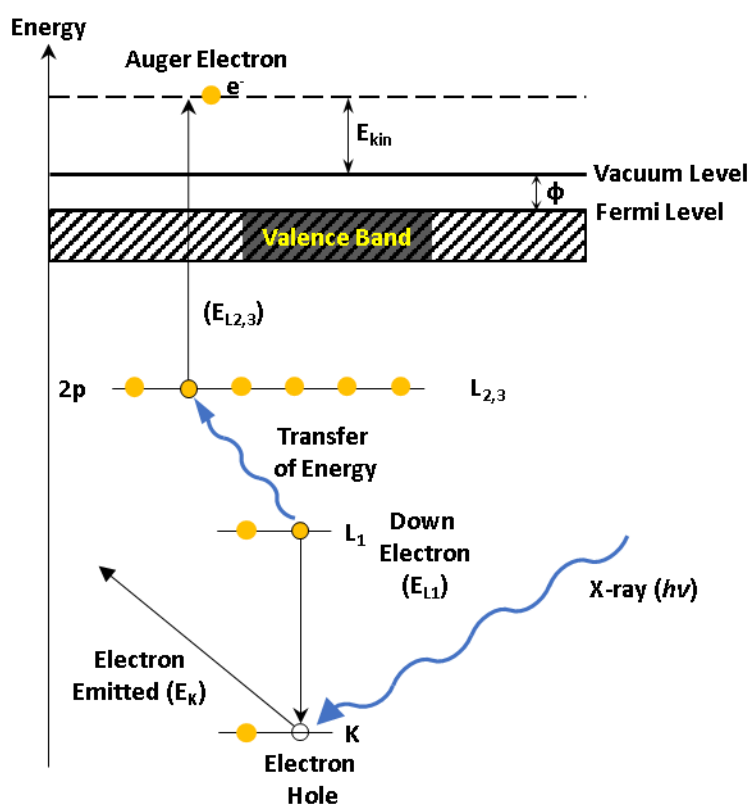


**Figure 2. 18** Schematic showing emission of an Auger electron.

The kinetic energy of an Auger electron does not shift as a function of excitation energy  $h\nu$  (incident photons), such as in XPS and can therefore be easily distinguished from XPS peaks.<sup>24</sup>

As a result of the Auger process, the Auger electron will have a kinetic energy ( $E_{kin}$ ) equal to:

$$E_{kin} = E_K - E_{L_1} - E_{L_{2,3}} - \Phi$$

**Equation 2. 9**

Where  $E_K$  is the binding energy of the initially emitted electron,  $E_{L1}$  is the binding energy of the down electron,  $E_{L2,3}$  is the binding energy of the Auger electron and  $\Phi$  is the work function (as described above). Auger peaks are characteristic of an element, due to the different energy levels associated with the atom, enabling chemical analysis.<sup>23,24,27</sup> The Auger peaks are usually assigned three letters associated with the different electron energy levels involved in the Auger electron process, hence, MNN for Ag (Figure 2. 19). Analogous to XPS, Auger electron spectroscopy can also provide information regarding the chemical environment of an element, such as a shift in the Auger kinetic energy associated with the oxidation of metals, such as  $\text{AgNO}_3$  (Figure 2. 19).<sup>23,24,27</sup>

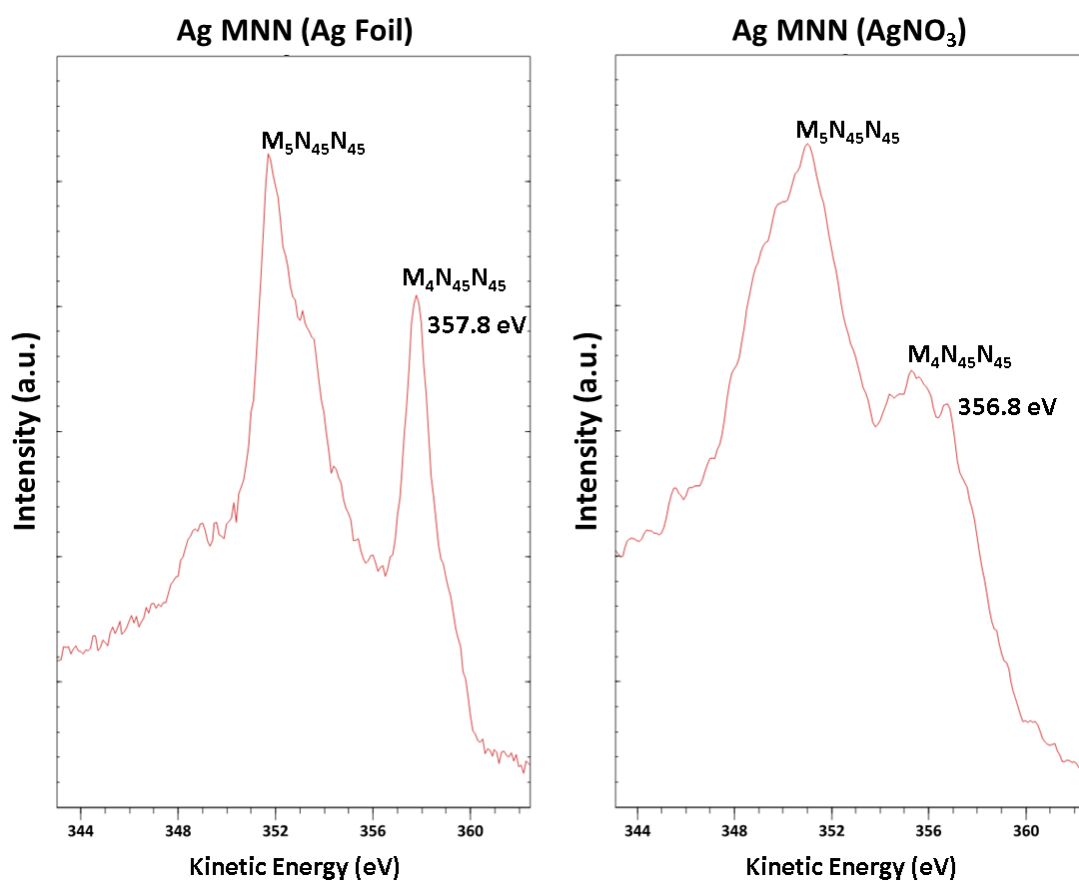


**Figure 2. 19** Auger spectra of the silver ( $\text{Ag}(0)$ ) MNN region for argon sputtered silver foil and silver nitrate ( $\text{Ag(I)NO}_3$ ) showing a negative shift in kinetic energy for the oxidised silver species,  $\text{AgNO}_3$ .

Another means of extracting information regarding the oxidation state of an element is the Auger parameter.<sup>24,30</sup> The Auger parameter is the addition of the XPS binding energy ( $E_B$ ) and the Auger kinetic energy ( $E_{kin}$ ) (Equation 2. 10) and is commonly used in identifying the oxidation states of metals.<sup>24,30</sup>

$$\text{Auger Parameter} = \text{XPS } E_B + \text{Auger } E_{kin} \quad \text{Equation 2. 10}$$

In this thesis, Auger electron spectroscopy was used to investigate the oxidation state of the nanomaterials discussed in chapter 5. Auger electron spectroscopic data was collected using a Kratos Axis Supra instrument in parallel to the collection of XPS data, as described previously. For further experimental details see chapter 5.

### 2.4.3.3 Energy Dispersive X-ray Spectroscopy (EDS)

EDS is an analytical technique used to identify the elemental composition of materials by the emission of x-rays as result of an electron transition, which are detected. The EDS process is similar to Auger electron spectroscopy, in which after initial excitation (usually by primary electrons) and emission of an electron, an electron from a higher energy level fills the electron hole. The energy released as a result of this transition is released in the form of an x-ray, which is then detected (Figure 2. 20).<sup>25,26</sup>

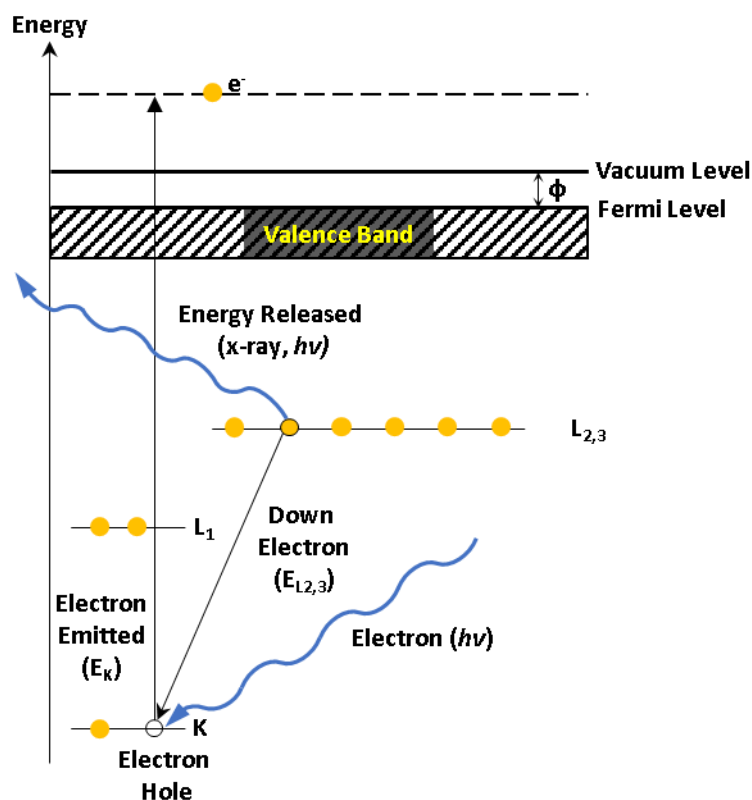


**Figure 2. 20** Schematic showing the EDS process.

In the case of figure 2. 20, the energy of the x-ray released ( $E_{h\nu}$ ) will be equal to:

$$E_{h\nu} = E_{L_{2,3}} - E_K$$

**Equation 2. 11**

Where  $E_{L_{2,3}}$  is the binding energy of the down electron and  $E_K$  is the binding energy of the emitted electron. The x-rays emitted are characteristic to specific elements and can therefore be used for chemical analysis of a sample. In addition, EDS can also probe further depths of a material, allowing for collection of chemical information from the bulk of a material.<sup>25,26</sup>

EDS detectors are usually found connected to electron microscopy instruments, which utilise the electron beam associated with the instrument for the excitation process.<sup>31</sup> EDS can also be used in parallel with electron microscopy imaging for mapping the chemical composition of a material.<sup>32-35</sup> In this work, EDS along with EDS mapping was used to characterise the chemical composition of the nanomaterials discussed in chapter 5. EDS data was collected using an EDAX Octane T Optima windowless 60 mm<sup>2</sup> SDD EDS detector coupled to a JEOL 2100F S/TEM. For further experimental details and examples of EDS data see chapter 5.

## 2.5 Microscopy Techniques

Microscopy involves the study of objects that are too small to be examined by the naked eye and is commonly used for imaging biological and non-biological materials less than 100  $\mu\text{m}$  in size. There are various types of microscopy techniques used for examining small objects and these can be subcategorised depending on the probing method used in the microscopy technique. For example, electron microscopy uses electrons and optical microscopy uses visible light.<sup>36</sup>

### 2.5.1 Electron Microscopy

Electron microscopy is a technique performed under vacuum and is used for obtaining detailed images of biological and non-biological samples. The high resolution of electron microscopy results from the use of electrons as the source of illumination, which have very short de Broglie wavelengths. De Broglie proposed that just as light has both wave-like and particle-like properties, electrons also have wave-like properties, where the wavelength ( $\lambda$ ) of an electron is associated with its momentum ( $p$ ), through Planck's constant ( $h$ ,  $6.626 \times 10^{-34}$  Js) (Equation 2. 12).<sup>36</sup>

$$\lambda = \frac{h}{p} = \frac{h}{mv}$$

**Equation 2. 12**

The momentum ( $p$ ) is equal to the mass of an electron ( $m$ ) multiplied by its velocity ( $v$ ). As a result, electrons have smaller wavelengths than light and can therefore be used for high resolution imaging of smaller samples into the nanometre scale, which can be associated with the Abbe diffraction limit (Equation 2. 13).<sup>36</sup>

$$d = \frac{0.61(\lambda)}{n \sin \alpha}$$

**Equation 2. 13**

Where  $d$  is the resolution,  $n$  is the index of refraction and  $\alpha$  is half the aperture angle in radians (i.e. half the angle of the cone of illumination from specimen plane accepted by the objective). In electron microscopy  $\alpha$  is exceedingly low and the index of refraction is effectively 1. As a result, the resolution ( $d$ ) in electron microscopy is mainly dependent on the wavelength of electrons, which can be adjusted by changing the acceleration voltage, allowing for the imaging of exceedingly small samples.<sup>36</sup> Modern advancements in electron microscopy have even allowed for imaging of atoms and crystallographic planes.<sup>37,38</sup> Electron microscopy encompasses a range of techniques including scanning electron microscopy (SEM), transmission electron microscopy (TEM) and scanning transmission electron microscopy (STEM). For the purpose of this thesis we will discuss TEM and STEM.

#### 2.5.1.1 Transmission Electron Microscopy (TEM)

TEM is an electron microscopy technique in which a beam of high energy electrons are transmitted through a sample to form an image. The electrons are produced by an electron gun made of a cathodic material with a high negative potential as a filament, such as tungsten (W) or lanthanum hexaboride (LaB<sub>6</sub>). A high voltage of electricity is applied, and the filament heats up to emit electrons. The emitted electrons are then accelerated through the vacuum towards the sample by an anode located below the electron gun assembly, that is electrically at ground, creating a positive attraction for the negatively charged electrons emitted from the cathode. The accelerated electrons are focussed using electromagnetic condenser lenses to form a fine beam of electrons, which then pass through a very thin sample. The electrons are then either scattered by the sample or magnified by the electromagnetic objective lens, which are then projected onto a luminescent screen at the bottom of the electron microscope (Figure 2. 21).<sup>36</sup>

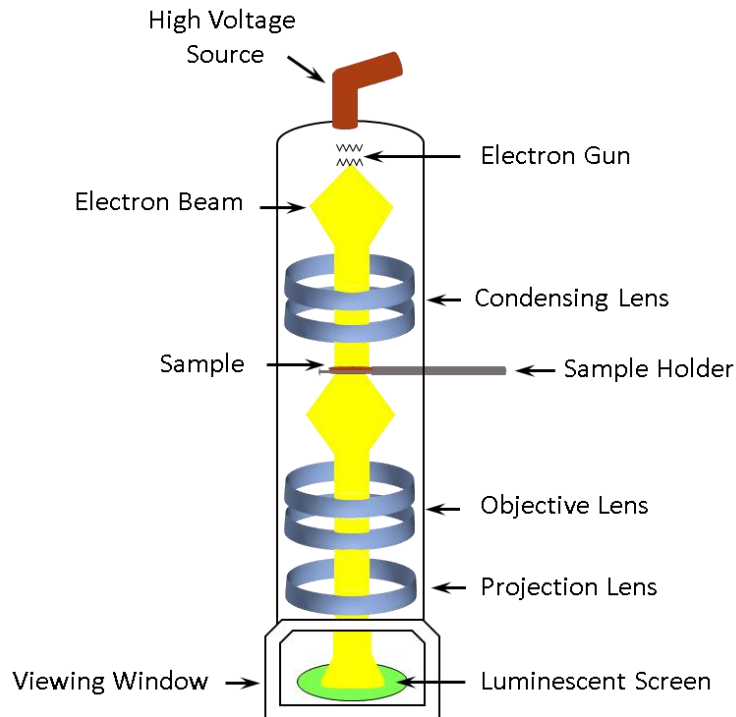


**Figure 2. 21** Schematic showing the general configuration of a TEM.

An image is formed on the luminescent screen by scintillation (i.e. conversion of electrons to light), with different contrasts relevant to the electron density of the different areas of the sample (Figure 2. 22). As a result, materials composed of heavy elements interact strongly with the electron beam and are relatively easy to image, while materials of low electron density, such as biological materials can prove difficult to image and require further preparation prior to imaging. Direct imaging of biological samples via electron microscopy can lead several issues, including dehydration of wet biological samples under high vacuum conditions, damage to biological materials due ionised radiation from the electron beam and degradation of image quality due to charging effects, associated the accumulation of static charge on the specimen owing to the non-conductive nature of the biological material.<sup>39</sup>

To overcome these limitations, biological samples such as cells (e.g. bacteria) can be fixed to preserve mechanical stability of the sample using fixatives of aldehyde mixtures and osmium tetroxide which cross link proteins and lipids, followed by increasing the electron density of the sample using electron dense stains (e.g. uranyl acetate) to bind to nucleic acids and

phospholipids. The sample is carefully dehydrated using increasing concentrations of ethanol. For TEM imaging, the sample is then embedded in an epoxy resin and a thin slice (60-100 nm) of the epoxy resin is cut using an ultramicrotome and placed on a TEM grid.<sup>39</sup> Images of the samples can then be studied directly at the TEM viewing window or photographed using a specialist camera, with a built-in scintillation film, converting the incident electrons into photons of light, which are subsequently detected using a CCD detector.<sup>36</sup>

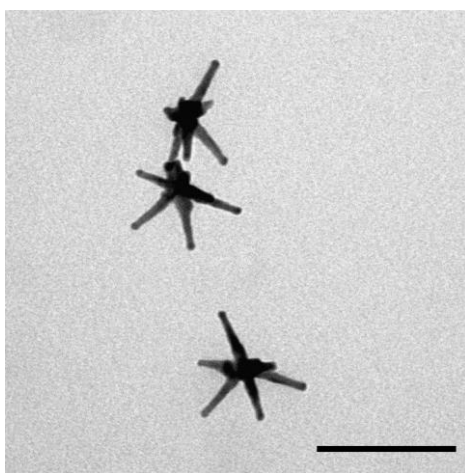


**Figure 2. 22** TEM image of gold nanostars (scale bar is 100 nm).

In this work, TEM was used for examining the morphology of the nanomaterials discussed in chapters 4 and 5. All TEM images were collected using a FEI Tecnai G2 Spirit TEM, with 120 keV and processed using Fiji software. For further experimental details see chapters 4 and 5.

### 2.5.1.2 Scanning Transmission Electron Microscopy (STEM)

STEM is an analogous technique to TEM, which works on similar principles. However, the configuration of the system is slightly different (Figure 2. 23). TEM instruments can also be adapted with a STEM option, allowing the instrument to function as both a TEM and STEM (Figure 2. 23). After the electron beam passes through the condenser lens, an objective lens is used to limit the maximum angle of illumination, which focuses the electron beam onto a small spot on the sample. The focussed beam is then scanned across the sample by a set of

scanning coils in a raster motion and the signals of transmitted and scattered electrons are collected point by point by bright-field and dark-field detectors (Figure 2. 23) to form an image (Figure 2. 24 A and B).<sup>36</sup>

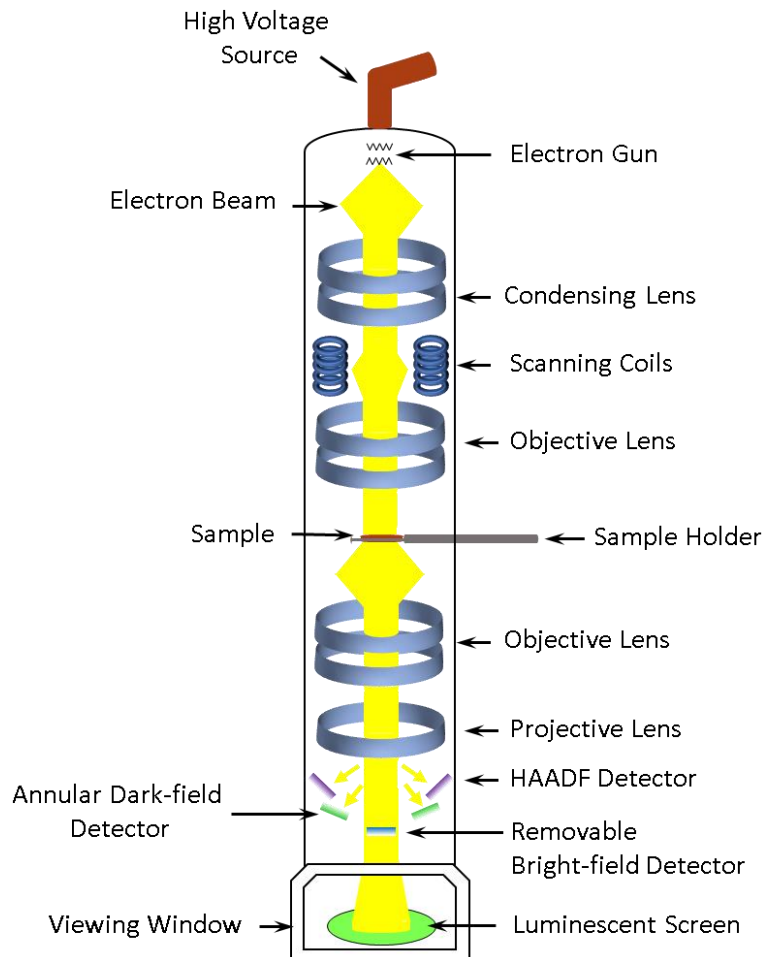


**Figure 2. 23** Schematic showing the general configuration of a combined STEM and TEM.

The bright-field detector intercepts the transmitted beam and annular dark-field detectors collect scattered electrons, with high-angle annular dark-field (HAADF) detectors collecting inelastically scattered electrons at high angles generating an image displaying the integrated intensities of the electrons in synchronism with the incident probe position. Heavier elements scatter electrons at higher angles due to greater electrostatic interaction between the atomic nucleus and the electron beam, as a result HAADF detector detects more signal from the elements with higher atomic number and therefore heavy atoms will appear as brighter, while lighter elements will appear dark, such as the dark-field STEM image of CdS QDs displayed

in figure 2. 24 B.<sup>36</sup> Annular dark field detectors can also be found in some TEM only systems, which work on the same principle.

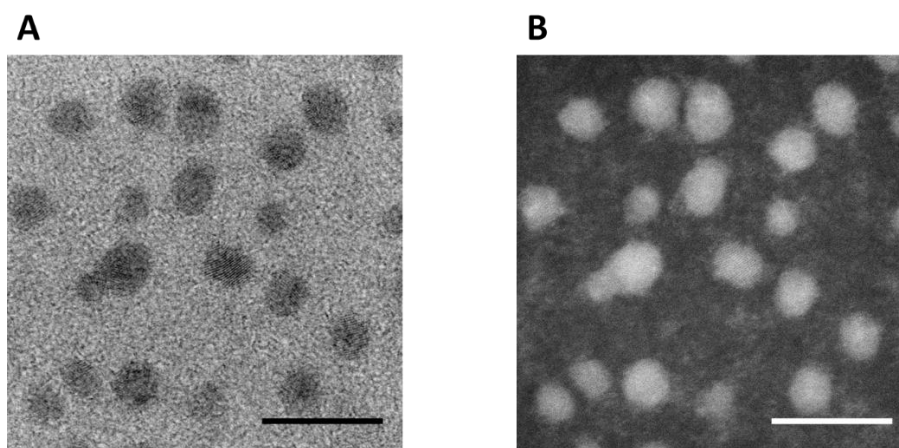


**Figure 2. 24** STEM bright-field (A) and dark-field (B) image of CdS QDs (scale bars are 10 nm).

In this work, STEM was used for examining the morphology of the nanomaterials discussed in chapters 5. STEM coupled with EDS was also used for mapping the chemical composition of some of these nanomaterials, as mentioned above. All STEM images were collected at 200 keV using a JEOL 2100F Cs corrected S/TEM in STEM mode. All images were processed using Fiji software. For further experimental details see chapter 5.

### 2.5.2 Fluorescence Microscopy

Fluorescence microscopy is a technique that allows quantitative and temporal visualisation of fluorescent material in microscope samples. Due to this capability, many researchers have used this technique to investigate biologically relevant questions. Fluorescence is a property observed for some atoms and molecules, where light of lower energy is emitted after excitation by incident light ( $h\nu$ ) and decay between singlet electronic states. A singlet state is a molecular electronic state such that all electron spins are paired ( $\uparrow\downarrow$ ). Molecules that undergo electronic transitions and emit fluorescence are known as fluorophores. After initial excitation, the fluorophore will remain in an excited state for an interval time, which then relaxes back to the

ground state by the emission of light at higher wavelengths (low energy), known as fluorescence (Figure 2. 25).<sup>40,41</sup>

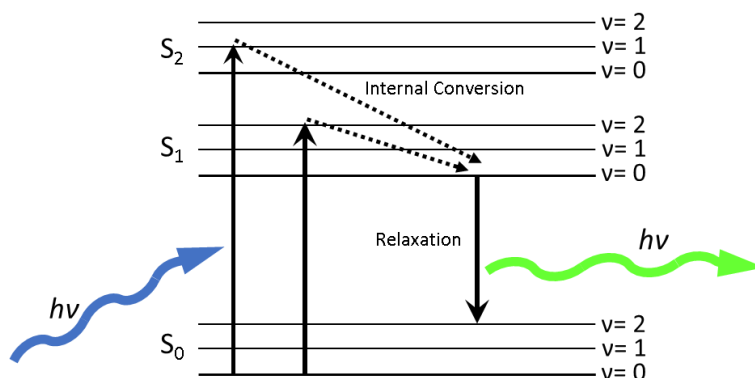


**Figure 2. 25** Jablonski diagram showing the different fluorescence processes.

During the excitation process, the fluorophore can be either excited to a singlet state ( $S_1$ ) from the ground state ( $S_0$ ), followed by an internal conversion to the lowest vibrational energy level of the  $S_1$  singlet state, which then undergoes relaxation back to the ground state ( $S_0$ ), releasing energy in the form of light (fluorescence) (Figure 2. 25). Alternatively, the fluorophore can be excited to the higher singlet state ( $S_2$ ), followed by the rapid internal conversion to a lower singlet state ( $S_1$ ) (Figure 2. 25). The fluorophore then relaxes back to the ground state ( $S_0$ ), releasing energy in the form of light (fluorescence). The shift in the wavelength between the maxima of the excitation/ absorbance and emission spectra is known as the Stokes shift (Figure 2. 26).<sup>40,41</sup>

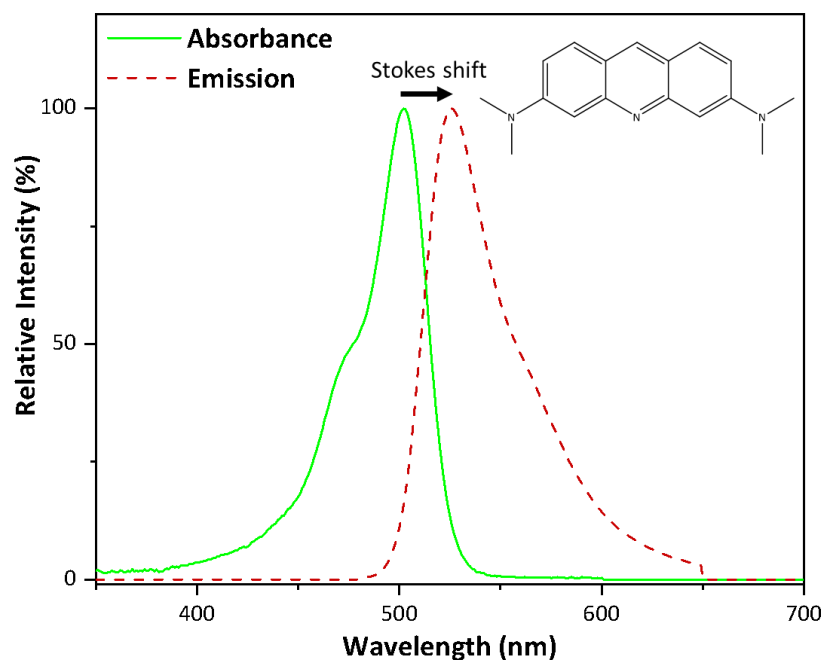


**Figure 2. 26** Absorbance (green solid line) and emission (red dashed line) spectra of acridine orange. Insert shows the molecular structure of acridine orange.<sup>42</sup>

The Stokes shift can have significant implications in fluorescence sensing. If both excitation and emission bands overlap, elastic light scattering of the incident light can interfere with the detection of the fluorescence emission.<sup>40</sup> In addition, fluorophores can also be quenched when interacting with specific chemical species in the environment, decreasing the amount of emitted fluorescence signal. This can be associated with the fluorescence resonance energy transfer (FRET) (Figure 2. 27), which is a mechanism that can lead to quenching when more than one type of fluorophore is used simultaneously (e.g. propidium iodide and SYTO 9 in BacLight Live/dead viability kit). In FRET, a donor fluorophore initially in the excited state can transfer energy to an acceptor fluorophore through non-radiative dipole-dipole coupling. As a result, rather than emitting fluorescence, the donor fluorophore will transfer energy to an acceptor molecule, which may subsequently emit fluorescence at a different wavelength (Figure 2. 27).<sup>41,43</sup> It is critical that these limitations are considered to interpret fluorescence data, as well as to implement optimal strategies for fluorescence imaging using fluorescence light microscopy, such as confocal fluorescence microscopy.

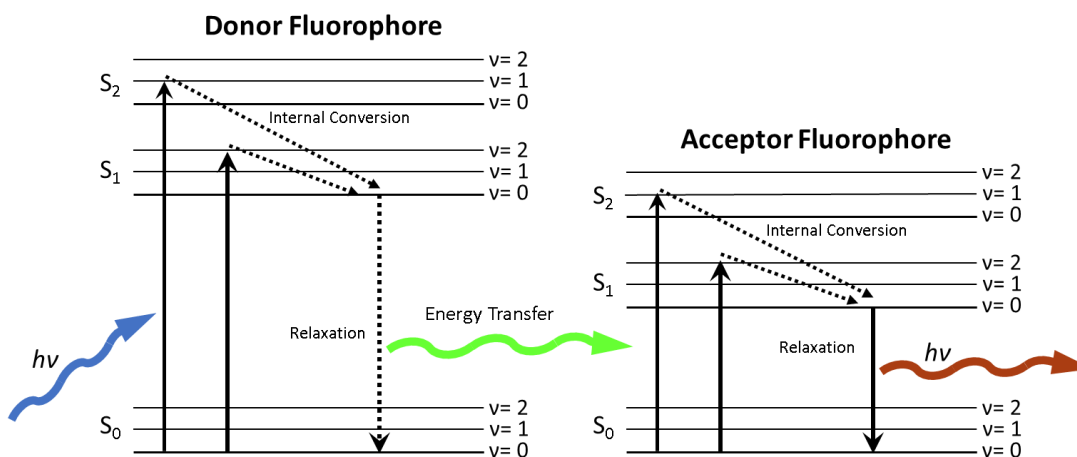


**Figure 2. 27** Jablonski diagram showing the mechanism of fluorescence resonance energy transfer (FRET) between a donor and acceptor fluorophore.

### 2.5.2.1 Confocal Fluorescence Microscopy

Confocal fluorescence microscopy (CFM) is a microscopy technique that can partially overcome limitations associated with the degradation of images due to low contrast and poor resolution. CFM has gained acceptance as an important microscopy technique owing to its capability to produce images free of out-of-focus light. In confocal fluorescence microscopy, the term confocal is used to describe the optical arrangement where both illumination and detection spots are focused to the same focal plane using a small diaphragm aperture, known as a pinhole. The pinhole at the illumination source changes the size and the shape of the incoming light, while the detection pinhole blocks the out of focus light coming from above and below the focal plane, therefore allowing only light at the focal point to be detected. As a result, remarkably detailed images can be obtained.<sup>44</sup> Combining this technique with lasers of specific wavelengths as illumination sources, associated with the excitation wavelength of individual fluorophores, allows for high-resolution imaging of a wide range of fluorescent specimens. A typical system based on this type of set-up is the confocal laser scanning microscope (CLSM) (Figure 2. 28).

In this type of system (Figure 2. 28), laser light is emitted from the illumination source and reaches the illumination pinhole. When the laser light exits this pinhole, the size and shape of the laser spot is altered, generating a narrow beam. The narrow laser beam is then reflected by a dichromatic mirror and focused by the objective lens towards the sample. Fluorescence emitted from the sample then passes back through the objective lens, and the dichromatic mirror and is focused at the detector pinhole, which excludes out-of-focus light. Only light at the focal point is then detected by a photomultiplier, which transforms the light into an electric impulse that can be read by the computer.<sup>44</sup>

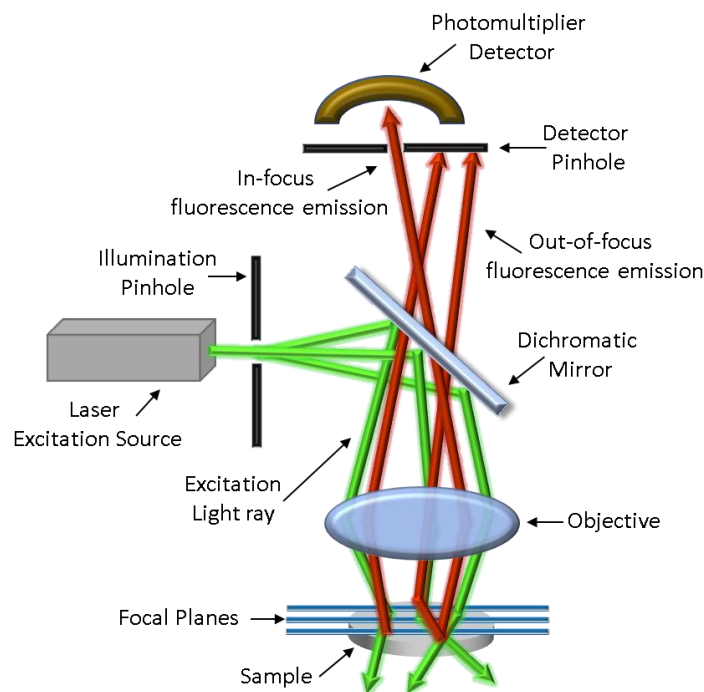


**Figure 2. 28** Schematic showing the optical pathway and general configuration of a confocal laser scanning microscope.

CLSM can be used to obtain qualitative and quantitative information of a specific system, such as using the combination of different fluorophores for differentiating live and dead bacteria. The combination of SYTO 9 and propidium iodide (PI) nucleic acid stains (Figure 2. 29) is commonly used for differentiating live and dead bacteria. These fluorophores differ in their spectral characteristics and their ability to penetrate bacterial membranes. SYTO 9 typically penetrates all bacteria, with both uncompromised and comprised cell membranes and exhibits

an absorbance/ emission maxima at around 480/500 nm (Figure 2. 29 A), while PI can only penetrate compromised cell membranes and exhibits an absorbance/ emission maxima around 535/620 nm (Figure 2. 29 B). PI is known to intercalate strongly between DNA bases with little or no sequence preference, whereas the mechanism associated with SYTO 9 is not known or has not been made publicly available. The optimum SYTO 9 and PI ratio in staining methods can vary depending on the bacterial organism and the environmental conditions. As seen in the spectra below for SYTO 9 and PI (Figure 2. 29), the emission spectrum for SYTO 9 and excitation spectrum of PI overlap. Therefore, it is important to note that FRET may occur under specific conditions.<sup>45</sup>

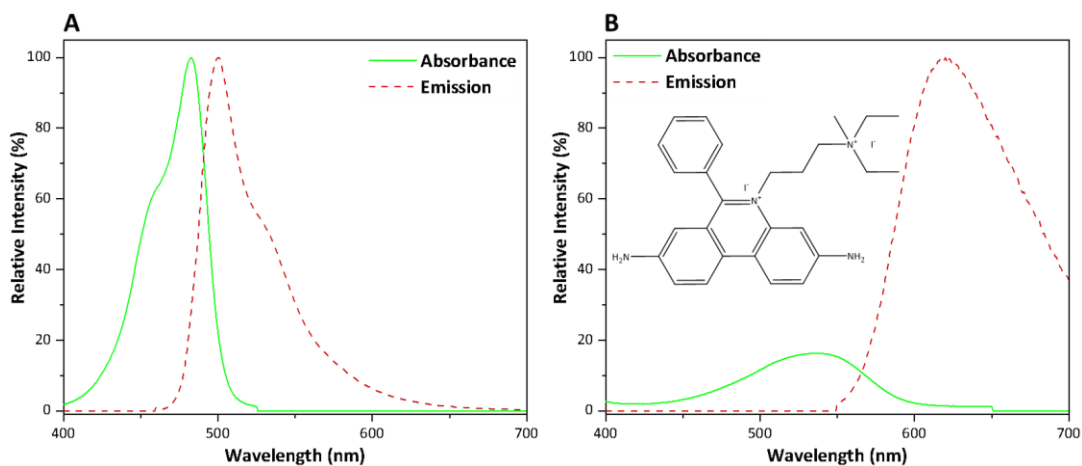


**Figure 2. 29** Absorbance and emission spectra of SYTO 9 green fluorescent stain (**A**) and propidium iodide red fluorescent stain (**B**). The insert in (**B**) shows the molecular structure of propidium iodide. Note: the molecular structure of SYTO 9 has not been disclosed by Thermofisher.<sup>45</sup>

Live/dead staining can be used on a wide a range of bacterial species to assess the viability of both planktonic (in solution) and surface attached bacteria. For example, figure 2. 30 shows an image of *S. aureus* bacteria attached to the surface of polydimethylsiloxane (PDMS).

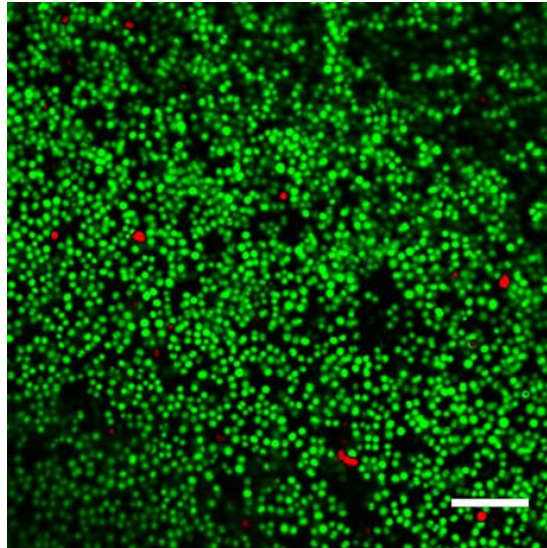


**Figure 2. 30** Representative merged CLSM image of *S. aureus* bacteria on PDMS, stained with SYTO 9 (green, live bacteria) and propidium iodide (red, dead bacteria) fluorescence dyes. (Scale bar is 10  $\mu\text{m}$ ).

In this work, CLSM along with live/dead staining of bacteria species with SYTO 9 and PI were used to determine the surface antimicrobial effect of the materials discussed in chapters 3 and 4. All images were collected using a confocal upright Zeiss LSM 880 Multiphoton microscope with excitation wavelengths of 488 nm for SYTO 9 and 561 nm for PI.

### 2.5.2.2 Confocal Fluorescence Microscopy Image Processing

CFM images of bacteria cells stained with propidium iodide or SYTO 9, can be used to determine the fraction of dead or live cells in a specimen. This is achieved by analysing the green and red channels and calculating the number (N) of green and red labelled cells in the image using an image processing software package, such as Fiji. Fiji (Fiji Is Just ImageJ) is a free, open-source, image analysis software based on ImageJ, with many built-in plugins and algorithms that can be automated (using a macro function) to process large sets of data.<sup>46</sup> It is important to note here, that for the purpose of analysis, all cells will stain green (SYTO 9) and the dead cells will stain red (PI). Therefore, to calculate the fraction of live or dead cells:

$$Live\ Ratio = \frac{N_{Green\ Only}}{N_{Green\ Only} + N_{Red}}$$

**Equation 2. 14**

$$Dead\ Ratio = \frac{N_{Red}}{N_{Green\ Only} + N_{Red}}$$

**Equation 2. 15**

The macro in Fiji (adapted from the Centre for Cell Imaging at the University of Liverpool, and further modified by Dr. Ioritz Sorzabal Bellido), first separates the two fluorescent channels and removes the background from each image (Figure 2. 31 A). A *Threshold* is then applied to segment the images, followed by a further segmentation using *Watershed* to separate two connected objects by creating *Watershed* lines (Figure 2. 31 B).<sup>47</sup> This process was optimised using a heuristic approach to determine the best *Threshold* for each set of images. After segmentation the macro creates a green only binary mask by subtracting the generated red mask from the green mask, in order to obtain a binary image with only live cells (Figure 2. 31 C). The number of green only ( $N_{Green\ Only}$ ) cells and red ( $N_{Red}$ ) cells are then counted using an *Analyse particles* function with an area ranging between 0.5  $\mu\text{m}$  and 5  $\mu\text{m}$ . The values obtained from this function can then be used in equations 2. 14 and 2. 15 to calculate the fraction of live or dead cells.

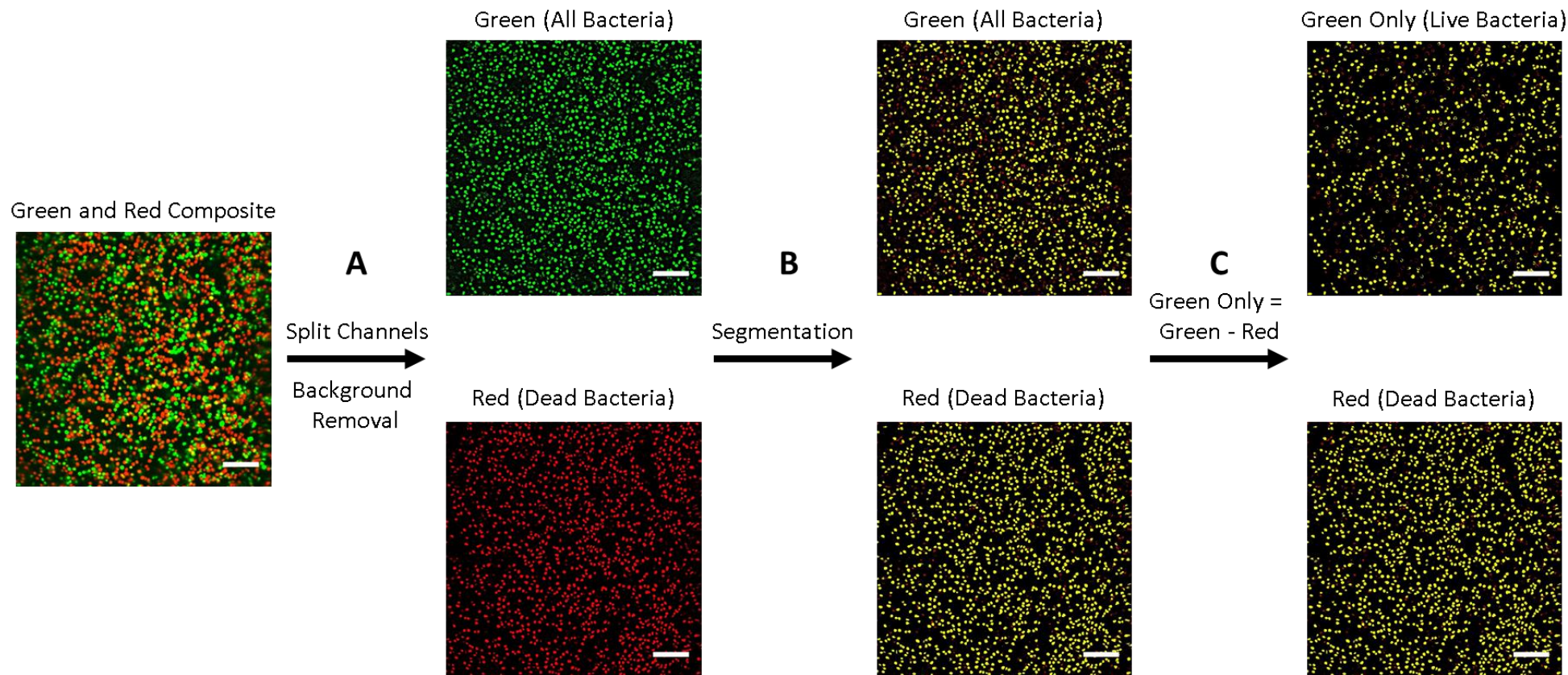


**Figure 2. 31** Schematic showing a general overview of the image processing of CFM images using Fiji macro. Example shown is a CLSM image of *S. aureus* bacteria on type I material after NIR irradiation at  $1174 \text{ mW/ cm}^2$  for 5 minutes. Bacteria are stained with SYTO 9 and PI fluorescence dyes. (A) Composite image is split into green and red channels and their backgrounds are removed. (B) The images are segmented using *Threshold* and *Watershed* functions. (C) Green only mask is generated by subtracting the red mask (dead bacteria) from the green mask (all bacteria). (Scale bars are  $10 \mu\text{m}$ ).

## 2.6 References

- 1 P. Gabbott and T. Mann, in *Principles of thermal analysis and calorimetry*, S. Gaisford, V. Kett and P. Haines, Royal Society of Chemistry, Cambridge, 2nd Edition, 2016, 67–103.
- 2 Y. Yuan and T. R. Lee, in *Surface Science Techniques*, G. Bracco and B. Holst, Springer, Heidelberg, 1st Edition, 2013, 3–34.
- 3 T. Young, *Philos. Trans. R. Soc. London*, 1805, **95**, 65–87.
- 4 Woodward Roger P., *First Ten Angstroms Inc Tech. Inf.*, 1999, **1**, 1–8.
- 5 E. Proksch, *J. Dermatol.*, 2018, **45**, 1044–1052.
- 6 F. W. Fifield and D. Kealey, *Principles and Practice of Analytical Chemistry*, F. W. Fifield and D. Kealey, Blackwell Science, Oxford, 5th Edition, 2000.
- 7 C. F. Poole, *Gas Chromatography*, Elsevier, C. F. Poole, Michigan, 1st Edition, 2012.
- 8 N. E. Battikha, in *Condensed Handbook of Measurement and Control*, N. E. Battikha, International Society of Automation, 4th Edition., 2018, 85–87.
- 9 M. Reichenbacher and J. Popp, in *Challenges in Molecular Structure Determination*, M. Reichenbacher and J. Popp, Springer, Heidelberg, 1st Edition, 2012, 63–143.
- 10 C. N. Banwell and E. M. McCash, in *Fundamentals of molecular spectroscopy*, C. N. Banwell and E. M. McCash, McGraw-Hill, Berkshire, 4th Edition, 1994, 55–99.
- 11 N. J. Harrick and K. H. Beckmann, in *Characterization of Solid Surfaces*, P. F. Kane and G. B. Larrabee, Springer US, Boston, 1st Edition, 1974, 215–245.
- 12 U. P. Fringeli, in *Encyclopedia of Spectroscopy and Spectrometry*, J. C. Lindon, G. E. Tranter and J. L. Holmes, Academic Press, London, 1st Edition, 1990, 58–75.
- 13 J. Coates, in *Encyclopedia of Analytical Chemistry*, R. A. Meyers, John Wiley & Sons,

Ltd, Chichester, 1st Edition, 2006, 10815–10837

- 14 G. Fang, H. Li and X. Liu, *Mater. Chem. Phys.*, 2010, **122**, 533–536.
- 15 P. Larkin, *Infrared and Raman Spectroscopy : Principles and Spectral Interpretation*, P. Larkin, Elsevier, Stamford, 2nd Edition, 2018.
- 16 C. N. Banwell and E. M. McCash, in *Fundamentals of molecular spectroscopy*, C. N. Banwell and E. M. McCash, McGraw-Hill, Berkshire, 4th Edition, 1994, 308.
- 17 M. Saggiu, J. Liu and A. Patel, *Pharm. Res.*, 2015, **32**, 2877–2888.
- 18 K. Czamara, K. Majzner, M. Z. Pacia, K. Kochan, A. Kaczor and M. Baranska, *J. Raman Spectrosc.*, 2015, **46**, 4–20.
- 19 S. P. Verma and D. F. H. Wallach, *Biochim. Biophys. Acta (BBA)/Lipids Lipid Metab.*, 1977, **486**, 217–227.
- 20 Y. Zhou and H. Cao, *Sci. World J.*, 2013, **2013**, 1–6.
- 21 T. Galeano Díaz, A. Guiberteau, J. M. Ortíz Burguillos and F. Salinas, *Analyst*, 1997, **122**, 513–517.
- 22 C. P. East, T. L. Schiller, C. M. Fellows and W. O. S. Doherty, in *Mineral Scales and Deposits*, Z. Amjad and K. D. Demadis, Elsevier, Amsterdam, 1st Edition, 2015, 681–699.
- 23 S. Hofmann, *Auger and X-ray Photoelectron Spectroscopy in Materials Science : A User-Oriented Guide*, G. Ertl, H. Luth and D. L. Mills, Springer, Heidelberg, 1st Edition, 2013.
- 24 P. Van der Heide, *X-ray Photoelectron Spectroscopy : An Introduction to Principles and Practices*, P. Van der Heide, Wiley-Blackwell, New Jersey, 1st Edition, 2012.
- 25 R. K. Mishra, A. K. Zachariah and S. Thomas, in *Microscopy Methods in Nanomaterials Characterization*, R. K. Mishra, A. K. Zachariah, S. Thomas and R.

- Thomas, Elsevier, 1st Edition, 2017, 383–405.
- 26 S. M. Hues and L. Lovejoy, in *Handbook of Silicon Wafer Cleaning Technology*, K. A. Reinhardt and W. Kern, Elsevier, Oxford, 3rd Edition, 2018, 728.
- 27 G. Attard and C. Barnes, in *Surfaces*, G. Attard and C. Barnes, Oxford University Press, Oxford, 1st Edition, 1998, 37–83.
- 28 G. A. Somorjai, *Chemistry in Two Dimensions: Surfaces*, G. A. Somorjai, Cornell University Press, Ithaca, 1st Edition, 1981.
- 29 S. W. Gaarenstroom and N. Winograd, *J. Chem. Phys.*, 1977, **67**, 3500–3506.
- 30 S. Bera, P. Gangopadhyay, K. G. M. Nair, B. K. Panigrahi and S. V. Narasimhan, *J. Electron Spectros. Relat. Phenomena*, 2006, **152**, 91–95.
- 31 M. Scimeca, S. Bischetti, H. K. Lamsira, R. Bonfiglio and E. Bonanno, *Eur. J. Histochem.*, 2018, **62**, 2841.
- 32 P. J. Thomas and P. A. Midgley, *Top. Catal.*, 2002, **21**, 109–138.
- 33 M. R. Lee, *Mineral. Mag.*, 2010, **74**, 1–27.
- 34 S. Utsunomiya and R. C. Ewing, *Environ. Sci. Technol.*, 2003, **37**, 786–791.
- 35 L. Yuan, R. Patterson, W. Cao, Z. Zhang, Z. Zhang, J. A. Stride, P. Reece, G. Conibeer and S. Huang, *RSC Adv.*, 2015, **5**, 68579–68586.
- 36 R. F. Egerton, *Physical principles of electron microscopy: An introduction to TEM, SEM, and AEM*, R. F. Egerton, Springer International Publishing, Switzerland, 2nd Edition, 2016.
- 37 H. Rösner, C. Kübel, Y. Ivanisenko, L. Kurmanaeva, S. V. Divinski, M. Peterlechner and G. Wilde, *Acta Mater.*, 2011, **59**, 7380–7387.
- 38 J. C. Meyer, C. O. Girit, M. F. Crommie and A. Zettl, *Nature*, 2008, **454**, 319–322.

- 39 J. J. Bozzola, in *Electron Microscopy, Methods and Protocols*, J. Kuo, Humana Press, Totowa, NJ, 3rd Edition, 2014, 1–21.
- 40 P. P. Mondal and A. Diaspro, *Fundamentals of Fluorescence Microscopy: Exploring Life with Light*, P. P. Mondal and A. Diaspro, Springer, Dordrecht, 1st Edition, 2014, 218.
- 41 B. Herman, *Fluorescence microscopy*, B. Herman, Bios Scientific Publishers, Oxford, 2nd Edition, 1998.
- 42 A. Pitchaimani, A. Renganathan, S. Cinthaikinian and K. Premkumar, *RSC Adv.*, 2014, **4**, 22123–22128.
- 43 J. B. Pawley, *Handbook of Biological Confocal Microscopy*, J. B. Pawley, Springer, Boston, 3rd Edition, 2006.
- 44 R. L. Price and W. G. Jerome, *Basic Confocal Microscopy*, R. L. Price and W. G. Jerome, Springer, New York, 1st Edition, 2011.
- 45 S. M. Stocks, *Cytom. Part A*, 2004, **61**, 189–195.
- 46 J. Schindelin, I. Arganda-Carreras, E. Frise, V. Kaynig, M. Longair, T. Pietzsch, S. Preibisch, C. Rueden, S. Saalfeld, B. Schmid, J.-Y. Tinevez, D. J. White, V. Hartenstein, K. Eliceiri, P. Tomancak and A. Cardona, *Nat. Methods*, 2012, **9**, 676–82.
- 47 P. Soille and L. M. Vincent, M. Kunt, International Society for Optics and Photonics, 1990, **1360**, 240–250.



# Chapter 3

## Controlled Release and Antimicrobial Activity of Fatty Acid Impregnated Polydimethylsiloxane (PDMS)

### 3.1 Introduction

#### 3.1.1 Polydimethylsiloxane

Polydimethylsiloxane (PDMS) is a biocompatible cross-linked organosilane based polymer, with interesting physical and chemical properties. PDMS can be easily fabricated using polymer cross linking in the presence of curing agents (Figure 3. 1) to form an optically transparent material; which is chemically inert, electrically non-conductive and has high elasticity.<sup>1-3</sup> The high elasticity of this material is due to the fact that the Si-O (1.64 Å) bond length is significantly longer than that of C-C (1.53 Å) bonds in organic polymers, along with the inequality in the Si-O bond angles (110° and 143°), which leads to the structure being in a *trans* configuration (Figure 3.2). As a result, there is less steric hinderance and intramolecular congestion, thus leading to a rubber like physical state of the final material, with a high dynamic flexibility and very low glass-transition temperature.<sup>1</sup>

A chemically crosslinked polymer, such as PDMS, can increase its volume several fold by absorbing large amounts of the non-polar solvent through a diffusion process. PDMS is a well-known to be hydrophobic material, with a literature static water contact angle of 110°,<sup>4</sup> allowing the material to interact strongly with non-polar solvents. Non-polar solvents such as

chloroform ( $\text{CHCl}_3$ ), hexane and tetrahydrofuran (THF) are examples of some solvents that swell PDMS to a remarkable degree, with an increased size ratio of 1.39, 1.35 and 1.38 for each solvent respectively, after swelling the PDMS for 24 hrs. However, when in contact with polar solvents such as water and methanol, PDMS is less susceptible to swelling and remains its original size.<sup>5</sup>

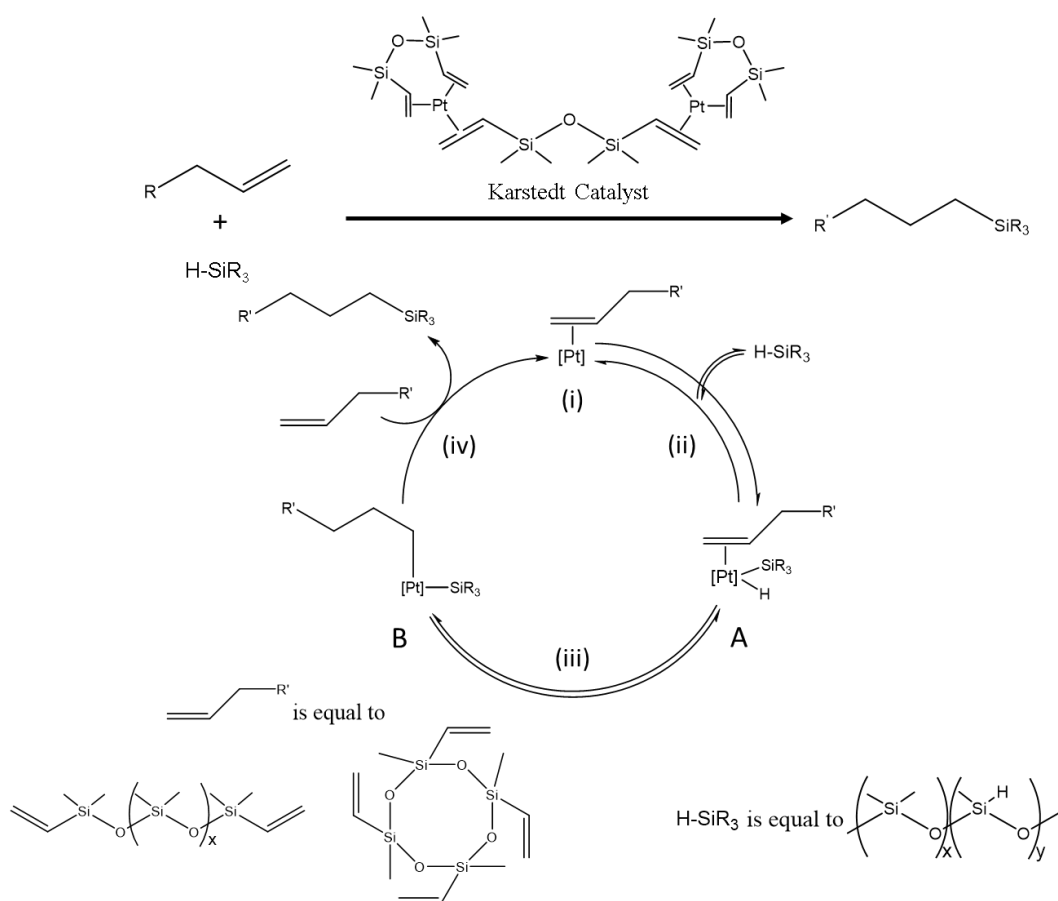


**Figure 3. 1** Proposed mechanism for the curing process of polydimethylsiloxane (PDMS) in the presence of platinum based Karstedt catalyst. (i) The platinum species coordinates to the alkene groups, (ii) followed by oxidative addition of  $\text{HSiR}_3$  to form species A. (iii) Species A is then in equilibrium with species B. (iv)  $\text{SiR}_3$  is then added to the equilibrated species and the final product is then released after reductive elimination. Figure reproduced from reference 2.<sup>2</sup>

The swelling behaviour of PDMS is believed to be associated with unreacted starting products, such as partially cross-linked macromolecules within the polymeric material. When the PDMS swells in contact with a non-polar solvent, the unreacted starting products act as an athermal solvent, interacting with the surrounding media. The unreacted starting products then begin to

diffuse out of the PDMS until an equilibrium is reached, preventing the further absorption of any non-polar materials.<sup>6</sup>

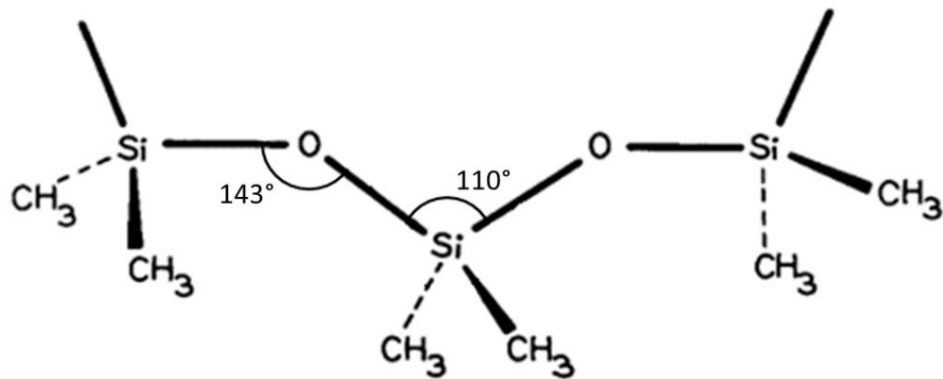


**Figure 3. 2** Schematic representation of polydimethylsiloxane (PDMS) showing the unequal Si-O bond angles responsible for the high structured flexibility of the material. Figure adapted from reference 1.<sup>1</sup>

As a result of the interesting chemical and physical properties discussed above, PDMS has been used in a wide range of biomedical applications such as: blood pumps, cardiac pacemaker leads, mammary prostheses, catheters, medical skin patches, drug-delivery systems and more.<sup>7-11</sup> PDMS is physiologically inert, has good blood compatibility, low toxicity, good oxidative stability, as well as antiadhesive properties.<sup>7</sup> However, the material also has some drawbacks. PDMS is prone to bacterial colonisation, which can lead to the formation of biofilms, eventually leading to device failure.<sup>12</sup> As a result, it is important that new approaches are required to overcome this issue, by imparting antimicrobial properties onto PDMS.

### 3.1.2 Modification of PDMS Towards Antimicrobial Activity

To tackle the issue of bacterial colonisation on PDMS, two main approaches have been proposed in the literature: 1) surface modification and 2) bulk modification of the polymer.<sup>7,11</sup>

#### 3.1.2.1 Surface Modification of PDMS

Surface modification of PDMS can be carried out following chemical treatments of the PDMS, such as: a layer-by-layer approach, or oxidation of the PDMS surface followed by further functionalisation.

By using a layer-by-layer approach, multilayer systems can be formed, and it is a common strategy to confer new properties on a materials surface. The surface of the material can be coated with a thin antibiotic film, via dip or spin-coating to form homogenous layers on the surface of the material, followed by heating. The thin antibiotic film adheres to the material through electro-static interactions or hydrogen bonding.<sup>11</sup> One example of this, is the preparation of antimicrobial polysiloxanes by coating with antibiotics, such as vancomycin.<sup>13</sup> This material was shown to reduce bacterial colonisation of *S. aureus* and *S. epidermis*. Unfortunately, using a layer-by-layer approach is inherently a batch process (single substrate), and optimising coating conditions can be a laborious task.

Alternatively, oxidation of PDMS can lead to the formation of hydroxyl moieties, substituting methyl groups at the surface of the PDMS, thus changing the properties of PDMS and making the material more hydrophilic.<sup>7,11,14</sup> These OH groups allow for further functionalisation and binding of functional molecules, such as biocides.<sup>15</sup> Oxidation of the surface can be easily achieved using oxygen or air plasma treatments (Figure 3. 3), however, plasma treated surfaces can be unstable.<sup>11,16</sup> Following plasma treatment, the oxidised surface can recover its original form over time by the recovery of hydrophobic methyl groups and therefore these materials

need to be functionalised immediately after plasma treatment. The return of the hydrophobic methyl groups at the surface of PDMS has been attributed to several mechanisms, involving the condensation of silanol groups with water, out-diffusion of untreated and unreacted polymer chains and molecular reordination of polar groups into the bulk of the material.<sup>16,17</sup>

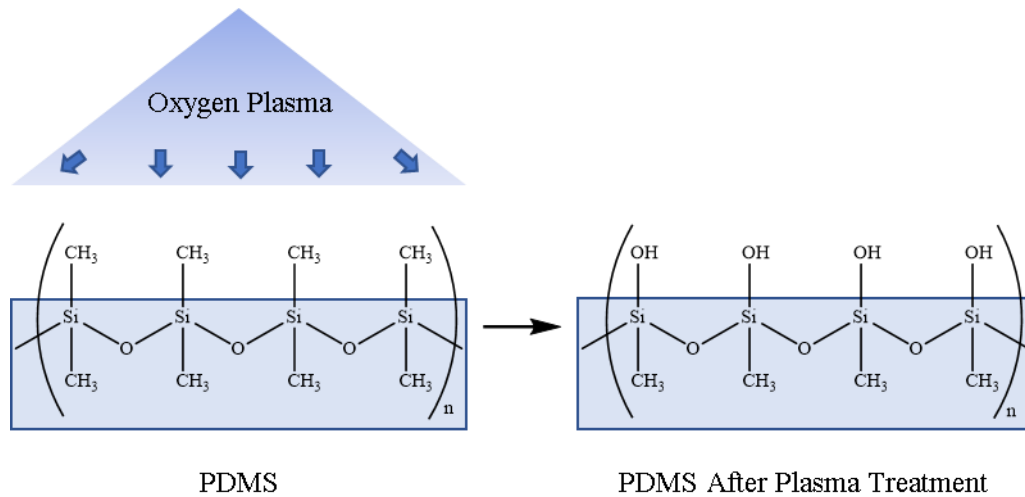


**Figure 3. 3** General overview for the surface modification of polydimethylsiloxane (PDMS) by oxygen plasma treatment. Figure adapted from reference 18.<sup>18</sup>

### 3.1.2.2 Bulk Modification of PDMS

In addition to surface modification, where the surface composition of PDMS materials can be directly modified, the bulk material can alternatively be modified using polymer blending or direct co-polymerisation.<sup>7,11</sup> As a result of the bulk modification process, the PDMS can exhibit a different surface composition, which can be targeted to have specific properties for a given application.<sup>7</sup>

Polymer blending is a method to produce materials with improved bulk and surface properties. The combination of two or more structurally dissimilar polymers can be facilitated for example, by hydrogen bonding (Figure 3. 4 i) and allow for the production of new types of materials, combining different properties from the individual component polymers.<sup>7,19</sup>

Siloxanes have been blended with various polymers for tailored biomedical applications.<sup>7</sup> One such polymer is C-Flex™, which is made by blending polysiloxanes with styrene-ethylene/butylene-styrene block copolymers to form a thermoplastic elastomer, which is relatively inexpensive and biocompatible.<sup>7</sup> Unfortunately, blending different polymers can lead to poor mechanical properties, as well as poor interfacial adhesion between phases, possibly leading to material break down and subsequent leach into biological media.<sup>7</sup>

Another method of altering the properties of a polymeric material is direct copolymerisation.<sup>7,11</sup> Direct copolymerisation relies on the polymerisation reaction between two or more different monomer types (Figure 3. 4 ii), and has been used in a range of biomedical implants due to their elasticity, gas permeability and inert nature in the human body.<sup>7,20</sup> Direct copolymerisation is often used to change the surface properties of a polymer, such as roughness and adhesion and has been shown to exhibit some anti-biofilm activity.<sup>11</sup> However, it has also been documented that the formation of copolymers induces reduced antimicrobial activity compared to their monomeric counterparts.<sup>7,21</sup>

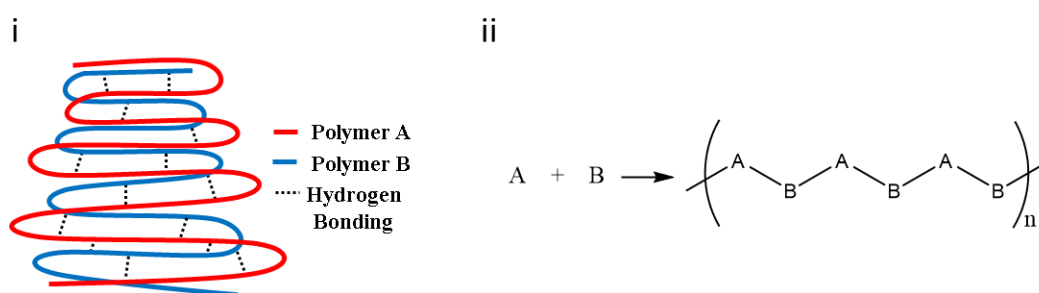


**Figure 3. 4** (i) Graphical illustration of polymer blends showing the interfacial adhesion between two polymers by hydrogen bonding and (ii) Graphical illustration showing the generic structure of a copolymer formed by reacting two different monomers.

By using a more simplified approach compared to the methods discussed above, we can take advantage of the hydrophobic nature of pristine PDMS, and its ability to swell upon contact with non-polar solvents to introduce non-polar or amphiphilic biologically active molecules

into the PDMS. One class of such biologically active molecules are fatty acids that will be discussed in the next section.

### 3.1.3 Fatty Acids

Fatty acids are biomolecules that naturally occur in most living organisms.<sup>22</sup> Fatty acids have been used by humanity for thousands of years, specifically in the preparation of soaps. The oldest literary reference to soap relates to the washing of wool and is found in Sumerian clay tablets dating to ~2500 BCE.<sup>23</sup> The structure of fatty acids consist of a long aliphatic chain, with a methyl group (-CH<sub>3</sub>) at one end of the chain and a carboxyl group (-COOH) at the other (Figure 3. 5). The aliphatic chain is hydrophobic, while the carboxyl group (-COOH) is hydrophilic and can be ionised (COO<sup>-</sup>) when solubilised in water. This makes the molecule amphiphilic. The length of the carbon chain can have a significant impact on the solubility of the molecules in water, due to the increased hydrophobicity with increasing carbon chain length (Figure 3.5). The number of carbon atoms varies, but most naturally abundant fatty acids have an even number of carbon atoms between 10-28. The fatty acid alkyl chain can have two main forms, either saturated or unsaturated. Saturated fatty acids only have C-C single bonds between the carbon atoms across the chain, while unsaturated fatty acids have one or more C=C double bonds in different positions within the chain (Figure 3. 5).<sup>24</sup>

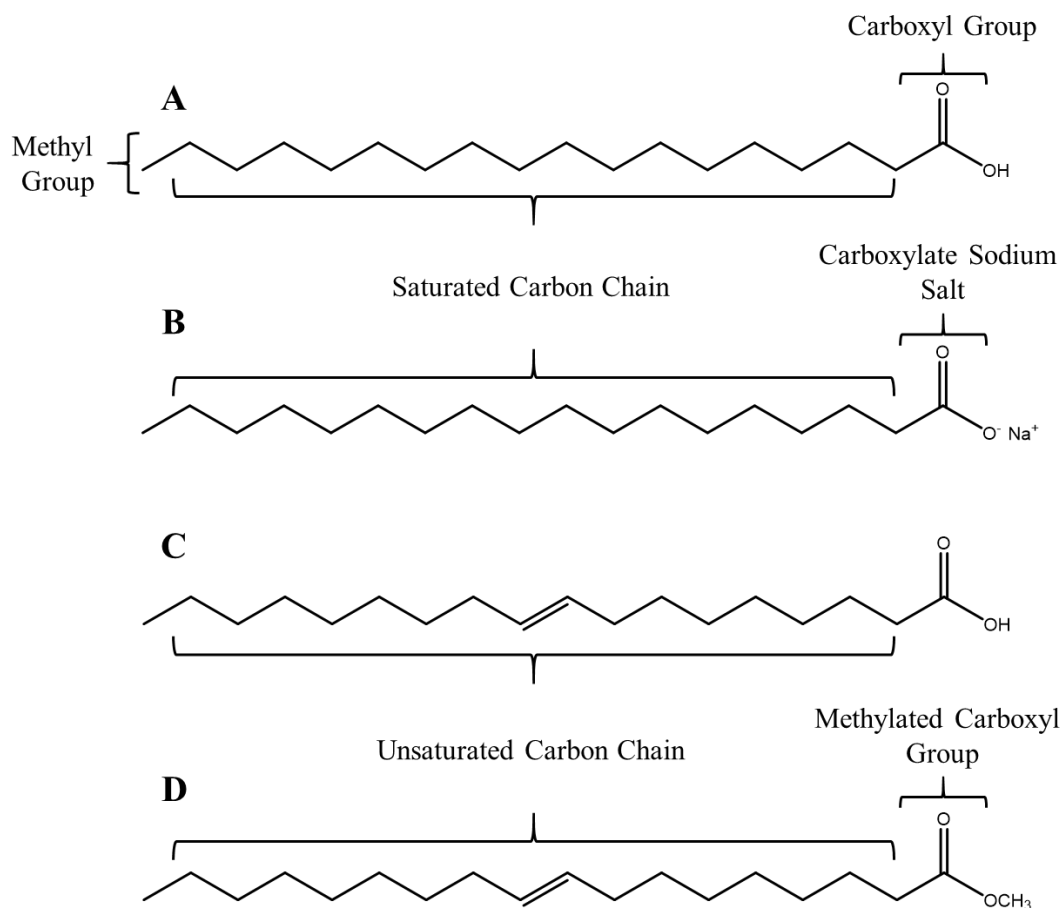


**Figure 3. 5** General structure of fatty acids and derivatives. Octadecanoic acid ( $C_{16}$ ) chosen as a representative structure. (A) Octadecanoic acid, (B) Sodium Octadecenoate, (C) *cis*-9-Octadecenoic acid and (D) Methyl *cis*-9-Octadecenoate.

The carbon chain length can also affect other properties, including the melting point and the acid dissociation ( $K_a$ ) of the fatty acid molecules (Table 3. 1). The acid dissociation constant ( $K_a$ ) is a quantitative measure of the strength of an acid in solution and is commonly denoted as  $pK_a$ , where  $pK_a$  is equal to the  $-\log_{10} K_a$ .<sup>25</sup> The  $pK_a$  of the fatty acid molecules significantly influences the solubility of the fatty acid in aqueous media (Table 3. 1), where the salt form of the fatty acid proves to be more water-soluble. Once the pH of an aqueous media moves above the  $pK_a$  of a specific fatty acid, the acid dissociates and can form a salt (Figure 3. 6). Interestingly the  $pK_a$  of fatty acids remains predominantly similar for short to medium chain fatty acids, however, fatty acids with an aliphatic chain length above  $C_{16}$  have an exceedingly high  $pK_a$  value (Table 3. 1).

**Table 3. 1** Literature data for some common saturated fatty acids. Carbon chain length, literature melting point (°C), acid dissociation constants (pKa) and aqueous solubility data.<sup>26-31</sup>

Fatty Acid	Carbon Chain Length	Literature Melting Point (°C)	Literature pKa	Aqueous Solubility (g L <sup>-1</sup> )	
				Fatty Acid (COOH)	Fatty Acid Salt (COO <sup>-</sup> )
Hexanoic Acid	6	-4.1 <sup>28</sup>	4.83 <sup>30</sup>	10.2 <sup>27</sup>	138.14 <sup>31</sup>
Octanoic Acid	8	16.51 <sup>28</sup>	4.89 <sup>29</sup>	0.8 <sup>27</sup>	58.336 <sup>29</sup>
Decanoic Acid	10	31.39 <sup>28</sup>	4.9 <sup>29</sup>	0.15 <sup>27</sup>	18.551 <sup>29</sup>
Dodecanoic Acid	12	43.82 <sup>28</sup>	5.3 <sup>29</sup>	0.055 <sup>27</sup>	5.113 <sup>29</sup>
Tetradecanoic Acid	14	54.16 <sup>28</sup>	5.8 <sup>29</sup>	0.02 <sup>27</sup>	1.727 <sup>29</sup>
Hexadecanoic Acid	16	62.49 <sup>28</sup>	8.6 <sup>30</sup>	0.0072 <sup>27</sup>	0.473 <sup>26</sup>
Octadecanoic Acid	18	69.3 <sup>28</sup>	10.15 <sup>30</sup>	0.0029 <sup>27</sup>	0.306 <sup>26</sup>

According to literature, as the carbon chain length of the fatty acid increases, van der Waals interactions between the chains of adjacent molecules increase, bringing these molecules closer to each other. When this happens, the proximity of the fatty acid carboxyl groups increases the tendency to form intramolecular hydrogen bonds. This effect leads to an increase of the pKa of the molecules.<sup>30</sup>

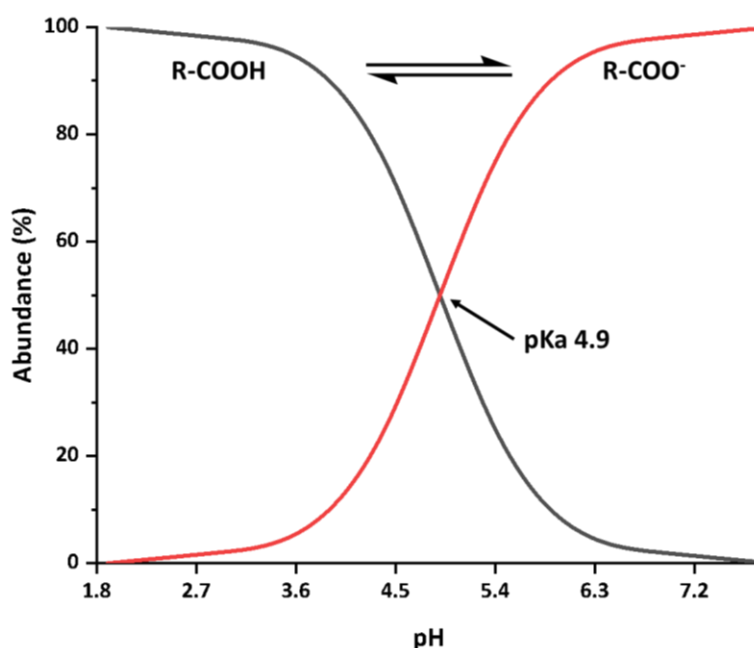


**Figure 3. 6** Schematic showing the acid base equilibria of fatty acids. Acid base equilibria of decanoic acid is shown as an example.

The relative abundance of fatty acids is high compared to other biomolecules. They are usually found bound to other compounds such as glycerol, sugars or phosphate head groups to form a variety of lipids. Lipids are essential components of various cell structures. The membranes of cells are typically composed of phospholipids and triglycerides.<sup>24</sup> Fatty acids can be cleaved from lipids, typically by enzymes, known as lipases (Figure 3. 7). Lipases hydrolyse triglycerides via a catalytic triad of amino acids, consisting of serine, histidine and aspartic acid, leading to glycerol and free fatty acid.<sup>32</sup>

Fatty acids can also be extracted from triglycerides on an industrial scale by a base catalysed hydrolysis, known as saponification (Figure 3. 7). In this process, hydroxyl anions attack the carbonyl group by nucleophilic addition, to form a tetrahedral intermediate. The tetrahedral intermediate can either reform the ester or release the alkoxide, leading to the formation of the the fatty acid salt. The reaction then continues until the final glycerol and fatty acid salt products have been produced. The free fatty acid can then be formed by addition of a strong acid, such as HCl, to neutralise the salt.<sup>33</sup>

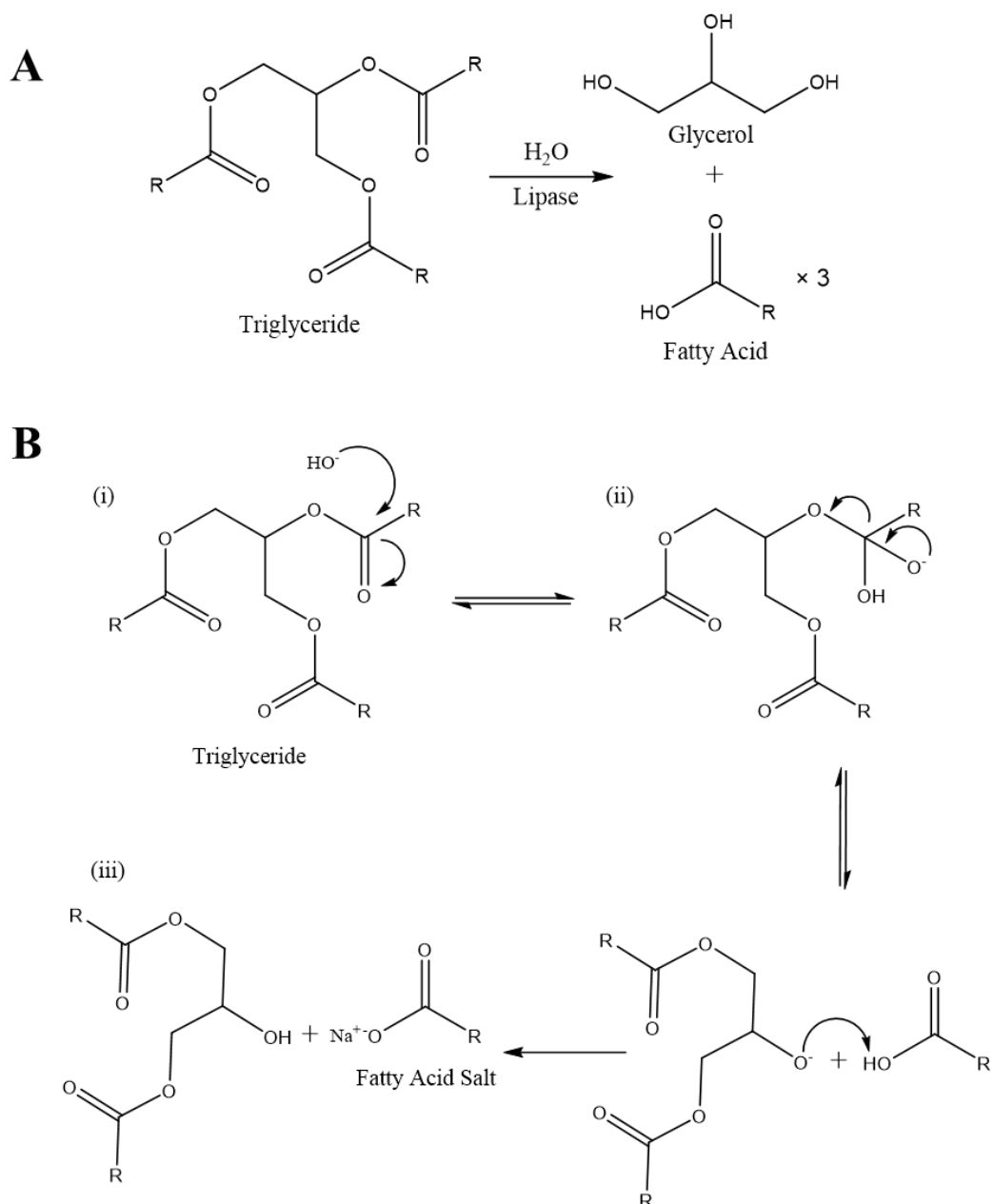


**Figure 3. 7 (A)** Digestion of triglyceride by enzymatic hydrolysis with lipase to produce fatty acid and glycerol.<sup>32</sup> **(B)** Base catalysed hydrolysis of triglyceride. **(i)** Triglyceride is broken down by nucleophilic addition to form a tetrahedral intermediate, **(ii)** followed by release of the alkoxide to form **(iii)** the fatty acid salt. The reaction cycle then repeats until the triglyceride is broken down into glycerol and fatty acids salts.<sup>33</sup> R in both **A** and **B** is equal to  $C_n$  aliphatic chain.

### 3.1.4 Antimicrobial Properties and Biocompatibility of Fatty Acids

Fatty acids are known to be biocompatible due to their inherent non-toxic properties, and have also been shown to exhibit antimicrobial activity.<sup>24,34-42</sup> The antimicrobial activity of fatty acids has long been known, with potencies comparable to natural antimicrobial peptides.<sup>39,43</sup> The biological activity of fatty acids plays a key role in host defences against potential pathogenic or opportunistic microorganisms, of particular importance is the growth inhibition or killing of bacteria.<sup>24</sup>

Fatty acids are considered to be one of the most active antimicrobial agents present on human skin, with typically 10-15  $\mu\text{g}/\text{cm}^2$ , of which dodecanoic acid, tetradecanoic acid, hexadecanoic acid, *cis*-6-hexadecenoic acid and *cis*-8-octadecenoic acid are the most abundant (Figure 3.8).<sup>24</sup> The fatty acids are produced on the skin by lipolytic cleavage of lipids secreted from the sebaceous glands and help to provide an antimicrobial barrier against bacterial microbiota.<sup>24,40</sup> In addition to their direct antimicrobial effect, fatty acids help to create unfavourable conditions for some bacteria to thrive on the surface of human skin, by acting as a buffer to maintain an acidic pH.<sup>44</sup> Fatty acids can also affect the expression of bacterial virulence factors that are integral for an infection to form, by disrupting cell-to-cell signalling.<sup>24</sup>

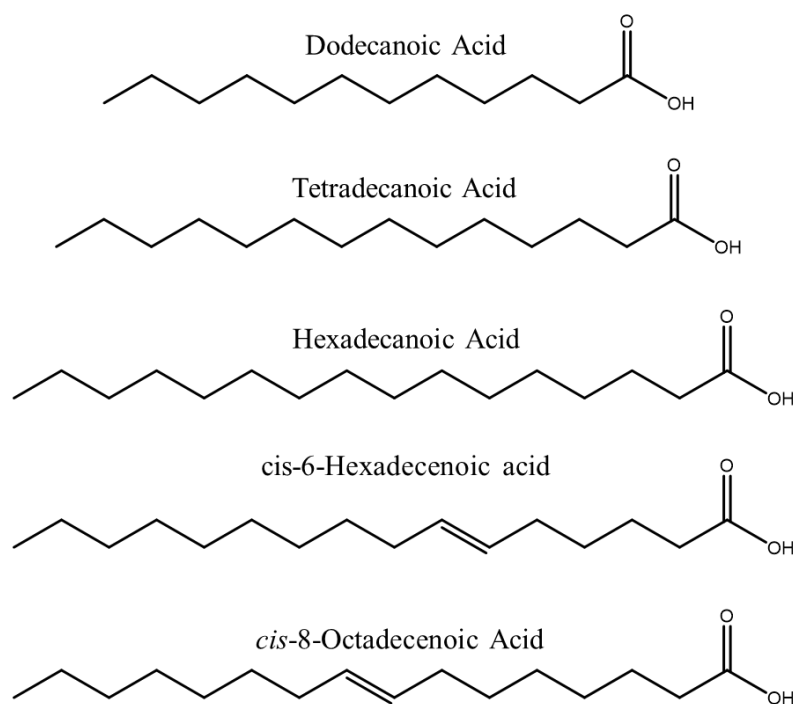


**Figure 3. 8** Schematic showing the most abundant antimicrobial fatty acids found on human skin.<sup>24</sup>

The antimicrobial activity of fatty acids is determined by the structure of the alkyl chain. The length of the carbon chain, along with the presence, number, position and orientation of double bonds can dictate the antimicrobial activity towards different bacterial species.<sup>24</sup> However, the literature regarding the antimicrobial activity of fatty acids is controversial. The carboxyl group (-COOH) (Figure 3. 5) in fatty acids seems to play an important role in the antimicrobial activity, since methylated (-OCH<sub>3</sub>) (Figure 3. 5) fatty acids often have reduced or no activity.<sup>24,45</sup> Medium and long chain unsaturated fatty acids have been found to be more active towards Gram-positive bacteria than towards Gram-negative bacteria, with the most active unsaturated fatty acids having between 10 and 16 carbon atoms.<sup>46-48</sup> While, saturated fatty acids with 10 or 12 carbons in the chain have an increased antimicrobial efficacy compared to shorter or longer saturated chain lengths.<sup>48,49</sup>

The use of fatty acids as antimicrobial agents have been cast aside in recent years in favour of synthetic antibiotics.<sup>39,43</sup> With the current increase in antibiotic resistance and challenges in antibiotic drug development, fatty acids require new attention as antimicrobial agents and can potentially help in the battle against drug-resistant bacteria.

As discussed above there are several methods by which polysiloxane materials can be modified to incorporate antimicrobial properties. Herein, we look at a simpler approach to tackling bacterial colonisation on PDMS surfaces. We utilise the swelling ability of PDMS to load the PDMS with fatty acids as potential antimicrobial agents and study their effect on bacterial colonisation.

## 3.2 Experimental Details

### 3.2.1 Chemicals

**Chemicals:** Sylgard 184 silicone elastomer kit (Dow Corning) was purchased from Univar Ltd. Hydrochloric acid (HCl, 37% w/v), glacial acetic acid (analytical grade), and ethanol (EtOH, absolute 99%) were purchased from Fisher Scientific. Sodium hydroxide (NaOH, 97%) and phosphate buffer saline (PBS) tablets were purchased from VWR. Lysogeny broth (LB) powder (Difco) was purchased from Scientific Laboratory Supplies (SLS). Live/ dead kit containing SYTO 9 and propidium iodide nucleic acid stains was purchased from ThermoFisher. All remaining chemicals listed were purchased from Sigma Aldrich: Decanoic acid (C<sub>10</sub>, 98%), Dodecanoic acid (C<sub>12</sub>, 98%), Tetradecanoic acid (C<sub>14</sub>, 98%), 4-(2-hydroxyethyl)-1-piperazineethanesulfonic acid (HEPES, 99.5%), sodium chloride (NaCl, 98%) and nutrient agar. All chemicals were used as received without further purification. Deionised water (Thermo Scientific Barnstead Smart2Pure), with a resistivity of 18 MΩ-cm was used throughout all experiments.

### 3.2.2 Fabrication of PDMS and Fatty Acid Impregnated PDMS (FAIP) Materials

**Fabrication of PDMS samples:** PDMS was fabricated using Sylgard 184 silicone elastomer kit (Dow Corning). PDMS base and curing agent were mixed in a 10:1 ratio (base: curing (w/w)), followed by the addition of chloroform (CHCl<sub>3</sub>) with a ratio of 2:1 (chloroform: base (v/w)). The mixture was then subject to vortex for 2 minutes to ensure homogeneity and pipetted (2.5 ml) into the wells of a non-stick baking tray. The tray was then loosely covered with aluminium foil and allowed to cure for 2 days in a fume hood at room temperature (RT) (approx. 25°C). The average weight of the PDMS material after curing was found to be 0.9055 g ± 0.088g.

**Loading of PDMS samples with fatty acid:** Decanoic ( $C_{10}$ ), Dodecanoic ( $C_{12}$ ) and Tetradecanoic ( $C_{14}$ ) acids were used to impregnate the PDMS owing to their amphiphilic properties, allowing the hydrophobic  $C_n$  chain to interact with the PDMS material through a diffusion process described in the introduction, to form PDMS  $C_{10}$ , PDMS  $C_{12}$  and PDMS  $C_{14}$ . In a typical experiment, PDMS samples were weighed after curing and then loaded with fatty acid. The fatty acids were melted in individual glass jars at  $37^\circ\text{C}$  ( $C_{10}$ ),  $50^\circ\text{C}$  ( $C_{12}$ ) and  $60^\circ\text{C}$  ( $C_{14}$ ), forming a viscous liquid. PDMS samples were swelled with fatty acid by placing the cured PDMS samples in individual wells of a 6-well plate and covering them with 3 ml of melted fatty acid. The wells were covered with a lid, sealed with black PVC insulation tape and then placed in the oven at the required melting temperature (as above), overnight for a minimum of 16 hrs. After swelling the PDMS samples overnight, the samples in the well plate were placed immediately in the freezer, causing the fatty acids to solidify. Once the fatty acids had solidified, the well plates were taken out of the freezer and the samples were removed. To remove the samples from the fatty acid in wells, the unincorporated solidified fatty acid had to be broken with tweezers and the PDMS sample removed. The fatty acid impregnated PDMS (FAIP) materials (PDMS  $C_{10}$ , PDMS  $C_{12}$  and PDMS  $C_{14}$ ) were washed quickly with ethanol and dried with compressed air to remove any unincorporated fatty acid. The samples were then weighed to determine the amount of fatty acid loaded in the material.

### 3.2.3 Characterisation of PDMS and FAIP Materials

**Chemical characterisation of pristine PDMS, fatty acids and FAIP materials:** Chemical characterisation of PDMS, fatty acids and FAIP materials was done using Raman spectroscopy. Raman spectra were recorded with a Renishaw inVia confocal Raman microscope using an excitation wavelength of 532 nm and a 20x objective lens. Different laser powers and acquisition times were used depending on the Raman experiment and particular fatty acid material. Raman spectra were processed using WiRE 4.4 software (Renishaw).

**Physical characterisation of pristine and FAIP materials by differential scanning calorimetry (DSC):** The raw fatty acid and PDMS materials, along with the FAIP samples were weighed and then analysed using DSC. DSC data were acquired in air using a TA Instruments Q2000 differential scanning calorimeter, equilibrated to  $-80^{\circ}\text{C}$  and then run with a ramp rate of  $5^{\circ}\text{C min}^{-1}$  to  $100^{\circ}\text{C}$ . The DSC data was used to identify the average  $T_{\text{Onset}}$  (temperature onset of melting),  $T_{\text{Max}}$  (temperature of complete melting) and enthalpy of change ( $\Delta H$ ) of the fatty acid materials. DSC data was acquired for the FAIP, the raw fatty acids and PDMS. Non-impregnated PDMS did not show DSC signals in the temperature range investigated (see appendix, Figure A3. 1).

**Raman spectroscopy of FAIP cross-section:** The distribution of fatty acid across the depth of the material was spectroscopically examined using a Renishaw inVia confocal Raman microscope. FAIP samples were cut and the Raman spectra of the FAIP samples were taken using a map image acquisition mode, with a spectrum recorded every  $5\ \mu\text{m}$  and starting from the top surface ( $X_0$ ) to the base of the material (Figure 3. 9). An excitation wavelength of  $532\ \text{nm}$  was used for all experiments.  $\text{C}_{10}$  swelled PDMS samples were analysed using 50% laser power and 20 s acquisition time;  $\text{C}_{12}$  swelled PDMS samples were analysed using 10% power and 4 s acquisition time;  $\text{C}_{14}$  swelled PDMS samples were analysed using 50% power and 5 s acquisition time. The baseline of each spectra was corrected using WiRE 4.4 software (Renishaw) and the distribution of fatty acid was determined using a component fit analysis against the Raman spectra of pure fatty acid material, using a direct classical least squared (DCLS) component fit analysis,<sup>50,51</sup> with mean centre and scale to unit variance normalisation.

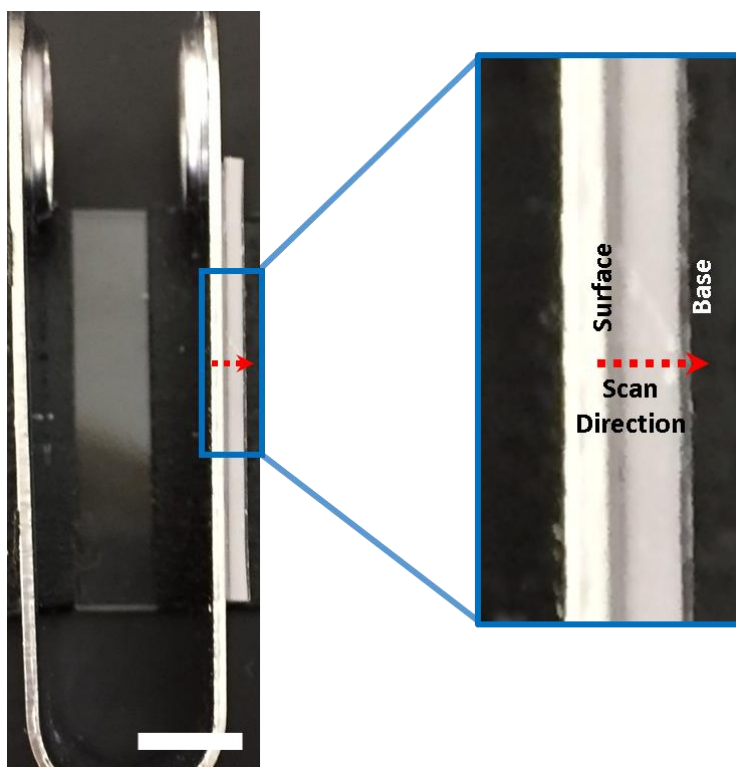


**Figure 3. 9** Image showing an example of the Raman cross section experiment. The sample is placed on a stand, exposing the side of the material, therefore allowing for the distribution of fatty acid across the depth of the sample to be analysed. Sample shown is PDMS C<sub>14</sub>. (Scale bar is 5 mm).

**Determining the distribution of fatty acid within the bulk of FAIP by Raman spectroscopy:** The distribution of fatty acid within the bulk of the FAIP was investigated using Raman spectroscopy with a Renishaw inVia confocal Raman microscope. The FAIP materials were examined immediately after preparation. Raman spectra were collected using a map image acquisition mode, at a depth of 500  $\mu\text{m}$  from the sample surface, with a spectrum recorded every 75  $\mu\text{m}^2$ , with a total of 100 acquisitions per sample across an area 1500 mm x 375 mm. An excitation wavelength of 532 nm, 100% laser power and 30 s acquisition time were used for all experiments. All collected data were processed according to the above cross section experiment.

### 3.2.4 Characterisation of Fatty Acid Release from FAIP

The release of fatty acid from the FAIP materials was investigated using several techniques, including: Gravimetric analysis, Raman spectroscopy and static contact angle measurements. The release of the fatty acid materials was carried out using pH 5 and pH 7 buffers, at different temperatures ranging from 5°C to 60°C.

**Release of fatty acid from FAIP by gravimetric analysis:** After impregnation of the PDMS with fatty acid, the FAIP samples were placed in 3 ml of either pH5 or pH 7 buffer at a given temperature, to monitor the release of fatty acid after 24 hrs. The mass of the loaded PDMS samples used in these experiments were 0.9812 g  $\pm$  0.1168 g for PDMS C<sub>10</sub>, 0.9666 g  $\pm$  0.1211 g for PDMS C<sub>12</sub> and 0.9343 g  $\pm$  0.0299 g for PDMS C<sub>14</sub>. The release temperature of the different FAIP samples were as follows: PDMS C<sub>10</sub> samples were carried out at 5°C and 37°C; PDMS C<sub>12</sub> samples were carried out at RT and 50°C; PDMS C<sub>14</sub> samples were carried out at RT and 60°C. pH 5 buffer was made by using 1 M acetic acid in water and adjusting the pH with aliquots of 5 M NaOH. pH 7 buffer was made using 1 M HEPES in water and adjusting the pH using aliquots of 5 M NaOH. After 24 hrs, the individual samples were washed quickly with 6 ml of ethanol, dried with compressed air and then weighed. Gravimetric measurements were carried out using an AND HR-100AZ analytical balance.

**Monitoring the distribution of fatty acid across the depth of FAIP materials by Raman spectroscopy after release:** The release of fatty acid from FAIP samples was carried out according to the protocol discussed above. The distribution of fatty acid across the depth of the sample after release was performed using Raman spectroscopy according to the Raman cross section experiment discussed previously.

**Static contact angle measurements FAIP:** After impregnation of the PDMS with the individual fatty acids, the wettability of the samples was investigated using static contact angle measurements. pH 5 and pH 7 buffers were used for determining the contact angle of the FAIP. Contact angle measurements were measured using a First Ten Ångstroms (FTA) 1000 instrument with a Gilmont GS-1201 micrometer dispenser syringe via the sessile drop method. Contact angle images were collected with a frame rate of 60 frames/ s. Contact angle data was then processed using FTA 32 drop shape analysis software (Version 2). The average contact angle of the FAIP samples was determined from 30 images per drop, for 3 drops on 3 different sample replicates using a non-spherical fit. The contact angle of both buffers on pristine PDMS was measured as a control.

### 3.2.5 Characterising the Antimicrobial Performance of FAIP Materials

**Preparation of bacterial cultures:** *S. aureus* (ATCC 6538P) and *E. coli* (ATCC 10798) were transferred from frozen glycerol stock to a fresh nutrient agar plate and incubated overnight at 37°C. For the individual bacterial species, a minimum of three colonies were taken from the agar plates and transferred to fresh LB (Lysogeny Broth) medium (Difco LB Broth Miller), then grown overnight in a shaking incubator (200 rpm, 37°C). The bacterial culture was subsequently diluted with fresh LB media, with a starting concentration of  $10^5$  colony forming units (CFU) ml<sup>-1</sup>, and incubated in a shaking incubator for 2-3 hrs until an optical density (OD) of 0.4 was achieved. This culture was then used for antimicrobial testing experiments.

**Determining the minimum inhibitory concentration (MIC):** Decanoic acid was chosen for antimicrobial testing due to its melting properties<sup>28</sup> and PDMS release data (see data presented in section 3.3.2). The solubility limit of decanoic acid in LB media was first determined before MIC testing could be conducted. Decanoic acid was weighed and added to LB media of both pH 5 and pH 7, which was then heated to 50°C and held at that temperature for 2-3 hrs to dissolve the decanoic acid. The natural pH of LB media was found to be pH 7. To achieve pH 5, the LB media was adjusted using 1 M HCl. The LB media with decanoic acid was then allowed to cool to room temperature and the solubility was determined by the formation of a precipitate. A solubility limit of 0.4 mg/ml and 0.5 mg/ml was achieved for decanoic acid in pH 5 and pH 7 LB media, respectively. The solutions were then filtered using 0.22 µm syringe filter. These solutions were then used for determining the MIC for both *S. aureus* (ATCC 6538P) and *E. coli* (ATCC 10798), using LB media of both pH 7 and pH 5. Bacterial culture was prepared according to the above conditions and then 100 µl of this was added to 4.9 ml of LB media of at either pH 5 or pH 7, with different concentration of decanoic acid ranging from 0.1 mg/ml to 0.32 mg/ml and 0.1 mg/ml to 0.4 mg/ml for pH 5 and pH 7 respectively. pH-specific LB media, excluding decanoic acid was used as the control. The samples were then incubated for 24hrs at 37°C. After 24 hrs of incubation, the solutions were serially diluted and plated on fresh nutrient agar plates using the Miles and Misra method.<sup>52</sup> The plates were then incubated overnight at 37°C, and the CFUs were counted. This experiment was conducted in three biological replicates for each pH.

**Viability of planktonic bacteria in contact with PDMS C<sub>10</sub>:** The PDMS C<sub>10</sub> samples were cut using a cork borer to a diameter of 7 mm. The cut samples were then placed in individual wells of a 6 well plate and covered with a PDMS frame to prevent the samples from floating. PDMS frames were fabricated in individual wells of 6 well plate using Sylgard 184 silicone elastomer kit (Dow Corning), at a ratio of 10:1 (base: curing agent). The mixture was stirred vigorously using a disposable spatula and then carefully poured into the individual wells of a

6 well plate, with 1g of mixture per well. The PDMS in the wells was then degassed under vacuum to remove trapped air bubbles and cured at 50°C overnight. The frame was formed by removing the cured PDMS from each well and cutting a 5 mm hole in the centre using a 5 mm cork borer. After carefully covering the PDMS C<sub>10</sub> samples with the PDMS frames, the samples were sterilised by UV irradiation for 30 minutes on both sides.

After sterilisation, 10 ml of pH-specific LB media, with individual bacterial species (*S. aureus* (ATCC 6538P) or *E. coli* (ATCC 10798)) at a concentration of 10<sup>5</sup> CFU ml<sup>-1</sup> were added to the individual wells of the 6 well plate with the PDMS C<sub>10</sub> samples. Bacterial suspensions were prepared as described above (10<sup>5</sup> CFU ml<sup>-1</sup>) with fresh pH specific LB media. Two sets of experiments were carried out simultaneously. One set of samples were incubated for 24 hrs at 37°C, at both pH 5 and pH 7. Another set of samples were incubated at 5°C, at both pH 5 and pH 7, with a starting concentration of 10<sup>8</sup> CFU ml<sup>-1</sup>. After 24 hrs of incubation, the planktonic suspension from each of the samples was collected, serially diluted and plated on fresh nutrient agar using the Miles and Misra method.<sup>52</sup> The agar plates were then incubated overnight at 37°C and the CFUs were counted. These experiments were conducted using three replicates for each condition: High T: High pH (37°C: pH 7), High T: Low pH (37°C: pH 5), Low T: High pH (5°C: pH 7) and Low T: Low pH (5°C: pH 5).

**Viability of sessile bacteria in contact with PDMS C<sub>10</sub>:** The viability of sessile bacteria was probed using confocal fluorescence microscopy. PDMS C<sub>10</sub> samples were incubated with individual bacterial species (*S. aureus* (ATCC 6538P) or *E. coli* (ATCC 10798)) as discussed in the previous section. After removing the planktonic suspension from the experiment discussed above, with the frames still in place, the PDMS C<sub>10</sub> samples were washed three times with 10 ml of sterile 0.85% (w/w) NaCl solution and then stained with live/dead BacLight bacterial viability kit (Molecular Probes, L7012). The staining process proceeded with the

addition of 1 ml of sterile 0.85% (w/w) NaCl solution containing a mixture of 5  $\mu$ M SYTO 9 (green-fluorescent nucleic acid stain for live cells), and 30  $\mu$ M propidium iodide (red-fluorescent nucleic acid stain for dead cells). The samples were incubated in the dark for 15 minutes with the dyes and then immediately analysed in 0.85% (w/w) NaCl (as the immersion media) using a confocal upright Zeiss LSM 880 multiphoton microscope. The collected confocal fluorescence images were processed using Fiji software.<sup>53</sup>

### 3.3 Results and Discussion

#### 3.3.1 Fabrication of PDMS and FAIP Materials

The fabrication of PDMS with Sylgard 184 silicone elastomer was adapted with the addition of a hydrophobic non-polar solvent ( $\text{CHCl}_3$ ), to increase the homogeneity between samples after curing. As a result, the final PDMS materials had an average weight of  $0.9055 \text{ g} \pm 0.0880\text{g}$ , as described in section 3.2.1. No further chemical modifications of the PDMS material were carried out following the curing process. Once the PDMS had been cured, the ability of PDMS to swell upon contact with hydrophobic non-polar materials was exploited and the material was loaded with different fatty acids by a diffusion process previously discussed in the introduction, at different temperatures (Table 3. 2), overnight for a minimum of 16 hrs. Figure 3. 10 shows the PDMS loaded with fatty acid. The sample is no longer colourless and transparent and shows a translucent white colour, which can be associated with the presence of the fatty acid within the polymeric matrix.

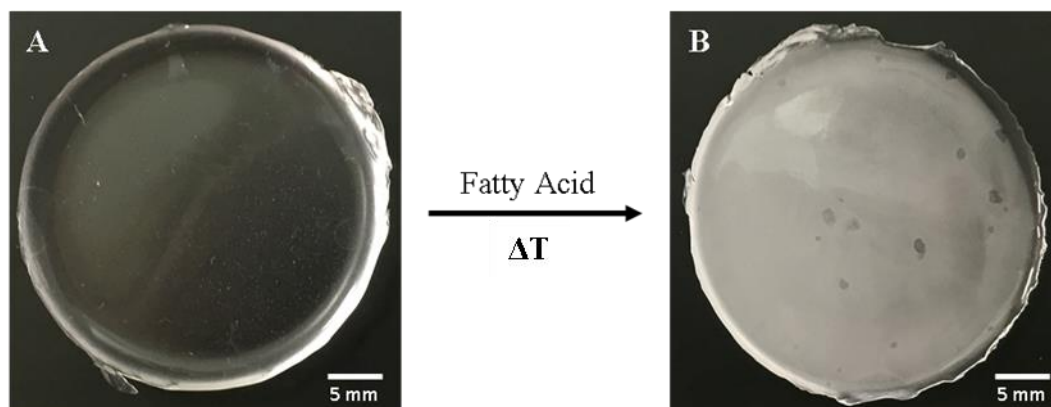


**Figure 3. 10** Photographs of cured PDMS before (A) and after loading with fatty acid (B). PDMS  $\text{C}_{10}$  showed as an example of FAIP.

The PDMS samples were weighed before and after loading with each fatty acid, to determine the average mass of fatty acid loaded into PDMS. (Table 3. 2).

**Table 3. 2** Loading temperature's and average mass of each fatty acid loaded in PDMS

PDMS Sample	Fatty Acid	Loading Temperature (°C)	Mass of Loading (g/g PDMS)
PDMS C <sub>10</sub>	Decanoic Acid	37	0.0891 ± 0.0125
PDMS C <sub>12</sub>	Dodecanoic Acid	50	0.0584 ± 0.0087
PDMS C <sub>14</sub>	Tetradecanoic Acid	60	0.0375 ± 0.0068

The length of the hydrophobic aliphatic chain in the fatty acid structure appears to have an effect on the degree of PDMS swelling, as seen in table 3.2, were a higher loading of fatty acid was observed for PDMS C<sub>10</sub>, suggesting that as the length of the aliphatic chain of the fatty acid increases, the degree of swelling the PDMS also decreases. This can be rationalised within the Wall-Flory-Rehner model,<sup>6,54,55</sup> also known as the 'affine network model', which suggests that the movement of network junctions in a polymer are restricted and therefore the maximum size of a molecule that can fit between the polymer network of PDMS is also restricted.<sup>6,54,55</sup> In consequence, the decanoic acid has a higher degree of freedom to move around the polymer networks, compared to dodecanoic acid or tetradecanoic acid, which have longer aliphatic chains.

### 3.3.2 Characterisation of PDMS and FAIP Materials

The presence of the fatty acid in the PDMS was further investigated by Raman spectroscopy and differential scanning calorimetry (DSC). The distribution of fatty acid in the PDMS and across the depth of the material was studied using Raman spectroscopy, while DSC was used to study the physical properties of the fatty acid within the FAIP.

The pure starting materials (PDMS and fatty acids) were characterised by Raman spectroscopy (Figure 3. 11) and the data from the pure components was used to investigate the distribution of fatty acid in the FAIP. The characteristic Raman peaks associated with PDMS are the Si-O-Si stretch ( $619\text{ cm}^{-1}$ ), Si-CH<sub>3</sub> symmetrical stretch ( $712\text{ cm}^{-1}$ ) and CH<sub>3</sub> symmetrical bend ( $1265\text{ cm}^{-1}$ ) (Figure 3. 11).<sup>56</sup> The pure fatty acids gave strong characteristic peaks associated with C-C stretch vibrations ( $1075\text{ to }1100\text{ cm}^{-1}$ ) and a  $\gamma\text{CH}_2$  twist vibration ( $1295\text{ cm}^{-1}$ ) associated with the aliphatic chain (Figure 3. 11).<sup>57</sup> The carbonyl peak (C=O,  $1640\text{ cm}^{-1}$ ) associated with the carboxylic acid had a moderate intensity (Figure 3. 11), indicating a local environment in which the carbonyl is hydrogen bonded.<sup>57</sup>

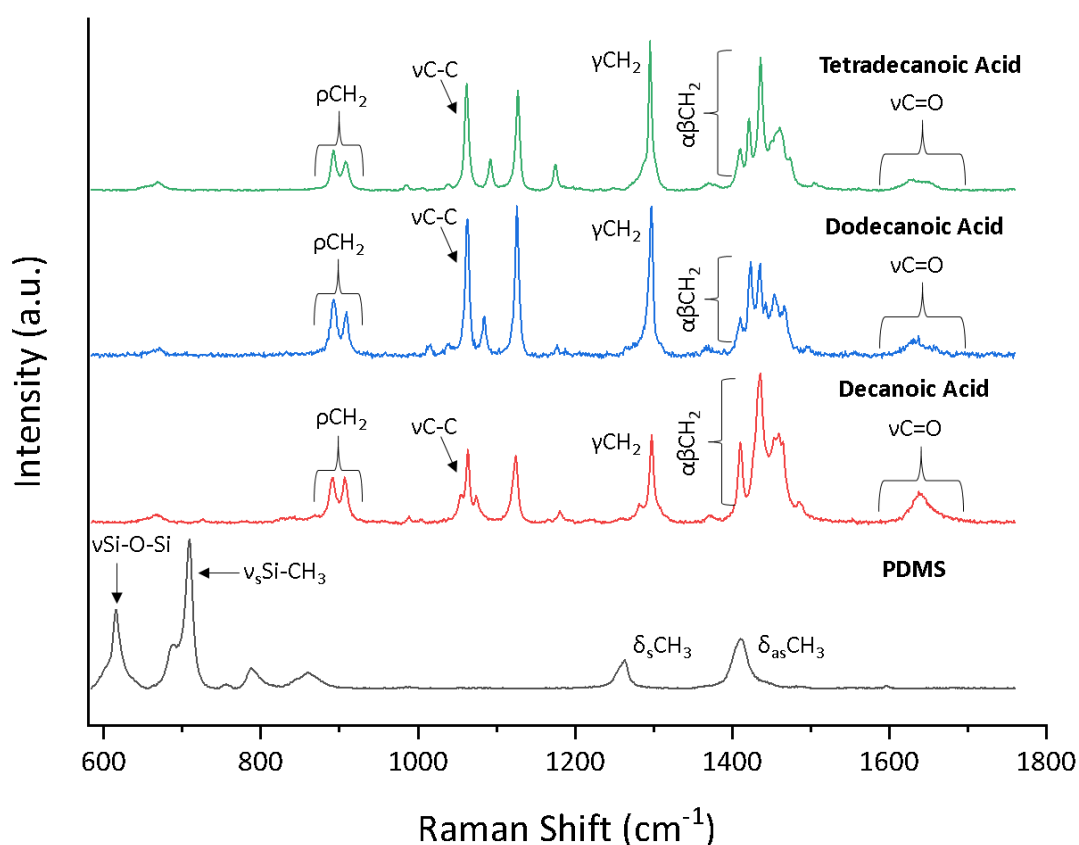


**Figure 3. 11** Raman spectra of pure starting materials prior to the impregnation of PDMS. **Black** is PDMS, **red** is decanoic acid (C<sub>10</sub>), **blue** is dodecanoic acid (C<sub>12</sub>) and **green** is tetradecanoic acid (C<sub>14</sub>).

The spectra of the FAIP samples showed the characteristic Raman peaks associated with C-C stretch vibrations ( $1075\text{ to }1100\text{ cm}^{-1}$ ) and  $\gamma\text{CH}_2$  twist vibration ( $1295\text{ cm}^{-1}$ ) of the fatty acids, confirming the presence of the fatty acids within the PDMS polymer matrix (Figure 3. 12).<sup>56</sup>

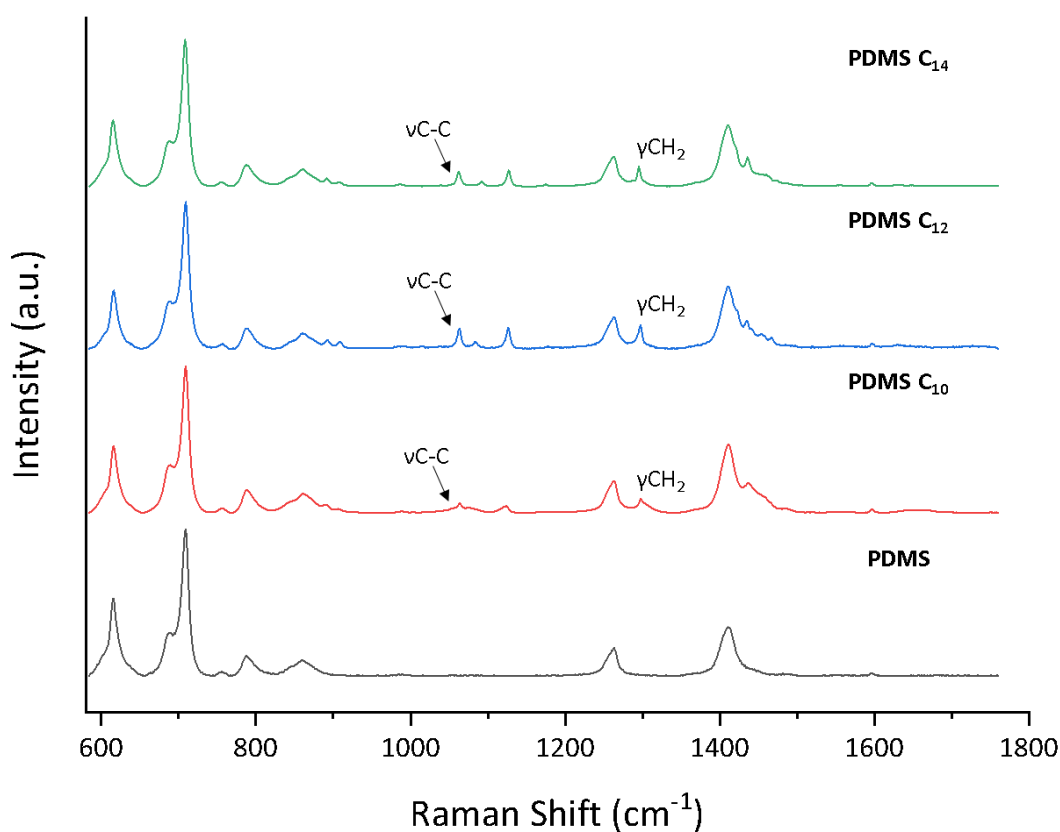


**Figure 3. 12** Raman spectra of PDMS and FAIP materials. **Black** is PDMS, **red** is PDMS C<sub>10</sub>, **blue** is PDMS C<sub>12</sub> and **green** is PDMS C<sub>14</sub>. Raman spectra of the FAIP were taken from a Raman cross section experiment and are an average of the spectral data recorded in the cross section.

The distribution of the fatty acid across the depth of the FAIP (Raman cross section experiment) was investigated by a map acquisition mode, using a direct classical least squares (DCLS) component fit analysis against the Raman spectra of the individual pure fatty acids. DCLS component fit analysis is a qualitative analysis where each spectrum in the data set is compared to reference spectra using a least squares algorithm, to identify the pure components contained within a sample.<sup>50,51</sup> As a result, the fatty acids were found to be predominately localised towards the core of the FAIP materials (Figure 3. 13). In addition to this, it also noted that the cross section of the different FAIP materials appear different in figure 3.13, this could be attributed to the different loadings of the fatty acids in the PDMS material or could also be associated with the arbitrary cutting method, revealing different cross sectional views of the material.

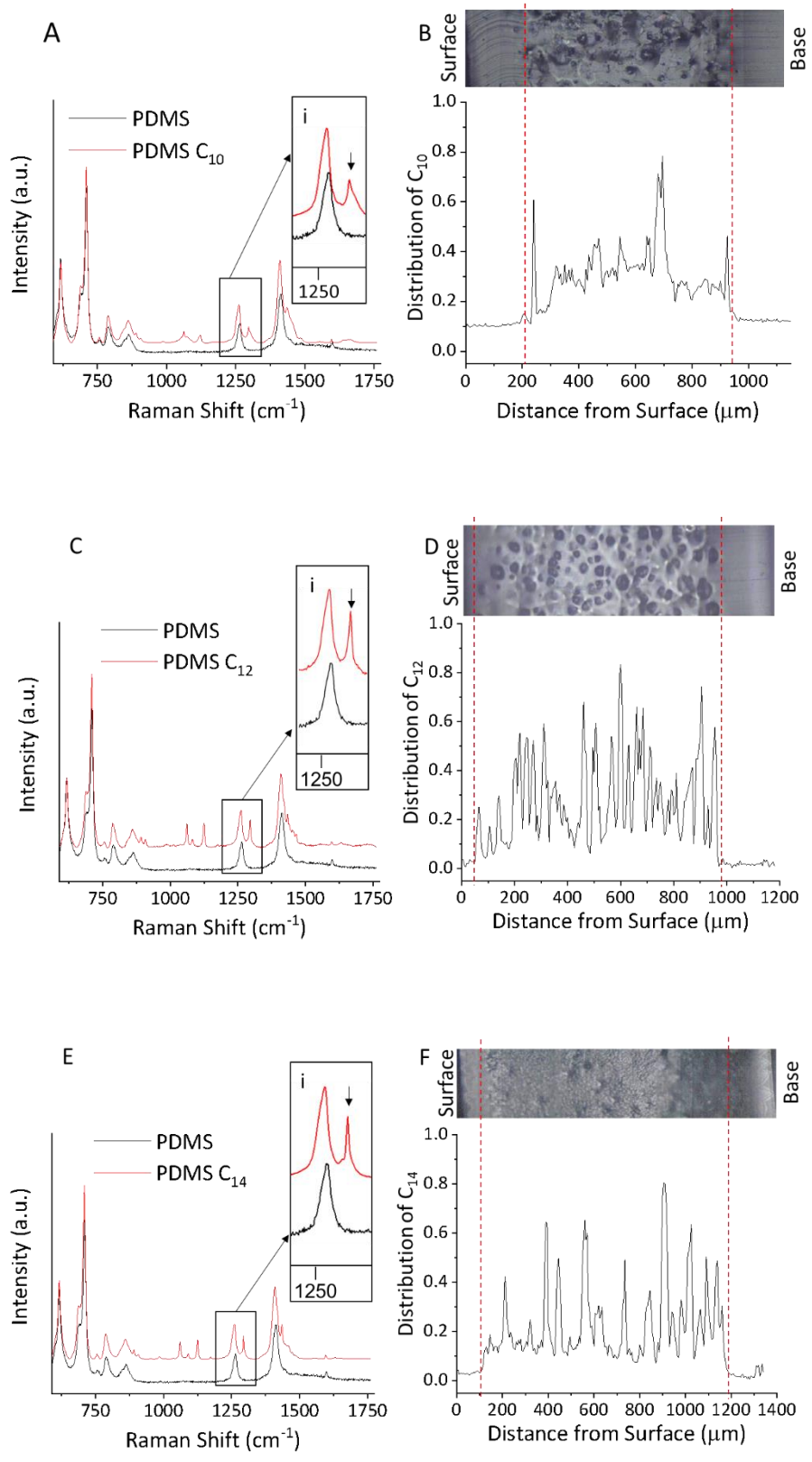


**Figure 3. 13** (A) Representative Raman spectra of PDMS (black) & PDMS C<sub>10</sub> (red), (B) distribution of decanoic acid across PDMS C<sub>10</sub>, (C) representative Raman spectra of PDMS (black) & PDMS C<sub>12</sub> (red), (D) distribution of dodecanoic acid across PDMS C<sub>12</sub>, (E) representative Raman spectra of PDMS (black) & PDMS C<sub>14</sub> (red), (F) distribution of tetradecanoic acid across PDMS C<sub>14</sub>. (i) Insert showing  $\gamma$ CH<sub>2</sub> twist vibration of the respective fatty acids.

The distribution of the fatty acid within the bulk of the FAIP materials was also investigated using a map image acquisition mode, with a DCLS component fit analysis against the Raman data for the individual raw fatty acids. The fatty acid distribution in the FAIP materials was normalised and zero centred for comparison purposes (Figure 3. 14).

Comparing the Raman distribution for each fatty acid, we found that the distribution of fatty acid in the FAIP was close to the average for dodecanoic acid and tetradecanoic acid, with both exhibiting a ‘gaussian like’ distribution (Figure 3. 14 B and C). However, the distribution of decanoic acid in the PDMS appeared to be irregular (Figure 3. 14 A), this may be due to the low melting point of decanoic acid, which is close to room temperature (25°C). As a result of this, the distribution of the fatty acid could change during Raman analysis.

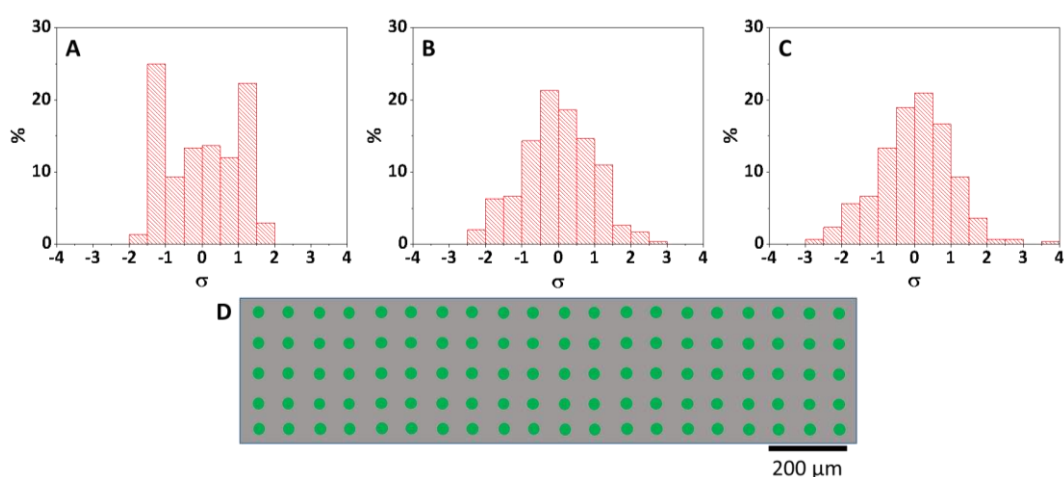


**Figure 3. 14** (A) Normalised histogram showing the distribution of decanoic acid in PDMS C<sub>10</sub>, (B) normalised histogram showing the distribution of dodecanoic acid in PDMS C<sub>12</sub>, (C) normalised histogram showing the distribution of tetradecanoic acid in PDMS C<sub>14</sub>, (D) schematic representation of the experiment, where each green dot (●) represents the area of acquisition across the sample, at a depth of 500 μm from the sample surface.

On the other hand, DSC data provides information on the melting point of the pure fatty acids and the fatty acids inside the PDMS (see appendix, Figure A3. 2-4). The values obtained from the DSC data suggest the inclusion of the fatty acids into the PDMS does not significantly change the properties of the fatty acids. The  $T_{\text{Onset}}$  and enthalpy of change ( $\Delta H$ ) for both the

FAIP and pure fatty acids were within standard deviation of each other (Table 3. 3). The average  $T_{\text{Onset}}$  for PDMS  $C_{10}$  was found to be close to room temperature (25°C), although still within the standard deviation of the pure decanoic acid DSC data. The significant standard deviation for PDMS  $C_{10}$ , could be attributed to environmental factors associated with room temperature, impacting the DSC results obtained.

**Table 3. 3** DSC melting transition data for pure fatty acids and FAIP.

Sample	Average T Onset (°C)	Average T Max (°C)	Average $\Delta H$ (J/g)
Decanoic Acid ( $C_{10}$ )	$30.66 \pm 0.25$	$32.74 \pm 0.15$	$156.37 \pm 2.76$
Dodecanoic Acid ( $C_{12}$ )	$43.62 \pm 0.42$	$45.18 \pm 0.32$	$180.07 \pm 3.93$
Tetradecanoic Acid ( $C_{14}$ )	$53.73 \pm 0.37$	$55.43 \pm 0.67$	$190.77 \pm 0.55$
PDMS $C_{10}$	$26.28 \pm 4.31$	$30.20 \pm 0.25$	$148.37 \pm 26.35$
PDMS $C_{12}$	$42.97 \pm 0.56$	$45.19 \pm 1.80$	$182.40 \pm 41.03$
PDMS $C_{14}$	$53.24 \pm 0.82$	$54.73 \pm 0.52$	$160.92 \pm 32.83$

### 3.3.3 Characterisation of Fatty Acid Release from FAIP

#### Materials

We also investigated the release of the fatty acids from the FAIP, under different pH and temperature conditions. The amount of fatty acid released from the FAIP was determined via gravimetric analysis, by weighing the samples before and after the release for each sample, with an average taken from 8 samples for each experimental condition. The release experiments were carried out over a 24 hr period. The rationale followed in these release experiments was to control the release of incorporated fatty acid from the PDMS by a combination of melting-transition and pH dependent solubility of the fatty acids.

Model physiological buffers with a pH of 7 and 5, to simulate the pH environments associated with the internal human body and human skin respectively,<sup>58</sup> were used for the release experiments. 1 M solution of HEPES buffer, pH adjusted with NaOH was used as the pH 7 buffer and a 1 M solution of acetic acid, pH adjusted with NaOH was used for pH 5 buffer (Table 3. 4). The temperatures used for the release experiments, were selected from DSC data, taking temperatures higher and lower than the  $T_{\text{Onset}}$  for the FAIP (Table 3. 4).

**Table 3. 4** Release conditions for the fatty acid release experiments

Sample	Release Conditions			
	Condition 1	Condition 2	Condition 3	Condition 4
PDMS C <sub>10</sub>	5°C pH 5	5°C pH 7	37°C pH 5	37°C pH 7
PDMS C <sub>12</sub>	25°C pH 5	25°C pH 7	50°C pH 5	50°C pH 7
PDMS C <sub>14</sub>	25°C pH 5	25°C pH 7	60°C pH 5	60°C pH 7

After completion of the 24 hr release experiments with the FAIP, a ‘gel’ like material could be seen around the surface of the FAIP associated with the released fatty acid. We found the optimum conditions for the release of fatty acid from the FAIP was high temperature and high pH for all fatty acids, where 100% of the fatty acid was released from the FAIP samples (Figure 3. 15). At low temperature for both pHs, and at high temperature with low pH, a reduced amount of fatty acid was released from the FAIP materials, according to the gravimetric analysis (Figure 3. 15). The lowest amount of fatty acid released from the FAIP was observed to be at low temperature and low pH conditions, with a release of 6% ± 2% for PDMS C<sub>10</sub>, 7% ± 2% for PDMS C<sub>12</sub> and 3% ± 1% for PDMS C<sub>14</sub> (Figure 3. 15). When the temperature or pH is increased, a fractional increase in the amount fatty acid released from the FAIP materials is observed (Figure 3. 15).

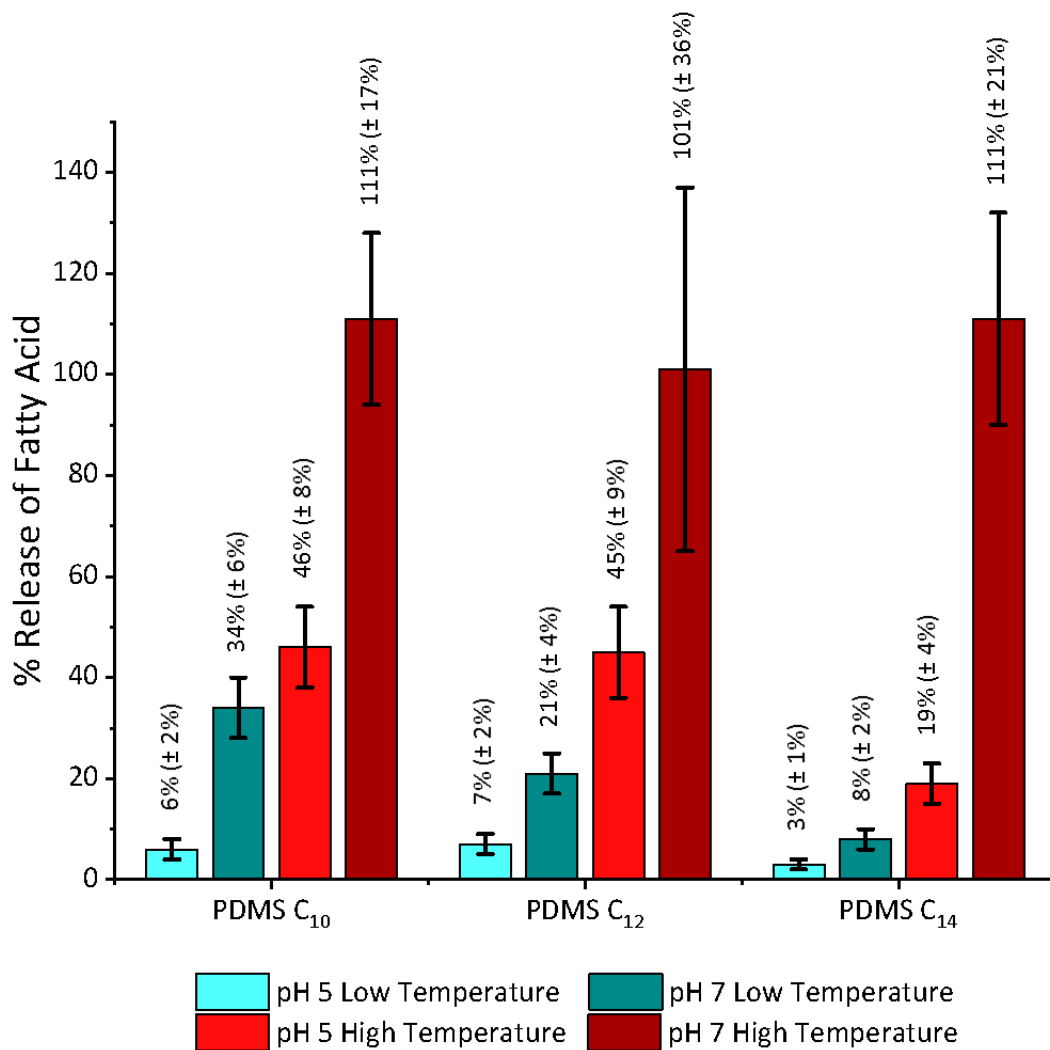


**Figure 3. 15** Chart showing the release of fatty acids from the FAIP after 24 hrs. C<sub>10</sub> is decanoic acid, C<sub>12</sub> is dodecanoic acid and C<sub>14</sub> is tetradecanoic acid. High temperature and high temperature release show over 100% release, however this is within standard error.

As we know from the DSC analysis (Table 3. 1), the  $T_{\text{Onset}}$  of each fatty acid in the FAIP is above the low temperature parameter in all the release experiments, and therefore as expected there was a minimal release of fatty acid at temperatures lower than the  $T_{\text{Onset}}$ . When we increase the temperature above the  $T_{\text{Onset}}$ , a physical change in the material was observed in table 3. 1, an endothermic transition occurs with the fatty acid in the FAIP, causing the fatty acid to melt and as a result the fatty acid can be released from the sample. Once the sample is cooled following the release experiment, a ‘gel’ like substance forms on the surface of the PDMS.

The pH also appeared to play a key role in the release experiments. At pH 7 we see an increase in the amount of fatty acid released from the FAIP (Figure 3. 15) at both temperatures, in comparison to their counterpart at pH 5. This can be attributed to the pKa of the fatty acids (Table 3. 5). When the pH of the release buffer is significantly above the pKa of the fatty acid, the fatty acid is deprotonated and forms a salt with Na<sup>+</sup>, and the solubility of the fatty acid increases (Figure 3. 15). However, when the pH of the physiological buffer is close to the pKa, the fatty acid is protonated, and the solubility of the fatty acid is decreased. This interpretation is supported by literature data (Table 3. 5), showing that the salts of fatty acids are much more soluble than the protonated species.<sup>27-29</sup>

**Table 3. 5** Acid dissociation constants and solubility of fatty acids.<sup>27-29</sup>

Sample	pKa	Aqueous Solubility (g L <sup>-1</sup> )	
		Fatty Acid (COOH)	Fatty Acid Salt (COO <sup>-</sup> )
Decanoic Acid	4.89 <sup>29</sup>	0.15 <sup>27</sup>	18.55 <sup>29</sup>
Dodecanoic Acid	5.3 <sup>29</sup>	0.055 <sup>27</sup>	5.11 <sup>29</sup>
Tetradecanoic Acid	5.8 <sup>29</sup>	0.02 <sup>27</sup>	1.73 <sup>29</sup>

If we consider both the effect of temperature and pH and take into account the DSC data (Table 3. 3), along with the literature pKa values for the fatty acids (Table 3. 5), we can explain why at high temperature and high pH, 100% of the fatty acid is released, yet in a low pH environment the release of the fatty acid is reduced. At high temperatures, regardless of the pH, the fatty acid in the FAIP melts (Table 3. 3) and can be released from the FAIP material (Figure 3. 15). At a higher pH the fatty acid is deprotonated and can form a salt (Figure 3. 16 and Table 3. 5), which is increasingly more soluble than the acidic form of the fatty acid and therefore an increased amount of fatty acid is released into the buffer media. At low temperature, but high pH the fatty acid doesn't melt, however the increasing pH of the buffer

can dissolve some of the fatty acid in the form of a salt, resulting in a higher release compared to low temperature and low pH conditions.

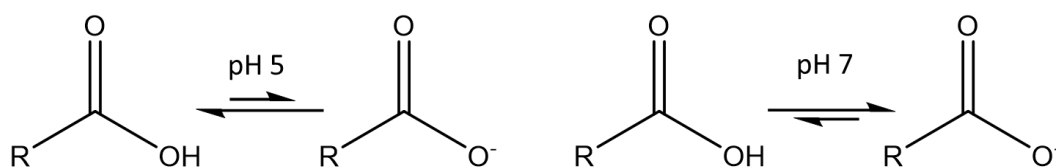


**Figure 3. 16** Schematic representation showing the effect of pH on the carboxyl group in fatty acids. R is equal to  $\text{C}_n$  aliphatic chain.

Raman spectroscopy also provided qualitative information on the distribution of the fatty acid in the FAIP, following the release experiments. The distribution of fatty acid in the FAIP was analysed by Raman cross section experiments after 24 hrs release. Data shows that at low temperature and low pH, the distribution of fatty acid across the depth of the material, remains similar to the original distribution for  $\text{C}_{12}$  and  $\text{C}_{14}$  fatty acids (Figure 3. 17 B and see appendix, Figure A3. 6), in agreement with the minimal release seen in the gravimetric data (Figure 3. 15). However, the distribution of  $\text{C}_{10}$  fatty acid in the FAIP was marginally different before (Figure 3. 13 B) and after (see appendix, Figure A3. 5) the low temperature low pH release, with an increased intensity for decanoic acid distribution, confined towards core of the material. While the release of  $\text{C}_{10}$  was carried out at  $5^\circ\text{C}$ , Raman analysis was carried out at room temperature, due to experimental limitations. The Raman analysis being conducted at room temperature is close the  $T_{\text{Onset}}$  of PDMS  $\text{C}_{10}$  and therefore could account for the changes observed for PDMS  $\text{C}_{10}$  during Raman analysis, allowing the fatty acid within the FAIP redistribute.

When the temperature or the pH is increased independently in the release experiments, we observed a decrease in the average peak intensity for the  $\gamma\text{CH}_2$  twist vibration, associated with the fatty acid. The distribution of fatty acid across FAIP materials changes, where we observe less fatty acid distributed across the depth of the FAIP (Figure 3. 17 and see appendix, Figures A3. 5 and 6) materials. The change in the distribution of fatty acid across the FAIP after low

temperature, high pH and high temperature, low pH release conditions, suggests that some of the fatty acid has been released from the material, which is consistent with the small fraction of fatty acid released, observed in the gravimetric data (Figure 3. 15). The change in the distribution of fatty acid in the FAIP after these release conditions is more evident in PDMS C<sub>10</sub> (see appendix, Figure A3. 5) compared to the other FAIP samples. Although, the difference in the fatty acid distribution compared to PDMS C<sub>12</sub> and PDMS C<sub>14</sub>, could be attributed to the T<sub>Onset</sub> for PDMS C<sub>10</sub> being close to room temperature (Table 3. 3), as mentioned previously, and therefore the distribution of fatty acid during Raman analysis could change, effecting the results. For this reason, we focus on the Raman data of dodecanoic and tetradecanoic acid to get a better understanding of the distribution of fatty acid in the FAIP after release (Figure 3. 17 and see appendix, Figure A3. 6).

At optimum release conditions (high temperature, high pH), we observe a significant change for the distribution of fatty acid across the FAIP materials. The peak for  $\gamma$ CH<sub>2</sub> twist vibration is significantly reduced (Figure 3. 17 and see appendix, Figure A3. 6), and in some instances the signal is lost (see appendix, Figure A3. 5). The data also shows that the distribution of fatty acid across the depth of the FAIP is significantly reduced after the optimum materials were subject to optimum release conditions. This is consistent with the gravimetric data, which shows a significant loss of fatty acid from the FAIP materials after release (Figure 3. 15).

We can understand the process of release of fatty acid from FAIP, by considering the mechanism of PDMS swelling discussed previously. Since the fatty acid is amphiphilic, the carboxylic group of the fatty acid in the PDMS can interact with the physiological buffer, encouraging the fatty acid to be released from the FAIP. The temperature and pH have a significant effect on the release, due to the increased solubility of the fatty acid in the form of a salt and melting of the fatty acid above T<sub>Onset</sub>. Melted fatty acid can migrate out of the PDMS,

and the release from the surface will be controlled by the solubility of fatty acid, by the pH of the surrounding media. When the temperature is decreased on cooling, following the release experiment, the fatty acid solidifies to form a 'gel' like substance on the surface of the FAIP.

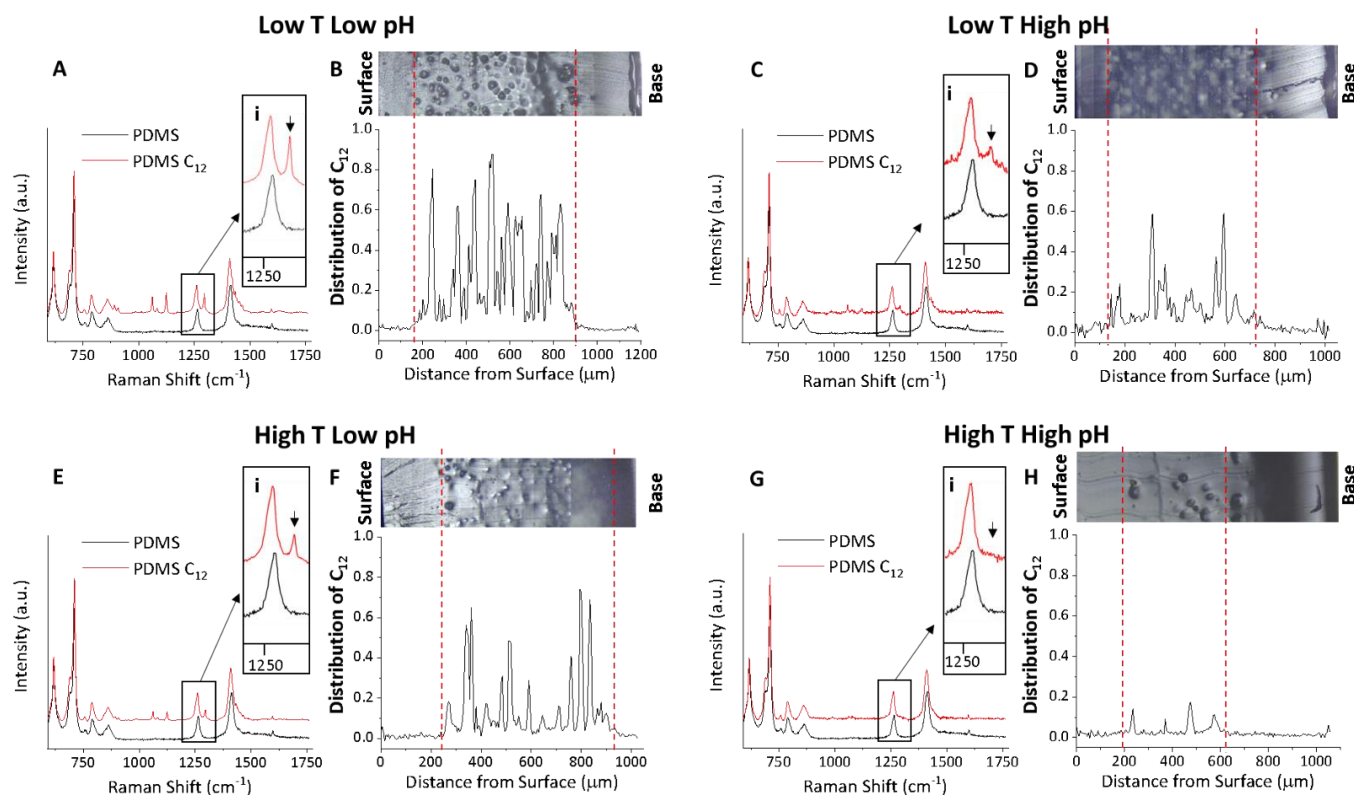


**Figure 3.** 17 Representative Raman data for PDMS C<sub>12</sub> after each release condition. (A and B) Low temperature, low pH release (A) Representative Raman spectra of PDMS (black) & PDMS C<sub>12</sub> (red), (B) Distribution of dodecanoic acid across PDMS C<sub>12</sub>. (C and D) Low temperature, high pH release (C) Representative Raman spectra of PDMS (black) & PDMS C<sub>12</sub> (red), (D) Distribution of dodecanoic acid across PDMS C<sub>12</sub>. (E and F) High temperature, low pH release (E) Representative Raman spectra of PDMS (black) & PDMS C<sub>12</sub> (red), (F) Distribution of dodecanoic acid across PDMS C<sub>12</sub>. (G and H) High temperature, high pH release (G) Representative Raman spectra of PDMS (black) & PDMS C<sub>12</sub> (red), (H) Distribution of dodecanoic acid across PDMS C<sub>12</sub>. (i) Insert showing  $\gamma$ CH<sub>2</sub> twist vibration of dodecanoic acid for each release condition.

We also investigated the wettability of the FAIP samples by static contact angle measurements, using the buffers used in the release experiments. As a result, we observe a decrease in the contact angle with respect to pristine PDMS for PDMS C<sub>10</sub> and PDMS C<sub>12</sub> at both pH 5 and pH 7 (Figure 3. 18). While we only see a significant change in the contact angle for PDMS C<sub>14</sub> at pH 7. Specifically, for contact angle experiments conducted at pH 7, the contact angle values for the FAIP were significantly reduced compared to pristine PDMS (Figure 3. 18).

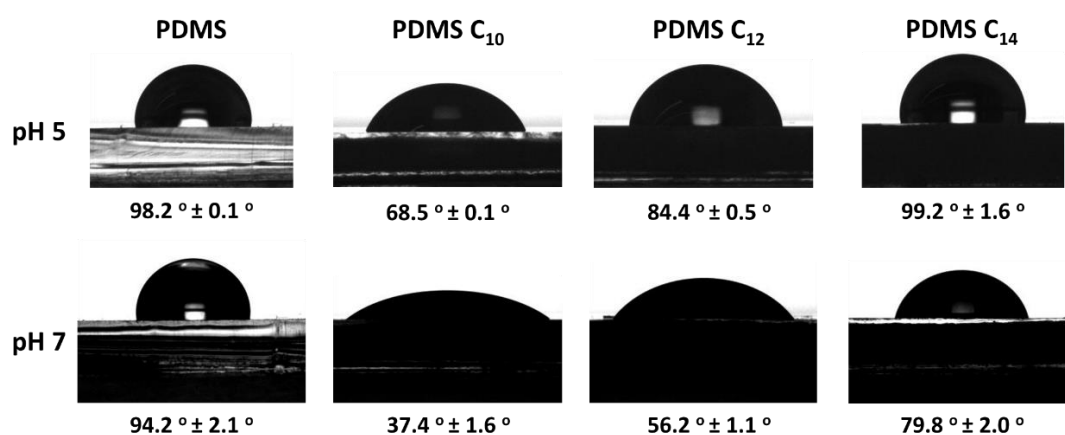


**Figure 3. 18** Contact angle measurements for PDMS and FAIP with pH 5 and pH 7 buffers at room temperature.

The decrease in the contact angle suggests a change in the surface properties of the PDMS after swelling with fatty acid, with a high susceptibility to wetting at pH 7. This enhanced wettability can be attributed to the increased solubility of the fatty acid in its salt form (Table 3. 5) and is consistent with the proposed mechanism for release, previously discussed.

As a result of our data, we have shown that we can successfully load PDMS with a selection of fatty acids, that can then be subsequently released at physiological conditions. Considering this, along with the literature associated with antimicrobial properties of fatty acids, we decided to investigate the potential use of this system as an antimicrobial material, with a controlled biocidal release.

### 3.3.4 Characterising the Antimicrobial Performance of FAIP Materials

To test the antimicrobial activity of the FAIP, model wound and skin pathogens *E. Coli* (ATCC 10798) and *S. aureus* (ATCC 6538P) were chosen for antimicrobial testing.<sup>53,59–62</sup> PDMS C<sub>10</sub> material was chosen as the best candidate for the antimicrobial tests, considering the optimum release observed at internal physiological conditions (37°C, pH 7), matching the T<sub>Onset</sub> observed in the DSC data (Table 3. 3). The antimicrobial activity of PDMS C<sub>10</sub> was also tested at pH 5, considering the slightly acidic nature of human skin.<sup>58</sup>

#### 3.3.4.1 Antimicrobial Testing of PDMS C<sub>10</sub> against *E. coli* (ATCC 10798)

Antimicrobial testing began by determining a minimum inhibitory concentration (MIC) (Figure 3. 19) for decanoic acid against *E. coli* bacteria. We first started by determining the solubility limit of decanoic acid in LB media. As a result, we reached saturation at 0.5 mg/ml for pH 7 and 0.4 mg/ml for pH 5. The low solubility of decanoic acid observed at pH 5 can further explain the effect we see in the release experiments, with the formation of a ‘gel’ like substance on the surface of the PDMS.

Once the solubility limit for decanoic acid in LB media was determined, MIC experiments were carried out. MIC experiments were performed with a starting concentration of 10<sup>5</sup> CFUs ml<sup>-1</sup> of *E. coli* in LB media adjusted to pH 5 and pH 7. Different concentrations of decanoic acid, with a maximum concentration of 0.4 mg/ml and 0.32 mg/ml for pH 7 and pH 5 LB media respectively were used, due to the nature of the experiment, requiring the addition of fresh bacterial culture. The solutions were incubated for 24 hrs, at 37°C and then serially diluted and plated according to the Miles and Misra method.<sup>52</sup> The MIC was determined by counting CFUs.

MIC experiments for decanoic acid alone (excluding PDMS), with *E. coli* bacteria (Figure 3. 19), revealed a gradual reduction in the viability of *E. coli* bacterial cells with increasing concentrations of decanoic acid. A final inhibitory effect of 90% at 0.4 mg/ml at pH 7 and 0.32 mg/ml at pH 5 was achieved. These results were consistent with literature, where the inhibitory effect of fatty acids proved to be pH dependent.<sup>63,64</sup>

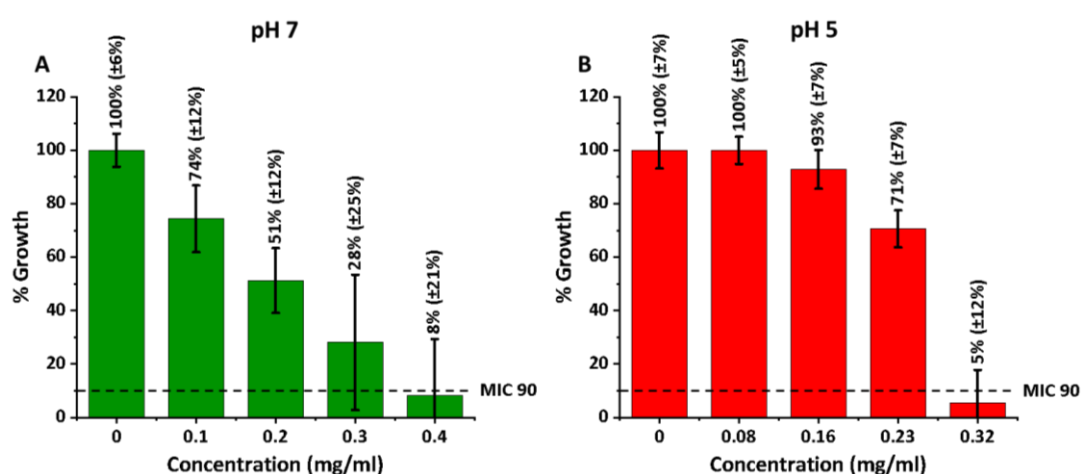


**Figure 3. 19** Planktonic MIC results for *E. coli* (ATCC 10798) against decanoic acid at different concentrations in LB media. (A) MIC results for pH 7, (B) MIC results for pH 5. Average percentage (%) growth is determined per replicate for 3 replicates.

After completion of the MIC experiment with decanoic acid alone, we moved to antimicrobial testing of PDMS C<sub>10</sub> against *E. coli*. In these experiments, 7 mm diameter samples of PDMS C<sub>10</sub> were placed in buffer media (LB media), adjusted to pH 5 or pH 7, with *E. coli* bacterial species and incubated at different temperatures for 24 hrs. High temperature experiments were seeded at 10<sup>5</sup> CFU ml<sup>-1</sup> of bacteria and incubated at 37°C for 24 hrs, while the low temperature experiments were seeded at 10<sup>8</sup> CFUs ml<sup>-1</sup> and incubated at 5°C for 24 hrs. Low temperature samples were seeded at 10<sup>8</sup> CFUs ml<sup>-1</sup> due to the dormant state of *E. coli* bacterial species at low temperatures, therefore allowing us to determine the antimicrobial effect of the PDMS C<sub>10</sub> material in all release conditions.<sup>65</sup> After 24 hrs of incubation, the growth of bacteria in the planktonic state, in comparison to the control (pristine PDMS) was determined by counting CFUs (Figure 3. 20) and the samples of PDMS C<sub>10</sub> used in these experiments were analysed using confocal fluorescence microscopy with Live/ dead staining, to assess the viability of surface attached bacteria.

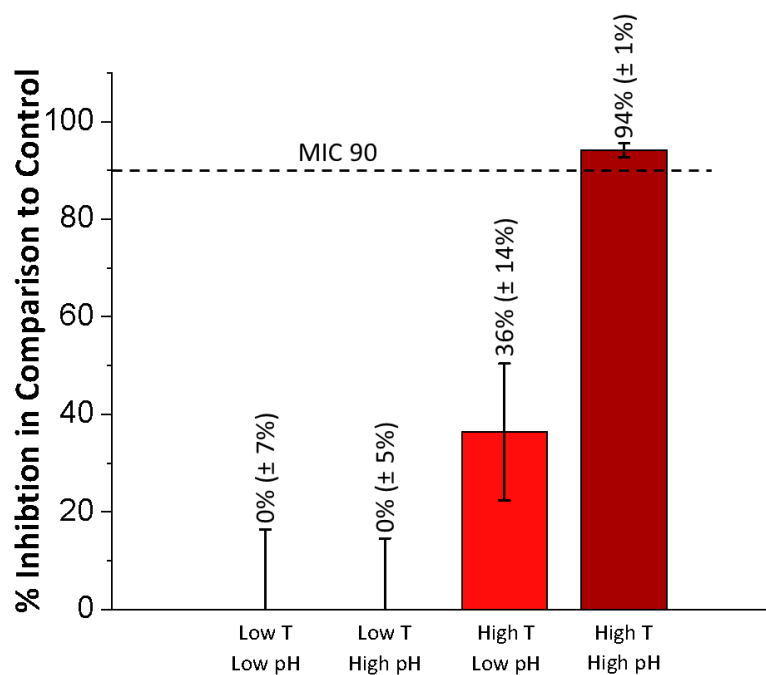


**Figure 3. 20** Planktonic inhibition of *E. coli* (ATCC 10798) on PDMS C<sub>10</sub>.

In comparison to the MIC experiments with decanoic acid alone (Figure 3. 19), we also observe an inhibitory effect of 90%, under optimum release conditions (37°C, pH7) for PDMS C<sub>10</sub> (Figure 3. 20). At lower temperatures and pH, there was a decreased inhibition of *E. coli* (Figure 3. 20). This is consistent with the release data (Figure 3. 15), where less of the fatty acid is released at lower temperatures and pH conditions, thus resulting in a decreased inhibitory effect on the *E. coli* bacteria.

When we examine the viability of surface attached *E. coli*, confocal fluorescence microscopy (CFM) revealed an increase in the fraction of dead bacteria on PDMS C<sub>10</sub> compared to the non-impregnated PDMS control samples. High temperature and low pH conditions exhibited the highest antimicrobial effect, with average fractions of 78.1% ± 3.7% dead cells (Figure 3. 21 and 22). These results are consistent with the release data (Figure 3. 15), where at high temperature and low pH we observe a reduced amount of fatty acid released into the bulk solution, due to poor solubility at pH 5 (Table 3. 5). As a result, there is a higher concentration of decanoic acid localised at the surface, and a consistent increase in the fraction of dead cells at the surface of PDMS C<sub>10</sub> (Figure 3. 21 and 22).

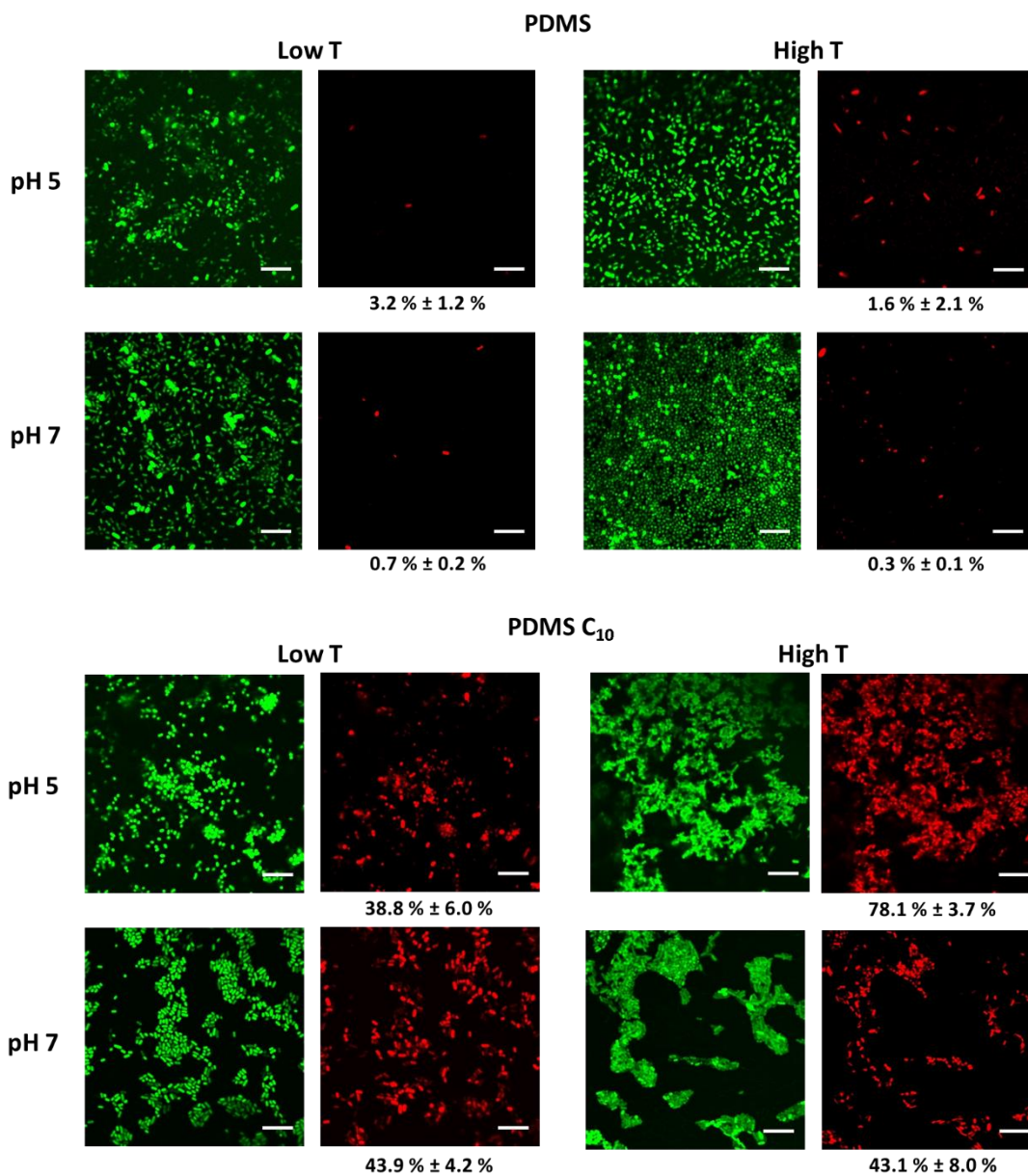


**Figure 3. 21** Confocal fluorescence microscopy images of *E. coli* (ATCC 10798) on PDMS and PDMS C<sub>10</sub>, showing percentage of dead bacteria. Bacteria imaged using Live/dead viability kit, where all bacteria are stained green and dead bacteria are stained red. Scale Bars shown in all images are 10  $\mu$ m.

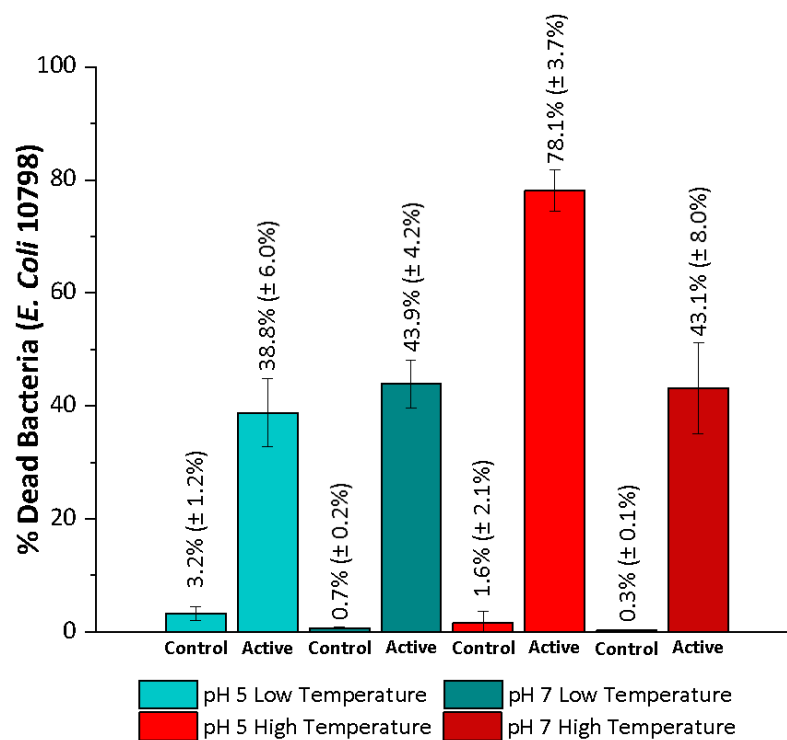


**Figure 3. 22** Bar Chart showing summary of the CFM data with Live/ Dead staining for *E. coli* 10798 on PDMS (Control) and PDMS C<sub>10</sub> (Active) under different pH and temperature conditions.

### 3.3.4.2 Antimicrobial Testing of PDMS C<sub>10</sub> against *S. aureus* (ATCC 6538P)

The antimicrobial effect of PDMS C<sub>10</sub> against gram-positive bacteria, *S. aureus* bacteria, was also investigated. All antimicrobial testing was conducted according to the same methods used for *E. coli* bacteria. For the MIC experiments with decanoic acid alone with *S. aureus* bacteria, an initial increase in bacterial growth was observed with increasing decanoic acid concentration, compared to the control, especially in pH 7 media (Figure 3. 23). At higher concentrations of decanoic acid, (0.4 mg/ml for pH 7 and 0.32 mg/ml for pH 5) we began to observe an inhibition of the bacterial growth, reaching a MIC 50. (Figure 3. 23)

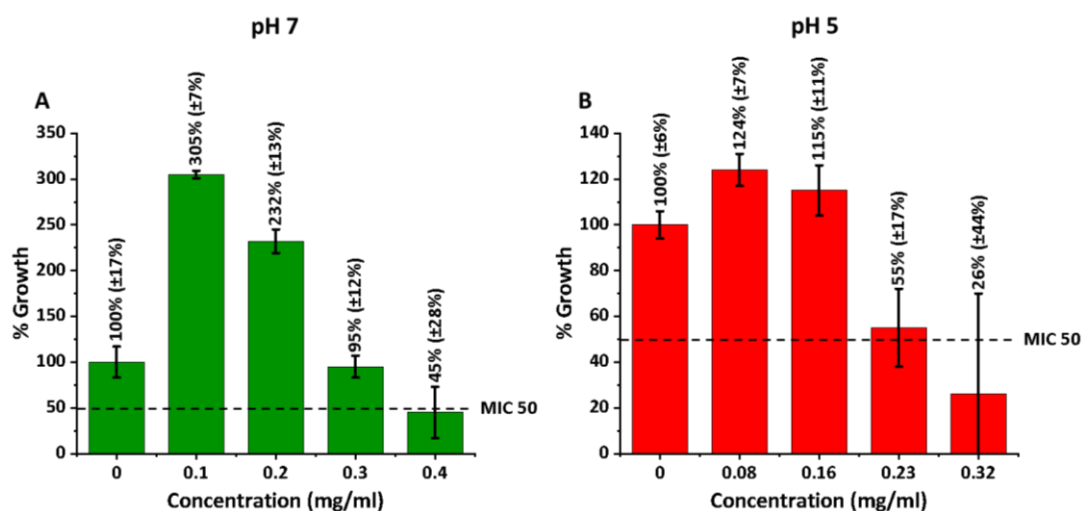


**Figure 3. 23** Planktonic MIC results for *S. aureus* (ATCC 6538P) against decanoic acid of different concentrations in LB media. (A) MIC results for pH 7, (B) MIC results for pH 5.

In the planktonic experiments for PDMS C<sub>10</sub> with *S. aureus* bacteria, in comparison to the MIC data with decanoic acid alone (Figure 3. 24), no inhibitory effect was observed (Figure 3. 24). However, we observed an increase in bacterial growth outside of the standard deviation of the control samples only in the high temperature experiments. This data suggests that the release of decanoic acid from the PDMS C<sub>10</sub> may be gradual and not instantaneous. The gradual release of decanoic acid into the planktonic media from the PDMS C<sub>10</sub> is initially below the MIC 50 and appears to encourage bacterial growth, which is consistent with the increased bacterial growth observed at low concentrations of decanoic acid in the MIC experiments with *S. aureus* (Figure 3. 23).

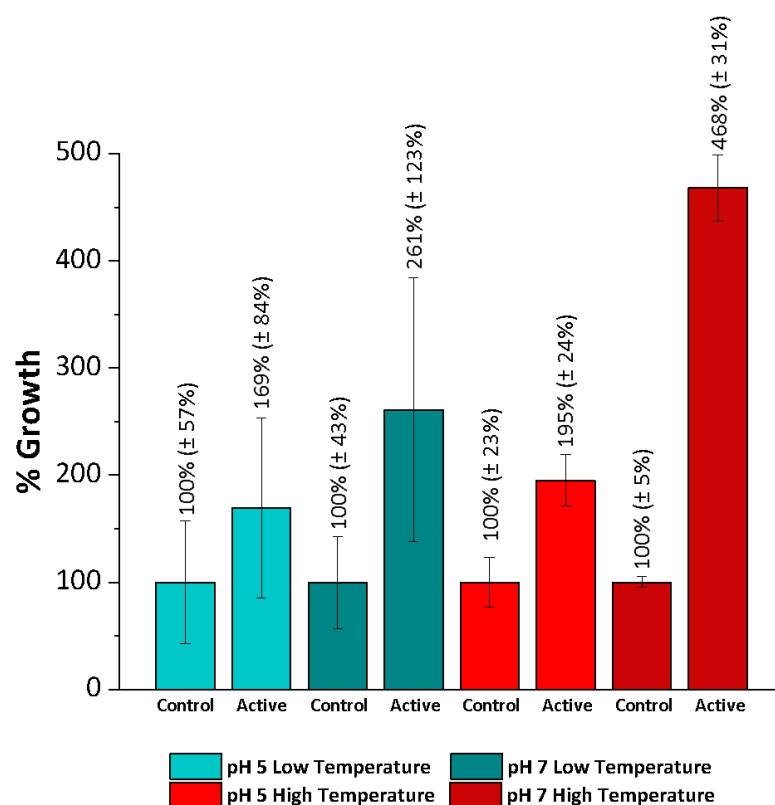


**Figure 3. 24** Planktonic % growth of *S. aureus* (ATCC 6538P) in contact with PDMS C<sub>10</sub> in LB media. The percentage (%) growth of control solutions incubated with PDMS alone, are shown for comparison. According to literature, the interaction of fatty acids with *S. aureus* bacteria and the effects observed in our experiments can be explained. *S. aureus* bacteria have been reported to exhibit an improved growth due to the uptake of fatty acid.<sup>66,67</sup> The fatty acids can be incorporated into the phospholipids of *S. aureus* bacteria via fatty acid phosphorylation. An enzyme composed of two dissociable protein subunits encoded by separate genes, are used to form an acyl-phosphate. Protein A binds to adenosine triphosphate (ATP), which then interacts with two fatty acid binding proteins (protein B), to form the acyl-phosphate species.<sup>66</sup> Acyl-phosphates then contribute to initiating membrane phospholipid synthesis.<sup>68</sup> This mechanism associated with the uptake of fatty acid by *S. aureus*, has also proven to be universal for other gram-positive species, e.g. *Lactobacillus*, also exhibits improved growth associated with the uptake of fatty acids.<sup>69</sup>

Surprisingly, however, when examining the viability of sessile *S. aureus* bacteria on the surface of PDMS C<sub>10</sub>, CFM revealed a remarkable increase in the fraction of dead bacteria for all the pH and temperature conditions used, compared to the non-impregnated PDMS control samples (Figure 3. 25 and 26). In these experiments, it is believed that the release of decanoic acid from the PDMS C<sub>10</sub> may be gradual, and therefore due to the gradual release of decanoic acid from PDMS C<sub>10</sub>, the concentration of decanoic acid around the surface is too high for the *S. aureus* bacteria to consume during stages of bacterial attachment, resulting in bacterial cell death.

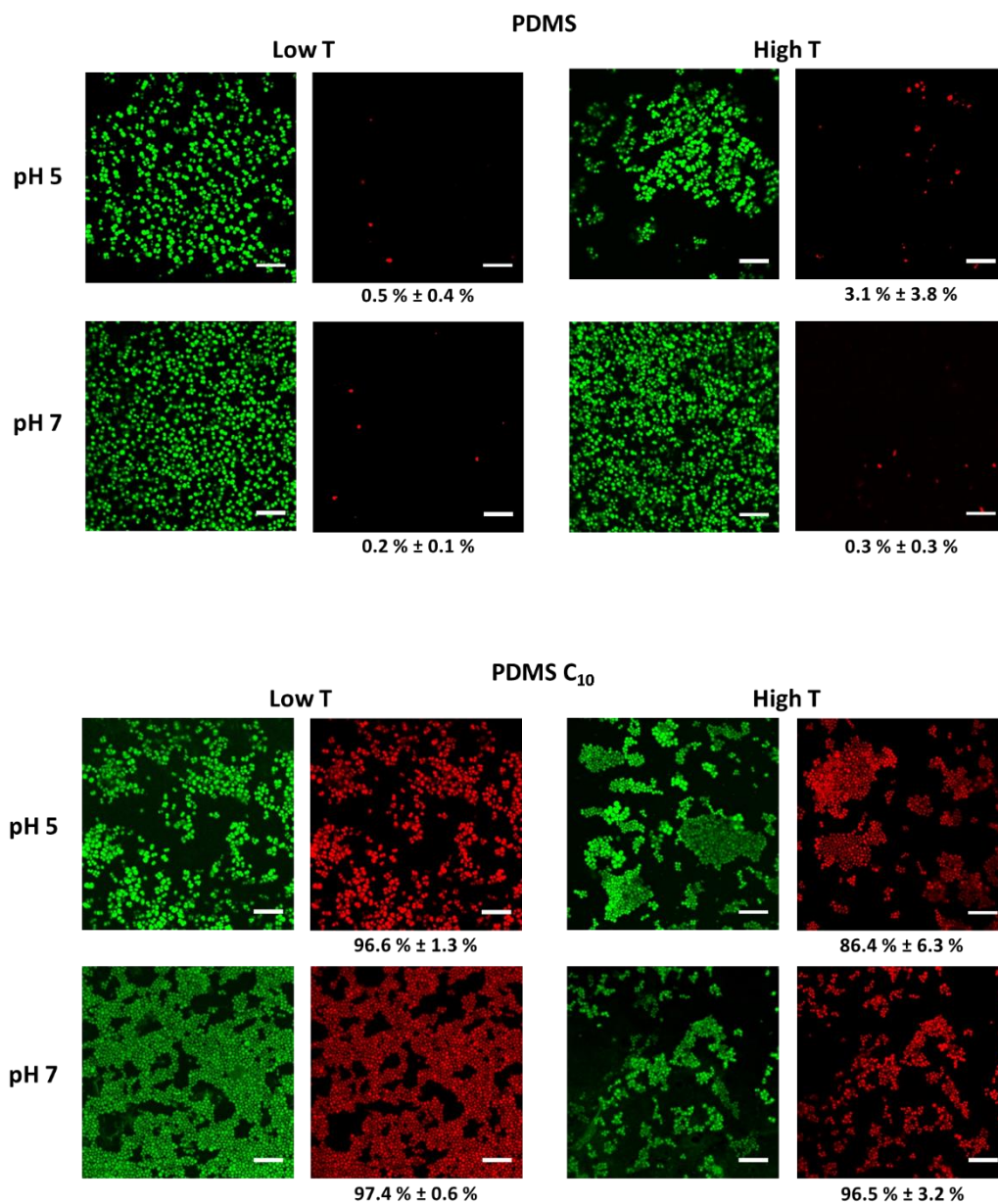


**Figure 3. 25** Confocal fluorescence microscopy images of *S. aureus* (ATCC 6538P) on PDMS and PDMS C<sub>10</sub>, showing percentage of dead bacteria. Bacteria imaged using Live/dead viability kit, where all bacteria are stained green and dead bacteria are stained red. Scale Bars shown in all images are 10 μm.

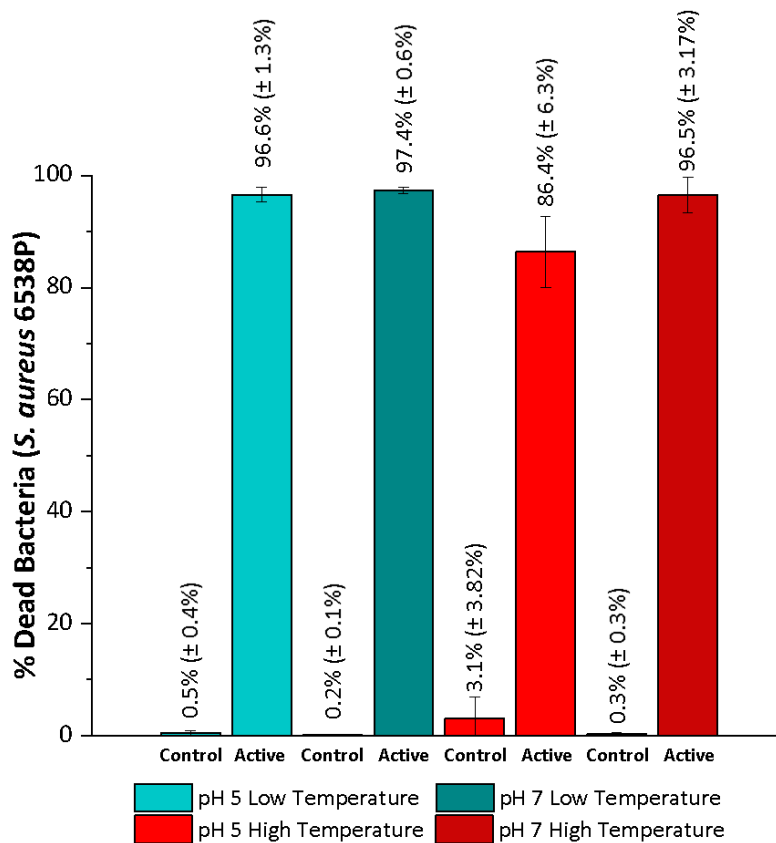


**Figure 3. 26** Bar Chart showing summary of the CFM data using Live/ Dead staining for *S. aureus* 6538P on PDMS (Control) and PDMS C<sub>10</sub> (Active) under different pH and temperature conditions.

In summary of the antimicrobial experiments with PDMS C<sub>10</sub>, we observed antimicrobial activity at the surface for both bacteria types (*S. aureus* and *E. coli*). PDMS C<sub>10</sub> proved effective as an antimicrobial surface towards *S. aureus* bacteria for all pH and temperature conditions tested. While high temperature and low pH conditions exhibited the highest fraction of dead *E. coli* bacteria on the surface of PDMS C<sub>10</sub>. However, in the planktonic experiments with PDMS C<sub>10</sub> an inhibitory effect was observed for *E. coli* only, with the highest growth inhibition of bacteria observed under optimum release conditions (high temperature, high pH). Conversely, for *S. aureus* bacteria an increased growth in the planktonic state was observed for PDMS C<sub>10</sub>. This is consistent with the literature, where an improved growth of *S. aureus* bacteria has been reported, attributed to the incorporation of fatty acids into the phospholipids of *S. aureus* bacteria.<sup>66-68</sup>

As a result, we observe a ‘logic gate like’ activity for PDMS C<sub>10</sub>, where the release of fatty acid and inhibition of *E. coli*, either at the surface or in the planktonic state, can be controlled by adjusting the temperature and/ or pH of the surrounding media (Figure 3. 27). When optimum release conditions (high temperature, high pH) are met, the AND logic gate activates, allowing 100% of the fatty acid to be released, resulting in an inhibition of 90% of *E. coli* in the planktonic state (Figure 3. 27 A). When we have a higher temperature, but low pH, less fatty acid is released from PDMS C<sub>10</sub> and the XOR-AND logic gate is activated, resulting in an increased fraction of dead *E. coli* bacterial cells on the surface of PDMS C<sub>10</sub> (Figure 3. 27 B).

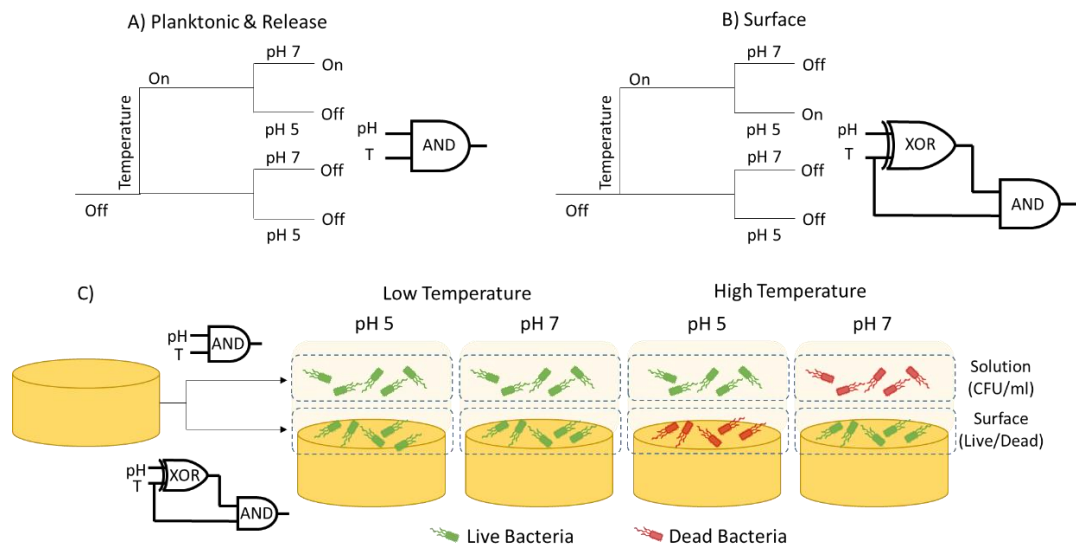


**Figure 3. 27** Mechanism of PDMS C<sub>10</sub> logic gate. (A) *E. coli* planktonic inhibition and C<sub>10</sub> release switch, (B) *E. coli* surface Inhibition switch, (C) Graphical display of PDMS C<sub>10</sub> logic gate mechanism towards *E. coli* bacteria.

### 3.4 Conclusions

In this work, we produced an antimicrobial material with a logic gate like activity. After curing the PDMS, the ability of PDMS to swell upon contact with hydrophobic non-polar materials was exploited and the material was successfully loaded with fatty acid. The presence of fatty acid within the PDMS was observed as a colour change from colourless and transparent to a translucent white colour, and further confirmed, according to gravimetric analysis, Raman spectroscopy and DSC data. The degree of swelling the PDMS with fatty acid proved to be associated with the length of the aliphatic chain, which can be explained according to the 'Wall-Flory-Rehner model'.<sup>6,54,55</sup> The movement of network junctions in the PDMS material are restricted and therefore the size of the molecules that can fit between the polymer network is also restricted. As a result, decanoic acid has a higher degree of freedom to move around the polymer network compared to dodecanoic acid or tetradecanoic acid, which have longer aliphatic chains. As a result of PDMS swelling, the mass of fatty acid loaded in the FAIP samples were as follows: 0.0891 g/ g PDMS  $\pm$  0.0125 g for PDMS C<sub>10</sub>, 0.0584 g/ g PDMS  $\pm$  0.0087 g for PDMS C<sub>12</sub> and 0.0375 g/ g PDMS  $\pm$  0.0068 g.

After fabricating the FAIP materials, we demonstrated that we could also release the fatty acid from the PDMS under physiological conditions. We were able to control the amount of fatty acid released from all FAIP materials using different pH and temperature conditions. This was confirmed by gravimetric analysis (Figure 3. 15) and Raman spectroscopy (Figure 3. 17 and see appendix, Figures A3. 5 and 6), with the optimum release of fatty acid from FAIP materials found at high temperature and high pH conditions, resulting in a 'logic gate like' (AND) activity (Figure 3. 27).

A mechanism for fatty acid released from PDMS, associated with the ‘Wall-Flory-Rehner model’ of PDMS swelling was proposed, using static contact angle measurements and DSC data to support our hypothesis. The surface properties of the PDMS after swelling with fatty acid change from hydrophobic and become susceptible to wetting with aqueous buffer, specifically with pH 7 buffer. Since the fatty acid is amphiphilic, the carboxylic group of the fatty acid in the PDMS can interact with the physiological buffer, encouraging the fatty acid to be released from the FAIP. The temperature and pH can have a significant effect on the release, due to the increased solubility of the fatty acid in the form of a salt and melting of the fatty acid above  $T_{\text{onset}}$ . Melted fatty acid can migrate out of the PDMS and the release from the surface is controlled by the solubility of fatty acid depending on the pH of the media. When the temperature is decreased below the  $T_{\text{onset}}$ , following the release experiment, the fatty acid solidifies to form a ‘gel’ like substance on the surface of the FAIP.

We also tested the antimicrobial activity of FAIP material, PDMS C<sub>10</sub>. PDMS C<sub>10</sub> was chosen as the best candidate for antimicrobial tests, considering the optimum release observed at physiological conditions at 37°C, pH 7, matching the  $T_{\text{onset}}$  observed in the DSC data. The antimicrobial activity of PDMS C<sub>10</sub> was also tested at pH 5, considering the slightly acidic nature of human skin.<sup>58</sup> As a result, PDMS C<sub>10</sub> demonstrated antimicrobial activity at the surface for both bacteria types (*S. aureus* and *E. coli*), with a high fraction of dead bacteria in all conditions tested for *S. aureus*. While high temperature low pH conditions exhibited the highest fraction of dead *E. coli* bacteria on the surface of PDMS C<sub>10</sub>. However, in planktonic experiments with PDMS C<sub>10</sub> an inhibitory effect was observed for *E. coli* only, with the highest growth inhibition of bacteria observed under optimum release conditions (high temperature, high pH). Conversely, for *S. aureus* bacteria an increased growth in the planktonic state was observed for PDMS C<sub>10</sub>. This is consistent with literature, where an improved growth of *S. aureus* bacteria has been reported, attributed to the incorporation of fatty acids into the phospholipids of *S. aureus* bacteria.<sup>66–68</sup>

As a result, we observe a ‘logic gate like’ activity for PDMS C<sub>10</sub>, where the release of fatty acid and inhibition of *E. coli*, either at the surface or in the planktonic state, can be controlled by adjusting the temperature and/ or pH of the surrounding media (Figure 3. 27). When optimum release conditions (high temperature, high pH) are met, the AND logic gate activates, allowing 100% of the fatty acid to be released, resulting in an inhibition of 90% for *E. coli* in the planktonic state (Figure 3. 27 A). When we have a higher temperature, but low pH, less fatty acid is released from PDMS C<sub>10</sub> and the XOR-AND logic gate is activated, resulting in an increased dead fraction of *E. coli* bacterial cells on the surface of PDMS C<sub>10</sub> (Figure 3. 27 B).

### 3.5 Future Work

Initially, in the tests conducted with *S. aureus* bacteria, an inhibitory effect was observed in the MIC experiments at increasing concentrations of decanoic acid (Figure 3. 23). While in the planktonic experiments with PDMS C<sub>10</sub>, when 100% of the fatty acid is released (Figure 3. 15), we observed an increased growth in planktonic bacteria (Figure 3. 24). This data suggested that the release of fatty acid from the PDMS may be gradual, and the initial release of fatty acid in the planktonic is of a low concentration. At low concentrations of fatty acid, the *S. aureus* appear to utilise the fatty acid as a potential 'food source', increasing their growth rate.

To gain a better understanding of these findings, the release of fatty acid from the FAIP materials could be investigated over a time course, thus providing a better insight into the mechanism for the release of fatty acids from PDMS. Contact angle measurements could also be investigated following the release experiments, to determine any changes in the surface properties of the PDMS. The uptake of fatty acid by *S. aureus* bacteria, can also be further studied. Starting with a known concentration of fatty acid in biological media, a fatty acid quantification assay with fluorescence probe, could be used to determine the concentration of fatty acid, before and after 24 hrs of incubation with *S. aureus* bacteria, by fluorescence spectroscopy. If after 24 hrs of incubation a decrease in the concentration of fatty acid is observed, along with an increase in bacterial growth compared to a control, we can justifiably confirm the uptake of fatty acid by the *S. aureus* bacteria.

In addition to the above experiments, further testing of PDMS C<sub>10</sub> could be conducted with other bacterial species, of both gram-negative and gram-positive species, in order to confirm the antimicrobial efficacy of PDMS C<sub>10</sub>. From these experiments, we could also conclude if

the increased growth observed with *S. aureus* planktonic bacteria, associated with the uptake of fatty acid, is specific to *S. aureus*, or whether the uptake of fatty acid is a characteristic of other gram-positive bacteria. By using thermophile type bacteria, we could also test the antimicrobial efficacy of PDMS C<sub>12</sub> and PDMS C<sub>14</sub> materials at higher temperatures, thus exploring the antimicrobial efficacy of our other FAIP materials.<sup>70</sup> Fatty acids have also demonstrated an anti-fungal effect towards fungal species, such as *Candida albicans*<sup>37</sup> and therefore testing our FAIP materials against these types of microbes could open another avenue of research for our materials.

## 3.6 References

- 1 J. E. Mark, H. R. Allcock and R. West, *Inorganic Polymers*, J. E. Mark, H. R. Allcock and R. West, Oxford University Press, Oxford, 2nd Edition, 2005.
- 2 T. K. Meister, K. Riener, P. Gigler, J. Stohrer, W. A. Herrmann and F. E. Kühn, *ACS Catal.*, 2016, **6**, 1274–1284.
- 3 D. Ortiz-Acosta and C. Densmore, *Sylgard® Cure Inhibition Characterization*, 2012.
- 4 C. Yu, C. Yu, L. Cui, Z. Song, X. Zhao, Y. Ma and L. Jiang, *Adv. Mater. Interfaces*, 2017, **4**, 1600862.
- 5 J. N. Lee, C. Park and G. M. Whitesides, *Anal. Chem.*, 2003, **75**, 6544–6554.
- 6 S. Nandi and H. H. Winter, *Macromolecules*, 2005, **38**, 4447–4455.
- 7 F. Abbasi, H. Mirzadeh and A. A. Katbab, *Polym. Int.*, 2001, **50**, 1279–1287.
- 8 M. K. Kwak, H. E. Jeong and K. Y. Suh, *Adv. Mater.*, 2011, **23**, 3949–3953.
- 9 S. Barr, E. W. Hill and A. Bayat, *Acta Biomater.*, 2017, **49**, 260–271.
- 10 R. K. Malcolm, K. L. Edwards, P. Kiser, J. Romano and T. J. Smith, *Antiviral Res.*, 2010, **88**, 30–39.
- 11 A. Kottmann, E. Mejía, T. Hémerly, J. Klein and U. Kragl, *Chem. - An Asian J.*, 2017, **12**, 1168–1179.
- 12 H. Kanematsu and D. M. Barry, *Biofilm and Materials Science*, H. Kanematsu and D. M. Barry, Springer, Heidelberg, 1st Edition, 2015.
- 13 H. Li, M. R. Fairfax, F. Dubocq, R. O. Darouiche, A. Rajpurkar, M. Thompson, M. V Tefilli and C. B. Dhabuwala, *Am. Urological Assoc. Inc.*, 1998, **160**, 1910–1913.
- 14 I. J. Chen and E. Lindner, *Langmuir*, 2007, **23**, 3118–3122.

- 15 K. G. Owen, D. F. Davidson and R. K. Hanson, *J. Thermophys. Heat Transf.*, 2016, **30**, 274–278.
- 16 M. Morra, E. Occhiello, R. Marola, F. Garbassi, P. Humphrey and D. Johnson, *J. Colloid Interface Sci.*, 1990, **137**, 11–24.
- 17 S. H. Tan, N. T. Nguyen, Y. C. Chua and T. G. Kang, *Biomicrofluidics*, 2010, **4**, 32204.
- 18 G. Pasirayi, V. Auger, S. M. Scott, P. K.S.M. Rahman, M. Islam, L. O’Hare and Z. Ali, *Micro Nanosyst.*, 2012, **3**, 137–160.
- 19 G. H. Kim, D. Lee, A. Shanker, L. Shao, M. S. Kwon, D. Gidley, J. Kim and K. P. Pipe, *Nat. Mater.*, 2015, **14**, 295–300.
- 20 K. Senshu, T. Furuzono, N. Koshizaki, S. Yamashita, T. Matsumoto, A. Kishida and M. Akashi, *Macromolecules*, 1997, **30**, 4421–4428.
- 21 F. Lim, C. Z. Yang and S. L. Cooper, *Biomaterials*, 1994, **15**, 408–416.
- 22 J. Orsavova, L. Misurcova, J. Vavra Ambrozova, R. Vicha and J. Mlcek, *Int. J. Mol. Sci.*, 2015, **16**, 12871–12890.
- 23 L. Spitz, *SODEOPEC : soaps, detergents, oleochemicals, and personal care products*, L. Spitz, Taylor & Francis, Illinois, 1st Edition, 2004.
- 24 A. P. Desbois and V. J. Smith, *Appl. Microbiol. Biotechnol.*, 2010, **85**, 1629–1642.
- 25 G. Burrows, Andrew. Holman, John. Parsons, Andrew. Pilling, Gwen. Price, *Chemistry<sup>3</sup> : introducing inorganic, organic and physical chemistry*, G. Burrows, Andrew. Holman, John. Parsons, Andrew. Pilling, Gwen. Price, Oxford University Press, Oxford, 1st Edition, 2009.
- 26 S. M. Alawi and M. S. Akhter, *J. Korean Chem. Soc.*, 2011, **55**, 163–168.
- 27 L. . Gevantman, in *CRC Handbook of Chemistry and Physics*, D. R. Lide, CRC Press, New York, 85th Edition, 2003, 8.92-8.109.

- 28 D. R. Lide, in *CRC Handbook of Chemistry and Physics*, D. R. Lide, CRC Press, New York, 85th Edition, 2003, 3.1-3.736.
- 29 Nø. L. Prisle, T. Raatikainen, R. Sorjamaa, B. Svenningsson, A. Laaksonen and M. Bilde, *Tellus, Ser. B Chem. Phys. Meteorol.*, 2008, **60 B**, 416–431.
- 30 J. R. Kanicky and D. O. Shah, *J. Colloid Interface Sci.*, 2002, **256**, 201–207.
- 31 S. Y. Lee, R. Welbourn, S. M. Clarke, M. W. A. Skoda, L. Clifton and A. Zorbakhsh, *J. Colloid Interface Sci.*, 2013, **407**, 348–353.
- 32 L. Brady, A. M. Brzozowski, Z. S. Derewenda, E. Dodson, G. Dodson, S. Tolley, J. P. Turkenburg, L. Christiansen, B. Høge-Jensen, L. Nørskov, L. Thim and U. Menge, *Nature*, 1990, **343**, 767–770.
- 33 J. Clayden, N. Greeves and S. G. Warren, *Organic chemistry*, J. Clayden, N. Greeves and S. G. Warren, Oxford University Press, Oxford, 1st Edition, 2001.
- 34 M. Masuda, M. Era, T. Kawahara, T. Kanyama and H. Morita, *Biocontrol Sci.*, 2015, **20**, 209–213.
- 35 J. S. Choi, N. H. Park, S. Y. Hwang, J. H. Sohn, I. Kwak, K. K. Cho and I. S. Choi, *J. Environ. Biol.*, 2013, **34**, 673–676.
- 36 J. B. Parsons, J. Yao, M. W. Frank, P. Jackson and C. O. Rock, *J. Bacteriol.*, 2012, **194**, 5294–5304.
- 37 C. B. Huang, Y. Alimova, T. M. Myers and J. L. Ebersole, *Arch. Oral Biol.*, 2011, **56**, 650–654.
- 38 T. Kitahara, N. Koyama, J. Matsuda, Y. Aoyama, Y. Hirakata, S. Kamihira, S. Kohno, M. Nakashima and H. Sasaki, *Biol. Pharm. Bull.*, 2004, **27**, 1321–1326.
- 39 J. A. Jackman, B. K. Yoon, D. Li and N. J. Cho, *Molecules*, 2016, **21**, 1–19.
- 40 D. R. Drake, K. A. Brogden, D. V. Dawson and P. W. Wertz, *J. Lipid Res.*, 2008, **49**,

4–11.

- 41 J. J. Kabara, D. M. Swieczkowski, A. J. Conley and J. P. Truant, *Antimicrob. Agents Chemother.*, 1972, **2**, 23–28.
- 42 L. J. McGaw, A. K. Jäger and J. Van Staden, *South African J. Bot.*, 2002, **68**, 417–423.
- 43 P. Georgel, K. Crozat, X. Lauth, E. Makrantonaki, H. Seltmann, S. Sovath, K. Hoebe, X. Du, S. Rutschmann, Z. Jiang, T. Bigby, V. Nizet, C. C. Zouboulis and B. Beutler, *Infect. Immun.*, 2005, **73**, 4512–4521.
- 44 H. Takigawa, H. Nakagawa, M. Kuzukawa, H. Mori and G. Imokawa, *Dermatology*, 2005, **211**, 240–248.
- 45 C. J. Zheng, J. S. Yoo, T. G. Lee, H. Y. Cho, Y. H. Kim and W. G. Kim, *FEBS Lett.*, 2005, **579**, 5157–5162.
- 46 H. Galbraith, A. M. Paton and J. K. Thompson, *J. appl. Bact.*, 1971, **34**, 803–813.
- 47 M. F. Feldlaufer, D. A. Knox, W. R. Lusby and H. Shimanuki, *Apidologie*, 1993, **24**, 95–99.
- 48 J. J. Wille and A. Kydonieus, *Skin Pharmacol. Appl. Skin Physiol.*, 2003, **16**, 176–187.
- 49 S. W. Jung and S. W. Lee, *Korean J. Intern. Med.*, 2015, **31**, 30–35.
- 50 Y. Zhou and H. Cao, *Sci. World J.*, 2013, **2013**, 1–6.
- 51 T. Galeano Díaz, A. Guiberteau, J. M. Ortíz Burguillos and F. Salinas, *Analyst*, 1997, **122**, 513–517.
- 52 B. Y. A. A. Miles and S. S. Misra, *J. Hyg. (Lond.)*, 1931, **38**, 732–749.
- 53 A. Susarrey-Arce, I. Sorzabal-Bellido, A. Oknianska, F. McBride, A. J. Beckett, J. G. E. Gardeniers, R. Raval, R. M. Tiggelaar and Y. A. Diaz Fernandez, *J. Mater. Chem. B*, 2016, **4**, 3104–3112.

- 54 F. T. Wall and P. J. Flory, *J. Chem. Phys.*, 1951, **19**, 1435–1439.
- 55 P. J. Flory and J. Rehner, *J. Chem. Phys.*, 1944, **12**, 412–414.
- 56 D. Cai, A. Neyer, R. Kuckuk and H. M. Heise, *J. Mol. Struct.*, 2010, **976**, 274–281.
- 57 M. Saggu, J. Liu and A. Patel, *Pharm. Res.*, 2015, **32**, 2877–2888.
- 58 E. Proksch, *J. Dermatol.*, 2018, **45**, 1044–1052.
- 59 P. Pallavicini, B. Bassi, G. Chirico, M. Collini, G. Dacarro, E. Fratini, P. Grisoli, M. Patrini, L. Sironi, A. Taglietti, M. Moritz, I. Sorzabal-Bellido, A. Susarrey-Arce, E. Latter, A. J. Beckett, I. A. Prior, R. Raval and Y. A. Diaz Fernandez, *Sci. Rep.*, 2017, **7**, 5259.
- 60 N. Fernández-Hidalgo, J. Gavalda, B. Almirante, M. T. Martín, P. L. Onrubia, X. Gomis and A. Pahissa, *J. Antimicrob. Chemother.*, 2010, **65**, 525–530.
- 61 Y.-S. Kwak, S.-J. Kim and H.-Y. Kim, *Biomed. Res.*
- 62 K. M. Osman, A. D. Kappell, F. Elhofy, A. Orabi, A. S. Mubarak, T. M. Dawoud, I. Mi Moussa and A. M. Hessain, *Futur. Microbiol.*, 2018, 745–756.
- 63 M. Marounek, E. Skřivanová and V. Rada, *Folia Microbiol. (Praha)*, 2003, **48**, 731–735.
- 64 L. Prohaszka, *Vet. Med. B*, 1980, **27**, 631–639.
- 65 J. M. Willey, L. Sherwood, C. J. Woolverton and L. M. Prescott, *Prescott, Harley, and Klein's microbiology*, J. M. Willey, L. Sherwood, C. J. Woolverton and L. M. Prescott, McGraw-Hill Higher Education, New York, 7th Edition, 2008.
- 66 J. B. Parsons, T. C. Broussard, J. L. Bose, J. W. Rosch, P. Jackson, C. Subramanian and C. O. Rock, *Proc. Natl. Acad. Sci.*, 2014, **111**, 10532–10537.
- 67 R. A. Altenbern, *Antimicrob. Agents Chemother.*, 1977, **11**, 574–576.

- 68 Y. J. Lu, Y. M. Zhang, K. D. Grimes, J. Qi, R. E. Lee and C. O. Rock, *Mol. Cell*, 2006, **23**, 765–772.
- 69 Y. Endo, S. Kamisada, K. Fujimoto and T. Saito, *J Gen Appl Microbiol*, 2006, **52**, 29–35.
- 70 M. T. Madigan, K. S. Bender, D. H. Daniel, H. Buckley, W. M. Sattley and D. A. Stahl, *Brock Biology of Microorganisms*, M. T. Madigan, K. S. Bender, D. H. Daniel, H. Buckley, W. M. Sattley and D. A. Stahl, Pearson Education Limited, London, 15th Edition, 2019.

### 3.7 Appendix

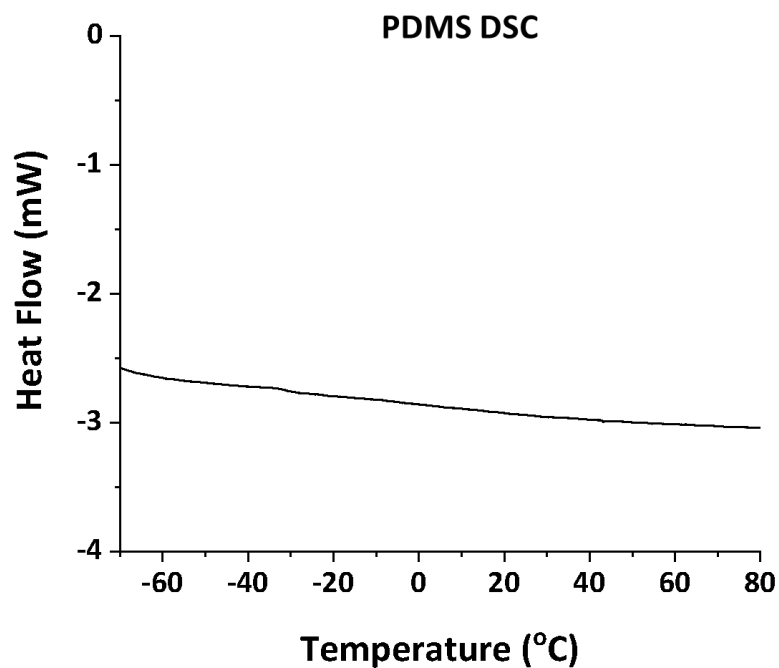


Figure A 3. 1 Representative DSC profile for PDMS

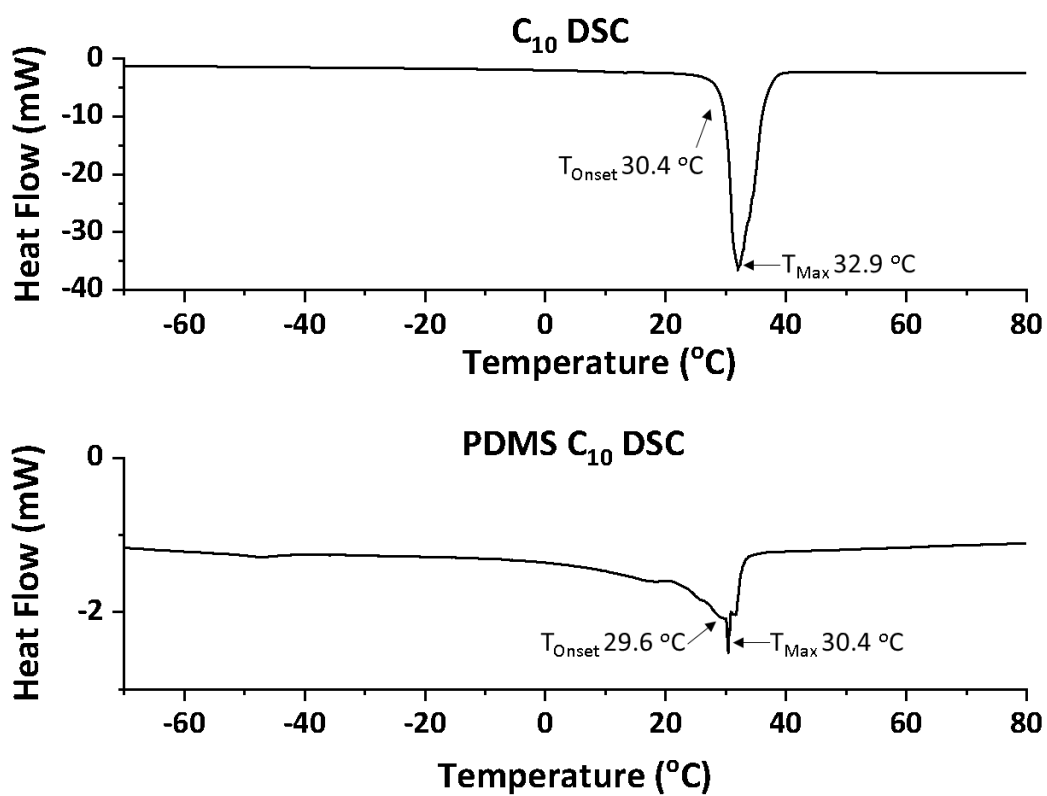


Figure A 3. 2 Representative DSC profiles for Decanoic Acid (A) and PDMS C<sub>10</sub> (B)

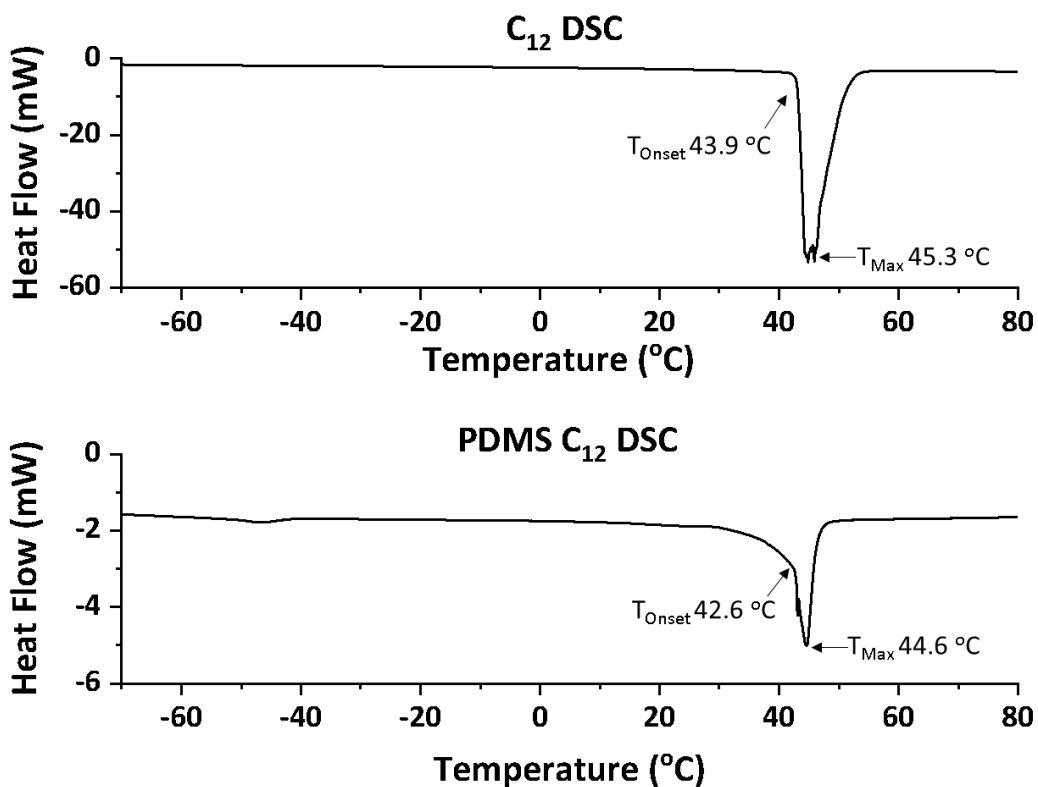


Figure A 3. 3 Representative DSC profiles for Dodecanoic Acid (A) and PDMS C<sub>12</sub> (B)

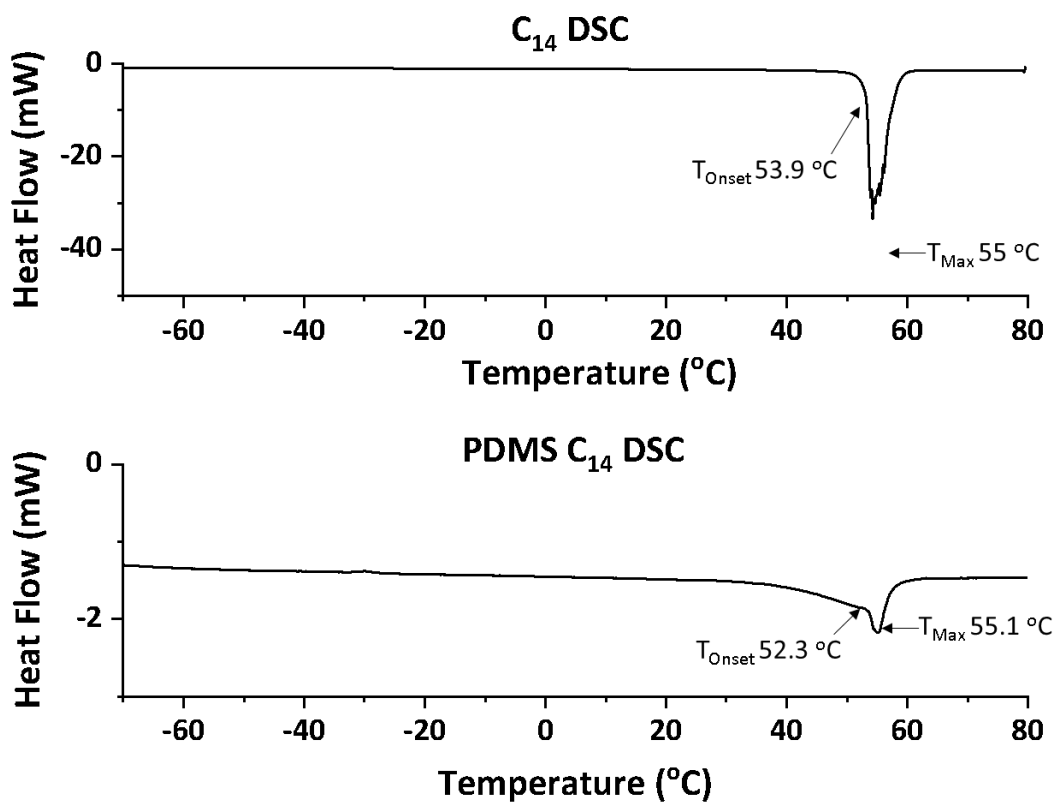
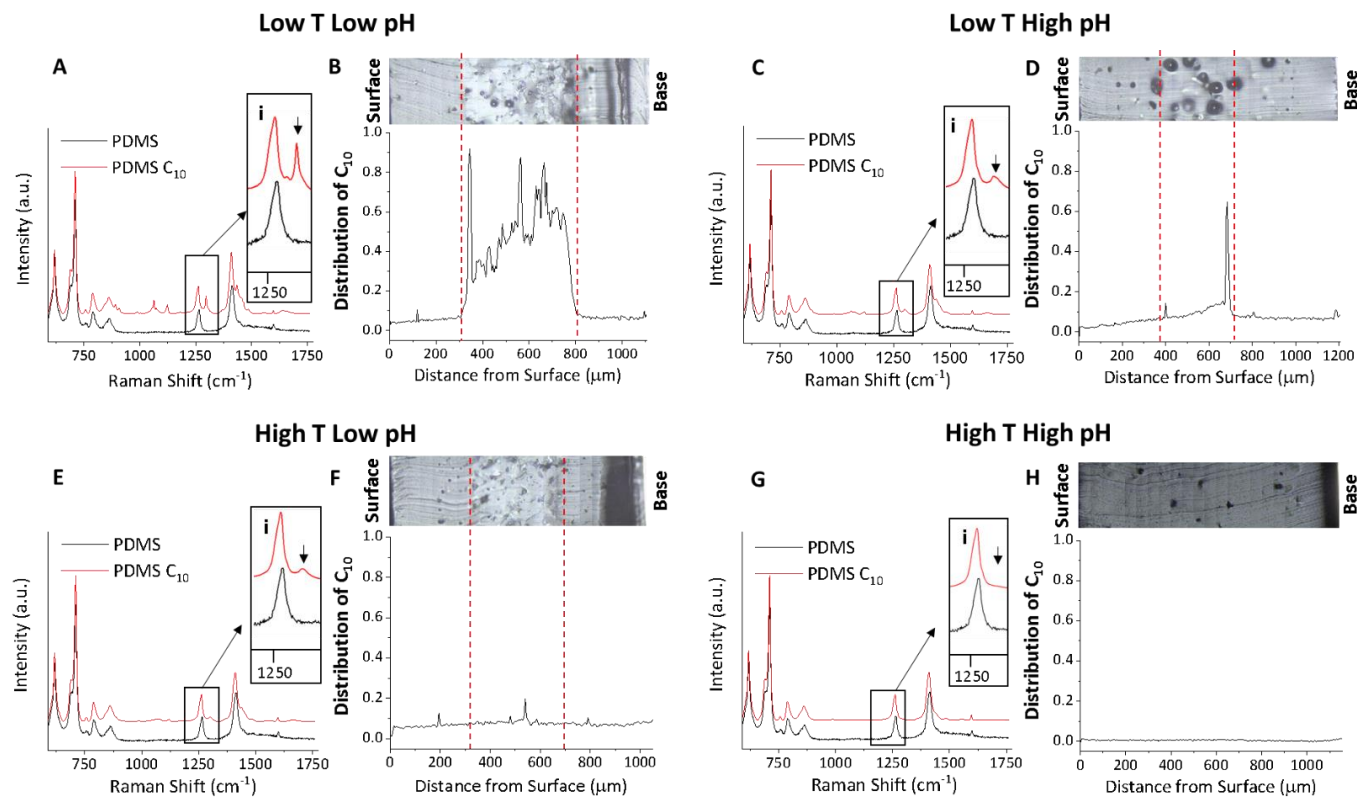
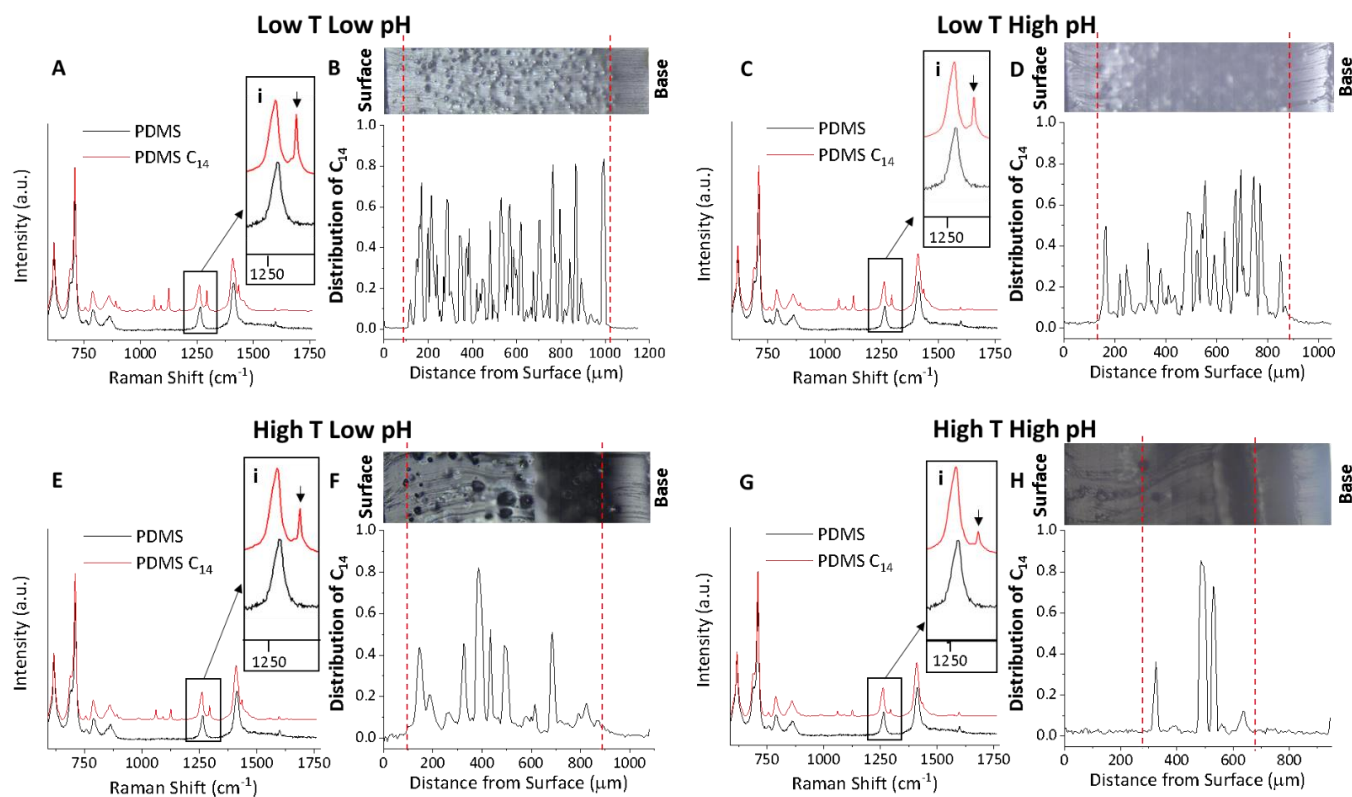


Figure A 3. 4 Representative DSC profiles for Decanoic Acid (A) and PDMS C<sub>14</sub> (B)



**Figure A 3. 5** Representative Raman data for PDMS C<sub>10</sub> after each release condition. **(A and B)** Low temperature, low pH release **(A)** Representative Raman spectra of PDMS (black) & PDMS C<sub>10</sub> (red), **(B)** Distribution of decanoic acid across PDMS C<sub>10</sub>. **(C and D)** Low temperature, high pH release **(C)** Representative Raman spectra of PDMS (black) & PDMS C<sub>10</sub> (red), **(D)** Distribution of decanoic acid across PDMS C<sub>10</sub>. **(E and F)** High temperature, low pH release **(E)** Representative Raman spectra of PDMS (black) & PDMS C<sub>10</sub> (red), **(F)** Distribution of decanoic acid across PDMS C<sub>10</sub>. **(G and H)** High temperature, high pH release **(G)** Representative Raman spectra of PDMS (black) & PDMS C<sub>10</sub> (red), **(H)** Distribution of decanoic acid across PDMS C<sub>10</sub>. **(i)** Insert showing  $\gamma$ CH<sub>2</sub> twist vibration of decanoic acid for each release condition.



**Figure A 3. 6** Representative Raman data for PDMS C<sub>14</sub> after each release condition. **(A and B)** Low temperature, low pH release **(A)** Representative Raman spectra of PDMS (black) & PDMS C<sub>14</sub> (red), **(B)** Distribution of tetradecanoic acid across PDMS C<sub>14</sub>. **(C and D)** Low temperature, high pH release **(C)** Representative Raman spectra of PDMS (black) & PDMS C<sub>14</sub> (red), **(D)** Distribution of tetradecanoic acid across PDMS C<sub>14</sub>. **(E and F)** High temperature, low pH release **(E)** Representative Raman spectra of PDMS (black) & PDMS C<sub>14</sub> (red), **(F)** Distribution of tetradecanoic acid across PDMS C<sub>14</sub>. **(G and H)** High temperature, high pH release **(G)** Representative Raman spectra of PDMS (black) & PDMS C<sub>14</sub> (red), **(H)** Distribution of tetradecanoic acid across PDMS C<sub>14</sub>. **(i)** Insert showing  $\gamma$ CH<sub>2</sub> twist vibration of tetradecanoic acid for each release condition.

# Chapter 4

## Combined Approach for the Photothermal Eradication of Bacteria and Photothermal Controlled Drug Release

### 4.1 Introduction

#### 4.1.1 Photothermal Materials

Photothermal materials have been widely studied for cancer treatment,<sup>1,2</sup> but are now emerging as alternative strategies in the field of antimicrobial surfaces.<sup>3-7</sup> Photothermal surfaces are fabricated using photo-responsive material (e.g. gold nanoparticles), thus allowing for the material to absorb light.<sup>3,4,6-8</sup> When light of a specific wavelength is absorbed by the photo-responsive material, it may transfer the absorbed energy in the form of heat (Figure 4. 1).<sup>3</sup> Localised heat released from the surface rises the temperature in the surrounding media, delivering a killing effect of the targeted cells.<sup>8</sup> For example, Pallavicini *et al*,<sup>3</sup> coated glass materials with gold nanostars using a (3-mercaptopropyl)trimethoxysilane (MPTS) linker, for the photothermal eradication of *S. aureus* biofilms (Figure 4. 1).

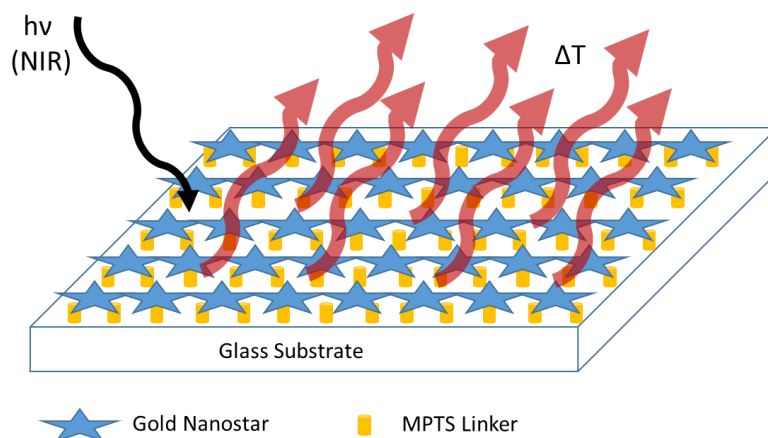


**Figure 4. 1** Schematic representation of a photothermal material. Adapted from Pallavicini *et al.*<sup>3</sup>

Elevated temperatures have shown to significantly reduce bacterial survival rates, both in the planktonic state and biofilms, suggesting that heat can be efficiently used as an alternative method for antimicrobial surfaces.<sup>8-10</sup> Temperature rises within the bacteria cell results in protein misfolding, leading to the formation of protein aggregates and cell death.<sup>11</sup>

Photothermal materials have predominantly been fabricated with the use of plasmonic nanoparticles, such as gold and silver nanomaterials, exploiting their unique tuneable optical properties, and their ability to generate heat, as result of their local surface plasmon resonance.<sup>1,3,4,6-8,12-14</sup> These materials have been previously reported to be effective towards a wide range of bacterial species, such as: *E. coli*, *S. aureus* and *S. epidermidis* bacteria.<sup>3,4,6,8</sup> The ability to tune the absorption of photo-responsive materials is a key aspect to consider when fabricating new photothermal surfaces, especially exploiting the near-infrared (NIR) region (700- 1100 nm) of the electromagnetic spectrum, where water and living tissues are transparent and, therefore, not susceptible to direct radiation damage (Figure 4. 2).<sup>4,7,15</sup>

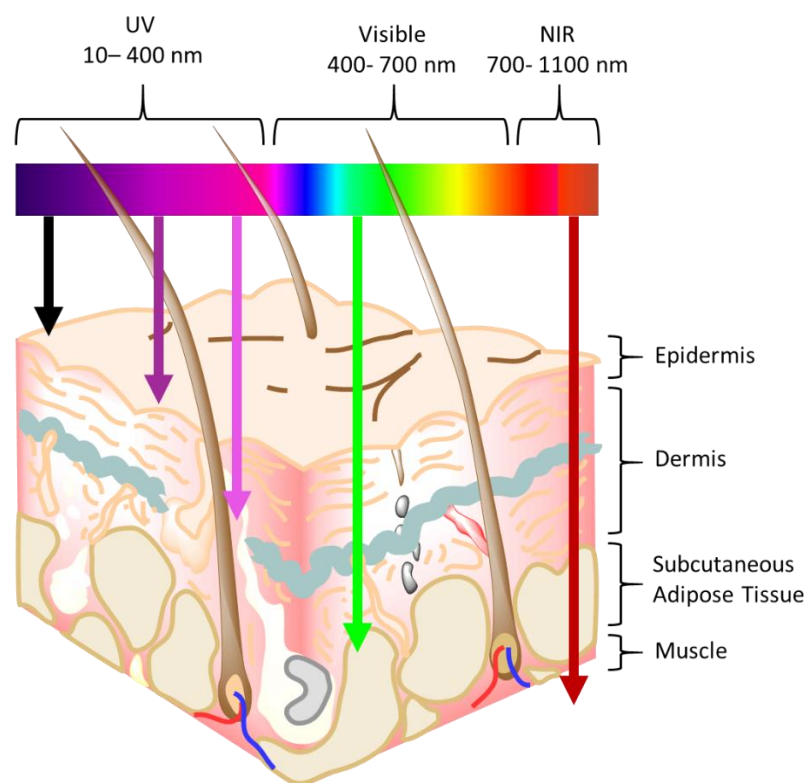


**Figure 4. 2** Illustration showing penetration depth of light at different wavelengths with human tissue.<sup>16</sup> Illustration created using template from ChemDraw.

Photothermal materials can also be used as drug delivery systems.<sup>2</sup> Photothermal controlled drug delivery systems utilise the heat generated by the photoexcited material to affect thermally sensitive components of drug delivery systems, which ultimately leads to the release of active components. Most of the research in this field, has again, predominately been focused on cancer treatment, using drugs coupled to a photo-responsive materials for controlled photothermal release.<sup>2</sup> Most of the literature focus on the use of plasmonic nanomaterials and include the use of polymeric micelles,<sup>17</sup> liposomes<sup>18,19</sup> or DNA cross linking,<sup>20</sup> for the incorporation of drugs and photo-responsive materials into controlled photothermal release systems.

Alternatively, carbon-based materials (e.g. carbon nanotubes (CNTs) and graphene), which are a considerably much cheaper alternative, have also been used as photothermal materials,<sup>5,21-29</sup> mainly focusing on the treatment of cancer.<sup>22-26,29</sup> Carbon based materials can

be sourced cheaply from the pyrolysis of organic waste e.g. waste plastics, cooking oils and biomass waste, making them inexpensive and environmentally friendly.<sup>30</sup>

#### 4.1.1.2 Carbon-based Photothermal Materials

The incorporation of carbon-based materials into photothermal systems for biomedical applications has become of increasing interest, not only due to their relatively low cost, but also related to their low toxicity and minimal environmental impact.<sup>2,31,32</sup> For example, pyrolytic carbon has been used for decades in biomedical implants and coatings, particularly in the manufacture of heart valve prostheses.<sup>32-34</sup> Initial studies of pyrolytic carbon have demonstrated good blood compatibility, with good adherence of endothelial cells and minimal adherence and activation of platelets.<sup>32,33</sup> In consequence, pyrolytic carbon remains one of the most widely used biomaterials in the manufacture of heart valve prostheses.<sup>32-34</sup>

Carbon-based materials, such as CNTs and graphene have only recently been employed as alternative photothermal materials towards antimicrobial applications,<sup>5,27,28</sup> although little is known regarding their use as photothermal drug delivery systems towards antimicrobial treatments. The broad light absorption range (including NIR) of carbon-based materials (e.g. carbon black) (Figure 4. 3), as well as the biocompatibility and low toxicity, suggest they are ideal candidates for photothermal antimicrobial applications. Carbon-based materials also offer a unique level of chemical and physical versatility and robustness, which makes them useful for the design of antimicrobial composites.<sup>27,35</sup>

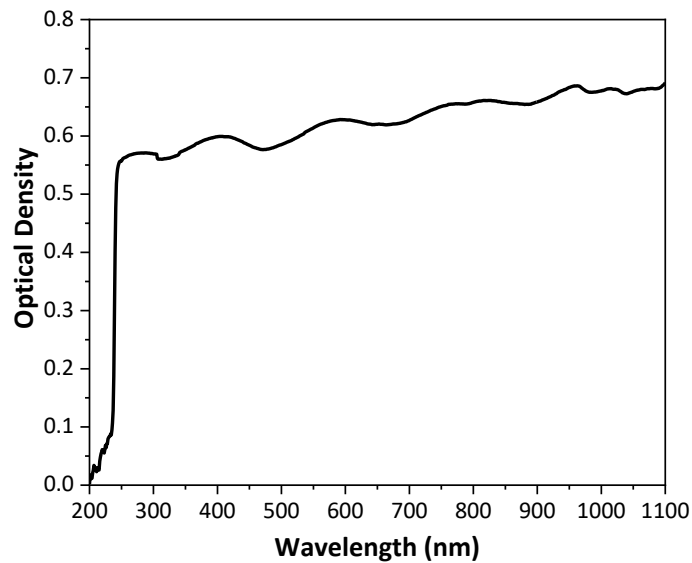


**Figure 4. 3** Absorbance spectrum of carbon nanopowder (CNP) dispersed in  $\text{CHCl}_3$  (Conc. 0.025% w/v).

The literature regarding carbon-based materials in photothermal antimicrobial systems are limited, but have demonstrated to be effective against bacterial species *E. coli* and *Streptococcus*.<sup>5,27,28</sup> For example, Akasaka *et al.*,<sup>5</sup> demonstrated the fabrication of a CNT/ agar composite for the NIR photothermal eradication of surface attached *Streptococcus* bacteria, resulting in a significant decrease in bacterial cell viability (Figure 4. 4).

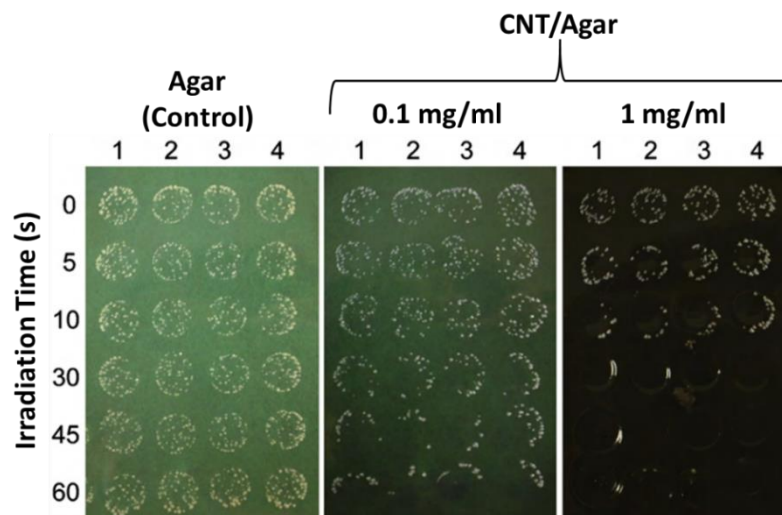


**Figure 4. 4** Images of *streptococcus* colonies on agar (control) and CNT/ agar composites irradiated with NIR light (800-1300 nm,  $1.3 \times 10^4 \text{ W/m}^2$ ). Samples inoculated with  $5 \mu\text{l}$   $6.8 \times 10^3 \text{ CFU/ml}$  bacterial suspension per spot before irradiation, and then incubated for 48 hrs. Brain Heart Infusion (BHI) agar used for control and active samples. mg/ml relates to concentration of CNTs used in fabrication of CNT/ agar samples. Figure adapted from Akasaka *et al.*<sup>5</sup>

Carbon-based materials, have also been implemented in drug delivery systems as photothermally active components, with focus on cancer treatment, using predominately CNTs or graphene.<sup>22–26,29</sup> Examples of carbon-based photothermal drug delivery systems are mainly colloidal based and use either polymer grafting on the surface of the material, or coupling to porous materials, such as mesoporous silica, to load and release drugs.<sup>22–26,29</sup> For example, Bani *et al.*,<sup>25</sup> grafted naphthol modified polyglycerol onto the surface of graphene, followed by loading the material with curcumin as an anti-cancer drug. On irradiation with NIR light, there was an observed increase in the amount of curcumin released from the material, along with a significantly reduced cancer cell viability. The loading and release of the curcumin was believed to be attributed to  $\pi$ - $\pi$  interaction between the  $\pi$  conjugated system of the graphene and the aromatic focal point of the naphthol modified polyglycerol. As a result of the photothermal heating, the increased molecular movement of the curcumin, resulted in the weakening of non-covalent  $\pi$ - $\pi$  bonding, leading to the release of the drug.

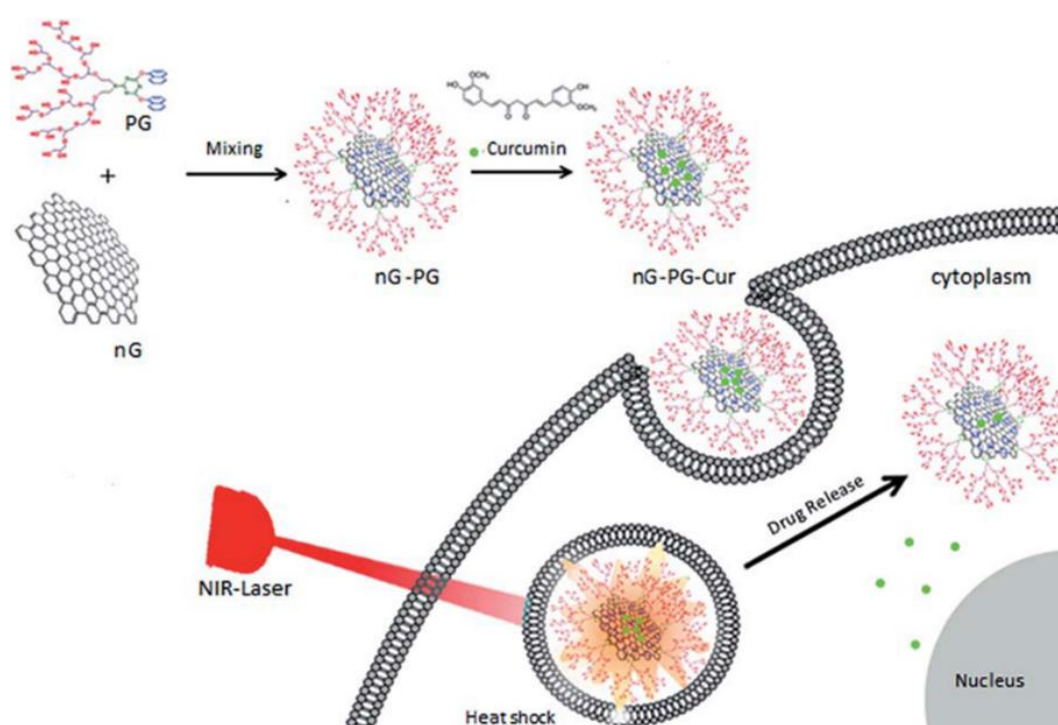


**Figure 4. 5** Schematic illustration for the preparation and release of the graphene based photothermal drug delivery system by Adeli *et al.*<sup>25</sup> PG → Naphthol modified polyglycerol, nG → nano graphene, nG-PG → nano graphene functionalised with naphthol modified polyglycerol, nG-PG-Cur → nano graphene functionalised with naphthol modified polyglycerol with captured curcumin drug. Figure reproduced from by Adeli *et al.*<sup>25</sup>

As we can see from the above discussion, carbon-based materials have made some great initial strides as photothermal materials. Although their use as photothermal materials, along with their implementation in drug delivery systems for antimicrobial applications is still lacking. Herein we report a novel approach for antimicrobial surfaces, combining PDMS and carbon nanopowder, a potentially renewable carbon-based material derived from waste products, for the photothermal eradication of surface attached bacteria (Type I), which in turn can be also loaded with antimicrobial agents, such as fatty acids, for a controlled photothermal release (Type II) (Figure 4.6).

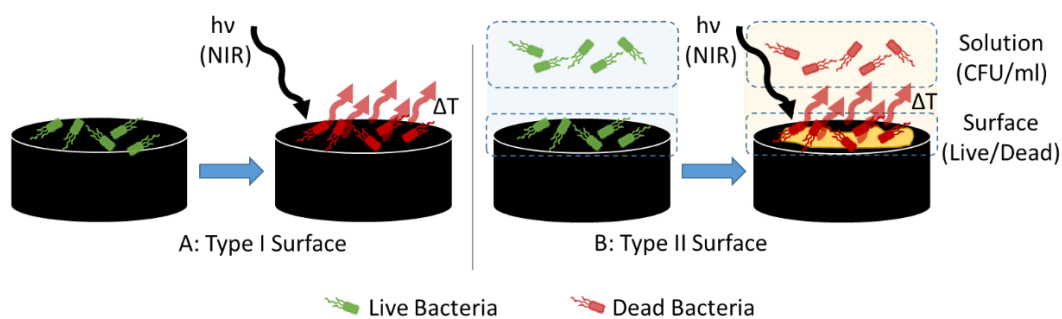


**Figure 4. 6** Schematic representation of type I and type II surface for photothermal eradication of surface attached bacteria (**Type I**) and controlled photothermal release antimicrobial agents (**Type II**).

## 4.2 Experimental Details

### 4.2.1 Chemicals

**Chemicals:** Sylgard 184 silicone elastomer kit (Dow Corning) was purchased from Univar Ltd. Hydrochloric acid (HCl, 37% w/v) and ethanol (EtOH, absolute 99%) were purchased from Fisher Scientific. Phosphate buffer saline (PBS) tablets were purchased from VWR. Lysogeny broth (LB) powder (Difco) was purchased from Scientific Laboratory Supplies (SLS). Live/ dead kit containing SYTO 9 and propidium iodide nucleic acid stains was purchased from ThermoFisher. All remaining chemicals listed were purchased from Sigma Aldrich: Carbon nanopowder (CNP), dodecanoic acid (98%), sodium chloride (NaCl, 98%), nutrient agar, MacConkey Agar and Mannitol Agar. All chemicals were used as received without further purification. Deionised water (Thermo Scientific Barnstead Smart2Pure), with a resistivity of 18 M $\Omega$ -cm was used throughout all experiments.

### 4.2.2 Fabrication of Type I Material for Photothermal

#### Eradication of Surface Attached Bacteria

**Fabrication of type I materials:** Type I materials were fabricated using Sylgard 184 silicone elastomer kit and carbon nanopowder (CNP). PDMS base and curing agent were mixed with 10:1 ratio (base: curing (w/w)), followed by the addition of CNP with a ratio of 1:20 (CNP: PDMS base (w/w)). The PDMS precursors were then subject to vortex for 2 minutes to form a homogenous black PDMS mixture, and then poured into wells of a 6 plate, with 1g of mixture per well. The PDMS mixture was then degassed under vacuum to remove trapped air bubbles and cured at 50°C overnight. This process led to black samples, with a reproducible thickness of 0.8 mm.

### 4.2.3 Characterisation of Type I Materials

**Physical characterisation of CNP by TEM:** A dilute dispersion of carbon nanopowder in  $\text{CHCl}_3$  was dropcast on a holey carbon coated copper grid (200 mesh) and then vacuum dried using a vacuum desiccator. The sample was then analysed using a FEI Tecnai G2 Spirit TEM, with 120 keV. Images were processed using Fiji software.

**Characterising the absorbance of PDMS and Type I material:** The absorbance of the PDMS and Type I materials were characterised using UV-Vis-NIR spectroscopy. Absorption measurements were collected using a Shimadzu UV-1800 with a resolution of 1 nm over a range of 200 nm to 1100 nm. Air was used as a baseline.

**Chemical characterisation of type I and raw materials:** Chemical characterisation of Type I and raw materials was performed using Raman spectroscopy. Raman spectra were recorded with a Renishaw inVia confocal Raman microscope using an excitation wavelength of 532 nm and a 20x objective lens. Different percentage (%) laser powers and acquisition times were used depending on the material analysed. Raman spectra were processed using WiRE 4.4 software (Renishaw).

**Mapping the distribution of CNP across the surface of type I materials by Raman spectroscopy:** The distribution of CNP across the surface of the type I materials was investigated using Raman spectroscopy with a Renishaw inVia confocal Raman microscope. Raman spectra were collected using a StreamLineHR map image acquisition mode, across the surface of the material, with an area of  $300\ \mu\text{m} \times 375\ \mu\text{m}$ , with a spectrum collected every  $3\ \mu\text{m}$ . Type I materials were analysed with an excitation wavelength of 532 nm, 5% laser power and 1s acquisition time. The baseline of each spectrum was corrected using WiRE 4.4 software

(Renishaw) and the distribution of CNP was determined using a signal to baseline analysis between 1550 and 1605  $\text{cm}^{-1}$ .

**Attenuated Total Reflection Infrared Spectroscopic (ATR-IR) characterisation of the PDMS and the type I material:** 9 mm diameter samples of PDMS and type I materials were cut from the material using a cork borer and then placed face down in contact with an ATR crystal, and the spectra was collected. ATR-IR measurements were carried out using a Bruker Tensor II FT-IR with platinum ATR module, with a resolution of 4  $\text{cm}^{-1}$ . Each spectrum collected was an average of 32 scans. The spectra were collected in a range of 400-3500  $\text{cm}^{-1}$  and analysed using OPUS Spectroscopy Software (Bruker).

## 4.2.4 Photothermal Experiments

### 4.2.4.1 Designing the Photothermal Experiment

**Designing the laser set-up for photothermal experiments:** A continuous wave laser set-up was built using a Thorlabs 808 nm laser diode (L808P1000MM) and a Thorlabs LDM90 temperature-controlled mount, with collimating lens (Figure 4. 7). The light emitted from the laser diode then passed through an anamorphic prism to transform the elliptical beam of the 808 nm laser diode into a quasicircular beam (Figure 4. 7). A right-angle mirror was then used to reflect the laser light upwards towards the sample stage (Figure 4. 7). A 5 mm diameter sample well fabricated using a glass bottomed dish and PDMS was used for irradiating the surface of the sample under physiological conditions (Figure 4. 7 and 8). A large SEM sample stub was used as a weight to hold the sample in place (Figure 4. 7 and 8).

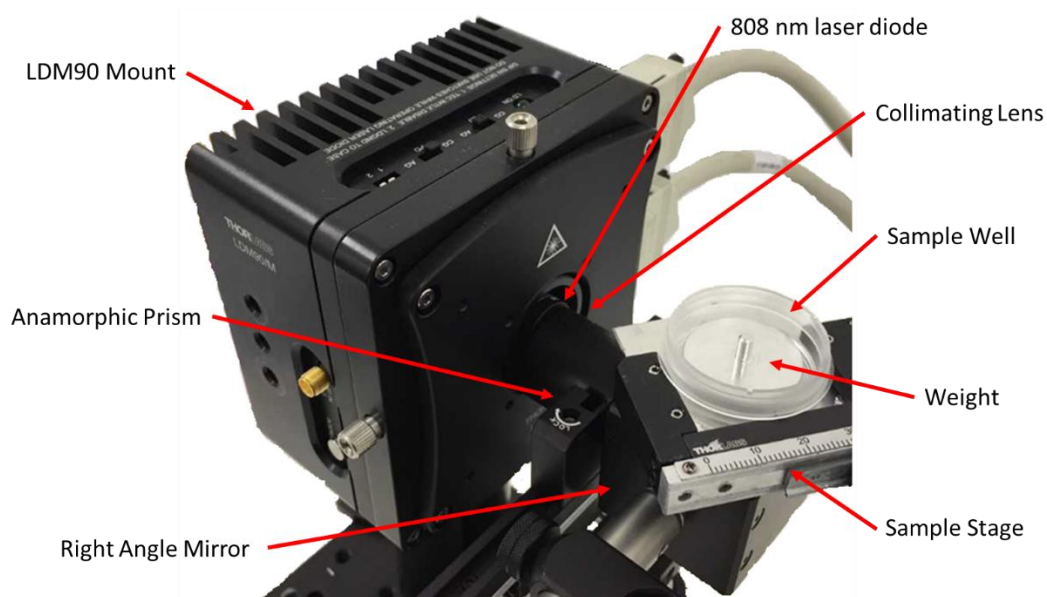


**Figure 4. 7** Photograph of laser set up for photothermal experiments with type I and type II surfaces.

The laser power was adjusted using a Thorlabs LDC240C laser diode controller to change the supplied current (mA). The laser power (mW) output of different currents (mA) used in the photothermal experiments were measured at the aperture in the sample stage, using a thermal power sensor (Thorlabs S302C).

**Fabrication of sample wells for photothermal experiments:** To fabricate the sample wells, PDMS was fabricated using Sylgard 184 silicone elastomer kit with a 10:1 ratio (base: curing (w/w)), and then 500mg of the PDMS mixture was poured into a glass bottomed dish. The PDMS was degassed under vacuum to remove trapped air bubbles and then cured at 50°C overnight. After curing the PDMS, the dish was placed on the sample stage of the laser set-up and a 5 mm hole aligned with the irradiation spot was carefully cut away from the PDMS using a cork borer.

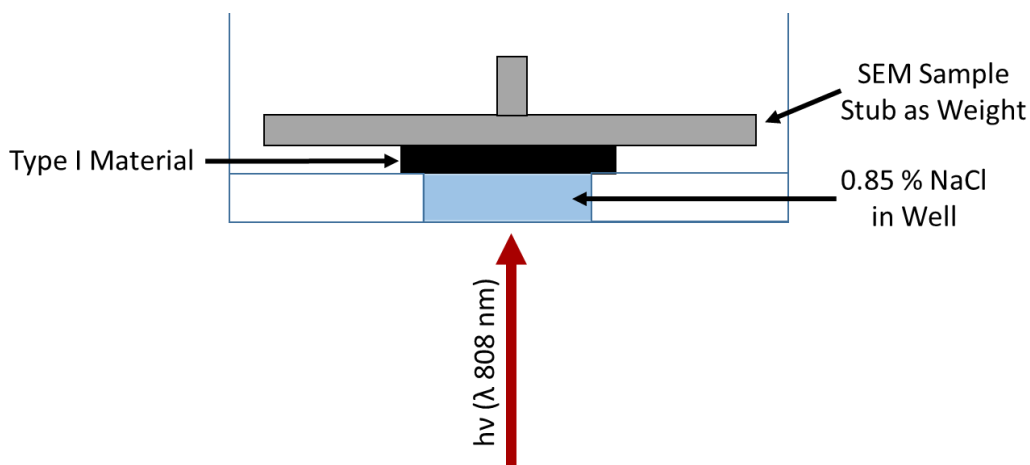


**Figure 4. 8** Schematic of the laser set up for photothermal experiments with type I and type II surfaces.

#### 4.2.4.2 Investigating the Photothermal Effect of Type I Materials

##### **Determining the temperature at the surface of type I materials during NIR photothermal**

**experiments:** A sample well with a K type thermocouple was fabricated using a modified approach according to the above fabrication technique for irradiation sample wells. A hole was drilled at the side of a glass bottomed dish and a K type thermocouple was thread through. A sample well from the photothermal experiments was used as a template and the thermocouple was held carefully in place, aligned next to the irradiation spot. 500 mg of PDMS mixture was then poured into the glass bottomed dish and without degassing, it was cured at 50°C overnight on a hot plate. After curing the PDMS, the well was formed using a 5 mm cork borer as discussed above, while being careful not to damage the thermocouple. A small area where the thermocouple meets the sample was then cut out carefully using a scalpel and then cleaned up under a light microscope using tweezers. A piece of carbon tape, with the white peel left attached was used to avoid laser light directly hitting the thermocouple. 9 mm type I samples were then cut using a cork borer and placed faced down over a sample containing 40µl of sterile 0.85% (w/w) NaCl solution. The sample was then irradiated for 5 minutes using the laser set-up (as described above) and the temperature was measured using the thermocouple (Figure 4. 9) attached to a FLUKE 50S K/J thermometer. Different laser powers were used in the irradiation experiments to determine the effect of the laser power with the type I materials.

The laser power densities used in the experiments were as follows: 624 mW/cm<sup>2</sup> (700 mA), 881 mW/cm<sup>2</sup> (875 mA), 1174 mW/cm<sup>2</sup> (1075 mA), 1394 mW/cm<sup>2</sup> (1225 mA) and 1651 mW/cm<sup>2</sup> (1400 mA).

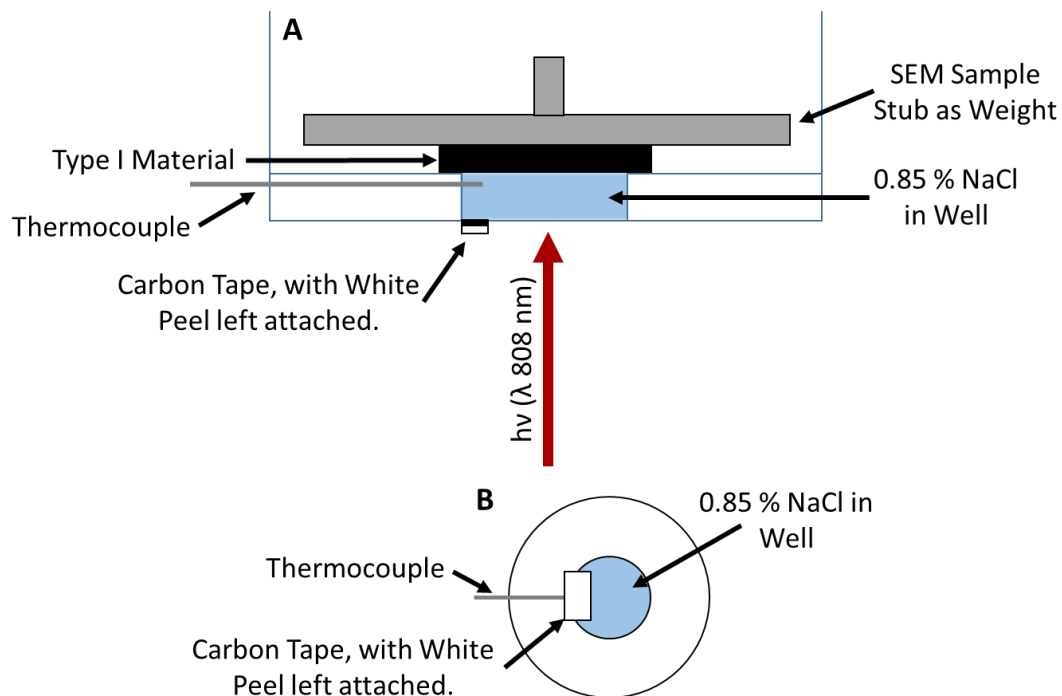


**Figure 4. 9** Schematic for the design of the sample well with thermocouple, for determining the temperature at the surface of the type I material during photothermal experiments. (A) side view, (B) underside view.

#### 4.2.4.3 Characterising the Antimicrobial Performance of Type I Materials after NIR Irradiation

**Preparation of bacterial cultures for antimicrobial testing:** *E. coli* (ATCC 10798) and *S. aureus* (ATCC 6538P) were transferred from frozen glycerol stock to a fresh nutrient agar plate and incubated overnight at 37°C. For the individual bacterial species, a minimum of three colonies were taken from the agar plates and transferred to fresh LB medium (Difco LB Broth Miller) and then grown overnight in a shaking incubator (200 rpm, 37°C) to a concentration of 10<sup>8</sup>- 10<sup>9</sup> colony forming units (CFUs) ml<sup>-1</sup>. The bacterial culture was subsequently diluted

with fresh LB media to a starting concentration of  $10^5$  CFUs  $\text{ml}^{-1}$  and used in the antimicrobial experiments.

**Viability of sessile bacteria on type I materials after NIR irradiation:** The viability of sessile bacteria after NIR irradiation was studied using confocal fluorescence microscopy. Type I materials were first cut using a 9 mm diameter cork borer and then placed in individual wells of a 24 well plate. The samples were then sterilised by UV irradiation on both sides for 30 minutes prior to addition of bacteria. 1ml of LB media, with individual bacterial species (*E. coli* (ATCC 10798) or *S. aureus* (ATCC 6538P)) of  $10^5$  CFU  $\text{ml}^{-1}$  were then added to the individual wells with the type I samples and incubated for 24hrs at  $37^\circ\text{C}$ . After 24hrs of incubation the planktonic suspension from each sample was removed and the samples were washed three times with 1 ml of sterile 0.85% (w/w) NaCl solution. 40 $\mu\text{l}$  of sterile 0.85% (w/w) NaCl solution was then added to a PDMS sample well for irradiation and a type I sample was placed face down over the well. The sample was then irradiated for 5 minutes using the laser set-up (as described above) and then placed back in the well plate with 0.85% (w/w) NaCl. Different laser powers were used in the irradiation experiments to determine the effect of the laser power with the type I materials. The laser power densities used in the experiments were as follows: 624  $\text{mW}/\text{cm}^2$  (700 mA), 881  $\text{mW}/\text{cm}^2$  (875 mA), 1174  $\text{mW}/\text{cm}^2$  (1075 mA), 1394  $\text{mW}/\text{cm}^2$  (1225 mA) and 1651  $\text{mW}/\text{cm}^2$  (1400 mA). Non-irradiated type I materials were used as controls. Following irradiation, the samples were then stained with a Live/dead BacLight bacterial viability kit (Molecular Probes, L7012) for confocal fluorescence imaging. The staining process consisted of the addition of 1 ml of sterile 0.85% (w/w) NaCl solution containing a mixture of 5  $\mu\text{M}$  SYTO 9 (green-fluorescent nucleic acid stain for live cells), and 30  $\mu\text{M}$  propidium iodide (red-fluorescent nucleic acid stain for dead cells). The samples were incubated in the dark for 15 minutes with the dyes and then immediately analysed in 0.85% (w/w) NaCl (as the immersion media) using a confocal upright Zeiss LSM 880 Multiphoton microscope. The collected confocal fluorescence images were processed using Fiji software.<sup>36</sup>

## 4.2.5 Heat Shock Experiments

### 4.2.5.1 Investigating the Temperature Profiles for Planktonic and Sessile Heat Shock Experiments

**Determining the temperature profile for planktonic heat shock experiments:** A hole was drilled into the top of a 1.5 ml tube and 900  $\mu$ l of 10 mM pH 7.4 Phosphate Buffer (PBS) was added. The tube was then heated to a required nominal temperature (50, 60, 70, 80 and 90°C) using a heat block and the heat block temperature was monitored using a glass thermometer. 100  $\mu$ l of PBS buffer (planktonic mimic) was then added to the heated solution in the heat block. A K type thermocouple was then thread through the hole of the 1.5 ml tube and the temperature was measured before the addition of 100  $\mu$ l of PBS and then every 30 seconds for 5 minutes after the addition of the 100  $\mu$ l PBS.

**Determining the temperature profile for the sessile heat shock experiments:** A hole was drilled into the top of a 2 ml tube and a 9 mm sample of the type I material was placed in the tube with 1 ml of sterile 0.85% (w/w) NaCl, with the active surface facing inwards towards the NaCl media. A separate 2 ml tube with 1 ml 0.85% (w/w) NaCl solution was then heated to a required nominal temperature (50, 60, 70, 80 and 90°C) using a heat block and the heat block temperature was monitored using a glass thermometer. The NaCl in the tube with the type I material was then removed and the heated NaCl was transferred to the tube with the type I material. A K type thermocouple was thread through the hole of the 1.5 ml tube and held close to the surface of the type I material. The temperature was measured before the removal of NaCl from the heated tube and then after transferring the heated NaCl to the tube with the type I sample. The temperature was measured every 30 seconds for 5 minutes after the addition of the heated NaCl to the type I sample. A further temperature measured was also collected after 10 minutes.

#### 4.2.5.2 Assessing the Viability of Planktonic and Sessile Bacteria after Heat Shock Treatment

**Viability of planktonic bacteria after heat shock treatment:** The planktonic media from the samples used in the sessile heat shock experiment were collected into a 1.5 ml tube, as previously discussed. A separate 1.5 ml tube of 900  $\mu$ l 10 mM pH 7.4 Phosphate Buffer (PBS) was then heated to a required nominal temperature (50, 60, 70, 80 and 90°C) using a heat block and then 100  $\mu$ l of planktonic media was added to the heated solution in the heat block. The tube was then left for a further 5 minutes in the heat block and the sample was collected. The sample was then serial diluted using 10 mM pH 7.4 PBS and plated on fresh nutrient agar using the Miles and Misra method.<sup>37</sup> The agar plates were then incubated overnight at 37°C and the CFUs were counted.

**Viability of sessile bacteria on type I materials after heat shock treatment:** The viability of sessile bacteria after heat shock treatment was studied using confocal fluorescence microscopy. Type I materials were prepared and incubated with individual bacterial species (*E. coli* (ATCC 10798) or *S. aureus* (ATCC 6538P)) according to the photothermal experiments. After 24hrs of incubation, the planktonic suspension was removed and kept in a 1.5 ml tube for planktonic heat shock experiments. The type I samples were then washed three times with 1 ml of sterile 0.85% (w/w) NaCl solution and placed carefully into a 2 ml tube with 1 ml of sterile 0.85% (w/w) NaCl, with the active surface facing inwards towards the NaCl media. A separate 2 ml tube with 1 ml 0.85% (w/w) NaCl solution was heated to a required temperature using a heat block. The NaCl in the tube with the type I material was then removed and the heated NaCl was transferred to the tube with the type I material. This was then placed in the heat block for 5 minutes, subsequently removed and transferred to a well of a 24 well plate with 1ml of fresh 0.85% (w/w) NaCl. The nominal temperatures used in the heat shock treatment were 50, 60, 70, 80 and 90°C. Following heat shock treatment, the samples were

then stained with a Live/dead BacLight bacterial viability kit (Molecular Probes, L7012) and imaged using confocal fluorescence microscopy, according to the photothermal experiment discussed above.

#### 4.2.6 Preparation of Type II materials for Photothermal Drug Delivery

**Preparation of type II materials by loading type I materials with dodecanoic acid:** Dodecanoic acid was melted in a glass jar at 50°C forming a viscous liquid. Type I materials were then swelled with dodecanoic acid by placing the type I materials in individual wells of a 6-well plate and covering them with 3 ml of melted dodecanoic acid. The wells were covered with a lid, sealed with black PVC insulation tape, and placed in the oven at 50°C, overnight for a minimum of 16 hrs. After swelling the type I materials overnight, the samples in the well plate were placed immediately in the freezer, causing the dodecanoic acid to solidify. Once the dodecanoic acid had solidified, the well plates were taken out of the freezer and the now type II materials were removed. To remove the type II materials from the dodecanoic acid in the wells, the unincorporated solidified dodecanoic acid had to be broken with tweezers and the type II samples removed. The type II materials were then washed quickly with ethanol and dried with compressed air to remove unincorporated dodecanoic acid. The samples were then weighed to determine the amount of loaded fatty acid material.

#### 4.2.7 Characterisation of Type II Materials

The type II material was characterised using ATR-IR, gravimetric analysis and static contact angle measurements. ATR-IR was used to confirm the presence of dodecanoic acid in the material, along with qualitatively investigating the release of dodecanoic acid at the surface of the material, after photothermal experiments. Gravimetric analysis was used to quantitatively

investigate the release of dodecanoic acid during photothermal experiments. Static contact angle measurements were used to determine the wettability of type II material.

**Confirming the presence of dodecanoic acid in the Type II material by ATR-IR:** To confirm the presence of dodecanoic acid in the type II material, a 9 mm diameter sample was cut from the material using a cork borer and then ATR-IR measurements were carried out according to the above ATR-IR experiment performed with type I materials.

**Quantifying the release of dodecanoic acid from type II materials during photothermal experiments:** A batch of 10 pre-cut 9 mm samples of the type II material were collectively weighed twice before and after irradiation at  $881 \text{ mW/cm}^2$ . Samples were irradiated for 5 minutes according to the photothermal experiments with the type II material, however using LB media in the sample well. After irradiation, the samples were washed quickly with ethanol and then dried with compressed air. A total of 3 replicates were carried out to determine the average release of dodecanoic acid from the type II material. Gravimetric measurements were carried out using an AND HR-100AZ analytical balance.

**ATR-IR measurements for the release of dodecanoic acid at the surface of the type II material, following photothermal experiments:** A 9 mm diameter sample of the Type II material was cut using a cork borer and then placed face down above a transparent well with  $40 \mu\text{l}$  of LB media. The well with sample was then placed on the sample stage of the laser-set up and irradiated with a power of  $881 \text{ mW/cm}^2$  (875 mA) for 5 mins. After irradiation, the sample was then removed from the sample well and analysed according to the above ATR-IR experiment.

**Static contact angle measurements on type II materials:** After impregnation of the type I material with dodecanoic acid to form the type II material, the wettability of the sample was measured using static contact angle measurements using 0.85% NaCl. Contact angle measurements were measured using a First Ten Ångstroms (FTA) 1000 instrument with a Gilmont GS-1201 micrometer dispenser syringe via the sessile drop method. Contact angle images were collected with a frame rate of 60 frames/ s. Contact angle data was then processed using FTA 32 drop shape analysis software (Version 2). The average contact angle of the type II samples was determined from 30 images per drop, for 3 drops on 3 different sample replicates using a non-spherical fit. The contact angle of pristine PDMS and of the type I material were also measured.

#### 4.2.8 Characterising the Antimicrobial Performance of Type II Materials

**Viability of sessile bacteria on type II materials after NIR irradiation:** Type II materials were cut using a 9 mm cork borer and then placed in a 6 well plate with a PDMS frame (see chapter 3 for fabrication of PDMS frames) to prevent the samples from floating. The samples were then sterilised on both sides by UV irradiation for 30 minutes prior to the addition of bacteria. The samples were then seeded with 10 ml of individual bacterial species (*E. coli* ATCC 10798 or *S. aureus* ATCC 6538P) at starting concentration of  $10^8$ -  $10^9$  CFUs ml<sup>-1</sup> in LB media and incubated at room temperature (25°C) for 24 hrs, to limit the release of the dodecanoic acid from the type II materials. After 24hrs of incubation, the samples were washed three times with 10 ml of sterile 0.85% (w/w) NaCl solution. The samples were then irradiated according to the photothermal experiments at 881 mW/cm<sup>2</sup> (875 mA) for 5 mins and then placed in a well of a 24 well plate with 1 ml sterile 0.85% (w/w) NaCl solution. Following the photothermal experiment, the samples were stained with a Live/dead BacLight bacterial

viability kit (Molecular Probes, L7012) and imaged using confocal fluorescence microscopy, according to the photothermal experiment for type I materials discussed above.

**Viability of planktonic bacteria with type II material after NIR irradiation:** Individual bacterial species (*E. coli* (ATCC 10798) or *S. aureus* (ATCC 6538P)) were grown in LB media overnight to a conc. of  $10^8 - 10^9$  CFUs ml<sup>-1</sup> at 37°C in a shaking incubator (200 rpm), and then 40 µl of this was added to an irradiation sample well at room temperature. A 9 mm diameter sample of type II material was then placed face down over the well and irradiated at 881 mW/cm<sup>2</sup> (875 mA) for 5 mins. The sample was then removed after a further 5 mins and 20 µl of the planktonic suspension in the sample well was collected, serial diluted with 10 mM pH 7.4 PBS and plated on fresh nutrient agar plates using the Miles and Misra method.<sup>37</sup> The agar plates were then incubated overnight at 37°C and the CFUs were counted. Selective agar was used for plating in these experiments, to minimise environmental contamination, due to the non-sterile conditions of the laser set-up. MacConkey agar was used for plating *E. coli* and Mannitol agar was used for plating *S. aureus*. The growth of *S. aureus* on Mannitol agar was slow and took 2 days of incubation prior to counting CFUs.

## 4.3 Results and Discussion

### 4.3.1 Fabrication and Characterisation of Type I Materials

The fabrication of type I materials was carried out using Sylgard 184 silicone elastomer and carbon nanopowder (CNP) (Figure 4. 10) to form a black organosilane based polymeric material after the curing process. As a result, an average sample mass of 0.9852g ( $\pm$  0.0198g), with a sample thickness of 0.8 mm was achieved after curing. No further chemical modifications of the type I material were carried out following the curing process. The type I material exhibited a saturated absorbance spectrum, with a broad light-absorption range, including the NIR region (700-1100 nm) (Figure 4. 11).

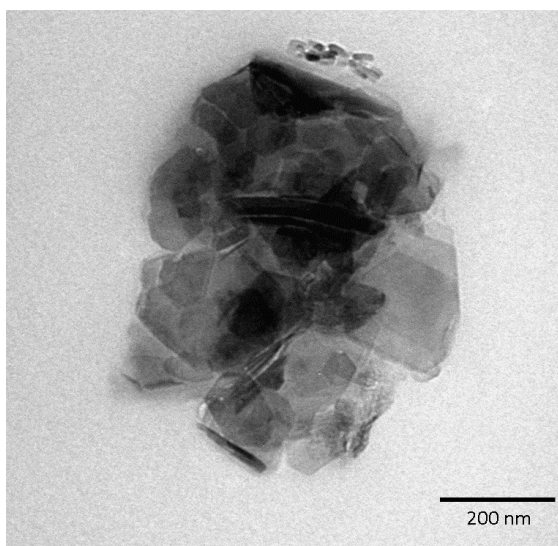


**Figure 4. 10** TEM image of carbon nanopowder (CNP). (Scale bar is 200 nm)

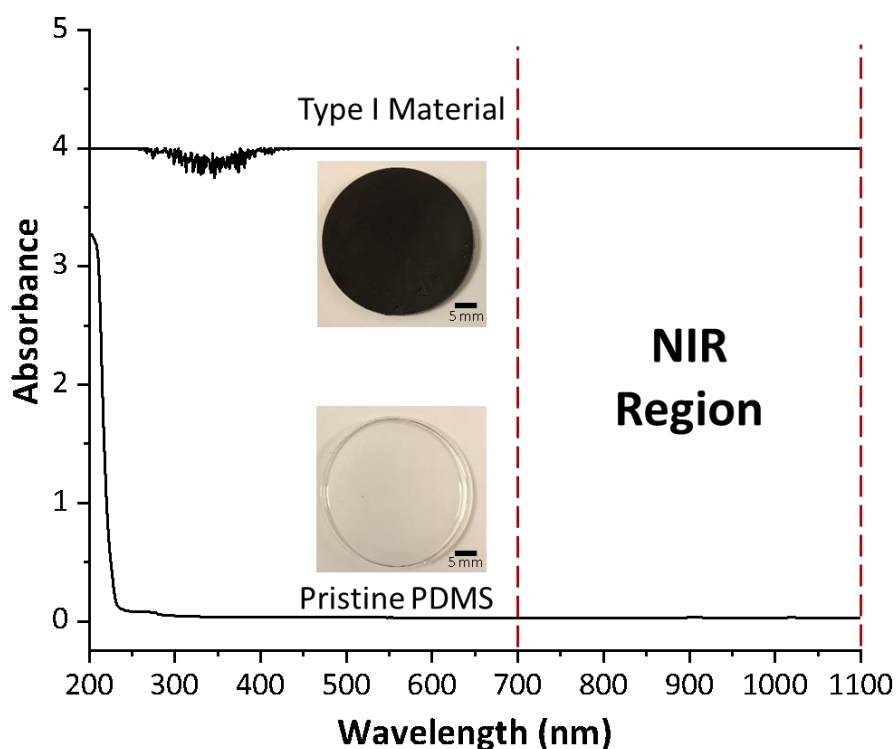


**Figure 4. 11** Absorbance spectrum of pristine PDMS and type I material (air used as baseline). Path length is equal to sample thickness (approx. 0.8 mm). Inserts show the pristine PDMS and type I materials after fabrication (Scale bars are 5 mm).

The distribution of CNP across the surface of the type I material was investigated using Raman spectroscopy. The raw starting materials (PDMS and CNP) were first characterised by Raman spectroscopy (Figure 4. 12), and then used as a reference in further Raman experiments for investigating the distribution of CNP across the surface of the type I material. Pristine PDMS was identified by the characteristic Raman peaks, such as Si-O-Si Stretch ( $619\text{ cm}^{-1}$ ), Si-CH<sub>3</sub> symmetrical stretch ( $712\text{ cm}^{-1}$ ) and CH<sub>3</sub> symmetrical bend ( $1265\text{ cm}^{-1}$ ) (Figure 4. 12).<sup>38</sup> The raw CNP gave two characteristic peaks associated to sp<sup>2</sup> hybridised carbon, known as the G band ( $1564\text{ cm}^{-1}$ ) and D band ( $1340\text{ cm}^{-1}$ ) vibration modes. The G Band vibration mode is assigned to the in-plane stretching vibration of sp<sup>2</sup> carbon (Figure 4. 12), while the D band vibration mode is assigned to a lattice breathing mode (Figure 4. 12).<sup>39</sup> A broad peak around  $800\text{ cm}^{-1}$  was also observed for the CNP (Figure 4. 12). This peak has been previously observed in literature in the Raman spectra of graphite, although this peak does not appear in Raman spectroscopic analysis of graphene.<sup>40</sup> This suggests this peak is most likely associated to

disorder in the graphitic material or may be associated with atoms of carbon in more than one plane.

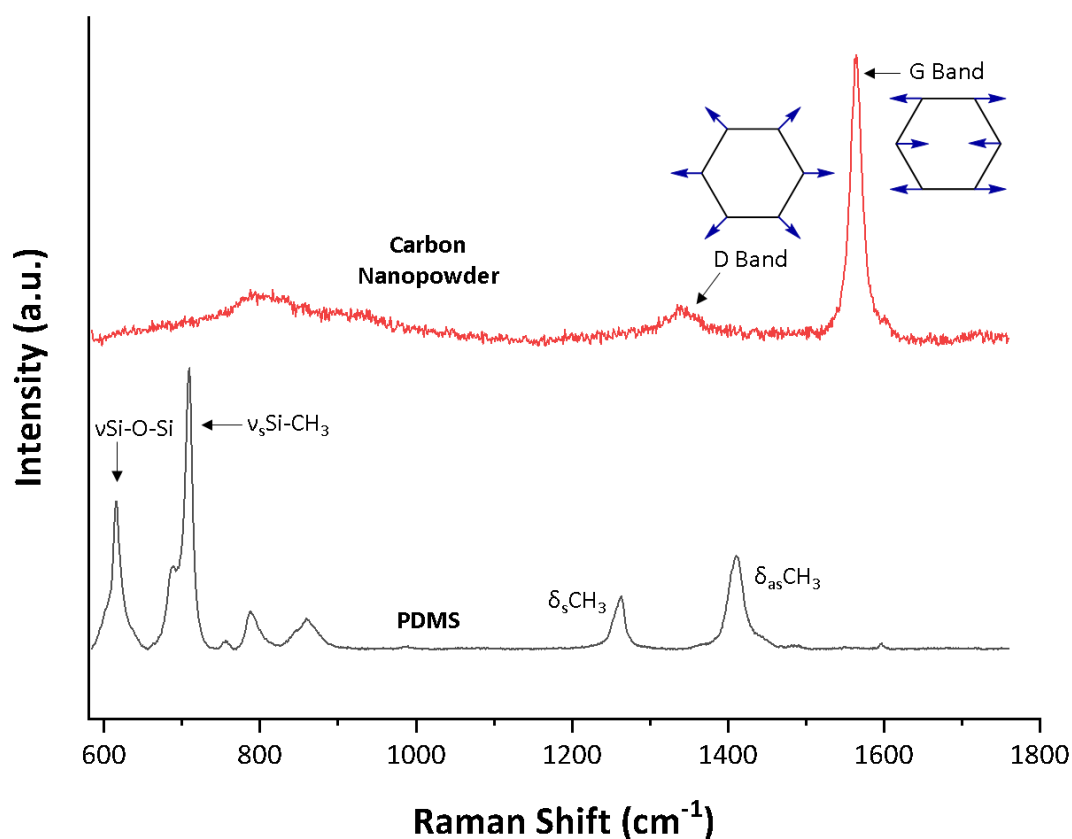


**Figure 4. 12** Raman spectra of raw materials used to fabricate type I materials. Black is PDMS and Red is **CNP**. Inserts show the vibration modes associated with the D and G bands of the CNP.

When combining PDMS with CNP to form the type I material, the characteristic peaks associated with PDMS remain unchanged, with additional peaks arising, associated with the D and G bands of the CNP (Figure 4. 12). Interestingly, both D and G band peaks present in the type I material were shifted in comparison to the raw CNP material ( $1340\text{ cm}^{-1}$  to  $1350\text{ cm}^{-1}$ , and  $1564\text{ cm}^{-1}$  to  $1580\text{ cm}^{-1}$ ). The shift in the D and G band vibration modes may be attributed to compressive strain on the carbon bonds of the graphitic CNP, when embedded into the PDMS material. <sup>41</sup>

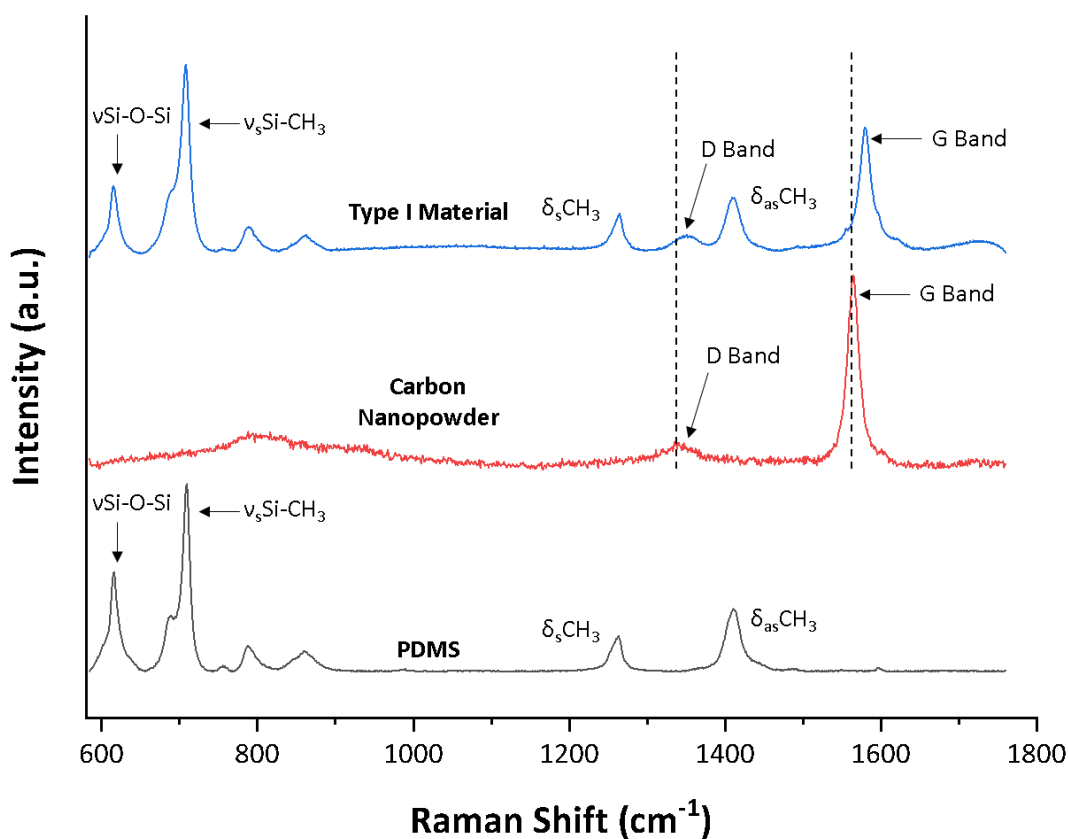


**Figure 4. 13** Raman spectra of raw materials and type I material. Black is PDMS, Red is CNP and Blue is the Type I material. Dashed lines show the shift in the D and G bands of CNP when incorporated into the type I material.

After obtaining data from the Raman analysis of the raw materials, the distribution of CNP across the surface of the type I material was investigated, using map acquisition mode, with a signal to baseline analysis between 1550 and 1605  $\text{cm}^{-1}$ , associated with the G band vibration mode of the CNP. Unlike in chapter 3, a DCLS component fit analysis could not be used here, due to the shift of the D and G bands in the type I material, and therefore signal to baseline mapping was implemented. As a result of these experiments, a scattered distribution for CNP across the surface of the type I material was observed (Figure 4. 14). The map data for the surface analysis was normalised and zero centred to gain a statistical view for the distribution of CNP across the surface of the type I material (Figure 4. 14 C). As a result, we observe a normal distribution (Figure 4. 14 C), despite the local inhomogeneity in the map, which can be associated with a random distribution of CNP across the sample, which proved to be

consistent between different samples (see appendix, Figure A4. 2). This suggests the fabrication method for type I materials is reproducible.

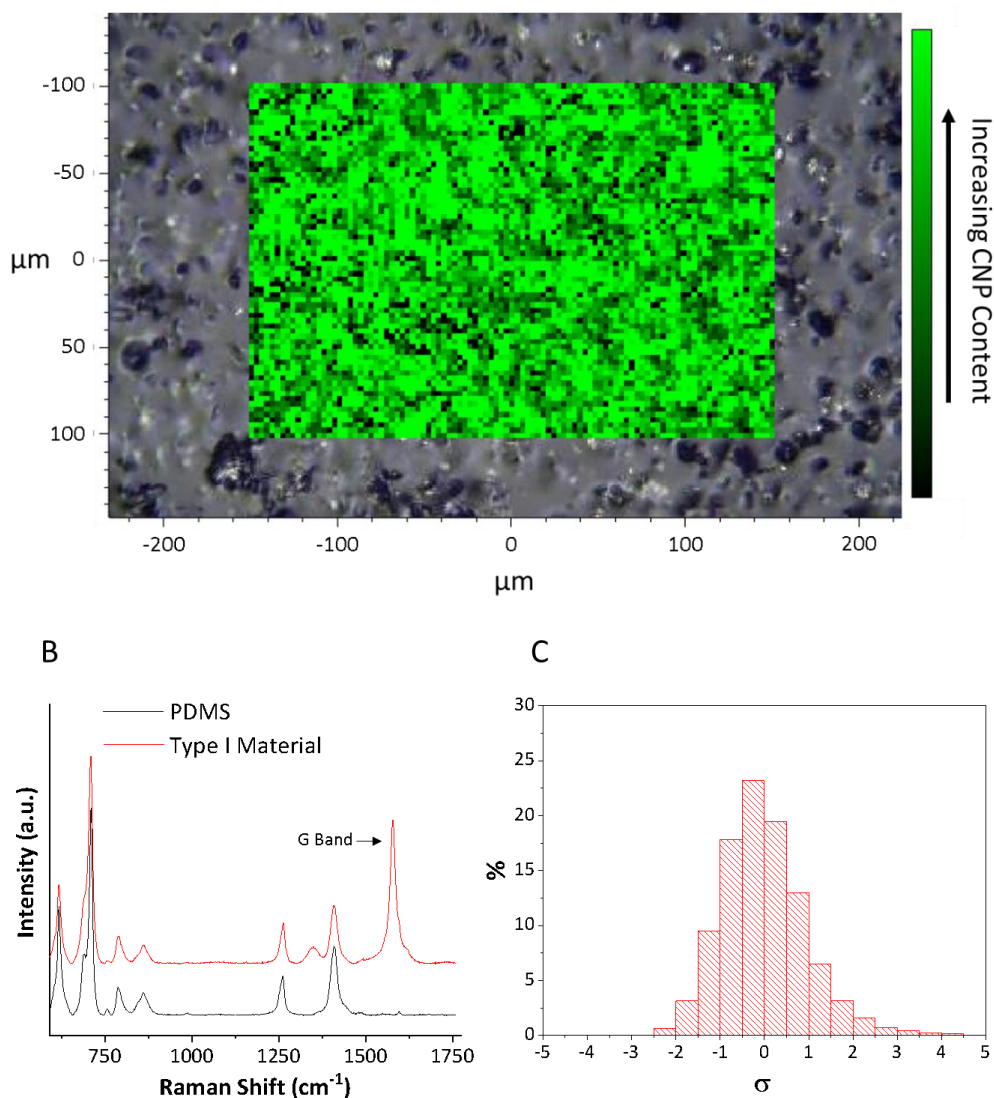


**Figure 4. 14** (A) Representative Raman map for the distribution of CNP across the surface of type I material, (B) Raman spectrum of PDMS (Black) and averaged Raman spectrum of the type I material (Red), (C) Representative normalised histogram showing the distribution of CNP across the surface of the type I material.

We also analysed the type I material by ATR-IR spectroscopy (see appendix, Figure A4. 3). As a result of these experiments, no additional peaks associated with the CNP were observed, other than the characteristic peaks associated with PDMS, such as Si-CH<sub>3</sub> stretching (788 cm<sup>-1</sup>), Si-O-Si stretching (1010 cm<sup>-1</sup>) and CH<sub>3</sub> stretching (2962 cm<sup>-1</sup>) (see appendix, Figure A4. 2).<sup>38</sup> According to literature, it has been reported that graphitic type materials, such as graphene

and carbon black are infrared inactive, hence they do not exhibit features in ATR-IR spectroscopy.<sup>42,43</sup>

## 4.3.2 Photothermal Experiments

### 4.3.2.1 Designing the Photothermal Experiment

After completing the characterisation of the type I material, we performed the photothermal experiments for antimicrobial testing of the type I material under NIR irradiation. A continuous wave laser set-up was used for the photothermal experiments, at a wavelength of 808 nm (Figure 4. 8), with the laser light irradiating the sample from below (Figure 4. 7 and 8). By irradiating the sample from below we minimised convection forces, associated with the gradient of temperature and density of water (Figure 4. 15). Therefore, the heat generated by the type I material under NIR irradiation will remain predominantly at the surface (Figure 4. 8).

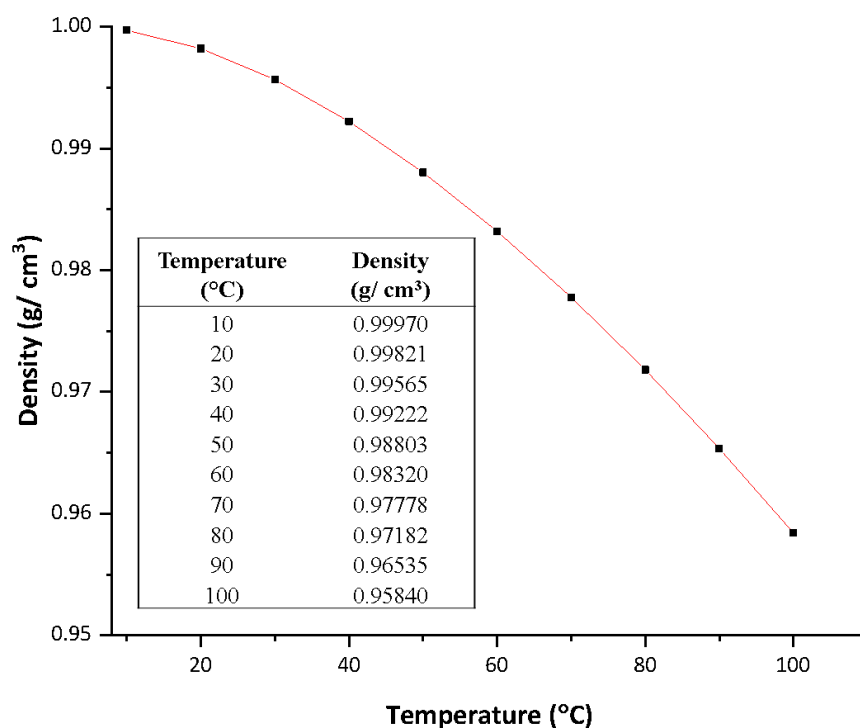


**Figure 4. 15** Graph showing the density of water (H<sub>2</sub>O) as a function of temperature, in a range of 10°C to 100 °C at 1 ATM (atmospheric pressure). Insert shows a table for density values of water at temperatures in the range of 10°C to 100 °C.<sup>44</sup>

The power output of the laser set-up at the aperture of the sample stage was measured using a thermal power sensor (Thorlabs S302C) and the laser power densities (Figure 4. 16) were determined according to the diameter of the aperture in the sample stage (7 mm). The measured laser power densities from the laser set-up were then used for the photothermal experiments with the type I material.

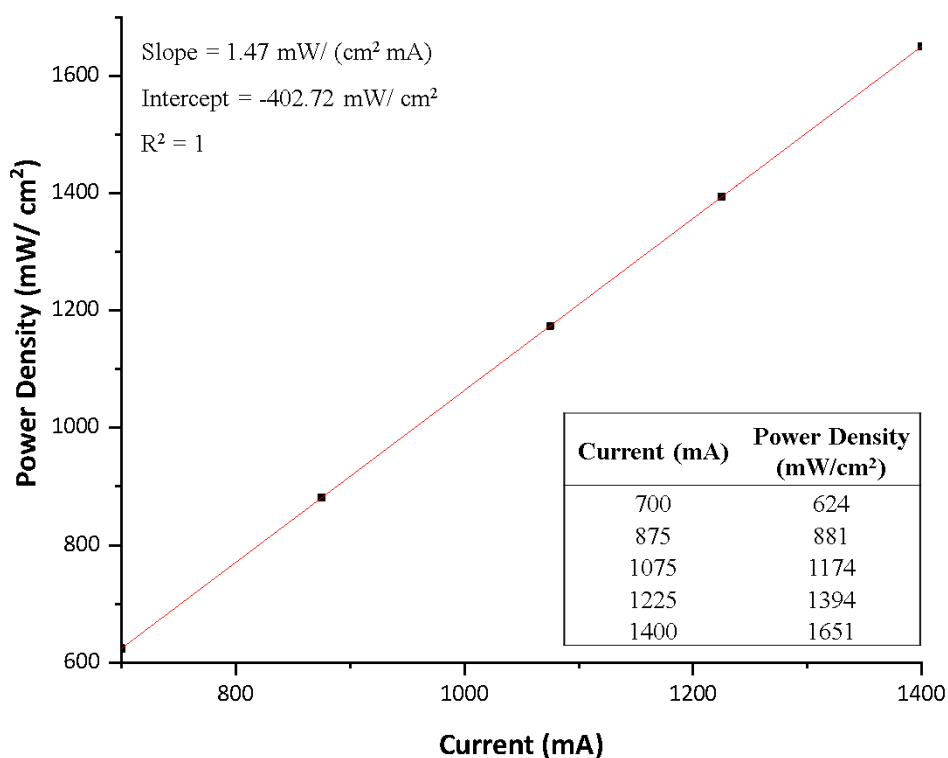


**Figure 4. 16** Graph showing laser power density (mW/ cm<sup>2</sup>) as a function of current (mA) measured at the sample stage for the continuous wave laser set-up. Insert shows a table of the measured values.

#### 4.3.2.2 Investigating the Photothermal Effect of Type I Materials

To investigate the photothermal effect of the type I material under NIR irradiation, we determined the temperature close to the surface of the type I material during photothermal experiments. We used a sample well, modified with the addition of a K type thermocouple (Figure 4. 8) to monitor the increase in temperature during NIR irradiation of the type I material. The thermograms showed an increase in temperature over time, reaching a stationary phase after 200s (Figure 4. 18 and see appendix, Table A4.1). A maximum stationary

temperature of  $69.5^{\circ}\text{C} \pm 1.5^{\circ}\text{C}$  was observed at the maximum laser power density investigated ( $1651 \text{ mW}/\text{cm}^2$ ).

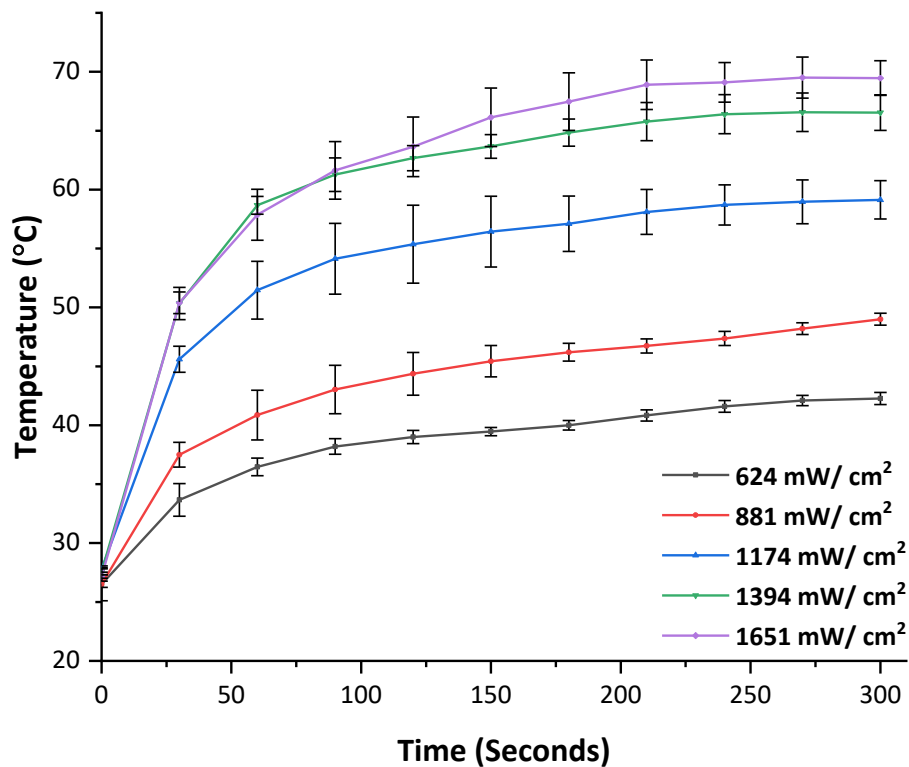


**Figure 4. 17** Thermograms for the type I material during photothermal experiments, measured using a K type thermocouple.

Qualitatively, similar trends for the temperature increase were observed for all the laser power densities investigated (Figures 4. 17 and 4. 18). The temperature initially increases and eventually reaches a plateau (Figure 4. 17), resulting in stationary conditions. We can therefore assume that the photothermal conversion of light to heat is equal to the heat dissipation from the surface of the type I material and can be rationalised by equation 4.1, related to the Stefan-Boltzman law (see appendix, Equation A4. 1).<sup>45</sup>

$$j_{Generated} = \Delta j_{Emitted}$$

**Equation 4. 1**

Where  $j_{Generated}$  represents the heat generated by the surface of the type I material under NIR irradiation and is equal to the incident density power ( $P_{w_{incident}}/\text{Area}$ ) multiplied by a proportionality constant ( $\alpha$ ), shown in equation 4.2.

$$j_{Generated} = \frac{\alpha \cdot Pw_{Incident}}{Area} = \alpha \cdot j_{Incident}$$

**Equation 4. 2**

The proportionality constant ( $\alpha$ ) depends on other physical properties of the photothermal system, such as percentage of absorbing component (CNP) at the surface of the type I material and the loss of heat dissipated outside of the photothermal set-up (e.g. heat dissipated into the PDMS of the type I material (see appendix, Figure A4.4)).

The Stefan-Boltzmann law states that the total energy radiated per unit surface area of a black body across all wavelengths is directly proportional to the fourth power of the black body's thermodynamic temperature (see appendix, Equation A4. 1)<sup>45</sup>. We can therefore assume that the heat generated ( $j_{Generated}$ ) by the type I material is directly proportional to the heat emitted ( $\Delta j_{Emitted}$ ) by the type I material, as seen in equation 4. 1 and can be expressed as follows:

$$\Delta j_{Emitted} = 4\sigma T_0^3 \Delta T$$

**Equation 4. 3**

Where  $\sigma$  is the Stefan-Boltzmann constant,  $T_0$  is the starting temperature and  $\Delta T$  is the difference in temperature with respect to the surrounding environment. The linear relationship represented by equation 4.3 can be observed in figures 4. 18 and see appendix, A4. 5.

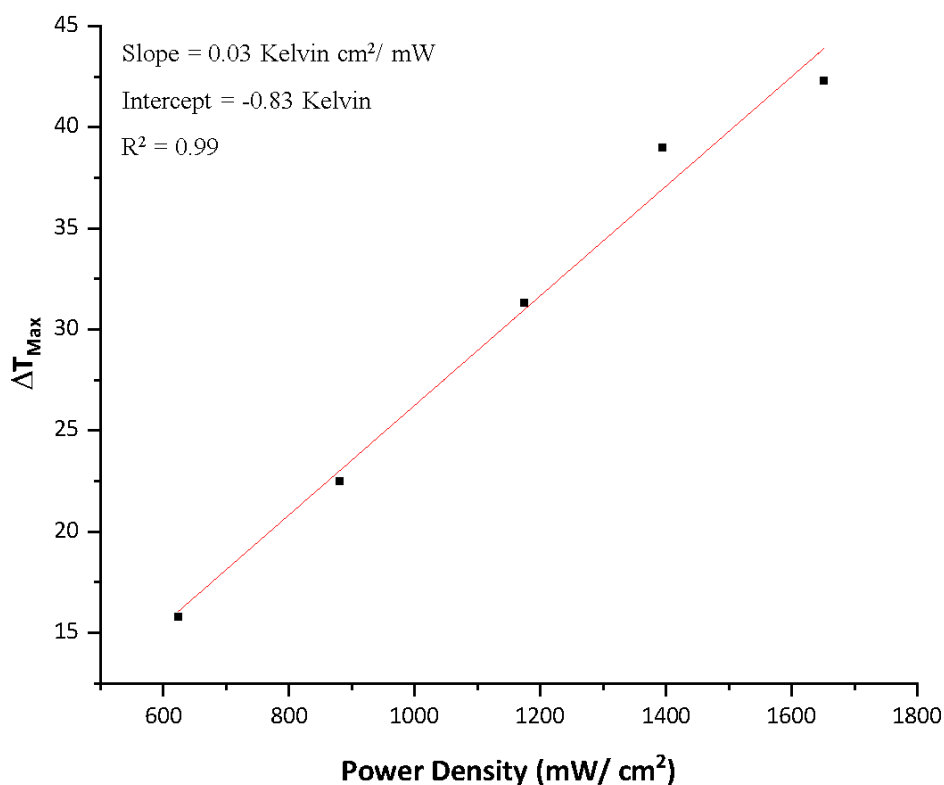


**Figure 4. 18** Graph showing the linear relationship between power density (mW/ cm<sup>2</sup>) and the temperature at stationary conditions ( $\Delta T_{\text{Max}}$ ) measured with the thermocouple during photothermal experiments with the type I material.

#### 4.3.3.3 Characterising the Antimicrobial Performance of Type I Materials after NIR Irradiation

After investigating the photothermal effect of the type I material under NIR irradiation, the antimicrobial performance of the type I material was tested against both *E. coli* (ATCC 10798) and *S. aureus* (ATCC 6538P) bacteria. In these experiments, 9 mm diameter samples of type I material and PDMS controls were incubated for 24 hrs with individual bacterial species at 37°C, with a starting concentration of 10<sup>5</sup> CFUs ml<sup>-1</sup>. After incubation, the samples were washed three times with 0.85% (w/w) NaCl and then irradiated with an 808 nm laser under physiological buffer for 5 mins (Figure 4. 7 and 8). Different laser power densities, ranging from 624 mW/cm<sup>2</sup> to 1651 mW/cm<sup>2</sup> (Figure 4. 16) were used to observe the effect of the laser power densities on the type I material after photothermal treatment. After irradiation, the

samples were imaged using confocal fluorescence microscopy (CFM) with Live/ dead staining.

In the CFM images (Figure 4. 19) of *E. coli*, we observed an increase in the fraction of dead bacteria at the surface of the type I material, following irradiation with increasingly higher laser power densities. This can be associated with the increase in temperature at the surface of type I material, with increasingly laser power density, as seen in figure 4. 18. The increase in the fraction of dead *E. coli* cells was first observed at a laser power of 881 mW/ cm<sup>2</sup>, with a fraction of 17.72% ± 3.5% dead cells (Figure 4. 19 and 21) and at the maximum laser power density investigated (1651 mW/ cm<sup>2</sup>), a fraction of 65.54% ± 4.86% dead *E. coli* cells was observed (Figure 4. 19 and 21). Interestingly, at laser powers 1394 mW/ cm<sup>2</sup> and 1651 mW/ cm<sup>2</sup> the fraction of dead bacteria cells are within standard deviation of each other (Figure 4. 19), suggesting a similar antimicrobial activity due to the photothermal effect at the surface of the type I material at these high laser power densities.

Similarly, for CFM images of *S. aureus* bacteria (Figure 4. 20), we observed an increase in the fraction of dead bacteria cells as the laser power density was increased. However, compared to *E. coli* (Figure 4. 19 and 21), *S. aureus* proved to be initially more resistant to photothermal treatment (Figure 4. 20 and 22), as the first increase in the fraction of dead cells was observed at a higher laser power density (1174 mW/ cm<sup>2</sup>, with a fraction of 62.48% ± 5.32%), suggesting the transition from live to dead bacteria, lies between 881 mW/cm<sup>2</sup> and 1174 mW/cm<sup>2</sup>. At maximum laser power (1651 mW/ cm<sup>2</sup>), a fraction of 79.48% ± 3.49% dead cells were observed. Unlike with *E. coli* (Figure 4. 19 and 21), for *S. aureus*, a significant difference in the fraction of dead bacteria cells was observed for both 1394 mW/ cm<sup>2</sup> and 1651 mW/ cm<sup>2</sup> laser power densities (Figure 4. 20 and 22), suggesting we did not reach a plateau at the higher laser power densities investigated.

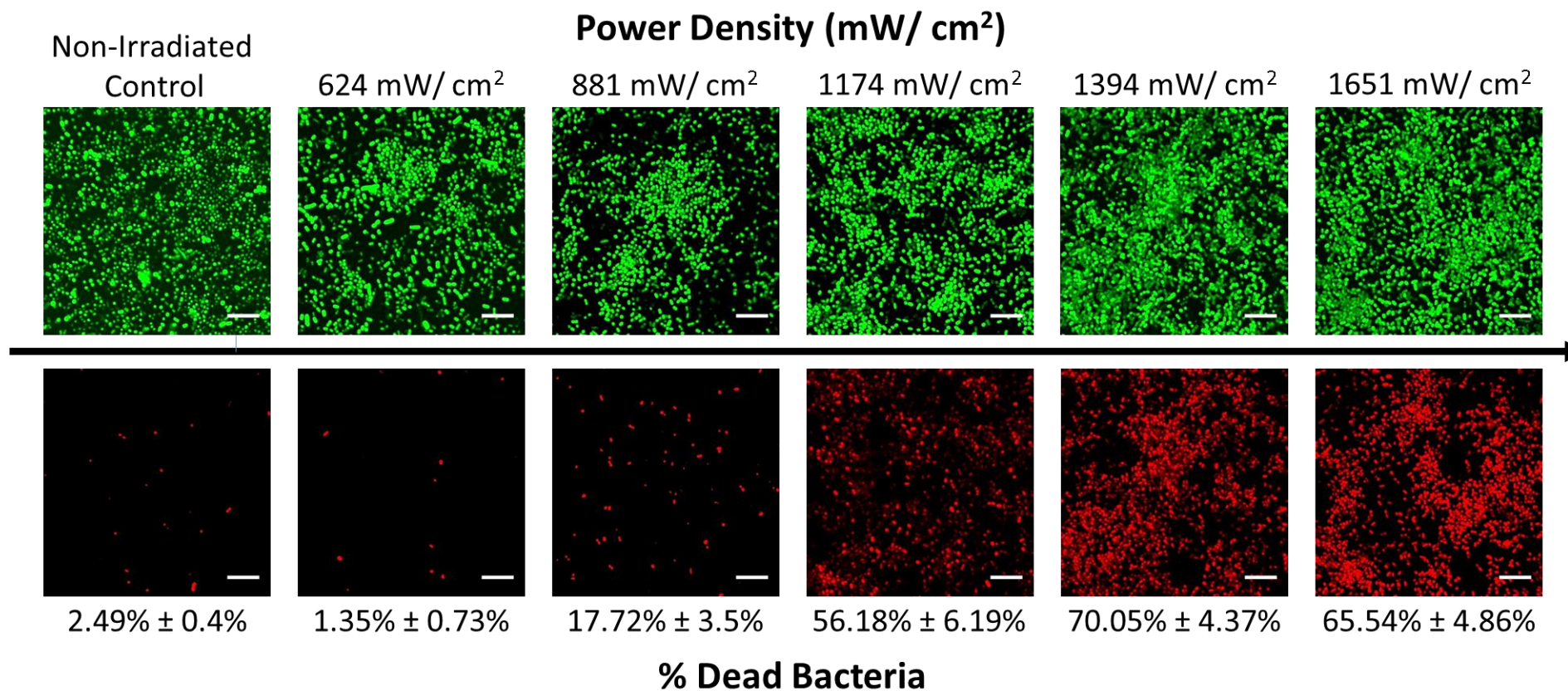


**Figure 4. 19** Confocal fluorescence microscopy images of *E. coli* (ATCC 10798) on type I materials showing percentage of dead bacteria, after 5 mins irradiation under physiological conditions, at 808 nm wavelength using different laser power densities. Bacteria imaged using Live/dead viability kit. (Green: All bacteria), (Red: Dead bacteria). (Scale bars are 10 μm).

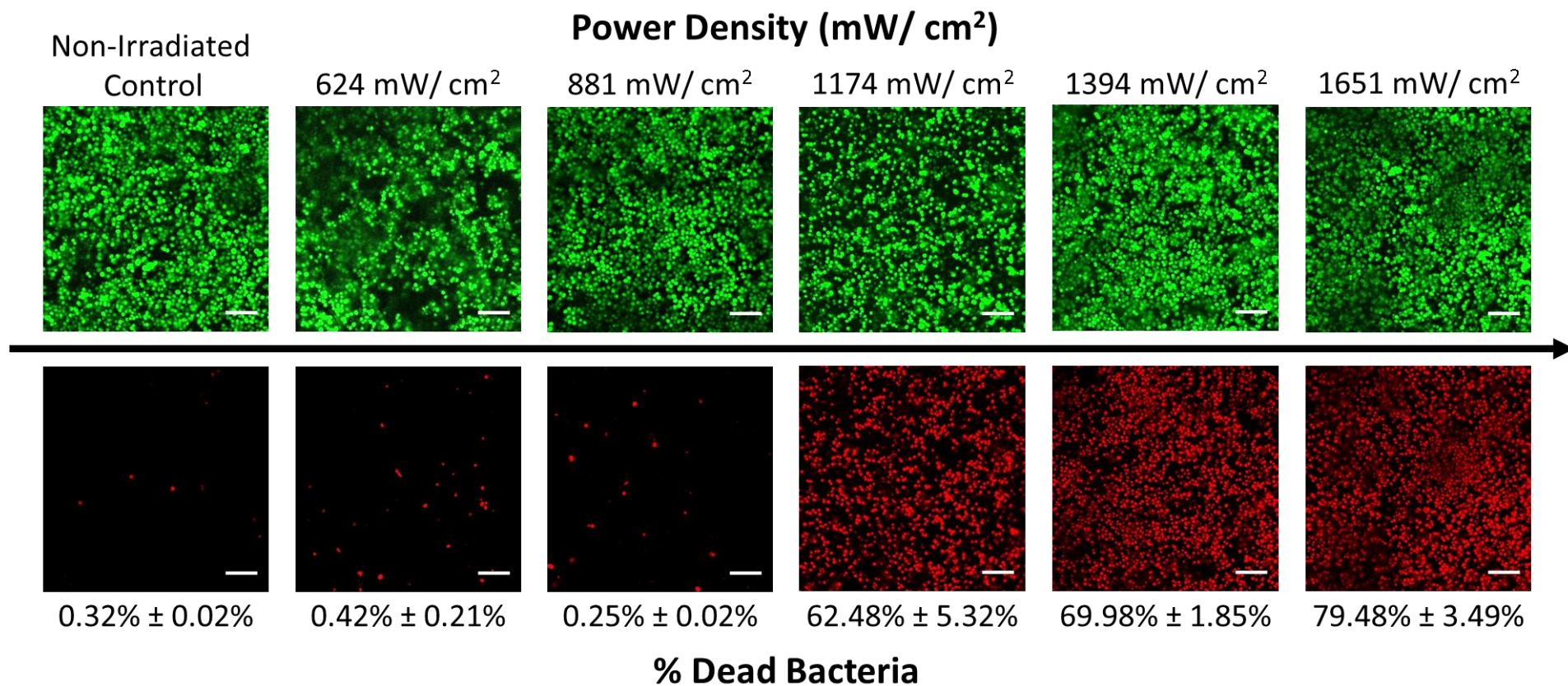


**Figure 4. 20** Confocal fluorescence microscopy images of *S. aureus* (ATCC 6538P) on type I material showing percentage of dead bacteria, after 5 mins irradiation under physiological conditions at 808 nm wavelength using different laser power densities. Bacteria imaged using Live/dead viability kit. (Green: All bacteria), (Red: Dead bacteria). (Scale bars are 10 μm).

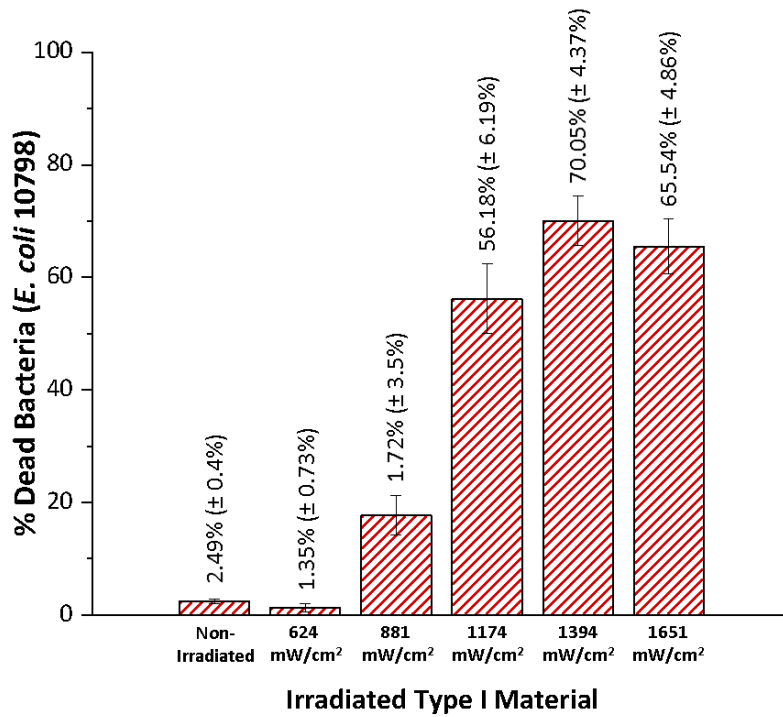


**Figure 4. 21** Bar Chart showing summary of the CFM data with Live/ Dead staining for *E. coli* 10798 on non-irradiated and irradiated type I materials.

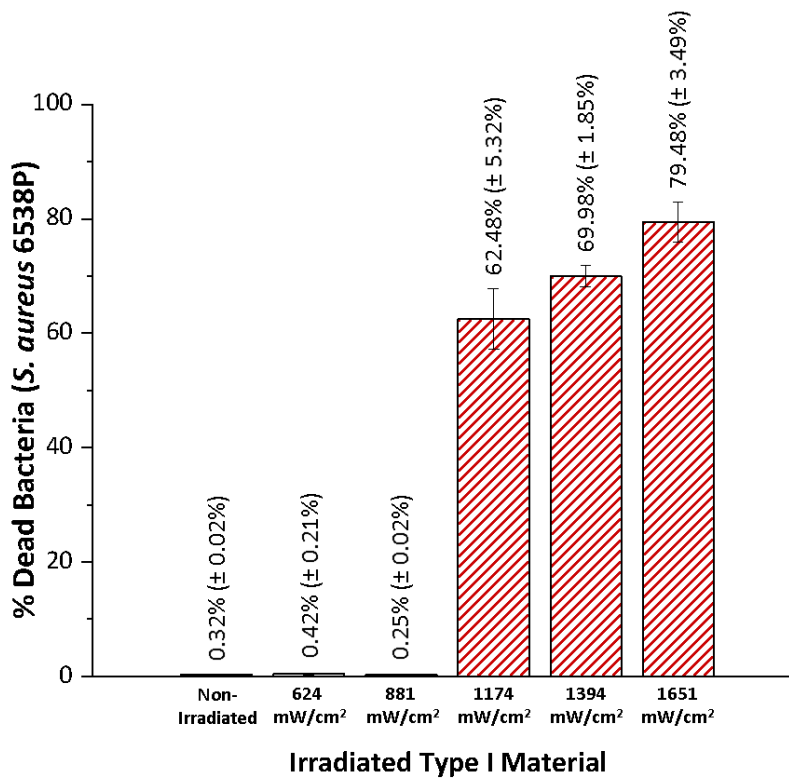


**Figure 4. 22** Bar Chart showing summary of the CFM data with Live/ Dead staining for *S. aureus* 6538P on non-irradiated and irradiated type I materials.

Photothermal experiments on the transparent PDMS controls were tested at the maximum laser power density investigated ( $1651 \text{ mW/ cm}^2$ ), to confirm the photothermal effect of the type I material for both bacteria types (*E. coli* and *S. aureus*). As a result, a low fraction of dead bacteria was observed for both *E. coli* and *S. aureus* bacteria (Figure 4. 23 and 24).

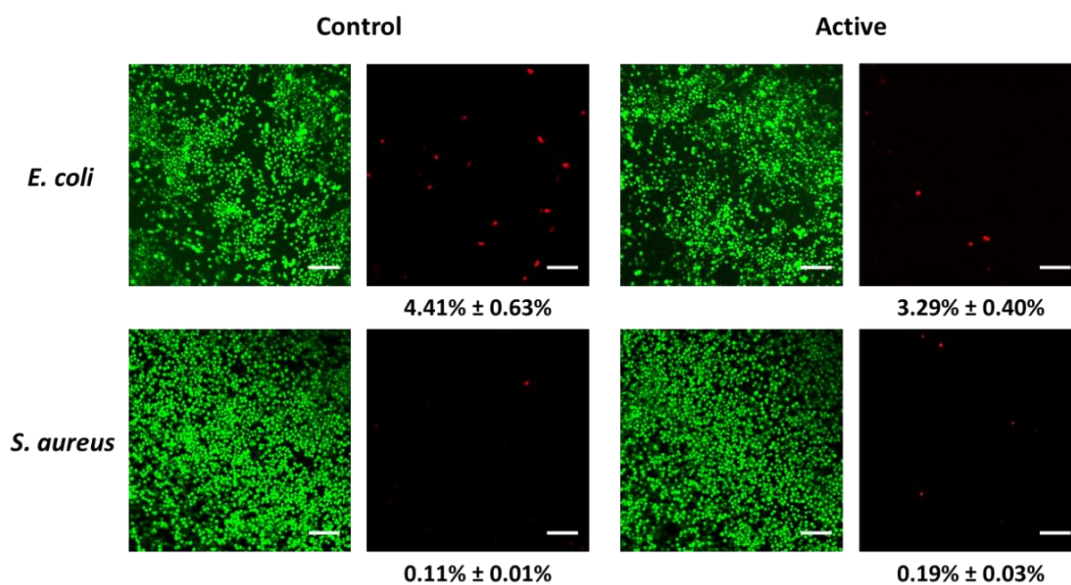


**Figure 4. 23** Confocal fluorescence microscopy images of *E. coli* (ATCC 10798) and *S. aureus* (ATCC 6538P) on transparent PDMS showing percentage of dead bacteria, after 5 mins irradiation under physiological conditions, at 808 nm wavelength with a laser power of  $1651 \text{ mW/ cm}^2$ . Non-irradiated transparent PDMS shown as control. Bacteria imaged using Live/dead viability kit. (Green: All bacteria), (Red: Dead bacteria). (Scale bars are  $10 \mu\text{m}$ ).

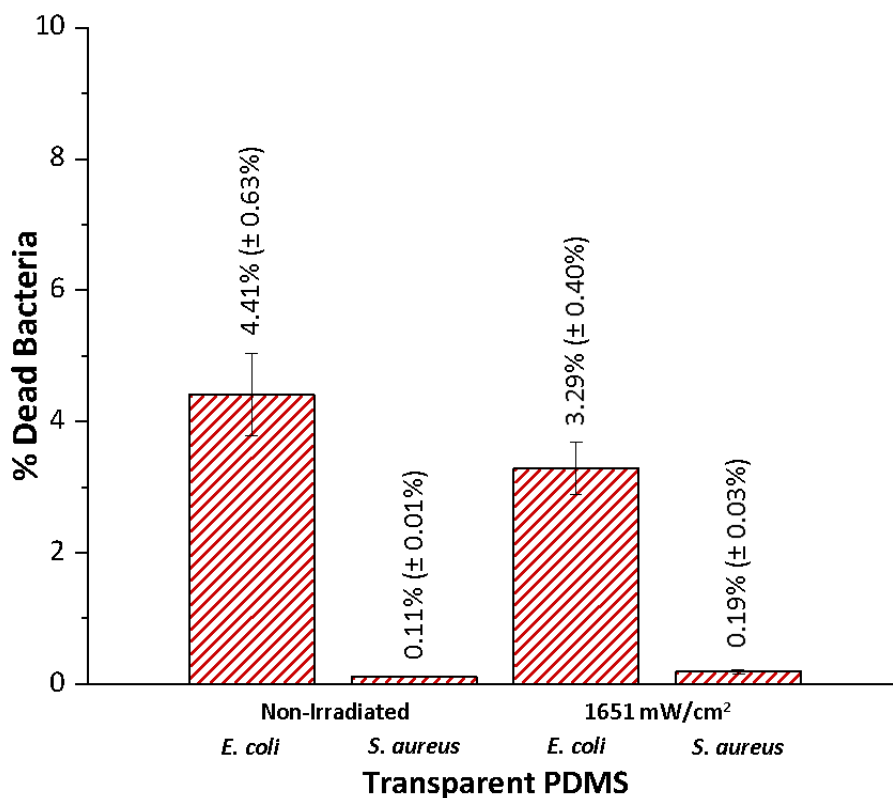


**Figure 4. 24** Bar Chart showing summary of the CFM data with Live/ Dead staining for *E. coli* 10798 and *S. aureus* 6538P on non-irradiated and 1651 mW/ cm<sup>2</sup> irradiated transparent PDMS.

### 4.3.3 Assessing the Viability of Sessile and Planktonic Bacteria after Heat Shock Treatment

After completing the photothermal experiments, we investigated the heating effect on both sessile and planktonic bacteria, using nominal temperatures ranging from 50°C to 90°C. The temperature profile for both planktonic and sessile heat shock experiments were first investigated prior to bacteriological experiments.

#### 4.3.3.1 Planktonic Heat Shock Experiments

To investigate the temperature profile for planktonic heat shock experiments, 900 µl of PBS was first heated to required nominal temperature (50°C to 90°C) in a 1.5 ml tube using a

heating block. 100µl of fresh PBS buffer was then added to the heated solution in the heat block and the temperature was measured every 30 seconds for 5 minutes (Figure 4. 25), using a K type thermocouple threaded through a hole in the top of the tube.

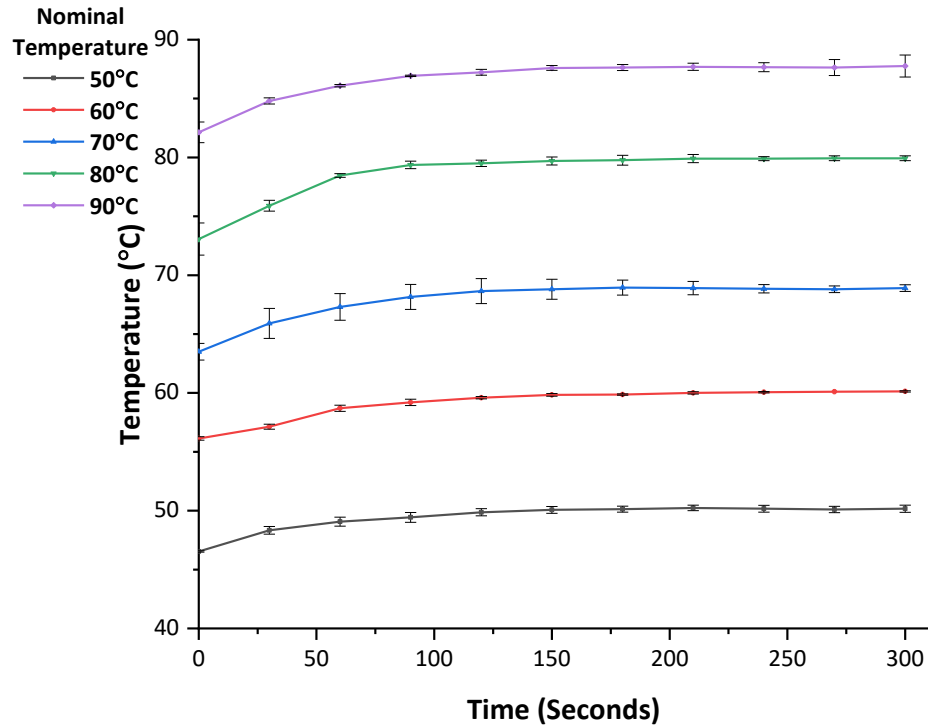


**Figure 4. 25** Thermograms for the planktonic heat shock experiments, measured using a K type thermocouple.

As a result, an initial decrease in the temperature was observed on addition of 100 µl PBS to the pre-heated solution, as expected (Figure 4. 25 and see appendix, Table A4. 2). However, the temperature soon increases and begins to plateau, reaching a stationary phase after 90s (Figure 4. 25). Interestingly, at higher nominal heat shock temperatures, the nominal temperature was not reached (Table A 4. 2), which could be attributed to the sample tube behaving as an insulation layer. Therefore, for convenience, we will from now on refer to the nominal temperatures. However, the actual temperatures must be considered for the correct interpretation of the data.

After completing the temperature profiles for the planktonic heat shock experiments, we then moved to testing the viability of planktonic *E. coli* and *S. aureus* bacteria under heat shock

treatment. The planktonic heat shock experiment was performed as discussed above (excluding the thermocouple measurements) using 100  $\mu$ l of bacteria culture with a starting concentration of  $10^8$ - $10^9$  CFUs  $\text{ml}^{-1}$ . The heat shock experiment was stopped after 5 minutes and the heated solutions were serially diluted and plated on fresh nutrient agar according to the Miles and Misra method.<sup>37</sup> The plates were incubated for 24 hrs and CFUs were then counted. As a result, we observed an initial decrease in the percentage viability of both *E. coli* and *S. aureus* bacteria at 50°C, with a percentage viability of  $41.31\% \pm 6.93\%$  and  $39.68\% \pm 10.77\%$ , respectively (Figure 4. 26). While at 60°C we observe nearly 100% death for both bacteria types (Figure 4. 26). At temperatures above 70°C, no CFUs formed on the nutrient agar, resulting a 100% death of planktonic bacteria, for both bacteria types (Figure 4. 26).

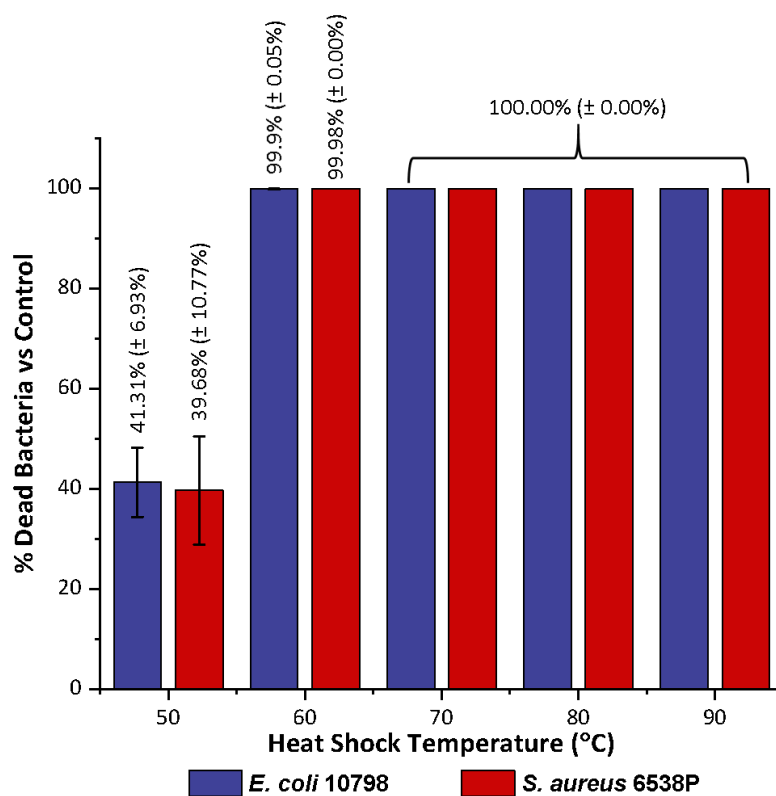


**Figure 4. 26** Percentage (%) dead *E. coli* (ATCC 10798) and *S. aureus* (ATCC 6538P) bacteria compared to control, in planktonic heat shock experiments.

### 4.3.3.2 Sessile Heat Shock Experiments with the Type I Material

After completing the planktonic heat shock experiments, we investigated the viability of sessile bacteria on the surface of the type I material. The temperature profile for the sessile heat shock experiments was first investigated over time using a K type thermocouple (Figure 4. 27), placed close to the surface of the type I material. In a typical experiment, a 9 mm sample of type I material was placed in a 2 ml tube facing inwards, along with 1 ml 0.85% NaCl. The NaCl in the tube was then exchanged with 1ml of pre-heated NaCl, heated to a required temperature (50°C to 90°C). The sample was then heated at a required temperature (50°C to 90°C) using a heat block and the temperature was measured every 30 seconds for 5 minutes (Figure 4. 27). A further temperature measurement was also collected after 10 minutes to confirm stationary conditions were met after 5 minutes of heat treatment (see appendix, Table A4. 3).

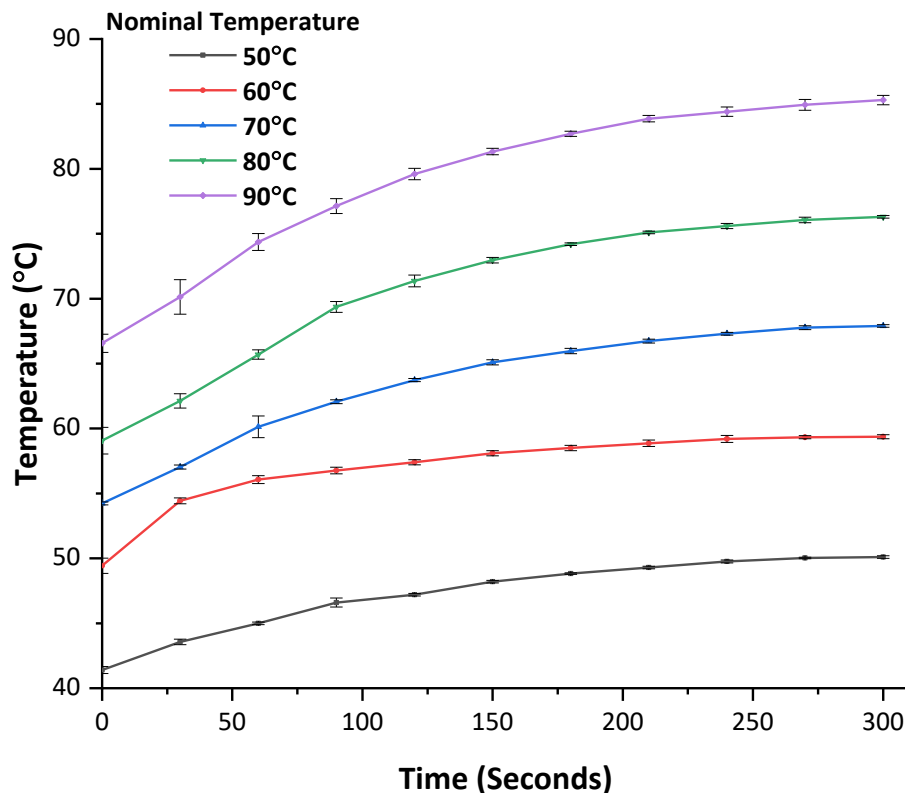


**Figure 4. 27** Thermograms for the type I material during sessile heat shock experiments, measured using a K type thermocouple.

As a result, an initial decrease in the temperature was observed after the exchange with the pre-heated NaCl solution (Figure 4. 27 and see appendix, Table A4. 3). The temperature then gradually increases and reaches a temperature close to plateau after 250s (Figure 4. 27). After 5 and 10 minutes of heat treatment, no significant difference in the temperature was observed, suggesting stationary conditions were reached (see appendix, Table A4. 3). Similar to the planktonic heat shock experiments, at higher nominal heat shock temperatures, the nominal temperature was not reached in the sessile heat shock experiments, which could be attributed to the sample tube behaving as an insulation layer as previously discussed.

After determining the temperature profile (Figure 4. 27) for the sessile heat shock experiments, we moved to investigating the viability of both *E. coli* and *S. aureus* bacteria on the surface of the type I material after heat shock treatment. In these experiments, 9 mm samples of type I material were prepared and incubated with the individual bacteria species according to the photothermal experiments discussed above. After incubation, the samples were washed three times with 1 ml sterile 0.85% (w/w) NaCl and then placed in a 2 ml tube, along with 1ml of NaCl, ensuring the active surface was facing inwards towards the solution. The sessile heat shock experiment was then repeated as discussed above (excluding the thermocouple measurements) for 5 minutes using the nominal temperatures (see appendix, Table A4. 3). After heat shock treatment, the samples were collected and imaged using CFM with Live/ dead staining.

In the sessile heat shock experiments with *E. coli*, an initial increase in the fraction of dead cells on the surface of the type I material was observed at 60°C, with a fraction of  $13.32\% \pm 1.88\%$  dead cells (Figure 4. 28 and 30). The fraction of dead cells on the surface of the type I material gradually increases with increasing temperature, reaching a fraction of  $77.16\% \pm 2.02\%$  dead cells at 90°C (Figure 4. 28 and 30). For the sessile heat shock experiments on the

type I material with *S. aureus*, the initial increase in the fraction of dead cells was observed at 70°C, with a fraction of  $75.93\% \pm 2.13\%$  (Figure 4. 29 and 31). Although, at 60°C, the fraction of dead *S. aureus* bacteria was similar to the control samples, with a fraction of  $0.81\% \pm 0.93\%$  dead bacteria (Figure 4. 29 and 31). This suggests the transition from live to dead *S. aureus* bacteria during heat shock experiments, lies between 60°C and 70°C. At the maximum temperature tested (90°C) in sessile heat shock experiments with *S. aureus*, a fraction of  $81.5\% \pm 3.44\%$  dead cells on the surface of the type I material was observed (Figure 4. 29 and 31).

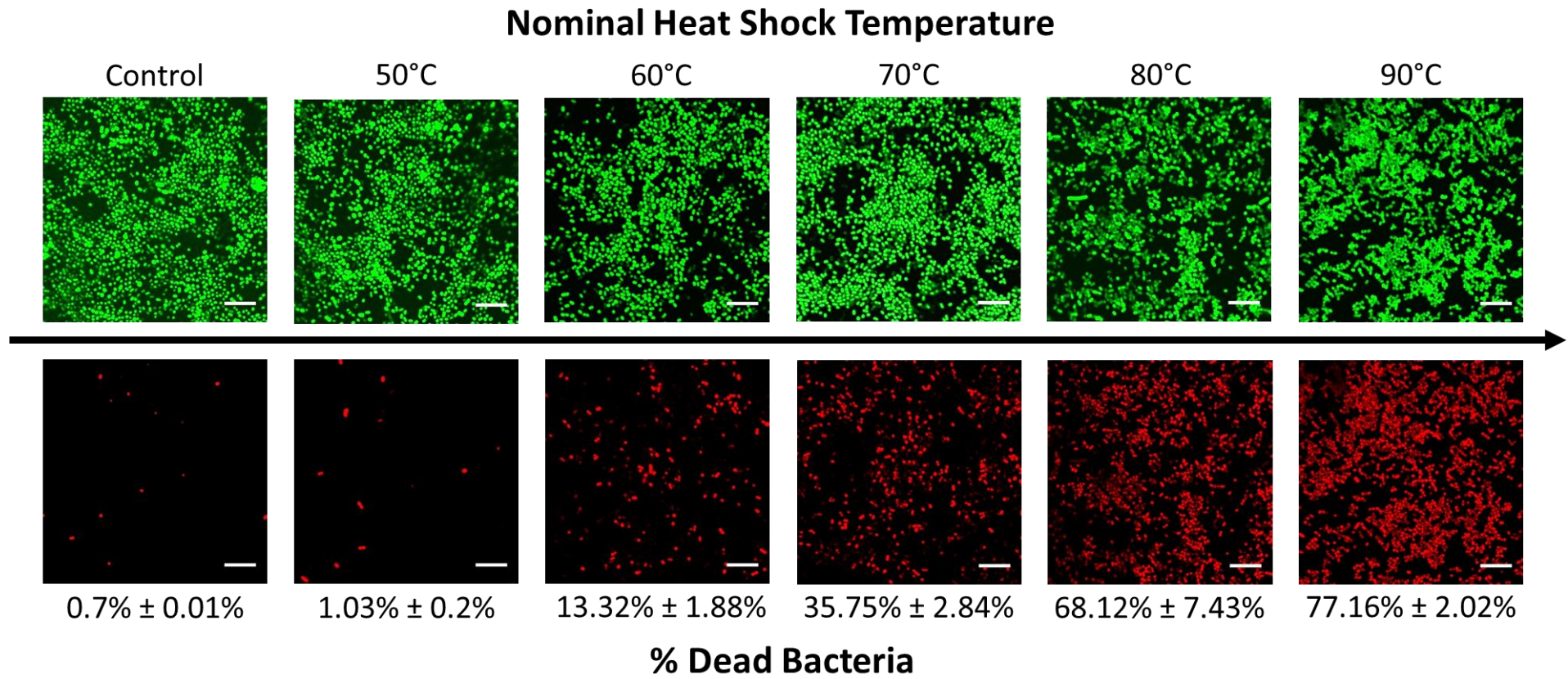


**Figure 4. 28** Confocal fluorescence microscopy images of *E. coli* (ATCC 10798) on type I materials showing percentage of dead bacteria after 5 mins heat shock treatment under physiological conditions, at different nominal temperatures. Bacteria imaged using Live/dead viability kit. (Green: All bacteria), (Red: Dead bacteria). (Scale bars are 10  $\mu$ m).

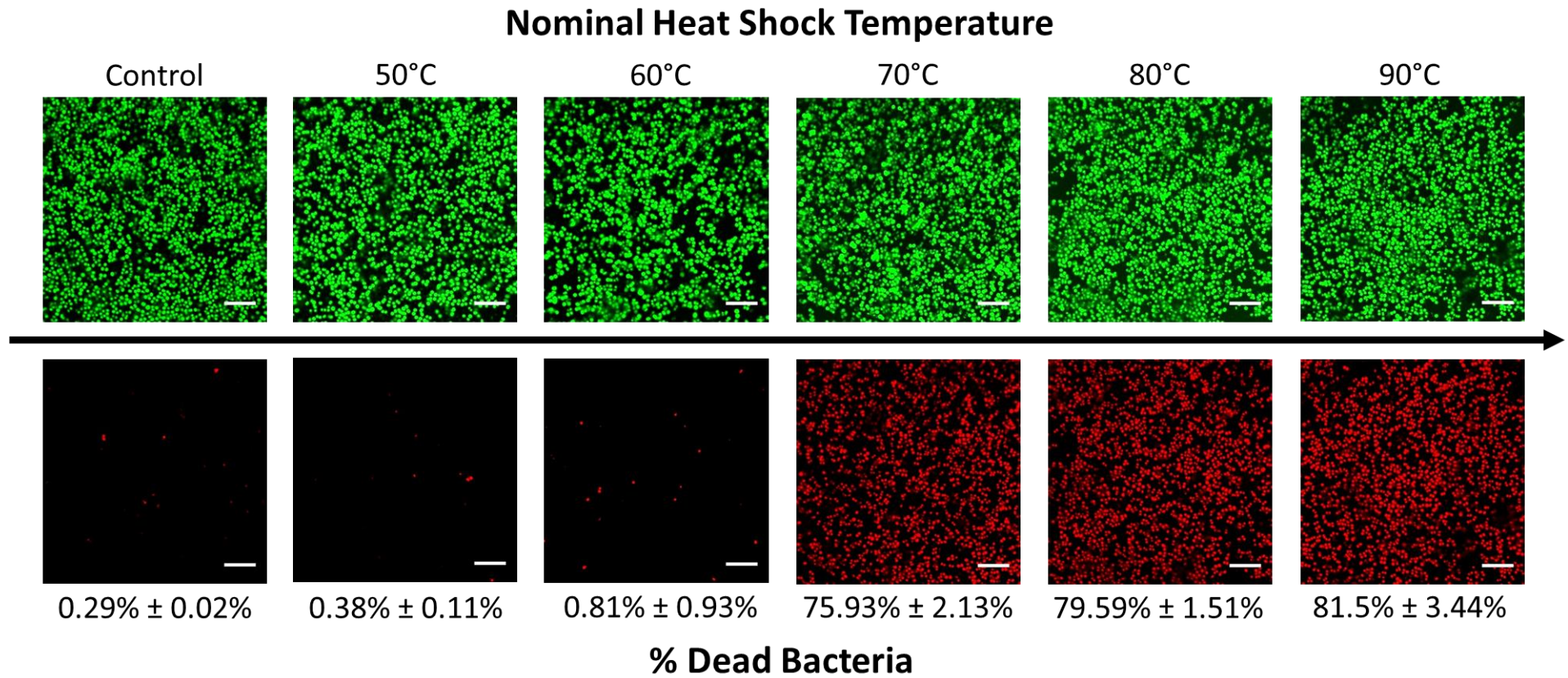


**Figure 4. 29** Confocal fluorescence microscopy images of *S. aureus* (ATCC 6538P) on type I materials showing percentage of dead bacteria after 5 mins heat shock treatment under physiological conditions, at different nominal temperatures. Bacteria imaged using Live/dead viability kit. (Green: All bacteria), (Red: Dead bacteria). (Scale bars are 10 μm).

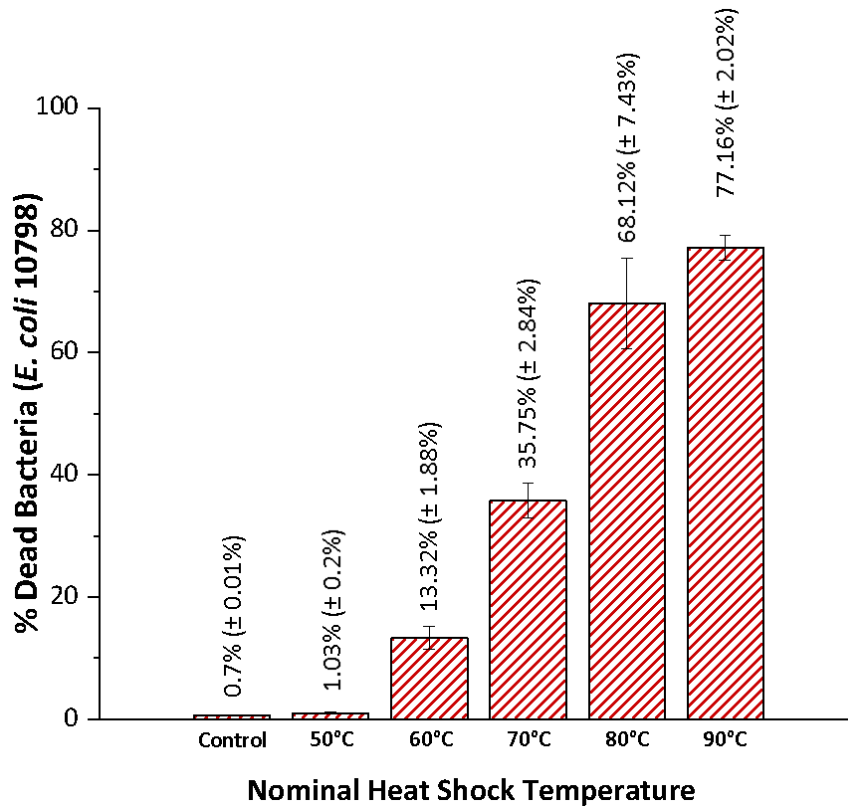


**Figure 4. 30** Bar Chart showing summary of the CFM data with Live/ Dead staining for *E. coli* 10798 on type I materials after 5 minutes of heat shock treatment at different nominal temperatures.

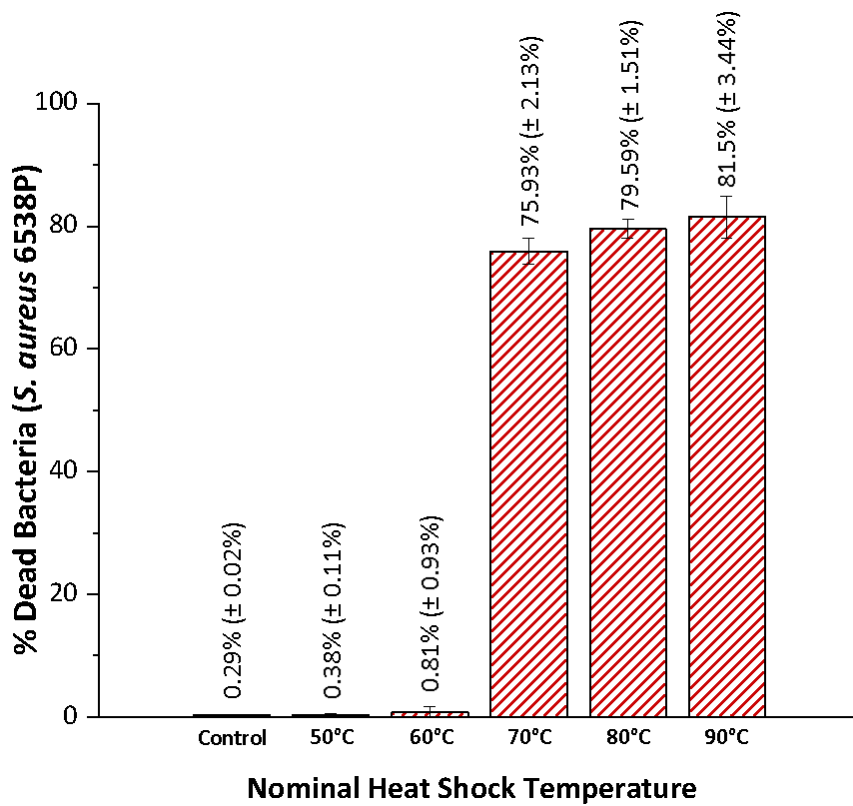


**Figure 4. 31** Bar Chart showing summary of the CFM data with Live/ Dead staining for *S. aureus* 6538P on type I materials after 5 minutes of heat shock treatment at different nominal temperatures.

## 4.3.4 Comparative Discussion for the Photothermal and Heat Shock Experiments

### 4.3.4.1 Photothermal vs Sessile Heat Shock

When comparing the CFM data for both the photothermal and sessile heat shock (Figure 4. 32) experiments for the type I material, *S. aureus* bacteria (Figures 4.32) exhibited an initial higher resistance to both increasing laser power densities and heat shock temperatures, compared to *E. coli* (Figure 4. 32). However, after the initial transition from live to dead sessile bacteria on the type I material, for both photothermal and heat shock experiments, the fraction of dead *E. coli* bacteria gradually increased (Figure 4. 32), while the fraction of dead *S. aureus* bacteria on the type I material remained consistent (Figures 4. 32).

We also observed a significant difference in the fraction of dead bacteria at lower temperatures between photothermal and sessile heat shock experiments (Figure 4. 32), according to the thermograms for the respective experiments (Figures 4. 17 and 4. 27 and see appendix, Tables A4. 1 and A4. 3). For example, at low irradiation power densities, such as 1174 mW/ cm<sup>2</sup>, where a temperature ( $T_{5 \text{ Mins}}$ ) of  $59.1^{\circ}\text{C} \pm 1.6^{\circ}\text{C}$  was measured (see appendix, Table A4.1), a fraction of  $56.18\% \pm 6.19\%$  dead *E. coli* (Figure 4. 32) and  $62.48\% \pm 5.32\%$  dead *S. aureus* bacteria (Figure 4. 32) was observed. Whereas, for the  $60^{\circ}\text{C}$  (nominal temperature) sessile heat shock experiments, with a final measured temperature ( $T_{5 \text{ Mins}}$ ) of  $59.4^{\circ}\text{C} \pm 0.2^{\circ}\text{C}$  (see appendix, Table A4. 3), a fraction of  $13.32\% \pm 1.88\%$  for dead *E. coli* (Figure 4. 32) and  $0.81\% \pm 0.93\%$  dead *S. aureus* (Figure 4. 32) was observed. The difference in the fraction of dead sessile bacteria in photothermal and sessile heat shock experiments, could be attributed to different factors. In both photothermal and sessile heat shock experiment, the heat diffusion will be different. In the photothermal experiments, the heat is generated from the surface of the type I material by the conversion of light into heat, whereas in the sessile heat shock experiments, the surface is heated by the surrounding media, and therefore the local heat

diffusion in both experiments will be different, resulting in a significant decrease in the fraction of dead bacteria observed at the surface of the type I material in sessile heat shock experiments.

In addition to this, bacteria at the surface of the type I material can form a biofilm. As a result, the bacteria within the biofilm may have increased resistance from the heat in the surrounding media, which has been evidenced in the literature.<sup>46,47</sup> Whereas, in the photothermal experiments, the heat is generated directly from the surface of the type I material and therefore the bacteria at the surface may have a decreased resistance to heat, resulting in the lower fraction of dead cells observed at lower temperatures for the sessile heat shock experiment (Figures 4. 32).

#### 4.3.4.2 Planktonic Heat Shock vs Sessile Heat Shock

Interestingly, when comparing both planktonic and sessile heat shock experiments (Figure 4. 32), we observe differences for both bacteria types (*E. coli* and *S. aureus*). For example, at 50°C, we observed a planktonic percentage viability of  $41.31\% \pm 6.93\%$  and  $39.68\% \pm 10.77\%$  for *E. coli* and *S. aureus* bacteria, respectively (Figure 4. 32). Whereas in the sessile heat shock experiments with the type I material at 50°C, we observed a dead fraction of  $1.03\% \pm 0.2\%$  and  $0.38\% \pm 0.11\%$  for sessile *E. coli* (Figure 4. 32) and *S. aureus* (Figure 4. 32) bacteria, respectively. These differences in the viability observed for planktonic heat shock experiments compared to the sessile heat shock experiments (Figure 4. 32) could be attributed to different factors, discussed below.

If we consider the thermograms for both the planktonic (Figure 4. 25) and sessile (Figure 4. 27) heat shock experiments, we observed stationary conditions at an earlier stage in the planktonic heat shock experiments. This can be attributed to the specific heat required to raise

the temperature in both planktonic and sessile heat shock experiments, because PDMS has a higher heat capacity than water (Table 4. 1).<sup>44,48</sup> Therefore, the amount of heat required to raise the temperature of the type I material is higher. As a result, the planktonic bacteria will endure higher temperatures for a longer period, which could result in a lower effect on the viability of bacterial cells.

**Table 4. 1** Thermal Properties of carbon nanopowder, water and PDMS

<b>Material</b>	<b>Heat Capacity (J mol<sup>-1</sup> K<sup>-1</sup>)</b>	<b>Heat Conductivity (W m<sup>-1</sup> K<sup>-1</sup>)</b>
Carbon Nanopowder	8.5 <sup>49</sup>	100.0 <sup>50</sup>
Water	75.2 <sup>44</sup>	0.6 <sup>51</sup>
PDMS	118.0 <sup>48</sup>	0.2 <sup>48</sup>

In addition, in the sessile experiments, the bacteria are able to form a biofilm on the surface of the type I material, as previously discussed. Bacteria within biofilms have increased resistance from the heat in the surrounding media, which may result in the increased viability in sessile bacteria cells observed (Figure 4. 32). Assessing the viability of bacterial cells at surfaces by fluorescent staining has also been reported to exhibit limitations.<sup>52</sup> Fluorescent stains, such as propidium iodide, are commonly used for assessing the membrane integrity of bacterial cells, by crossing the cell membrane and binding to internal nucleic acids.<sup>52,53</sup> However, techniques based on assessing membrane integrity can result in an overestimation of viable bacterial cells, because lethal stress, (e.g. heat induced shock) may not lead to an immediate disruption of the bacterial cell membrane.<sup>52,53</sup> As a result, the fluorescence stain cannot cross the cell membrane, and the cells are observed to remain viable.

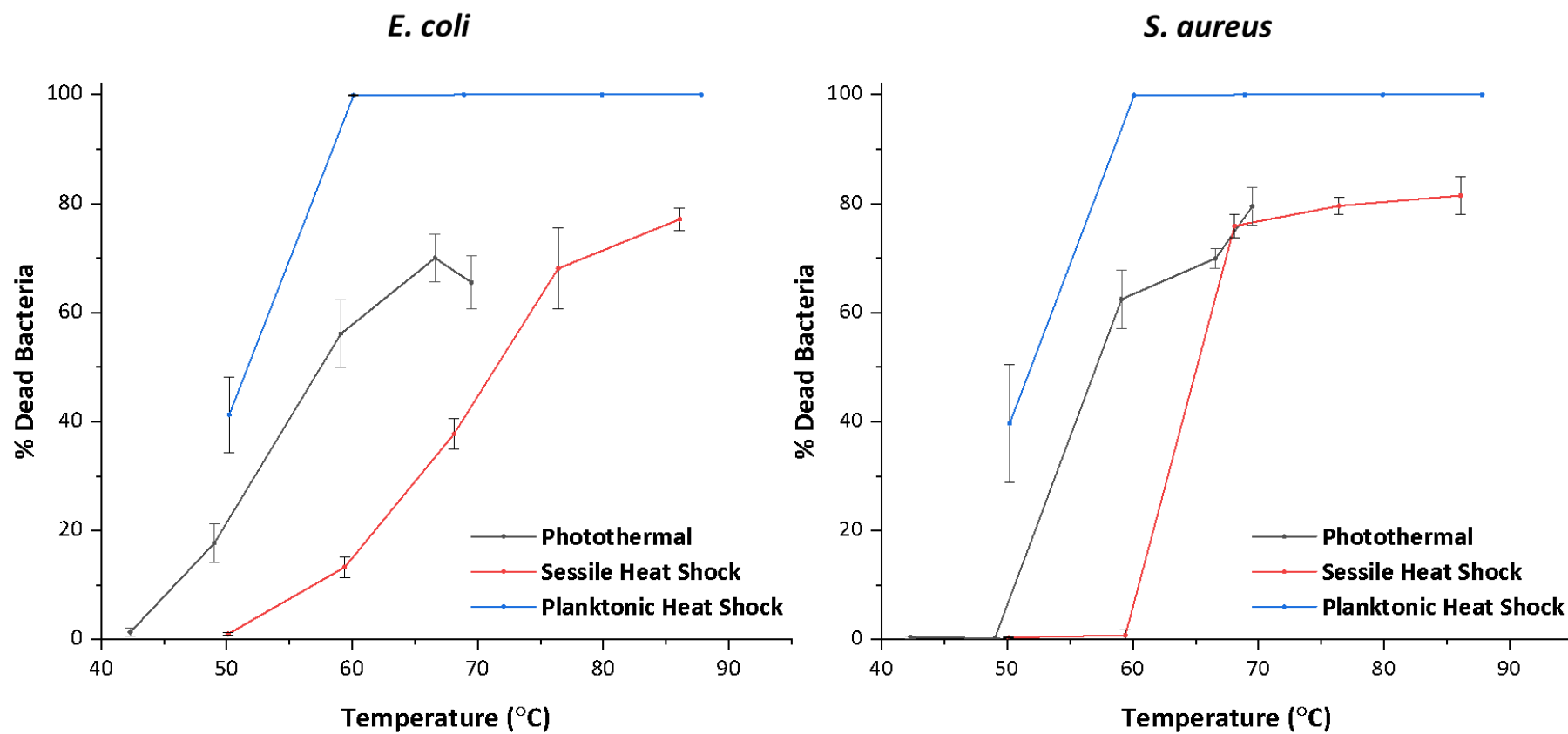


Figure 4. 32 Summary of photothermal and heat shock experiments with *E. coli* and *S. aureus* bacteria showing % of dead bacteria vs temperature measured (according to thermograms).

### 4.3.5 Fabrication and Characterisation of Type II

#### Materials

Considering the success of the type I material as a photothermal antimicrobial surface, we also investigated the use of the type I material as a potential system for a photothermal controlled drug release. Thus, providing an additional antimicrobial effect under NIR irradiation. Following the strategy reported in chapter 3, we incorporate dodecanoic acid into the type I material as a potential biocide, by swelling type I materials with melted dodecanoic acid. This led to an average loading of 43.4 mg/ g type I material  $\pm$  4.3 mg (see appendix, Table A4. 4). This new material was named type II.

The type II material was probed using Raman spectroscopy to identify the presence of dodecanoic acid in the material. However, upon irradiation of the type II material with the Raman laser, a local heat was generated causing dodecanoic acid to melt and therefore this technique could not be used. Alternatively, the type II material was then analysed using ATR-IR spectroscopy to confirm the presence of dodecanoic acid (Figure 4. 33). As a result, the presence of dodecanoic acid in type II material was identified by the characteristic C=O carbonyl stretch ( $1700\text{ cm}^{-1}$ ) and  $\text{CH}_2$  symmetrical stretch ( $2848\text{ cm}^{-1}$ ) (Figure 4. 33).<sup>54</sup>

Due to the difficulties encountered during the Raman spectroscopic analysis of the type II material, along with the limitations of the ATR-IR instrumentation, further investigation into the distribution of the dodecanoic acid in the type II material was not feasible.

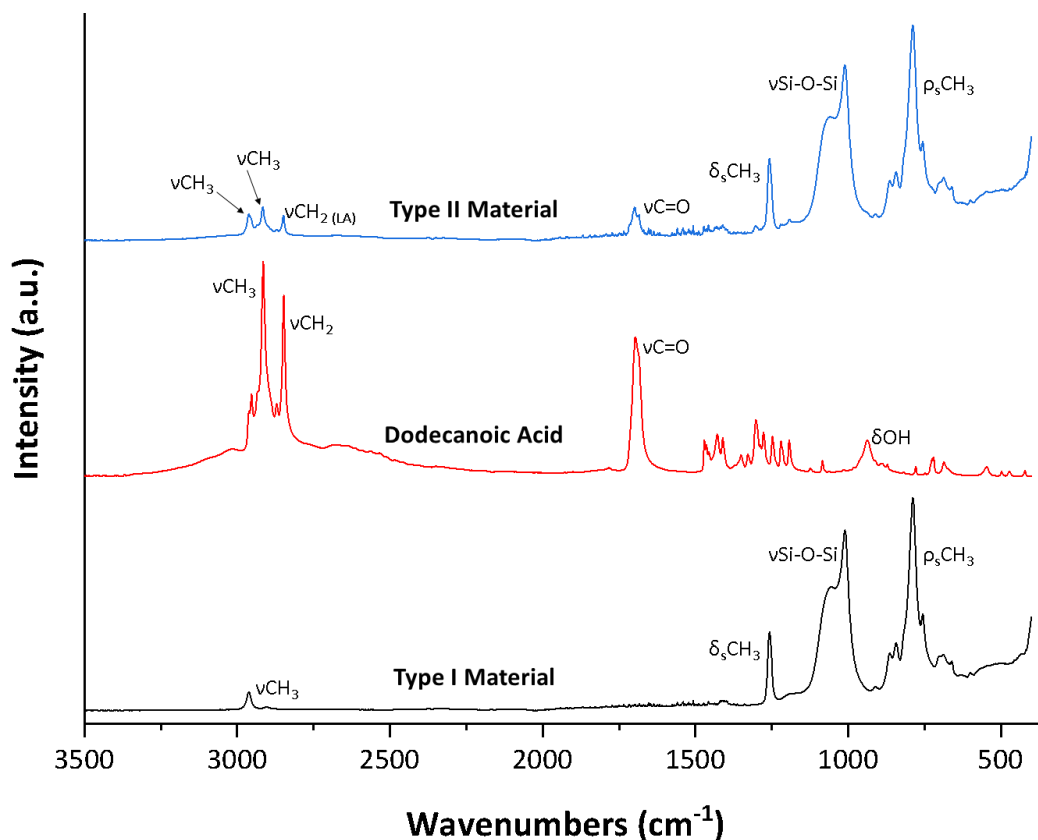


**Figure 4. 33** ATR-IR spectroscopy data of type I material (**Black**), dodecanoic acid (**Red**) and type II material (**Blue**).

Subsequently, we focused on the investigation of the photothermal release of dodecanoic acid from type II materials, using gravimetric analysis and ATR-IR measurements. Photothermal release experiments were performed following the same approach used previously for the type I materials, although using LB media instead of NaCl in the sample well to mimic the photothermal planktonic experiments, which will be discussed later. All photothermal experiments with the type II material were carried out using 881 mW/ cm<sup>2</sup> laser power density, due to the temperature reached at stationary conditions in the thermocouple experiments (Figure 4. 17 and see appendix, Table A4. 1) being just above the literature melting point of dodecanoic acid (43.8°C).<sup>55</sup>

In the gravimetric analysis for the photothermal release of dodecanoic acid from the type II materials, a batch of 10 pre-cut type II samples were collectively weighed before and after irradiation, completing a total of 3 replicates. This data was used to determine the % mass of dodecanoic acid released from the type II material, resulting in an average release of  $12\% \pm 3\%$  (see appendix, Table A4. 5). In ATR-IR analysis, the type II materials were also analysed before and after photothermal treatment. After photothermal treatment, ATR-IR measurements revealed an increase in the relative intensity of vibrational peaks associated with dodecanoic acid at the surface of the type II material (Figure 4. 34). This suggests there is an increased concentration of dodecanoic acid at the surface of the type II material and can be attributed to the photothermal release of dodecanoic acid.

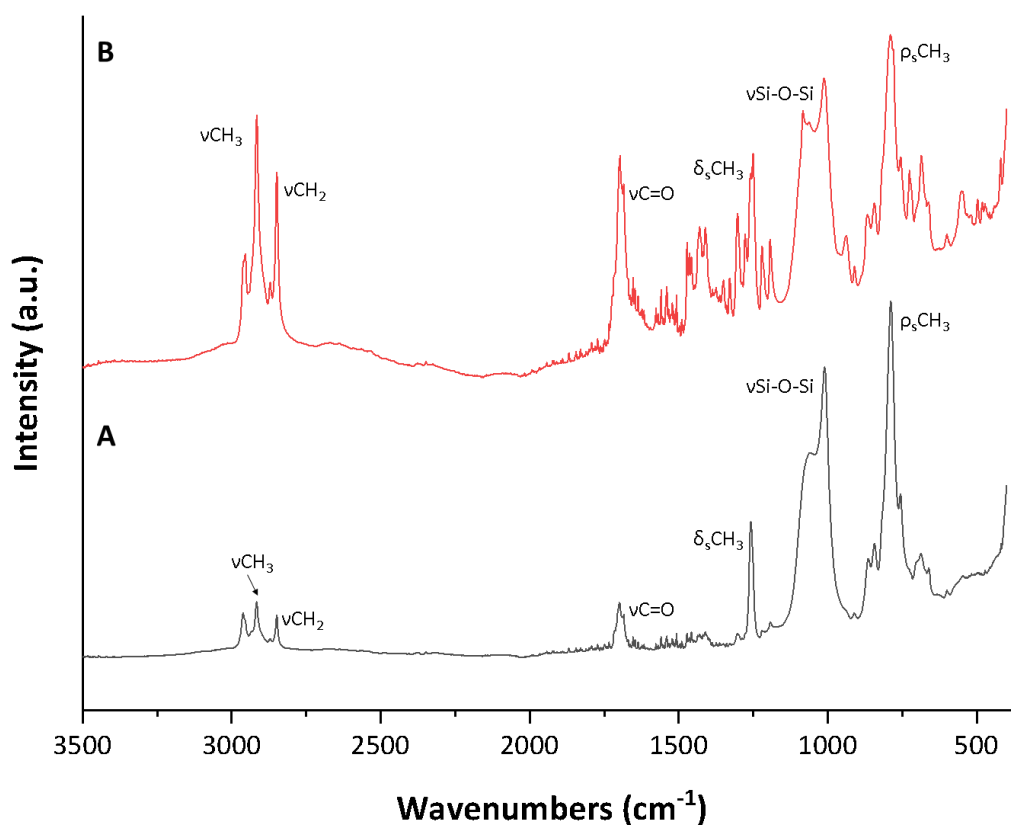


**Figure 4. 34** ATR-IR spectroscopy data of type II material before (A) and after (B) irradiation at 881  $\text{mW/cm}^2$  for 5 mins.

In addition to the photothermal release experiments on type II materials, we also examined the wettability of these materials by static water contact angle measurements (Figure 4. 35). Contact angles were measured using 0.85% NaCl as a model physiological buffer. We observed that the contact angle for the type I materials was comparable to PDMS, while type II materials had a marginal decreased contact angle, that may be associated with the presence of dodecanoic acid (Figure 4. 35)

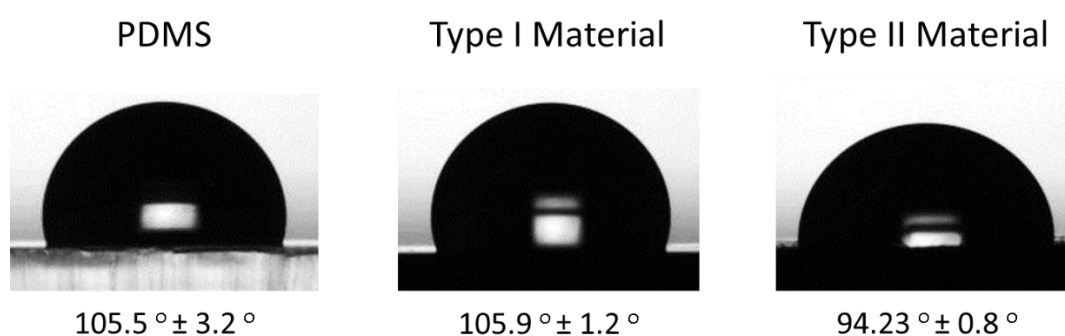


**Figure 4. 35** Contact angle measurements for PDMS, type I materials and type II materials with 0.85% NaCl.

#### 4.3.6 Characterising the Antimicrobial Performance of Type II Materials

After completing the characterisation of the type II material, the antimicrobial performance of type II materials under NIR irradiation was tested against both *E. coli* (ATCC 10798) and *S. aureus* (ATCC 6538P) bacteria, using the photothermal set-up previously described. The laser power density of 881 mW/cm<sup>2</sup> was used for all photothermal experiments, as previously discussed.

#### 4.3.6.1 Assessing the Viability of Surface Attached Bacteria on Type II Materials after Photothermal Treatment

Sessile photothermal experiments with the type II material were performed on 9 mm diameter samples of both type I and type II materials incubated for 24hrs with individual bacteria species (*E. coli* or *S. aureus*) at room temperature (25°C), using a starting concentration of  $10^8$ -  $10^9$  CFUs ml<sup>-1</sup>. Under these conditions dodecanoic acid is not released from the type II material. After incubation, the planktonic bacteria suspension was collected, and the samples were washed three times with sterile 0.85% NaCl, and then irradiated for 5 mins. After photothermal treatment, the samples were placed in a 24 well plate with fresh NaCl and examined using CFM with Live/ dead staining.

As a result of these experiments, we observed an increase in the fraction of dead bacteria for both types (*E. coli* (Figures 4. 36-39) on the surface of type II material, irrespectively of photothermal treatment. *S. aureus* displayed the most significant increase in the fraction of dead bacteria on the type II surface, with a dead fraction of  $85.9\% \pm 4.9\%$  and  $82.3\% \pm 1.8\%$  for non-irradiated and irradiated type II materials, respectively (Figure 4. 37 and 4. 39). Whereas for *E. coli*, we observed a dead fraction of  $33\% \pm 9\%$  and  $24\% \pm 5\%$  for non-irradiated and irradiated type II materials, respectively (Figure 4. 36 and 4. 38).

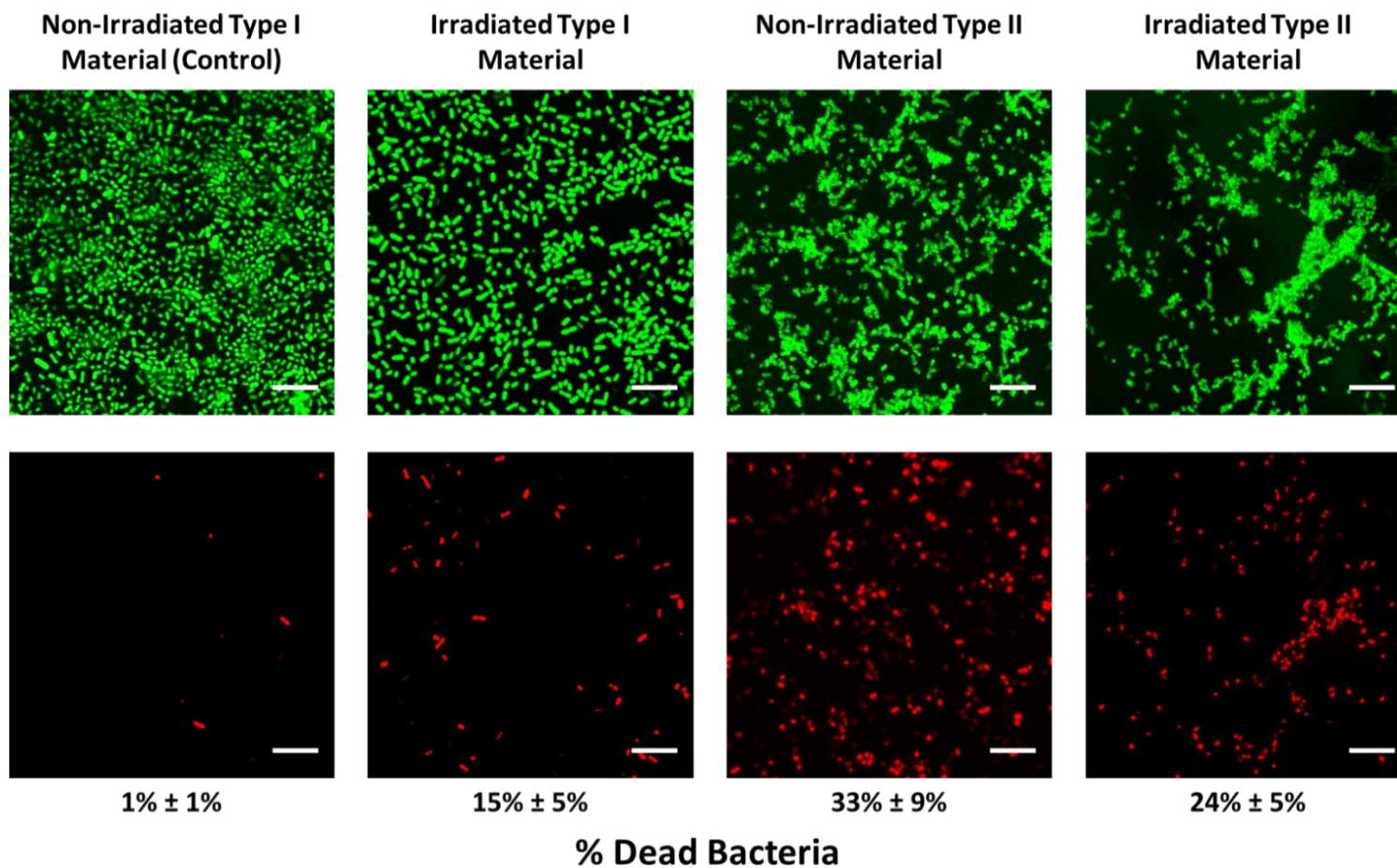


**Figure 4. 36** Confocal fluorescence microscopy images of *E. coli* (ATCC 10798) on non-irradiated and irradiated, type I and type II materials, showing the percentage of dead bacteria. Samples were irradiated at a laser power density of 881 mW/cm<sup>2</sup> for 5 minutes using the photothermal set-up. Bacteria imaged using Live/dead viability kit. (Green: All bacteria), (Red: Dead bacteria). (Scale bars are 10 μm).

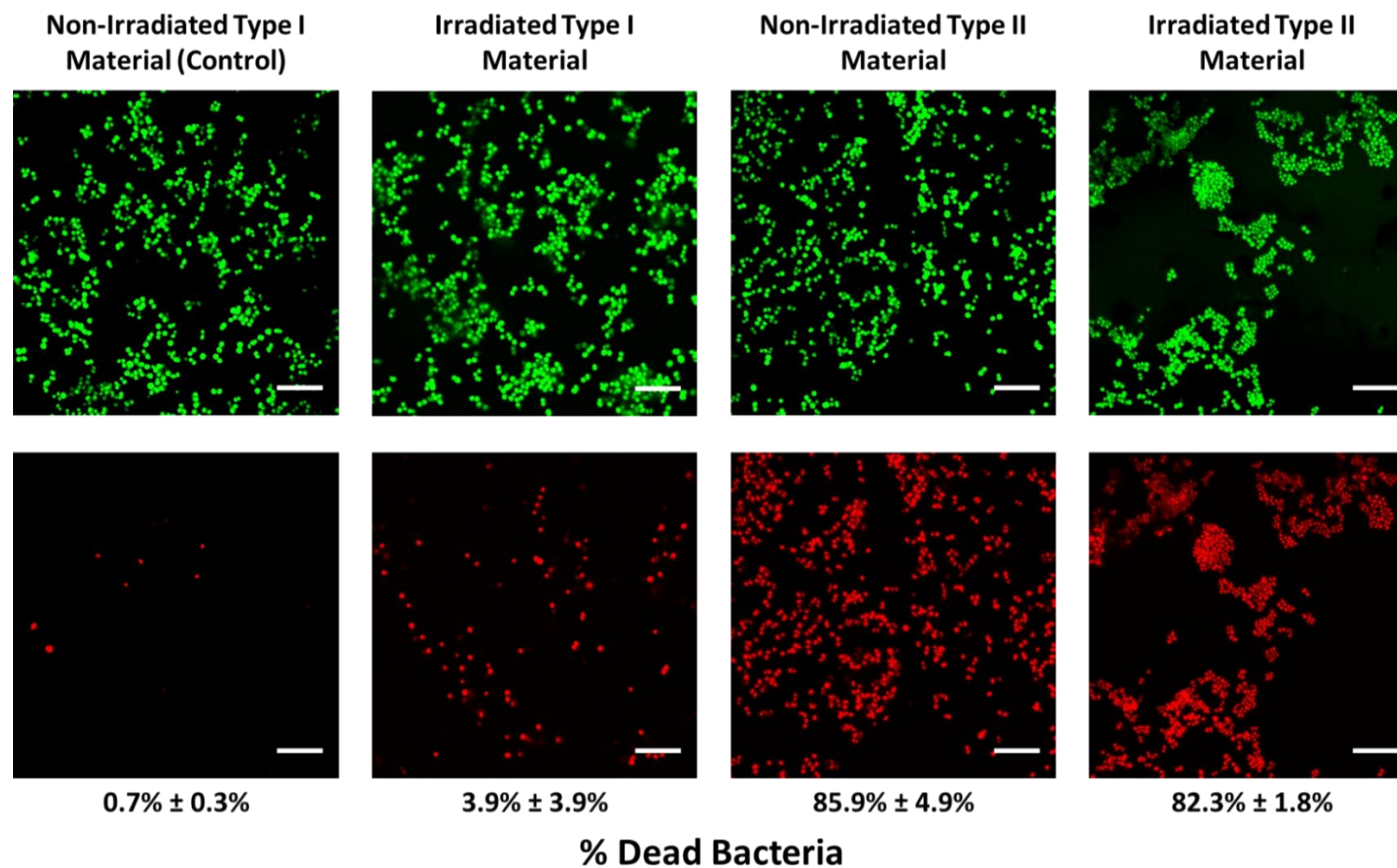


**Figure 4. 37** Confocal fluorescence microscopy images of *S. aureus* (ATCC 6538P) on non-irradiated and irradiated, type I and type II materials, showing the percentage of dead bacteria. Samples were irradiated at a laser power density of 881 mW/cm<sup>2</sup> for 5 minutes using the photothermal set-up. Bacteria imaged using Live/dead viability kit. (Green: All bacteria), (Red: Dead bacteria). (Scale bars are 10 μm).

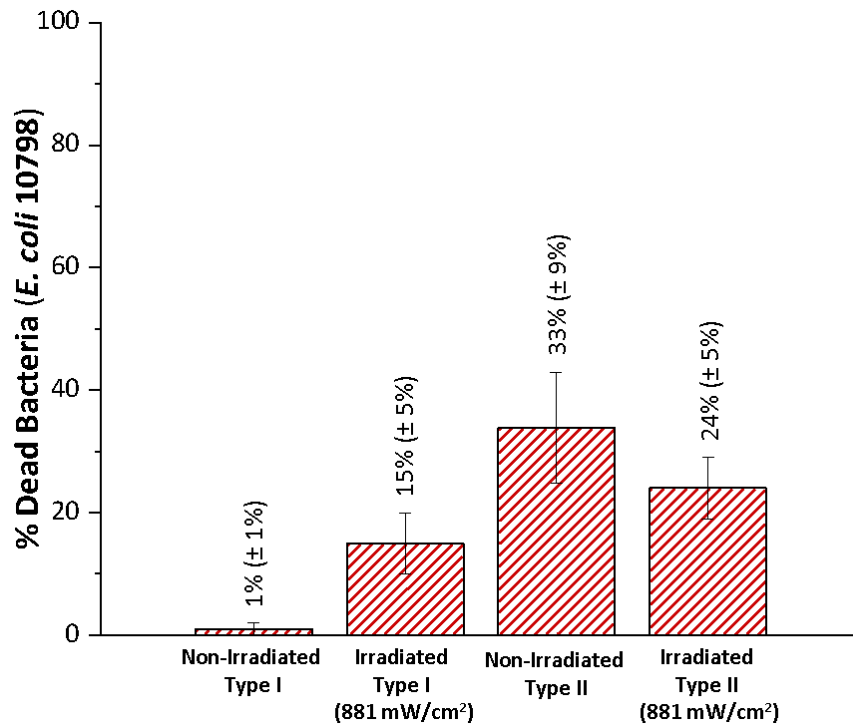


Figure 4. 38 Bar chart showing summary of CFM data with live/dead staining of *E. coli* 10798 on non-irradiated and 881 mW/cm<sup>2</sup> irradiated type I and type II materials.

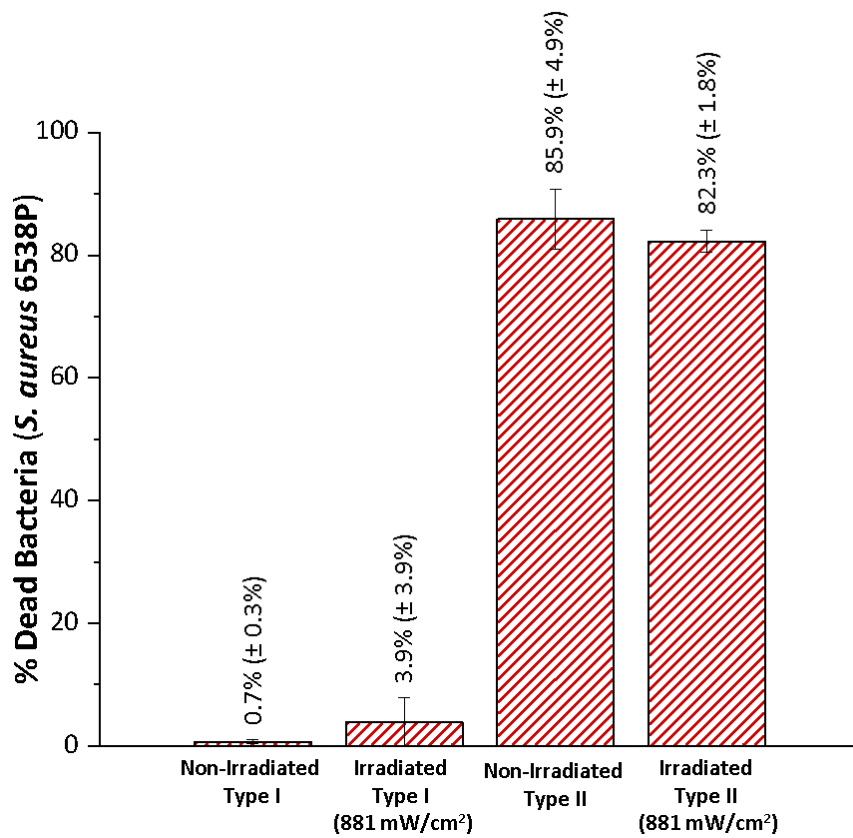


Figure 4. 39 Bar chart showing summary of CFM data with live/dead staining of *S. aureus* 6538P on non-irradiated and 881 mW/cm<sup>2</sup> irradiated type I and type II materials.

#### 4.3.5.2 Assessing the Viability of Planktonic Bacteria after Photothermal Treatment with Type II

##### Materials

After completing the sessile photothermal experiments with the type II material, the viability of planktonic bacteria under photothermal treatment with the type II materials was investigated. In a typical experiment, 40  $\mu\text{l}$  of bacteria suspension (*E. coli* or *S. aureus*), at a starting concentration of  $10^8 - 10^9$  CFUs  $\text{ml}^{-1}$  was placed in the irradiation sample well and covered with 9 mm diameter sample of the type I or II material. The samples were then irradiated according to the photothermal release experiments with the type II material, as previously described. A 20  $\mu\text{l}$  aliquot of planktonic media in the sample well was then collected, serially diluted and plated on fresh selective nutrient agar using the Miles and Misra method<sup>37</sup>. The viability of planktonic bacteria was determined by counting CFUs after incubation of the agar plates.

As a result, we observed a significant reduction in planktonic bacteria after irradiation of the type II material for both bacteria types, as well as an increased antimicrobial effect compared with the irradiated type I material (Figure 4. 40). After photothermal irradiation of the type II material, a percentage (%) planktonic viability of  $14\% \pm 2\%$  for *E. coli* and  $10\% \pm 8\%$  for *S. aureus* bacteria was observed (Figure 4. 40). However, unlike the sessile photothermal experiments with the type II material (Figure 4.36-39), no reduction in the viability of planktonic bacteria cells was observed for the non-irradiated type II material (Figure 4. 40), suggesting minimal or no dodecanoic acid was released into the planktonic media.

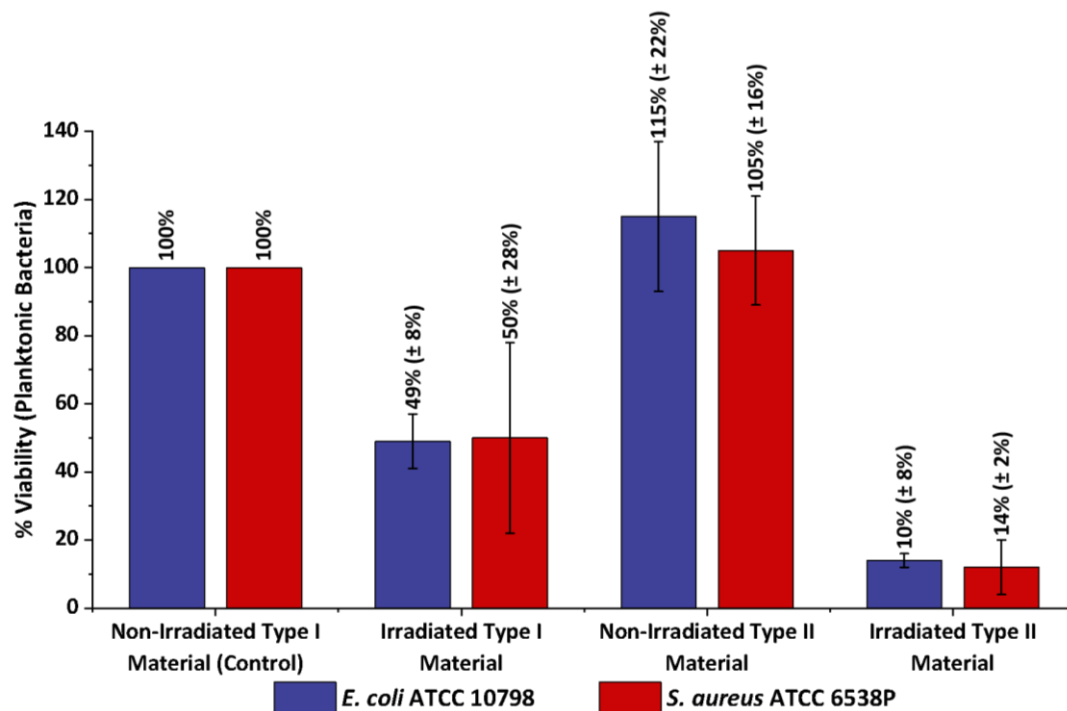


**Figure 4. 40** Percentage (%) viability of planktonic *E. coli* (ATCC 10798) (Blue) and *S. aureus* (ATCC 6538P) (Red) bacteria with irradiated type I and type II materials, and non-irradiated type II materials. Samples irradiated with 881 mW/cm<sup>2</sup> using photothermal set-up. Control is non-irradiated type I material.

In addition, when comparing the viability of bacteria cells for the sessile (Figures 4. 36-39) and planktonic (Figure 4. 40) experiments on the irradiated type I material, we observe an increased reduction in the viability of planktonic cells for both *E. coli* and *S. aureus* bacteria (Figure 4. 40). This could be attributed to different factors when comparing both experiments, including increased heat resistance from the surrounding media as a result of biofilm formation at the surface of the type I material<sup>46,47</sup> and the limitations of live/ dead staining as previously discussed.<sup>52,53</sup>

## 4.4 Conclusions

In this work, we produced a photothermal material (type I material) following a simple approach, by the incorporation of CNP into PDMS. After curing the PDMS, the type I material exhibited a saturated absorption spectrum spanning a broad light-absorption range, including the NIR region (700-1100 nm) (Figure 4. 11), making this an ideal photothermal material. The presence and distribution of CNP in the PDMS was also investigated by Raman analysis. Raman analysis revealed a shift in both the D and G vibration bands of the CNP when embedded in the PDMS (Figure 4. 13) and is believed to be associated with compression strain on the carbon bonds of the graphitic CNP.<sup>41</sup> The CNP was also shown to be scattered across the surface (Figure 4. 14) of the type I material, according to the signal to baseline mapping of the G vibration band of the CNP. ATR-IR was also used to analyse the type I material, however in this experiment we could only confirm the chemical properties of PDMS because the CNP proved to be infrared inactive, as previously reported.<sup>42,43</sup>

After characterising the type I material, the photothermal effect of the type I material under NIR irradiation was investigated. As a result, the type I material showed a linear dependence with increasing laser power at stationary conditions (Figure 4. 18 and see appendix, A4. 6). This behaviour can be modelled on the Stefan-Boltzmann Law, where the photothermal conversion of incident light to heat is equal to the heat dissipation from the surface (Equation 4. 1).<sup>45</sup> The antimicrobial performance of the type I material under NIR irradiation was also investigated against *E. coli* (Figure 4. 19 and 4. 21) and *S. aureus* (Figure 4. 20 and 4. 22) bacteria. The samples were imaged using CFM with live/ dead staining, showing an antimicrobial effect against both bacteria types. A gradual increase in the fraction of dead bacteria with increasing laser power density was observed for *E. coli* (Figure 4. 19 and 4. 21), whereas *S. aureus* (Figure 4. 20 and 4. 22) bacteria were initially more resistant at the lower

laser power densities investigated, which then reached an immediate transition from live to predominately dead bacteria at a laser power density of 1174 mW/ cm<sup>2</sup>.

The heating effect on both planktonic and sessile bacteria was also investigated by heat shock experiments. As a result, we observed a significant reduction in the viability of bacteria in planktonic experiments compared with the sessile bacteria, which can be attributed to several factors, including: a difference in the specific heat capacity for both experiments, increased heat resistance as a result of biofilm formation at the surface of the type I material<sup>46,47</sup> and limitations of live/ dead staining, due to an uncompromised cell membrane, leading to a false negative result.<sup>52,53</sup>

When comparing the CFM data for both the photothermal and sessile heat shock experiments (Figure 4. 32), we observed a similar trend in the reduction of both *E. coli* and *S. aureus* cells on the type I material. *S. aureus* was initially more resistant with increasing laser power densities and heat shock temperatures, which eventually reached a transition from live to predominately dead bacteria. Whereas, *E. coli* exhibited a gradual increase in the fraction of dead bacteria cells with increasing laser power densities and heat shock temperatures. We also observed a significant difference in the fraction of dead bacteria cells for both bacteria types at the lower laser power densities and heat shock temperatures investigated, with photothermal treatment having an increased antimicrobial effect. This was attributed to a couple of different factors, including a difference in the local heat diffusion of both experiments and increased heat resistance against the surrounding media as a result of biofilm formation at the surface of the type I material<sup>46,47</sup>

The type I material was also investigated as a potential photothermal drug release system by the incorporation of dodecanoic acid into the type I material as an antimicrobial drug, to form the type II material. As a result, a mass of 43.4 mg/ g type I material  $\pm$  4.3 mg of dodecanoic acid was loaded into the type I material (see appendix, Table A4. 4), which was further confirmed by ATR-IR analysis (Figure 4. 33). The dodecanoic acid could then be subsequently released upon 5 minutes of photothermal treatment at a laser power density of 881 mW/ cm<sup>2</sup>, resulting in a release of 12%  $\pm$  3% dodecanoic acid (see appendix, Table A4. 5). The release at the surface of the type II material following photothermal experiments was also confirmed by ATR-IR analysis (Figure 4. 34), exhibiting an increase in the relative intensity of characteristic vibrational peaks associated with dodecanoic acid. The type II material also appeared to show a change in the surface properties after loading the type I material with dodecanoic acid, with an improved surface wettability as seen in the static water contact angle measurements (Figure 4. 35).

When testing the antimicrobial activity of the type II material we observed a reduction in planktonic viability for both bacteria types after photothermal treatment (Figure 4. 36), with type II materials providing an additional antimicrobial effect compared with the type I material (Figure 4. 40). However, in the sessile photothermal experiments with the type II material, the material proved to be active towards both bacteria types irrespective of photothermal treatment (Figure 4. 36-39). Interestingly, we also observed a decrease in the viability of planktonic bacteria compared with sessile bacteria for the irradiated type I materials. This can be attributed to different factors, including increased heat resistance as a result of biofilm formation at the surface of the type I material<sup>46,47</sup> and the limitations of live/ dead staining as previously discussed.<sup>52,53</sup>

## 4.5 Future Work

In the photothermal experiments with planktonic bacteria, using the type I and type II materials, all experiments were performed using a laser power density of 881 mW/cm<sup>2</sup> and the data was compared with the sessile photothermal experiments. As a result, we observed a significant difference in the viability of planktonic and sessile bacteria cells after photothermal treatment. However, the antimicrobial effect of the other laser power densities with the type I and type II materials on the planktonic bacteria are still left to explore. The significant difference in the planktonic and sessile photothermal experiments was attributed to different factors. One plausible explanation for this was related to the limitation of live/ dead staining, particularly the cellular staining with propidium iodide.<sup>52,53</sup> Although, the bacteria at the surface may not possess an uncompromised cell membrane, the viability of the bacteria cells could be significantly reduced. One method of determining this, will be to plate the surface attached bacteria following photothermal treatment, using such methods as ISO 22196.<sup>56</sup> In this method a non-ionic surfactant is used to remove the surface attached bacteria after washings<sup>57</sup> and then plated using the Total Plate Counting (TPC) method.<sup>58</sup>

Alternatively, testing other laser power densities with the type I and type II materials, as well as different irradiation times could also provide a further insight into the reliability of live/ dead staining. Increased irradiation times could also induce an increased reduction in the viability of both planktonic and sessile bacteria cells, due to the increased endurance under lethal conditions. As a result, lower irradiation power densities could be potentially used to kill the bacteria with the type I material. In addition, increasing laser power densities and irradiation times could also result in an increased amount of dodecanoic acid released from the type II material under photothermal treatment, resulting in an increased reduction in the viability of both sessile and planktonic bacteria cells. This could also provide a better insight into the release kinetics of the type II material.

Little is known regarding the antimicrobial mechanism associated with the dodecanoic acid in the type II material, therefore metabolic assays could also be a potential future work to answer this question. The type I and type II materials could also be tested against other bacterial species, to confirm the antimicrobial efficacy of both materials. Thermophile type bacteria are a useful candidate for further testing the photothermal effect type I materials, owing to their preferential growth and increased heat resistance at high temperature conditions.<sup>59</sup>

## 4.6 References

- 1 Z. Bao, X. Liu, Y. Liu, H. Liu and K. Zhao, *Asian J. Pharm. Sci.*, 2016, **11**, 349–364.
- 2 Y. Zhou, H. Ye, Y. Chen, R. Zhu and L. Yin, *Biomacromolecules*, 2018, **19**, 1840–1857.
- 3 P. Pallavicini, A. Donà, A. Taglietti, P. Minzioni, M. Patrini, G. Dacarro, G. Chirico, L. Sironi, N. Bloise, L. Visai and L. Scarabelli, *Chem. Commun.*, 2014, **50**, 1969–1971.
- 4 P. Pallavicini, B. Bassi, G. Chirico, M. Collini, G. Dacarro, E. Fratini, P. Grisoli, M. Patrini, L. Sironi, A. Taglietti, M. Moritz, I. Sorzabal-Bellido, A. Susarrey-Arce, E. Latter, A. J. Beckett, I. A. Prior, R. Raval and Y. A. Diaz Fernandez, *Sci. Rep.*, 2017, **7**, 5259.
- 5 T. Akasaka, M. Matsuoka, T. Hashimoto, S. Abe, M. Uo and F. Watari, *Mater. Sci. Eng. B Solid-State Mater. Adv. Technol.*, 2010, **173**, 187–190.
- 6 K. C. L. Black, T. S. Sileika, J. Yi, R. Zhang, J. G. Rivera and P. B. Messersmith, *Small*, 2014, **10**, 169–178.
- 7 A. D’Agostino, R. Desando, G. Dacarro, M. Patrini, P. Pallavicini, P. Grisoli, A. Taglietti, M. Bini and L. Cucca, *Nanomaterials*, 2017, **7**, 7.
- 8 W. Jo and M. J. Kim, *Nanotechnology*, 2013, **24**, 195104.
- 9 P. F. Wheat, T. G. Winstanley and R. C. Spencer, *J. Clin. Pathol.*, 1985, **38**, 1055–1058.
- 10 E. Guisbert, † Takashi Yura, V. A. Rhodius and C. A. Gross, *Microbiol. Mol. Biol. Rev.*, 2008, **72**, 545–554.
- 11 W. Schumann, *Cell Stress Chaperones*, 2016, **21**, 959–968.
- 12 D. G. Meeker, S. V Jenkins, E. K. Miller, K. E. Beenken, A. J. Loughran, A. Powless,

- T. J. Muldoon, E. I. Galanzha, V. P. Zharov, M. S. Smeltzer and J. Chen, *ACS Infect. Dis.*, 2016, **2**, 241–250.
- 13 S. Boca-Farcau, M. Potara, T. Simon, A. Juhem, P. Baldeck and S. Astilean, *Mol. Pharm.*, 2014, **11**, 391–399.
- 14 S. C. Boca, M. Potara, A. M. Gabudean, A. Juhem, P. L. Baldeck and S. Astilean, *Cancer Lett.*, 2011, **311**, 131–140.
- 15 P. Pallavicini, A. Donà, A. Taglietti, P. Minzioni, M. Patrini, G. Dacarro, G. Chirico, L. Sironi, N. Bloise, L. Visai and L. Scarabelli, *Chem. Commun.*, 2014, **50**, 1969–1971.
- 16 J. Wang, G. Liu, K. Leung, R. Loffroy, P.-X. Lu and Y. J. Wáng, *Curr. Pharm. Des.*, 2015, **21**, 5401–5416.
- 17 A. Ambrosone, V. Marchesano, S. Carregal-Romero, D. Intartaglia, W. J. Parak and C. Tortiglione, *ACS Nano*, 2016, **10**, 4828–4834.
- 18 C. Zhan, W. Wang, J. B. McAlvin, S. Guo, B. P. Timko, C. Santamaria and D. S. Kohane, *Nano Lett.*, 2016, **16**, 177–181.
- 19 F. Martín-Saavedra, E. Ruiz-Hernández, C. Escudero-Duch, M. Prieto, M. Arruebo, N. Sadeghi, R. Deckers, G. Storm, W. E. Hennink, J. Santamaría and N. Vilaboa, *Acta Biomater.*, 2017, **61**, 54–65.
- 20 Y. Wang, L. Wang, M. Yan, S. Dong and J. Hao, *ACS Appl. Mater. Interfaces*, 2017, **9**, 28185–28194.
- 21 D. Han, Z. Meng, D. Wu, C. Zhang and H. Zhu, *Nanoscale Res. Lett.*, 2011, **6**, 457.
- 22 W. Zhang, J. Dai, G. Zhang, Y. Zhang, S. Li and D. Nie, *Nanoscale Res. Lett.*, 2018, **13**, 379–389
- 23 G. Xu, S. Liu, H. Niu, W. Lv and R. Wu, *RSC Adv.*, 2014, **4**, 33986–33997.
- 24 N. H. Levi-Polyachenko, E. J. Merkel, B. T. Jones, D. L. Carroll and J. H. Stewart IV,

- Mol. Pharm.*, 2009, **6**, 1092–1099.
- 25 F. Bani, M. Adeli, S. Movahedi and M. Sadeghizadeh, *RSC Adv.*, 2016, **6**, 61141–61149.
- 26 Y. Zeng, Z. Yang, H. Li, Y. Hao, C. Liu, L. Zhu, J. Liu, B. Lu and R. Li, *Sci. Rep.*, 2017, **7**, 43506.
- 27 J.-W. Kim, E. V Shashkov, E. I. Galanzha, N. Kotagiri and V. P. Zharov, *Lasers Surg. Med.*, 2007, **39**, 622–634.
- 28 N. Levi-Polyachenko, C. Young, C. MacNeill, A. Braden, L. Argenta and S. Reid, *Int. J. Hyperth.*, 2014, **30**, 490–501.
- 29 J. Liu, C. Wang, X. Wang, X. Wang, L. Cheng, Y. Li and Z. Liu, *Adv. Funct. Mater.*, 2015, **25**, 384–392.
- 30 J. Deng, Y. You, V. Sahajwalla and R. K. Joshi, *Carbon N. Y.*, 2016, **96**, 105–115.
- 31 C. Puia, C. Zdrehus, C. Iancu, L. Mocan, C. T. Matea, T. Mocan, T. Pop, O. Mosteanu, S. Suciuc and A. D. Buzoianu, *Cell. Mol. Life Sci.*, 2017, **74**, 3467–3479.
- 32 J. C. Bokros, *Carbon N. Y.*, 1977, **15**, 355–371.
- 33 C. Baquey, L. Bordenave, N. More, J. Caix and B. Basse-Cathalinat, *Biomaterials*, 1989, **10**, 435–440.
- 34 P.-Y. Litzler, L. Benard, N. Barbier-Frebourg, S. Vilain, T. Jouenne, E. Beucher, C. Bunel, J.-F. Lemeland and J.-P. Bessou, *J. Thorac. Cardiovasc. Surg.*, 2007, **134**, 1025–1032.
- 35 J. Zhu, J. Wang, J. Hou, Y. Zhang, J. Liu and B. Van der Bruggen, *J. Mater. Chem. A*, 2017, **5**, 6776–6793.
- 36 A. Susarrey-Arce, I. Sorzabal-Bellido, A. Oknianska, F. McBride, A. J. Beckett, J. G. E. Gardeniens, R. Raval, R. M. Tiggelaar and Y. A. Diaz Fernandez, *J. Mater. Chem.*

- B*, 2016, **4**, 3104–3112.
- 37 B. Y. A. A. Miles and S. S. Misra, *J. Hyg. (Lond)*., 1931, **38**, 732–749.
- 38 D. Cai, A. Neyer, R. Kuckuk and H. M. Heise, *J. Mol. Struct.*, 2010, **976**, 274–281.
- 39 F. Rosenburg, E. Ionescu, N. Nicoloso, R. Riedel, F. Rosenburg, E. Ionescu, N. Nicoloso and R. Riedel, *Materials (Basel)*., 2018, **11**, 93.
- 40 S. R. Dhakate, N. Chauhan, S. Sharma, J. Tawale, S. Singh, P. D. Sahare and R. B. Mathur, *Carbon N. Y.*, 2011, **49**, 1946–1954.
- 41 Z. Ni, Y. Wang, T. Yu and Z. Shen, *Nano Res*, 2008, **1**, 273–291.
- 42 D.T. Nguyen, Y.P. Hsieh and M. Hofmann, in *Carbon-related Materials in Recognition of Nobel Lectures by Prof. Akira Suzuki in ICCE*, S. Kaneko, P. Mele, T. Endo, T. Tsuchiya, K. Tanaka, M. Yoshimura, D. Hui, Springer, Switzerland, 1st Edition, 2017, 27–59.
- 43 K. Bustos-Ramírez, A. L. Martínez-Hernández, G. Martínez-Barrera, M. de Icaza, V. M. Castaño and C. Velasco-Santos, *Materials (Basel)*., 2013, **6**, 911–926.
- 44 D. R. Lide, in *CRC Handbook of Chemistry and Physics*, D. R. Lide, CRC Press, New York, 85th Edition, 2003, 6.2.
- 45 T. Muneer and Y. W. Tham, in *Handbook of Measurement in Science and Engineering, Volume One*, M. Kutz, Wiley, New York, 1st Edition, 2013, 692.
- 46 A. Almatroudi, S. Tahir, H. Hu, D. Chowdhury, I. B. Gosbell, S. O. Jensen, G. S. Whiteley, A. K. Deva, T. Glasbey and K. Vickery, *J. Hosp. Infect.*, 2018, **98**, 161–167.
- 47 M. Farhat, M. C. Trouilhé, E. Briand, M. Moletta-Denat, E. Robine and J. Frère, *J. Appl. Microbiol.*, 2010, **108**, 1073–1082.
- 48 J. Wen, in *Physical Properties of Polymers Handbook*, J. E. Mark, Springer, New York, 2nd Edition, 2007, 145–154.

- 49 K. . Gschneidner, in *CRC Handbook of Chemistry and Physics*, D. R. Lide, CRC Press, New York, 85th Edition, 2003, 4.135.
- 50 Y. Ueki, T. Aoki, K. Ueda and M. Shibahara, *Int. J. Heat Mass Transf.*, 2017, **113**, 1130–1134.
- 51 M. L. V. Ramires, C. A. Nieto de Castro, Y. Nagasaka, A. Nagashima, M. J. Assael and W. A. Wakeham, *J. Phys. Chem. Ref. Data*, 1995, **24**, 1377–1381.
- 52 J. B. Emerson, R. I. Adams, C. M. B. Román, B. Brooks, D. A. Coil, K. Dahlhausen, H. H. Ganz, E. M. Hartmann, T. Hsu, N. B. Justice, I. G. Paulino-Lima, J. C. Luongo, D. S. Lympelopoulou, C. Gomez-Silvan, B. Rothschild-Mancinelli, M. Balk, C. Huttenhower, A. Nocker, P. Vaishampayan and L. J. Rothschild, *Microbiome*, 2017, **5**, 86.
- 53 M. Berney, H. U. Weilenmann and T. Egli, *Microbiology*, 2006, **152**, 1719–1729.
- 54 G. Fang, H. Li and X. Liu, *Mater. Chem. Phys.*, 2010, **122**, 533–536.
- 55 D. R. Lide, in *CRC Handbook of Chemistry and Physics*, D. R. Lide, CRC Press, New York, 85th Edition, 2003, 3.1-3.736.
- 56 ISO22196, *Meas. Antibact. Act. Plast. other non-porous surfaces*, 2011.
- 57 J. K. M. Knobloch, S. Tofern, W. Kunz, S. Schütze, M. Riecke, W. Solbach and T. Wuske, *PLoS One*, 2017, **12**, 187442.
- 58 E. R. Sanders, *J. Vis. Exp.*, 2012, **3064**, 1–18.
- 59 M. T. Madigan, K. S. Bender, D. H. Daniel, H. Buckley, W. M. Sattley and D. A. Stahl, *Brock Biology of Microorganisms*, M. T. Madigan, K. S. Bender, D. H. Daniel, H. Buckley, W. M. Sattley and D. A. Stahl, Pearson Education Limited, London, 15th Edition, 2019.

## 4.7 Appendix

### 4.7.1 Characterisation of Type I Materials

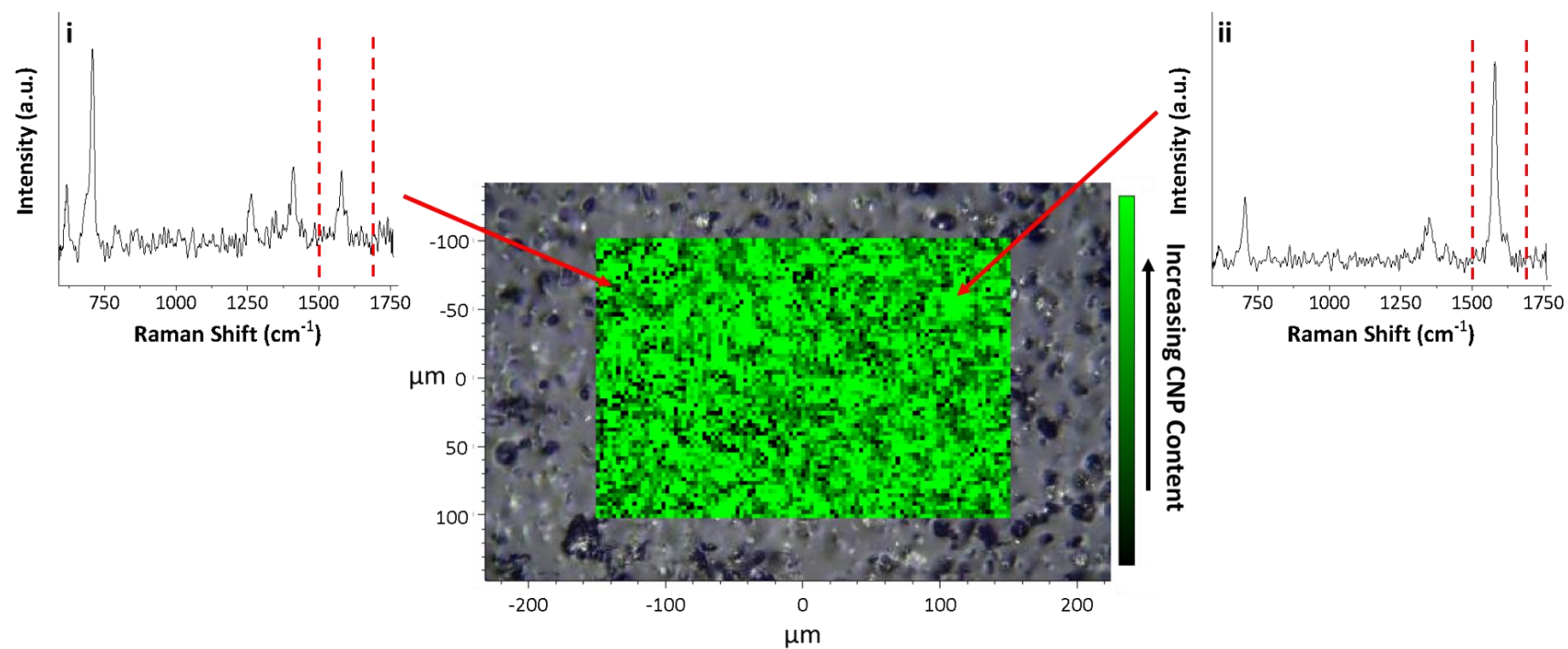


**Figure A4. 1** Representative Raman map for the distribution of CNP across the surface of type I material showing a representative Raman spectrum for low (i) and high (ii) CNP content in the type I material.

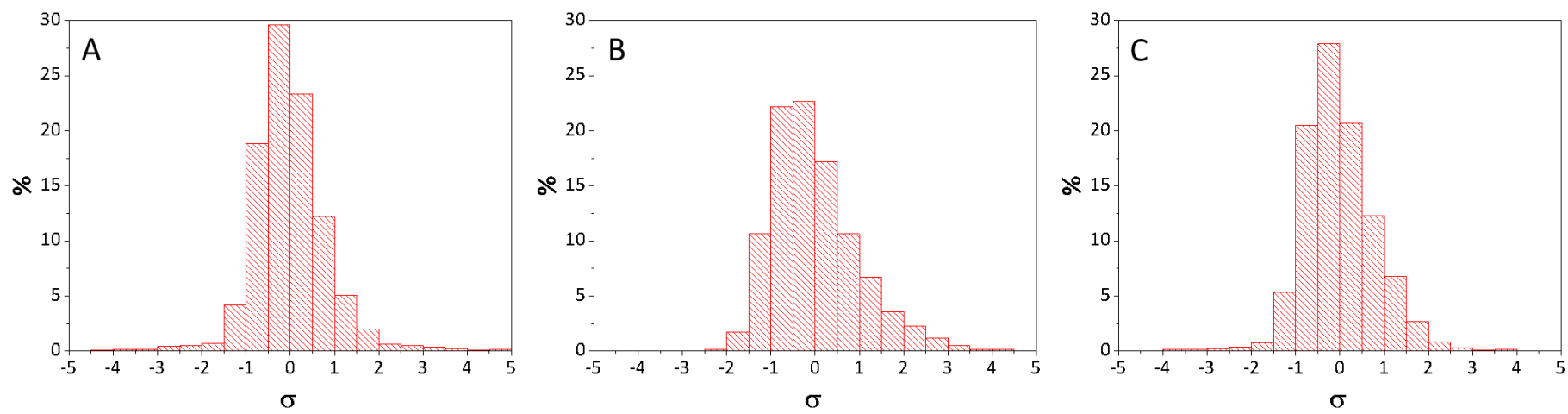


**Figure A4. 2** Normalised histograms showing the distribution of CNP across the surface of 3 individual type I materials

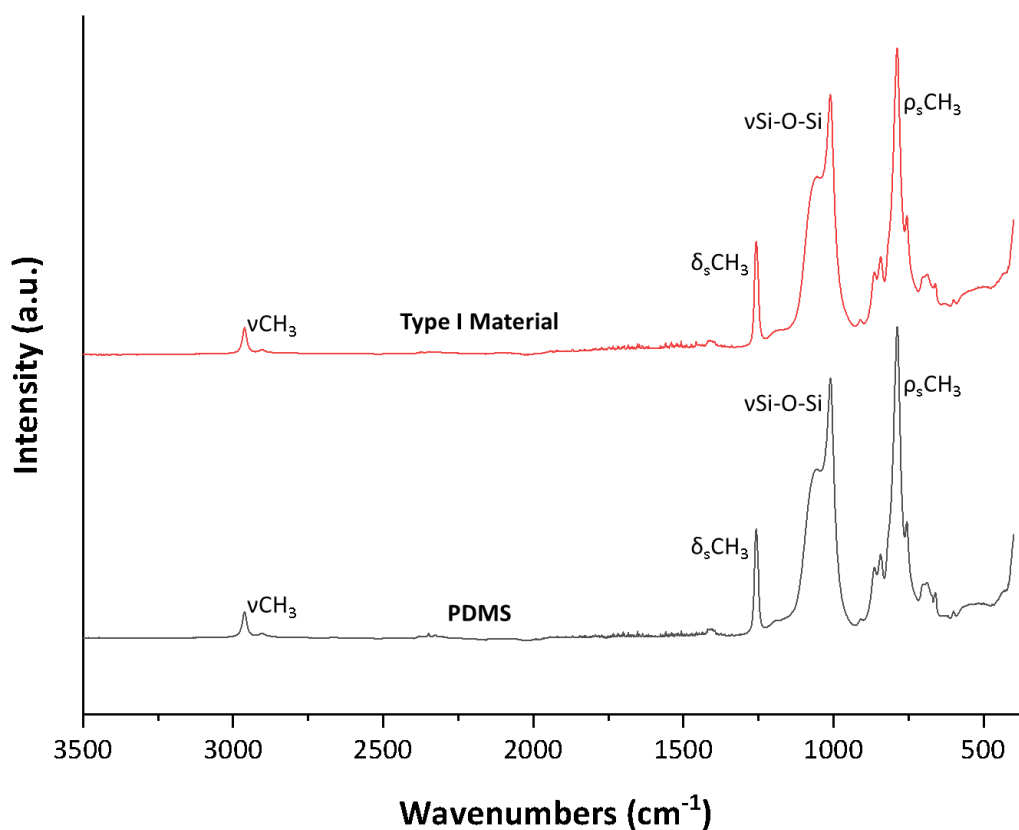


**Figure A4. 3** ATR-IR spectroscopy data of PDMS (Black) and type I material (Red).

#### 4.7.2 Investigating the Photothermal Effect of Type I Materials

**Table A4. 1** Temperatures measured by K type thermocouple at  $T_0$  and  $T_{5 \text{ Mins}}$  for the type I material during photothermal experiments at different laser powers.

Power Density (mW/ cm <sup>2</sup> )	Temperature at $T_0$ (°C)	Temperature at $T_{5 \text{ Mins}}$ (°C)	$\Delta T$
624	26.5 ± 1.4	42.3 ± 0.5	15.8
881	26.5 ± 0.3	49.0 ± 0.5	22.5
1174	27.8 ± 0.3	59.1 ± 1.6	31.3
1394	27.6 ± 0.3	66.6 ± 1.5	39
1651	27.2 ± 0.2	69.5 ± 1.5	42.3

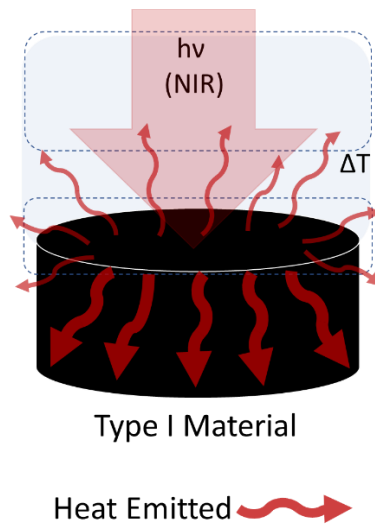


**Figure A4. 4** Schematic showing heat dissipation of the type I material under photothermal treatment, where a large % of heat may be dissipated into the bulk material and therefore only a small fraction of this is able to increase the temperature of the media in the sample well.

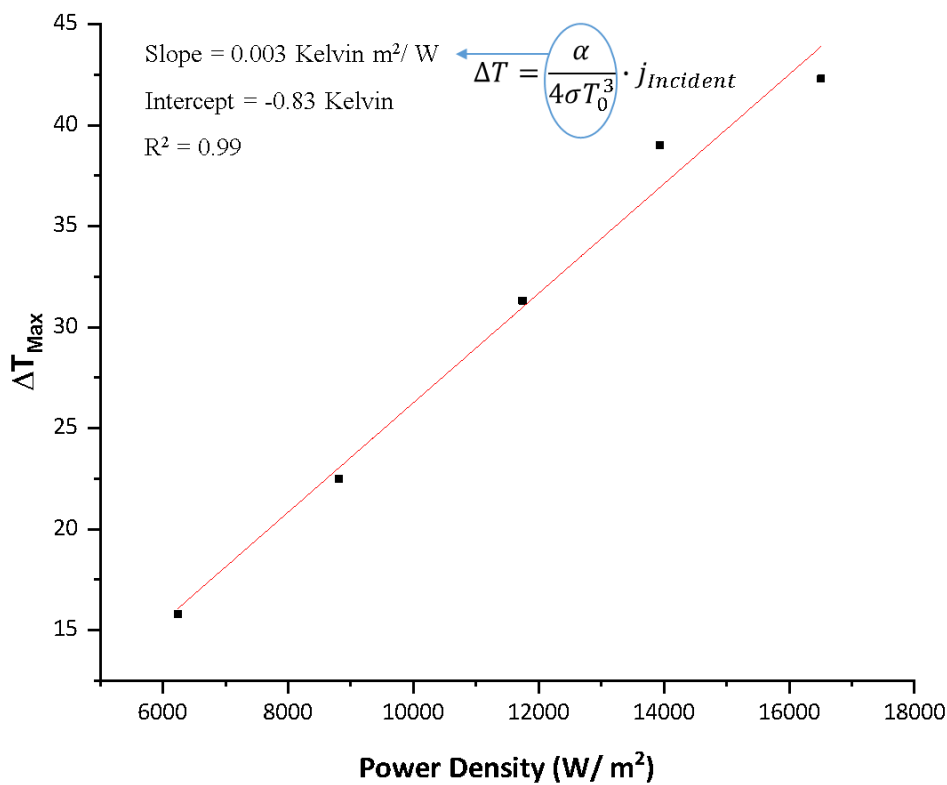


**Figure A4. 5** Graph used to determine  $\alpha$ , showing the linear relationship between power density in  $W/m^2$  vs the temperature at stationary conditions ( $\Delta T_{max}$ ) measured with the thermocouple during photothermal experiments with the type I material.  $T_0$  is the starting temperature and  $\sigma$  is the Stefan-Boltzmann constant ( $5.67 \times 10^{-8} W m^{-2} K^{-4}$ ).<sup>45</sup>

### 4.7.2.2 Linearisation of the Stefan-Boltzmann Equation

The Stefan–Boltzmann law describes the power radiated from a black body in terms of its temperature and states that the total energy emitted from the surface of an insulated black body ( $j^*$ ) is equal to the fourth power of its absolute temperature, as seen in equation A4. 1.<sup>45</sup>

$$j^* = \sigma T^4 \quad \text{Equation A4. 1}$$

Considering the broad light-absorption spectrum of the type I material (Figure 4. 11), we can assume that the type I material behaves as a black body. As a result, the energy emitted from the surface of the type I material in the form of heat will be:

$$\Delta J^* = \sigma(T^4 - T_0^4) \quad \text{Equation A4. 2}$$

Where  $T_0$  is temperature of the surrounding environment. This can then be factorised to form equation A4. 3:

$$\Delta J^* = \sigma(T^2 - T_0^2)(T^2 + T_0^2) \quad \text{Equation A4. 3}$$

And subsequently equation A4. 4:

$$\Delta J^* = \sigma(T - T_0)(T + T_0)(T^2 + T_0^2) \quad \text{Equation A4. 4}$$

If we introduce  $T - T_0 = \Delta T$  and  $T = T_0 + \Delta T$ , this expression assumes the following equation:

$$\Delta J^* = \sigma(2T_0 + \Delta T)(\Delta T^2 + 2\Delta T T_0 + 2T_0^2)(T^2 + T_0^2) \cdot \Delta T \quad \text{Equation A4. 5}$$

In our case the temperature increase ( $\Delta T$ ) observed under stationary conditions (Figure 4.17 and see appendix, Table A4. 1) is relatively small compared to the initial starting temperature ( $T_0$  in kelvins) and we can write equation 4.5 as follows:

$$\Delta J^* = 4\sigma T_0^3 \Delta T \quad \text{Equation A4. 6}$$

## 4.7.2 Planktonic and Sessile Heat Shock Experiments

**Table A4. 2** Temperatures measured by K type thermocouple at  $T_0$  and  $T_{5 \text{ Mins}}$  for the planktonic heat shock experiments at different nominal temperatures

Nominal Heat Shock Temperature (°C)	Temperature at $T_0$ (°C)	Temperature at $T_{5 \text{ Mins}}$ (°C)
50	$46.5 \pm 0.1$	$50.2 \pm 0.3$
60	$56.1 \pm 0.2$	$60.1 \pm 0.1$
70	$63.5 \pm 0.7$	$68.9 \pm 0.3$
80	$73.1 \pm 0.4$	$79.9 \pm 0.2$
90	$82.1 \pm 0.9$	$87.8 \pm 0.9$

**Table A4. 3** Temperatures measured by K type thermocouple at  $T_0$ ,  $T_{5 \text{ Mins}}$  and  $T_{10 \text{ Mins}}$  for the type I material during sessile heat shock experiments at different nominal temperatures.

Nominal Heat Shock Temperature (°C)	Temperature at $T_0$ (°C)	Temperature at $T_{5 \text{ Mins}}$ (°C)	Temperature at $T_{10 \text{ Mins}}$ (°C)
50	$41.4 \pm 0.3$	$50.1 \pm 0.1$	$50.1 \pm 0.1$
60	$49.4 \pm 0.6$	$59.4 \pm 0.2$	$59.4 \pm 0.1$
70	$54.2 \pm 0.1$	$67.9 \pm 0.1$	$68.1 \pm 0.2$
80	$59.1 \pm 1.0$	$76.3 \pm 0.1$	$76.4 \pm 0.3$
90	$66.6 \pm 0.7$	$85.3 \pm 0.4$	$86.1 \pm 0.2$

#### 4.7.4 Fabrication and Characterisation of Type II Materials

**Table A4. 4** Table showing the mass of dodecanoic acid loaded in the type I material.

<b>Mass of Sample Before Loading (g)</b>	<b>Mass of Sample After Loading (g)</b>	<b>Mass of Loaded Dodecanoic acid (g)</b>
1.0061	1.0534	0.0473
0.9666	1.0099	0.0433
0.9830	1.0210	0.0380

**Table A4. 5** Photothermal release data for the type II material, before and after irradiation at 881 mW/cm<sup>2</sup>.

<b>Average Mass of Samples Before Irradiation (mg)</b>	<b>Average Mass of Samples After Irradiation (mg)</b>	<b>Mass of Dodecanoic Acid Released After Irradiation (mg)</b>	<b>% Dodecanoic Acid Released/ g Type I Material</b>
1053.6 ± 0.5	1048.6 ± 0.8	5.0	11
1052.2 ± 0.4	1048.1 ± 0.4	4.3	10
1054.3 ± 0.3	1047.7 ± 0.1	6.7	15



# Chapter 5

## **Synthesis and Stability of Complex Nano-Hybrid Satellite Materials for Photocatalysis: Applications Towards Plasmonically Enhanced Evolution of Hydrogen from Water**

### 5.1 Introduction

#### 5.1.1 Photocatalytic Evolution of Hydrogen from Water

Photocatalytic evolution of hydrogen ( $H_2$ ) from water ( $H_2O$ ) has received much attention in the last few decades for its potential to provide a clean and sustainable energy alternative.<sup>1-3</sup> Both sunlight and water are in high abundance, making this method ideal to produce sustainable fuel sources.<sup>4</sup> Pioneering work as early as 1972 reported the production of hydrogen from water using a Titania ( $TiO_2$ ) semiconductor under ultra-violet (UV) irradiation.<sup>5</sup> However, UV light from the sun is predominately filtered out by ozone in the atmosphere<sup>6</sup> and therefore, other types of semiconductors for photocatalytic production of hydrogen from water are under investigation.

During the photocatalytic evolution of hydrogen from water, electrons within the valence band of semiconductor photocatalysts are excited into the conduction band by incident light with energy equal to or greater than the band-gap energy, leaving behind positively charged holes in the valence band. Electrons and holes can either recombine releasing the energy as heat or

light, or migrate to surface active sites of the semiconductor and participate in the hydrogen ( $H_2$ ) evolution reaction.<sup>7,8</sup> The electrons in the conduction band are used to reduce  $H^+$  to  $H_2$  known as the reductive hydrogen evolution reaction (HER), while the holes in the valence band are involved in the oxidation reaction of water to produce oxygen ( $O_2$ ), known as the oxidative oxygen evolution reaction (OER) (Figure 5. 1).<sup>8,9</sup>

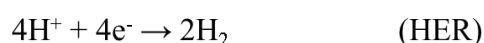
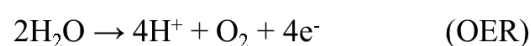


**Figure 5. 1** Overall reaction scheme for evolution of  $H_2$  from  $H_2O$ , where OER is the oxidative oxygen evolution reaction, HER is the hydrogen reductive evolution reaction and 4.92 eV is the Gibbs free energy ( $\Delta G$ ) stored by two  $H_2O$  molecules.<sup>8,9</sup>

In the hydrogen evolution process from water, 4 electrons ( $4e^-$ ) are required to be rearranged between the reactants and products, with the free energy change ( $\Delta G = 4.92 \text{ eV}$ ), representing the energy stored by two water molecules (Figure 5. 1). As a result, the theoretical minimal energy of 1.23 eV per electron is required for the dissociation of water to proceed, meaning that semiconductor materials with a minimal band gap of 1.23 eV are needed to drive the water reduction and oxidation reactions.<sup>8,9</sup> In order to initiate the hydrogen evolution from water, the potential energy levels of conduction and valence bands to facilitate both the reduction and the oxidation of water are also important. The potential energy of the lowest level of the conduction band must be more negative than the reduction potential of  $H^+$  to  $H_2$ , whereas the potential energy of highest level of the valence band needs to be more positive than the oxidation potential of water to oxygen (1.23 eV) (Figure 5. 2).<sup>8,10</sup>

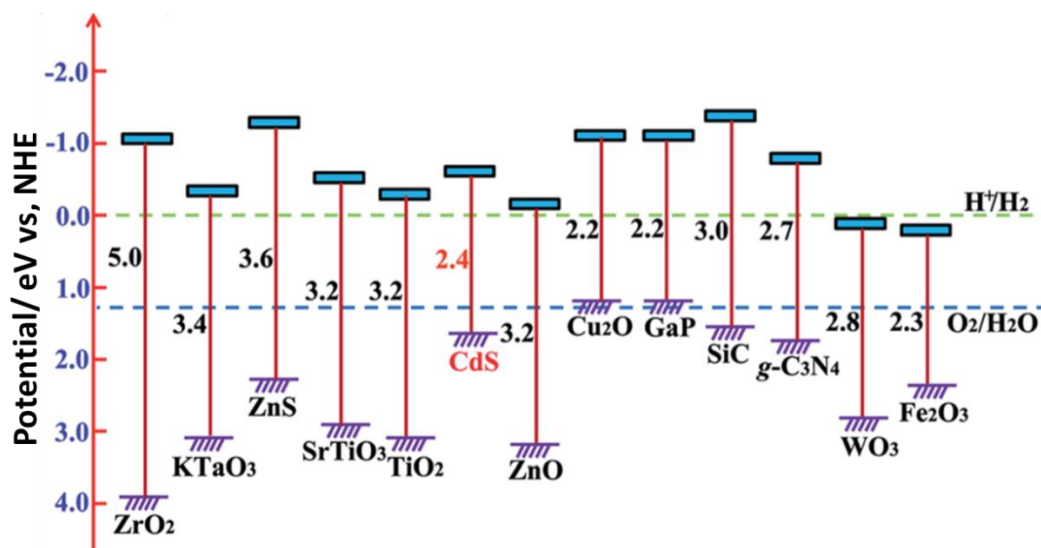


**Figure 5. 2** Relationship between band structure of semiconductor and redox potentials for the evolution of H<sub>2</sub> from H<sub>2</sub>O. Figure adapted from Yuan *et al.*<sup>8</sup>

There are many semiconductors which can provide the band structure requirement for the evolution of hydrogen from water (Figure 5. 2) and their electronic structures match well with the redox potential of water. However, many of these materials only absorb light in the UV region of the electromagnetic spectrum (EMS)<sup>11</sup> and can often suffer from parasitic loss, such as photoanodic corrosion, because they do not possess the required band alignments to catalyse both proton reduction and water oxidation reactions.<sup>12,13</sup> In addition, semiconducting materials possessing the correct band alignments for sufficient catalysis can also suffer from slow reactions at the surface, due to different kinetics of the two water splitting half reactions.<sup>14,15</sup> To overcome these limitations, semiconducting materials with an absorption in the visible region of the EMS have been explored, utilising a co-catalyst (e.g. Platinum (Pt) or Nickel (Ni)) as an electron sink for an accelerated product formation and a hole scavenger (e.g. sodium sulphite (Na<sub>2</sub>SO<sub>3</sub>)) as an electron donor to avoid photoanodic corrosion.<sup>16–21</sup> Materials such as chalcogenide based semiconductors (CdS, CdSe) in the form of quantum dots (QDs) feature prominently in studies as hydrogen evolution photocatalysts, with Pt and Ni often utilised as co-catalysts (Figure 5. 3) and remain the popular choice, as their absorption spans a broad range in the visible spectrum.<sup>19,22–27</sup>

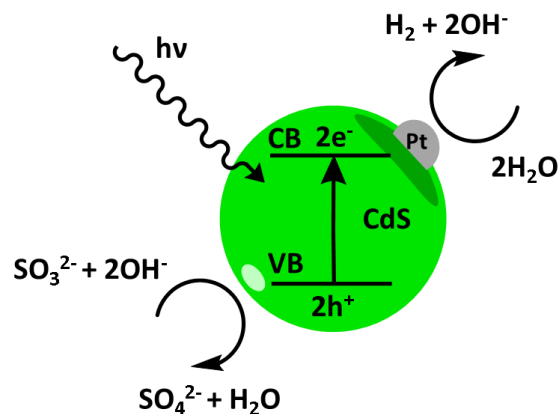


**Figure 5. 3** Schematic representation for the photocatalytic evolution of  $\text{H}_2$  from  $\text{H}_2\text{O}$  using Pt (co-catalyst) decorated chalcogenide based QDs in the presence of hole scavenger  $\text{Na}_2\text{SO}_3$ . Figure adapted from Li *et al.*<sup>19</sup>

### 5.1.2 Chalcogenide Based Quantum Dots (QDs)

Chalcogenide based QDs have pioneered a vast effort in the photocatalytic evolution of hydrogen from water and are a promising material in this field due to their unique tuneable optical and electronic properties.<sup>19,22–27</sup> QDs are quasispherical nanocrystals, with a physical radius comparable to the exciton Bohr radius of the material. The exciton Bohr radius is a quantity used to describe the distance between an electron-hole pair and defines the scale at which quantum confinement effects begin to affect the overall properties of a semiconductor nanocrystal, resulting in a change in their optical and electronic properties. As the size of the QD decreases relative to the exciton Bohr radius of the material, the energy levels become discrete and the band gap of the material gets larger (Figure 5. 4), resulting in shifts in the absorption wavelength of the material.<sup>28,29</sup> This remarkable property makes the QDs ideal for photocatalysis and has even proven to display size dependent effects on the rate of photocatalytic hydrogen evolution from water.<sup>19</sup>

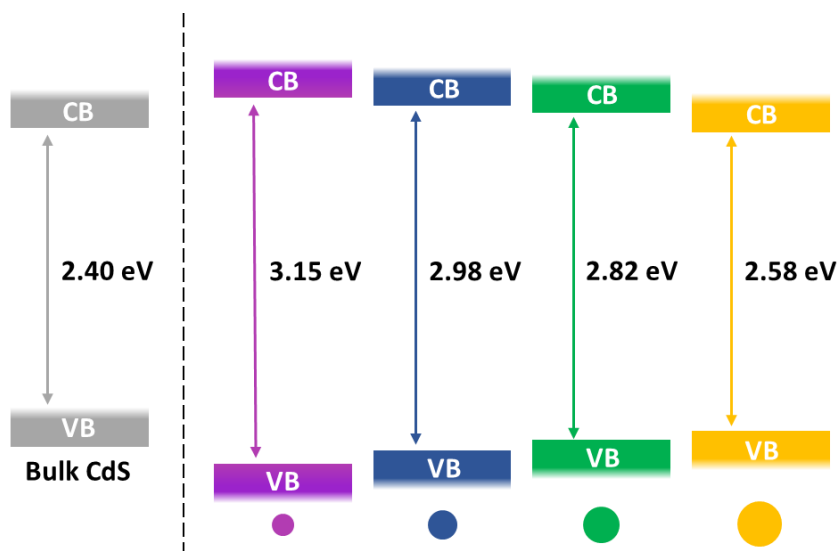


**Figure 5. 4** Schematic showing the increase in the band gap energy levels of CdS QDs as the size of the QD decreases. The QD sizes are 2.8 nm (purple), 3.1 nm (blue), 3.7 nm (green) and 4.6 nm (orange). The band gap energy for bulk CdS is shown for comparison. The band gap energies, QD size and figure are adapted from Li *et al.*<sup>19</sup>

However, due to stability and efficiency issues, these nanomaterials are still unsustainable for the photocatalytic evolution of hydrogen from water. As a result, there is increasing interest in finding methods to enhance their photocatalytic properties.<sup>4</sup> Self-assembly strategies can offer a way forward, by combining the properties of different nanomaterials for an increased photocatalytic effect.

### 5.1.3 Self-Assembly of Nanomaterials

Self-assembly refers to the process by which nanomaterials or molecules spontaneously organise into ordered structures, due to direct or indirect interactions,<sup>30</sup> and has emerged as a powerful technique for controlling the structure and properties of both organic and inorganic nanomaterials for a variety of applications.<sup>31–33</sup> The fabrication of self-assembled nanomaterials is challenging, and requires the careful design and fabrication of building blocks, to avoid uncontrolled aggregation.<sup>30,31,33,34</sup> Exploiting molecular interactions, such as covalent bonds, dipolar interactions, hydrogen bonding and donor-acceptor interactions, nanomaterials can be functionalised, to create ordered complex nanostructures.<sup>32,33</sup>

Complex nanostructures, formed by the self-assembly of nanomaterials, can display new electronic, magnetic and optical properties, as a result of interactions between the different components.<sup>31</sup> Exploiting new properties of self-assembled nanomaterials is of particular interest in catalytic applications, including the photocatalytic production of clean and sustainable fuels. One class of nanomaterial that has shown great potential in this area of research are plasmonic nanomaterials.<sup>4,35,36</sup> Plasmonic nanomaterials can be coupled with semiconducting materials by self-assembly to form a nano-hybrid material, with the potential to enhance the optical and photocatalytic processes of semiconductor photocatalysts.<sup>4,35,36</sup>

#### 5.1.4 Plasmonic Nanomaterials

Plasmonic nanomaterials have been known for their photoactive properties for over 160 years, first demonstrated by Michael Faraday in the 1850s with the formation of gold colloids as a by-product from his experiments with gold leaf.<sup>37</sup> The collective oscillation of free charge carriers (i.e. conduction band electrons for noble metals) localised at the surface of noble metal nanomaterials interact strongly with electromagnetic irradiation at specific frequencies and generates a highly enhanced and strongly localised electromagnetic field, known as local surface plasmon resonance (LSPR) (Figure 5. 5). As a result of this plasmon resonance, the nanomaterial can display unusually strong scattering and absorption properties.<sup>35,38</sup> The local electric field can potentially activate semiconductor nanomaterials, as well as increase their optical and catalytic activity.<sup>35</sup>

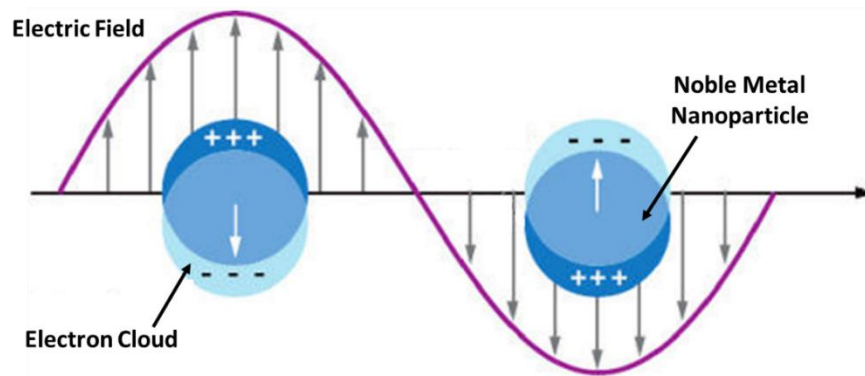


**Figure 5. 5** Schematic showing local surface plasmon resonance. Figure adapted from reference 38.<sup>38</sup>

The frequency in which the plasmon resonance of the metal nanomaterials occurs can be tuned by varying different parameters, such as size, morphology and chemical composition of the nanomaterials (e.g. Ag or Au and alloys) (Figure 5. 6).<sup>39-47</sup> Adjusting the spacing between individual nanoparticles and varying the dielectric constant of the surrounding medium can also change the resonance frequency of the plasmon.<sup>38,48,49</sup>

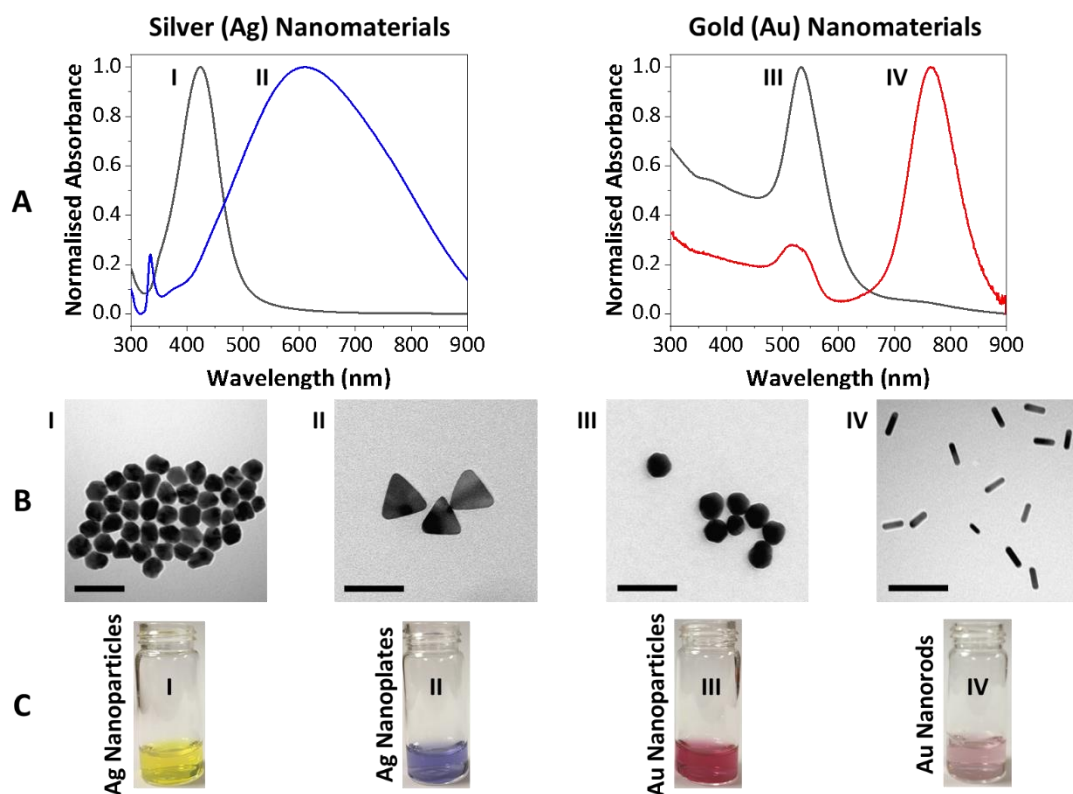


**Figure 5. 6** Examples of some plasmonic nanomaterials with different morphology and chemical composition. (A) Normalised absorbance spectrum for each nanomaterial, (B) TEM images for each nanomaterial (Scale bars are 100 nm) and (C) Nanomaterial colloidal solutions in H<sub>2</sub>O. (I) Quasispherical silver nanoparticles, (II) Silver nanoplates, (III) Quasispherical gold nanoparticles and (IV) Gold nanorods.

Several methods have been used to fabricate plasmonic nanomaterials including electron beam lithography,<sup>50</sup> seed mediated synthesis<sup>39,41,44–46,51,52</sup> and template assisted synthesis.<sup>53</sup> However, the most commonly used method for fabricating plasmonic nanomaterials is still the seed mediated synthesis, also known as the Turkevich method for the synthesis of gold nanoparticles.<sup>51,52</sup> This synthetic method is based on the formation of gold nanoparticles (AuNPs) via the reduction of chlorauric acid (HAuCl<sub>4</sub>) in the presence of sodium citrate (Na<sub>3</sub>Ct) as the reducing agent. The well-known Turkevich<sup>51</sup> synthesis has been modified and adapted numerous times allowing for the fabrication of AuNPs in a wide range of sizes and has also paved the way for the production of other plasmonic nanomaterials (e.g. silver nanoparticles (AgNPs)). Inspired by the Turkevich<sup>51</sup> synthesis, Lee and Meisel<sup>54</sup> produced silver nanoparticles (AgNPs) via the reduction of silver nitrate (AgNO<sub>3</sub>) using Na<sub>3</sub>Ct. However, unlike the AuNPs produced in the Turkevich<sup>51</sup> synthesis, the AgNPs were highly polydisperse. To overcome this problem, there are a number of new strategies leading to the controlled size synthesis of AgNPs.<sup>46,55,56</sup> For example, Bastus *et al*<sup>46</sup> showed that the addition of a complexing agent, such as tannic acid can be used to control the reduction kinetics of the reaction, leading to the formation of highly monodispersed AgNPs in a range of sizes.

Plasmonic nanomaterials are widely known for their application in several fields, such as surface enhanced Raman spectroscopy (SERS),<sup>38,54</sup> photocatalysis<sup>35</sup> and plasmonic hyperthermia.<sup>57–59</sup> However, only recently these materials have been considered for their role in plasmonic enhanced catalysis, in particular for the evolution of hydrogen from water.<sup>35,36</sup> Following a self-assembly approach, a few strategies have already been published for the formation of plasmonic-semiconductor hybrid materials with increased photocatalytic effects.<sup>60–65</sup> For example, Au-TiO<sub>2</sub> hybrids have been fabricated by Silva *et al*<sup>64</sup> for the photocatalytic production of hydrogen from water, allowing the material to absorb light both in the UV and visible region of the EMS. In these photocatalytic systems, it is believed that the plasmonic nanomaterials not only extends the absorption range of the material, but the

local electric field of the LSPR can also inject ‘hot’ electrons (excited electrons with higher energy than the metal Fermi energy) directly into the conduction band of the semiconductor, resulting in an enhanced photocatalytic activity.<sup>36,64</sup>

In some cases, however, the direct injection of ‘hot’ electrons is not applicable and the close proximity of plasmonic nanomaterials to semiconductor photocatalysts can result in quenching.<sup>66,67</sup> To overcome this obstacle, a dielectric spacer layer, such as silica ( $\text{SiO}_2$ ) can be placed between the plasmonic nanomaterial and the semiconductor to prevent quenching, allowing enhancement by the local electric field of the plasmonic nanomaterial.<sup>63,65</sup> For example, Torimoto *et al*<sup>63</sup> fabricated a AuNP@ $\text{SiO}_2$  core shell structure coupled with CdS@ $\text{SiO}_2$  QDs, with Rh clusters photodeposited on the surface of the QDs as a co-catalyst to drive the hydrogen evolution half reaction (Figure 5. 7). As a result, an enhancement factor of 1.5 was reported. However, it is unclear how this reaction proceeds, considering that in this study metal cations are not reduced directly on the surface of the semi-conducting material by surface trapped photoexcited electrons,<sup>19–21,68,69</sup> as the CdS QDs were coated with a layer of  $\text{SiO}_2$ .<sup>63</sup> This is unusual, considering that in photodeposition, surface trapped photoexcited electrons are used to reduce metal cations directly at the surface of the QD.

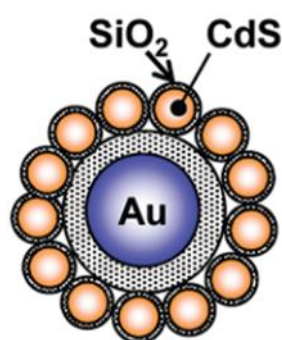


**Figure 5. 7** Schematic adapted from Torimoto *et al*,<sup>63</sup> showing the design of the plasmonic-semiconductor nano-hybrid material for plasmonically enhanced  $\text{H}_2$  evolution from  $\text{H}_2\text{O}$ . The nano-hybrid structure is composed of a AuNP plasmonic core and CdS@ $\text{SiO}_2$  QDs decorated with Rh clusters, separated by a  $\text{SiO}_2$  dielectric layer.

The enhancement factor for the evolution of hydrogen from water with these types of self-assembled hybrid materials has also proved to be dependent on the SiO<sub>2</sub> layer thickness.<sup>63,65</sup> For example, Khan *et al*<sup>65</sup> reported a distance dependence on the enhancement for photocatalytic production of hydrogen from water using a Pd/TiO<sub>2</sub> photocatalyst coated with thin films of gold, separated by an SiO<sub>2</sub> dielectric layer, with an enhancement factor of 4.

These previous studies introduced several strategies for increasing the photocatalytic activity of semiconductors towards the evolution of hydrogen from water using plasmonic nanomaterials, however these systems are still not sustainable. In addition, the stability of these photocatalytic systems under working conditions is somewhat overlooked in the literature and needs to be considered for the sustainable use of these photocatalytic materials. For a photocatalytic hydrogen evolution system to be sustainable, the photocatalysts not only need to generate enough hydrogen to compete with fossil fuels, but they also need to be re-usable and robust.<sup>13</sup> Gold nanomaterials have featured prominently in these studies, but little is known about the effect of AgNPs in these photocatalytic systems. AgNPs exhibit a sharp and intense plasmon peak at a lower wavelength than AuNPs in the visible region of the EMS (Figure 5. 6), and therefore the local electric field generated from the AgNPs is higher in energy than the local electric field of AuNPs. The increase in energy of local electric field could potentially improve the photocatalytic ability of semiconductor photocatalysts (e.g. chalcogenide based QDs) towards the evolution of hydrogen from water.

Herein, we report a novel wet chemical approach to fabricate a nano-hybrid satellite material using AgNPs as a plasmonic core and CdS QDs decorated with Pt clusters as satellite catalytic units. These two nanomaterials are separated by a dielectric spacer layer to avoid quenching. Using this type of structure, will allow for more photocatalytic units to be enhanced by the

plasmonic core. The photocatalytic activity towards the evolution of hydrogen from water and stability of these nanomaterials under active working conditions is also investigated.

## 5.2 Experimental Details

### 5.2.1 Chemicals

Cadmium oxide (CdO, 99.998%), 1-octadecene (ODE, technical grade, 90%), oleic acid (technical grade, 90%), ammonium hydroxide (NH<sub>4</sub>OH, 28% w/v), 4-(2-Hydroxyethyl) piperazine-1-ethanesulphonic acid (HEPES, 99.5%) and 2-(4-morpholinyl) ethanesulphonic acid hydrate (MES, 99%) were purchased from Alfa Aesar. Hydrochloric acid (HCl, 37% w/v), nitric acid (HNO<sub>3</sub>, 70% w/v), hexane (HPLC grade), methanol (MeOH, reagent grade), ethanol (EtOH, absolute 99%), chloroform (CHCl<sub>3</sub>, analytical grade) and sodium sulphite (Na<sub>2</sub>SO<sub>3</sub>, anhydrous) were purchased from Fisher Scientific. (3-aminopropyl) triethoxysilane (APTES, 98%), 3-(cyclohexylamino) propanesulphonic acid (CAPS, 98%) and 4-(4,6-dimethoxy-1,3,5-triazin-2-yl)-4-methylmorpholinium chloride (DMTMM, 97%) were purchased from Flurochem. Tetraethyl orthosilicate (TEOS, 99%) and triethanolamine (TEOA, 99%) were purchased from Merck. L-ascorbic acid (AA, 99%) was purchased from VWR. All remaining chemicals listed were purchased from Sigma Aldrich: silver nitrate (AgNO<sub>3</sub>, 99%), trisodium citrate dihydrate (Na<sub>3</sub>Ct, 99%), tannic acid (ACS reagent), sulphur (99.5%), 3-mercaptopropionic acid (MPA, 99%), tetramethylammonium hydroxide (TMAH, 97%), chloroplatinic acid hexahydrate (H<sub>2</sub>PtCl<sub>6</sub>·6H<sub>2</sub>O, BioXtra), 4-methylmorpholine (NMM, 99%) and oxalic acid (99%). All chemicals were used as received without further purification. Deionised water (DI) (Thermo Scientific Barnstead Smart2Pure), with a resistivity of 18 MΩ·cm was used throughout all experiments.

## 5.2.2 Fabrication of Nanomaterials

The fabrication of the nano-hybrid satellite material followed a wet chemical approach (Figure 5. 8) using several methods adapted from literature.<sup>19,22,46,70–73</sup>

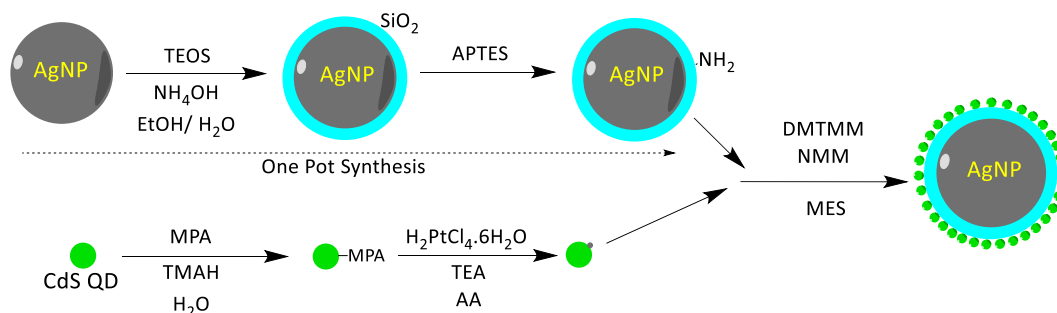


**Figure 5. 8** Reaction scheme for the fabrication of the AgNP@SiO<sub>2</sub>-CdS@Pt nano-hybrid satellite material.

**Synthesis of silver nanoparticles (AgNPs):** AgNPs were synthesised using a seed mediated approach adapted from Bastus *et al.*<sup>46</sup> All glassware was cleaned with aqua regia (3 HCl: 1 HNO<sub>3</sub>) and then rinsed thoroughly a minimum of 3 times with deionised (DI) water prior to use. In a 50 ml flask was added 44 ml of DI water, followed by the addition of 5 ml 50 mM sodium citrate (Na<sub>3</sub>Ct) and a 1 ml of 50 mM tannic acid to give a final volume of 50 ml. The solution was then heated under reflux at 110°C until bubbling. 1 ml of 25 mM silver nitrate (AgNO<sub>3</sub>) was then added rapidly to the solution forming a yellow coloured solution of AgNPs. The solution was then left to cool to room temperature (RT) (25°C) and centrifuged at 12000 Relative Centrifugal Force (RCF) for 30 minutes. The supernatant was removed and the AgNPs were then re-dispersed back to their initial volume in 2 mM Na<sub>3</sub>Ct.

**Preparation of AgNP@SiO<sub>2</sub>-NH<sub>2</sub>:** After fabrication of the AgNPs, they were coated with silica (SiO<sub>2</sub>) following a modified Stöber process<sup>70,71</sup> and further functionalised with (3-aminopropyl) triethoxysilane (APTES). In a typical synthesis, 3 ml of AgNP stock solution was centrifuged at 12000 RCF for 20 minutes. The supernatant was removed and the AgNPs were re-dispersed in 180 µl DI water. 62.5 µl of tetraethyl orthosilicate (TEOS) was the added

to the re-dispersed AgNPs. The mixed solution was then subject to vortex for 2 minutes. The mixture was then injected rapidly into a 50 ml flask containing 3 ml EtOH and 250  $\mu$ l of ammonium hydroxide (NH<sub>4</sub>OH) and stirred vigorously for 10 minutes. 62.5  $\mu$ l of APTES was then added to the solution and stirred for a further 4 minutes. An excess (40 ml) of EtOH was then added to quench the reaction, thus preventing further hydrolysis. The solution was collected and centrifuged at 12000 RCF for 20 minutes. The now coated AgNPs were re-dispersed in DI water.

**Synthesis of cadmium sulphide (CdS) QDs:** CdS QDs were fabricated following a procedure detailed by Yu and Peng.<sup>19,22</sup> In a three-necked 50 ml flask (flask 1) fitted with a thermocouple and a septum, connected to a Schlenk line, 57 mg of CdO, 20.25 ml 1-octadecene (ODE) and 2.15 ml oleic acid were mixed. In a separate two-necked flask (flask 2) fitted with a septum and connected to a Schlenk line, was added 12 ml of sulphur solution (38.5 mg sulphur in 60 ml ODE). Both solutions were degassed for 30 minutes by purging with N<sub>2</sub>. Flask 1 was heated to 300°C forming a clear colourless solution. The flask was then cooled to 250°C and allowed to stabilise. After cooling, 11.5 ml of the sulphur precursor in flask 2 was then injected rapidly into flask 1, while maintaining rapid stirring. The temperature of the solution was then brought back up to 250°C and held at that temperature for 10 minutes allowing the CdS nanocrystals to form. The heating jacket was then removed, and the solution was allowed to cool to RT. To purify the QDs, the reaction solution was divided into centrifuge tubes (~11 ml) and treated with a mixture of 10 ml hexane and 20 ml ethanol (EtOH), resulting in the formation of a yellow precipitate. The tubes were then cooled at 5 °C for 1 hour and centrifuged at 15000 RCF for 10 minutes and the clear supernatant was removed. The purification steps were repeated twice, and the final precipitate was re-dispersed back to the initial volume of the reaction solution in chloroform (CHCl<sub>3</sub>).

**Preparation of MPA functionalised CdS QDs:** A sufficient quantity of CdS QD stock was used to give a final optical density (OD) of 1.5 at a wavelength of 415 nm, in a total volume of 10 ml  $\text{CHCl}_3$  (e.g. 1.725 ml OD 8.7 QDs and 8.275 ml  $\text{CHCl}_3$ ). To this solution 10 ml of DI water and 60 mg of 3-mercaptopropionic acid (MPA) were added. The pH of the solution was then adjusted to ~pH 9.0 via the drop wise addition of 0.5 M tetramethylammonium hydroxide (TMAH). The solution was then transferred to a separating funnel and shook vigorously until the QDs moved into the upper aqueous layer. The biphasic mixture was then allowed to rest for 24 hours prior to discarding the organic  $\text{CHCl}_3$  layer. The QDs were then centrifuged at 15000 RCF for 20 minutes to separate them from any residual  $\text{CHCl}_3$ . The aqueous layer containing the QDs was then transferred carefully into a 5 kDa vivaspin tube and centrifuged at 8000 RCF for 60 minutes. The filtrate was removed and the QDs were re-dispersed in 15 ml DI water and centrifuged again at 8000 RCF for 60 minutes. The purification procedure was repeated once more and then the QDs were re-dispersed in 10 ml DI water giving a final OD of ~1.5 at a wavelength of 420 nm. The final solution was adjusted to pH 9.0 via the addition of 0.01 M TMAH prior to storing.

**Preparation of CdS@Pt QDs by Photodeposition:** In a beaker, 10ml of the 1.5 OD MPA functionalised QDs were added along with 651 mg of triethanolamine (TEOA), 65 mg L-ascorbic acid (AA), 11.67 ml DI water and 150  $\mu\text{l}$  of 0.05 M chloroplatinic acid ( $\text{H}_2\text{PtCl}_6$ ). The solution was stirred under continuous bubbling with argon for 30 minutes, followed by UV excitation at 365 nm for 20 minutes. The final solution was then decanted into a 5 kDa vivaspin tube and centrifuged at 8000 RCF for 60 minutes. The filtrate was collected and the QDs were re-dispersed in 15 ml DI water and centrifuged again. The final material was re-dispersed in 21 ml of DI water leaving a solution with an OD ~0.5 at a wavelength of 420 nm.

**Fabrication of the nano-hybrid satellite material:** 3 ml of the AgNP@SiO<sub>2</sub>-NH<sub>2</sub> were added to a clean 50 ml flask along with the drop-wise addition of 300 µl of 4.73 mg/ml 4-(4,6-dimethoxy-1,3,5-triazin-2-yl)-4-methylmorpholium chloride (DMTMM) and 300 µl 2.8 mg/ml of 4-methylmorpholine (NMM). 3 ml of 0.5 OD CdS@Pt QDs were then added to the reaction via a drop-wise addition. 1.5 ml of 0.2 M pH 5.5 MES buffer was added to maintain a stable pH for the coupling reaction to occur. The final reaction solution was left to stir overnight at RT. The reaction solution was then centrifuged at 12000 RCF for 30 minutes to collect the final material and then re-dispersed in 3 ml DI water.

## 5.2.2 Characterisation of Nanomaterials after Fabrication

### 5.2.2.1 Physical Characterisation of Nanomaterials after Fabrication

**Characterisation of nanomaterials by UV-Vis spectroscopy:** After fabrication, all the nanomaterials were characterised by UV-Vis spectroscopy in a quartz cuvette, with a path length of 1 cm. The solutions were diluted as required to avoid saturation of the detector. A Shimadzu UV-2600 spectrophotometer with a resolution of 1 nm was used for all measurements.

**Characterisation of plasmonic nanomaterials by transmission electron microscopy (TEM):** After fabrication all plasmonic nanomaterials were characterised using TEM. The nanomaterials were first concentrated by centrifugation at 8000 RCF for 15 mins, followed by drop-casting on a pioloform coated 200 mesh copper (Cu) grid, forming a droplet. The droplet was then disturbed causing the droplet to collapse and the grid was left to dry. All samples were imaged using a FEI Tecnai G2 Spirit TEM, with 120 keV. All mages were processed using Fiji software.

**Characterisation of nanomaterials by high resolution scanning transmission electron microscopy (STEM):** CdS QDs and the nano-hybrid satellite material were characterised using high resolution STEM. A dilute dispersion of the nanomaterials was drop-cast on a holey carbon coated Cu grid (200 mesh) and then vacuum dried using a vacuum desiccator. All samples were imaged at 200 keV using a JEOL 2100F Cs-corrected analytical S/TEM in STEM mode. All images were processed using Fiji software.

#### 5.2.2.2 Chemical Characterisation of Nanomaterials after Fabrication

The chemical composition of the AgNPs@SiO<sub>2</sub>-NH<sub>2</sub> and the nano-hybrid satellite material was confirmed using x-ray photoelectron spectroscopy (XPS). Auger spectroscopy and energy dispersive X-ray spectroscopy (EDS) mapping were also used for analysing the chemical composition of the nano-hybrid satellite material.

**Characterisation of AgNPs@SiO<sub>2</sub>-NH<sub>2</sub> by XPS:** XPS was used to confirm the chemical composition of AgNPs@SiO<sub>2</sub>-NH<sub>2</sub> after coating the AgNPs with silica (SiO<sub>2</sub>). The solution was drop-cast on an aluminium (Al) foil coated silicon (Si) wafer, to eliminate contribution from the Si substrate, and left to dry ready for XPS and Auger spectroscopy analysis. The XPS data were collected on a Kratos Axis Supra instrument using monochromatic Al K $\alpha$  radiation (1486.7 eV, 225 W), with a low-energy electron flood source for charge compensation. Charge correction was done using the carbon 1s binding energy (284.8 eV). The XPS binding energies associated with the specific elemental peaks were identified using Kratos ESCApe software during analysis and further processed using CASA XPS software for display purposes.

### **Characterisation of the nano-hybrid satellite material by XPS and Auger spectroscopy:**

XPS and Auger spectroscopy were used to confirm the chemical composition of the nano-hybrid satellite material after fabrication. The oxidation state of cadmium and sulphur was also confirmed using the combination of XPS and Auger spectroscopy. After purification, the nano-hybrid satellite material was drop-cast on a clean Si wafer and left to dry ready for XPS and Auger spectroscopy analysis. Another sample of the satellite solution was also analysed using XPS on an Al foil coated Si wafer to confirm the presence of the SiO<sub>2</sub> layer. XPS and Auger spectroscopy data were collected according to the XPS analysis of the AgNPs@SiO<sub>2</sub>-NH<sub>2</sub> using a Kratos Axis Supra instrument. The XPS binding energies and Auger kinetic energies associated with the specific elemental peaks were identified using Kratos ESCApe software during analysis and further processed using CASA XPS software for display purposes.

### **Characterisation of the nano-hybrid satellite material by EDS mapping:**

EDS mapping was used to map the chemical composition of the nano-hybrid satellite material after fabrication. After purification, a dilute dispersion of the nano-hybrid satellite material was drop-cast on a holey carbon coated Cu grid (200 mesh) and then vacuum dried using a vacuum desiccator. EDS mapping was carried out at 200 keV using a JEOL 2100F S/TEM, with EDAX Octane T Optima windowless 60 mm<sup>2</sup> SDD EDS detector.

## 5.2.3 Stability Testing of the Nano-Hybrid Satellite Material

### **Physical characterisation of the nano-hybrid satellite material under active working conditions by TEM:**

The morphology of nano-hybrid satellite material was tested under active conditions using different hole scavengers and pH buffers from literature.<sup>17–19,24,26,27,74,75</sup> After fabrication the solution was split into separate centrifuge tubes and centrifuged at 12000 RCF for 30 mins. The supernatants were collected, and the nano-hybrid satellite material was re-dispersed using solutions of different hole scavengers and pH buffers from literature. After

re-dispersion under active conditions, all samples were stored in the dark. 100  $\mu\text{l}$  of the individual solutions were collected after fabrication and after 24 hrs in solution and centrifuged at 12000 RCF for 30 minutes. The supernatant was removed, and the pellet was drop-cast on a pioloform coated 200 mesh copper (Cu) grid. The droplet was then disturbed causing the droplet to collapse and the grid was left to dry. All samples were then analysed using a FEI Tecnai G2 Spirit TEM, with 120 keV and the images were processed using Fiji software. The nano-hybrid satellite material in water was used as a control.

The stability of the nano-hybrid satellite material was then further studied by selecting a hole scavenger of both basic (20 mM  $\text{Na}_2\text{SO}_3$ ) and acidic (0.2 M L-ascorbic acid) media and examined using STEM, EDS mapping, XPS and Auger spectroscopy. The pH of the nano-hybrid satellite material dispersions was also crudely tested daily using pH paper to observe any drastic changes in the pH of the solutions.

**Physical and chemical characterisation of the nano-hybrid satellite material under selected active working conditions by high resolution scanning transmission electron microscopy (STEM) and EDS mapping:** The morphology and chemical composition of nano-hybrid satellite material re-dispersed in hole scavengers 20 mM  $\text{Na}_2\text{SO}_3$  and 0.2 M L-ascorbic acid were characterised using high resolution STEM and EDS mapping. A dilute dispersion of the nanomaterials was drop-cast on a holey carbon coated Cu grid (200 mesh) and then vacuum dried using a vacuum desiccator. All samples were imaged at 200 keV using a JEOL 2100F Cs-corrected analytical S/TEM in STEM mode. Images were processed using Fiji software. EDS mapping was collected using the same STEM instrument with EDAX Octane T Optima windowless 60  $\text{mm}^2$  SDD EDX detector.

**Chemical characterisation of the nano-hybrid satellite material under selected active working conditions by XPS and Auger spectroscopy:** XPS and Auger spectroscopy were used to assess the oxidation state of cadmium and silver in the nano-hybrid satellite material re-dispersed in hole scavengers 20 mM Na<sub>2</sub>SO<sub>3</sub> and 0.2 M L-ascorbic acid. After 24 hrs in solution, 100µl of the nano-hybrid satellite material was purified by centrifugation at 12000 RCF for 30 minutes and the supernatant was removed. The nanomaterial was then re-dispersed and drop-cast on a clean Si wafer and left to dry ready for XPS and Auger spectroscopy analysis. XPS and Auger spectroscopy data were collected according to the XPS analysis of the AgNPs@SiO<sub>2</sub> using a Kratos Axis Supra instrument.

## 5.2.4 Hydrogen Evolution Experiments

**Hydrogen evolution of the nano-hybrid satellite material:** Hydrogen evolution experiments were carried out in a 5 cm long cylindric gas-tight glass reaction vessel, with a total volume of 18.2 ml (Figure 5. 9). Two septum caps were fitted to the reaction vessel for deaerating the reaction solution and sampling the gas in the head space of the reaction vessel (Figure 5. 9).



**Figure 5. 9** Gas-tight glass reaction vessel used for the photocatalytic hydrogen evolution experiments. (Scale bar is 1 cm).

In a typical experiment, the nano-hybrid satellite material solution was prepared to a volume of 7 ml and an optical density (OD) of 0.3 at a wavelength of 430 nm, over the path length of the 5 cm reaction vessel. In the 7 ml solution 1.4 ml of 0.1 M sodium sulphite ( $\text{Na}_2\text{SO}_3$ ) was also added as a hole scavenger, leaving 11.2 ml of headspace. The solution was deaerated under magnetic stirring and bubbled with argon for 30 minutes and a sample of gas from the headspace was then collected and analysed using GC, to check for leaks and form a baseline prior to illumination. The sample was then illuminated with a 450 W FL-1039 Xe source (Horiba Scientific), fitted with a cooled IR filter to minimise heating of the sample. The lamp light was further attenuated using a band-pass filter ( $430 \pm 70$  nm). The spectrum of the filtered lamp output reaching the sample was measured by a USB2000+XR1 spectrometer (Ocean Optics) (Figure 5. 10). The power output of the lamp reaching the sample was measured using a thermal power sensor (Thorlabs S302C), to ensure equal incident power of  $50 \text{ mW/cm}^2$  on the reactor vessel for each experiment.

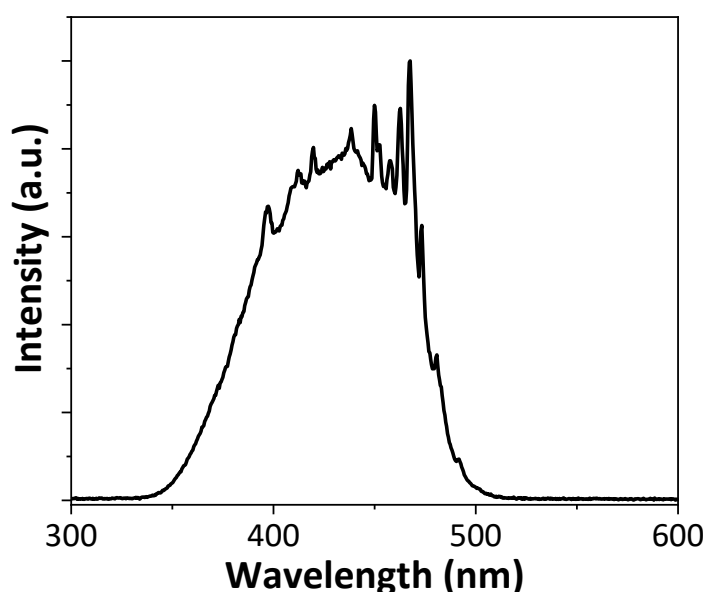


**Figure 5. 10** Spectrum of filtered lamp light reaching the sample, used to illuminate the photocatalyst samples.

A  $300 \mu\text{l}$  aliquot of the gas from the headspace was collected every hour for 4 hours and analysed by gas chromatography (GC) (Scion Instruments 436-GC) fitted with a BRP 81025 column (Bruker) packed with  $5 \text{ \AA}$  molecular sieves. Argon was used as a carrier

gas. The amount of hydrogen produced during the experiment was quantified by a thermal conductivity detector (TCD). The GC system was pre-calibrated using a commercial gas mixture (Scientific and Technical Gases Ltd) which contained  $1\% \pm 0.02\%$  of hydrogen, oxygen, and nitrogen in argon.

**Hydrogen evolution of the CdS@Pt QDs:** Hydrogen evolution experiments for the CdS@Pt QDs were carried out under the same conditions as the nano-hybrid satellite material, with an overall OD of 0.3 at a wavelength of 420 nm. A sample of the gas from the headspace was collected every hour for 4 hours and analysed by GC as detailed above.

**Determining the concentration of Ag, Cd and Pt in the hydrogen evolution reaction:**

After the hydrogen evolution experiments, the samples were collected and diluted by a factor of 2. These were then submitted for analysis by inductively couple plasma optical emission spectroscopy (ICP-OES) (Agilent 5110 ICP-OES spectrometer) to determine the concentration of Ag, Cd and Pt in the reaction solutions. This data was then used to calculate the concentration of Pt in the solution, thus allowing a turnover number for the evolution of hydrogen from water to be determined.

## 5.3 Results and Discussion

### 5.3.1 Fabrication and Characterisation of Nanomaterials

The nano-hybrid satellite material was fabricated following a wet chemical approach (Figure 5. 8) using several methods adapted from literature,<sup>46</sup> starting with the synthesis of citrate stabilised AgNPs. The AgNPs discussed in this chapter were synthesised using a seed mediated approach adapted from Bastus *et al.*,<sup>46</sup> by the reduction of AgNO<sub>3</sub> using Na<sub>3</sub>Ct in the presence of tannic acid. Tannic acid was employed in the reaction to control the reduction kinetics of the reaction, leading to the formation of highly monodispersed AgNPs with a diameter of 47 nm ± 4.7 nm, and plasmon resonance peak at 428 nm (Figure 5. 11).

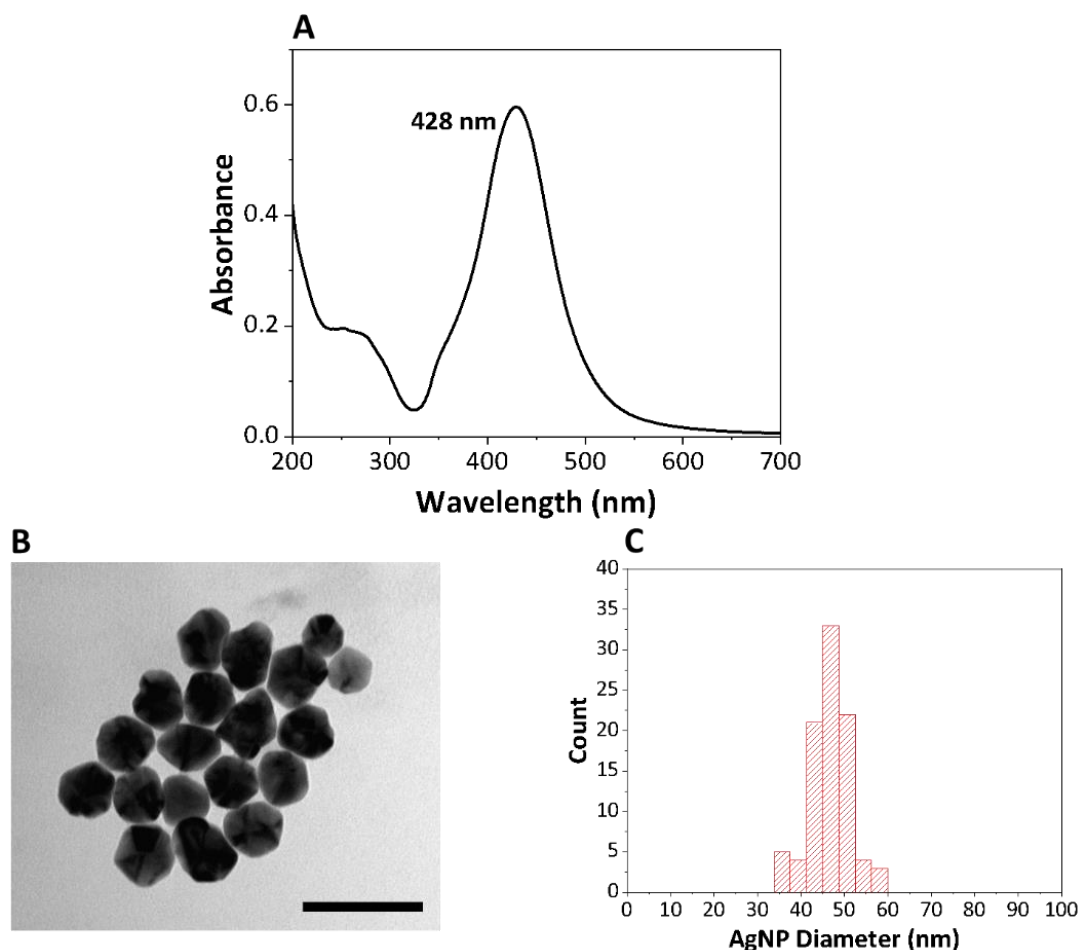


**Figure 5. 11** AgNPs synthesised following adapted method from Bastus *et al.*<sup>46</sup> (A) Representative UV-Vis spectra of AgNPs in DI H<sub>2</sub>O (10 x dilution vs stock). (B) Representative TEM image of AgNPs (scale bar is 100 nm) and (C) Histogram showing the size distribution of AgNPs, determined from several TEM images.

The AgNPs were subsequently coated with SiO<sub>2</sub>, following a modified Stöber process<sup>70,71</sup> and further functionalised with APTES in a ‘one pot synthesis’, using the AgNPs as nucleation sites for the SiO<sub>2</sub> layer to form. The final nanomaterial was denoted AgNP@SiO<sub>2</sub>-NH<sub>2</sub>. Ammonium hydroxide was employed in the reaction for the hydrolysis of the organo-silanes to SiO<sub>2</sub> and the reaction was quenched using an excess of ethanol (EtOH) to prevent further hydrolysis. The SiO<sub>2</sub> coating on the AgNPs was confirmed by TEM (Figure 5. 12 A), UV-Vis spectroscopy (Figure 5. 12 B) and XPS (Figure 5. 13). XPS was also used to confirm the presence of the APTES functional group (Figure 5. 13 D). The APTES functionality was added as an anchoring point for coupling with the CdS QDs in the formation of the nano-hybrid satellite material.

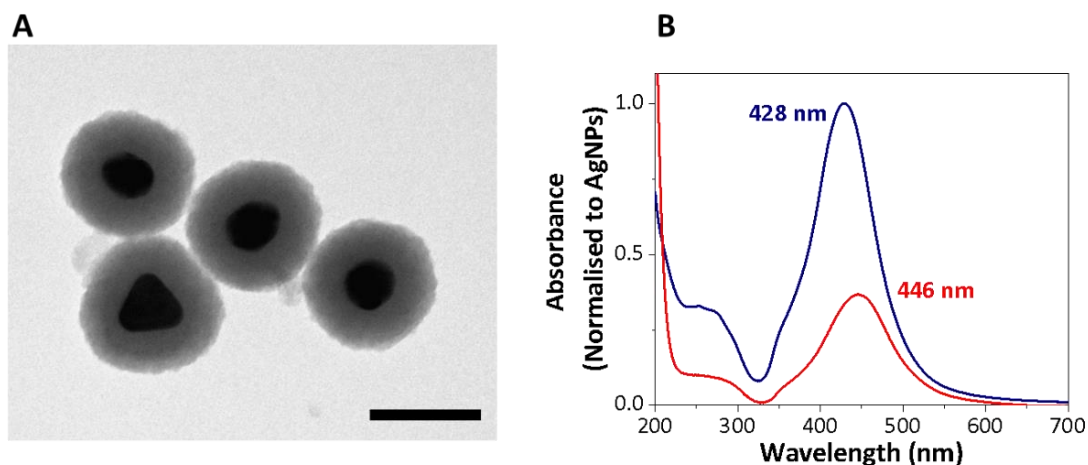


**Figure 5. 12** Combined SiO<sub>2</sub> coating and APTES functionalisation of AgNPs. (A) TEM image of AgNP@SiO<sub>2</sub>-NH<sub>2</sub> (scale bar is 100 nm) and (B) UV-Vis spectra of AgNPs (blue) and AgNP@SiO<sub>2</sub>-NH<sub>2</sub> (red) normalised with respect to the AgNPs.

Figure 5. 12 A shows TEM images of the AgNPs, successfully coated with SiO<sub>2</sub>, which can also be confirmed by a red shift in the plasmon frequency observed in the UV-Vis spectra (Figure 5. 12 B). The red shift can be attributed to a change in the dielectric of the medium surrounding the nanoparticles.<sup>48,49</sup> As a result of the coating and purification process, some AgNPs are also lost, reflected in the decrease in the OD after purification, observed in the UV-Vis spectra in figure 5. 12 B.

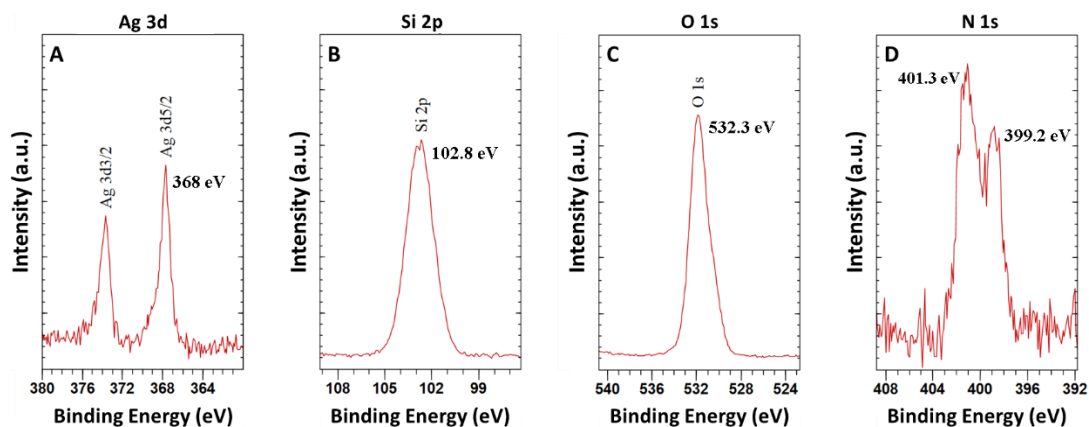


**Figure 5.13** Representative XPS data of the AgNP@SiO<sub>2</sub>-NH<sub>2</sub> material drop-cast on Al foil coated Si wafer. (A) silver Ag 3d spectra, (B) silicon Si 2p spectra, (C) oxygen O 1s spectra and (D) nitrogen N 1s spectra.

The XPS analysis of the AgNP@SiO<sub>2</sub>-NH<sub>2</sub> confirmed the presence of Ag, SiO<sub>2</sub> and APTES, with peak binding energies of 368 eV (Ag 3d<sub>5/2</sub>) associated with the AgNPs, 102.8 eV (Si 2p)<sup>76</sup> and 532.3 eV (O 1s)<sup>77</sup> in relation to the SiO<sub>2</sub> (Figure 5.13 B and C), and peak binding energies at 399.2 eV and 401.3 eV in the N 1s region, associated with the presence of APTES (Figure 5.13 D).<sup>78</sup> The peak splitting in the N 1s region (Figure 5.13 D) was attributed to intermolecular hydrogen bonding between the amino groups of APTES, due to the basic pH used in the coating process, that precludes protonation of APTES.<sup>79</sup> Interestingly, we also observe a lower intensity of the Ag 3d XPS binding energies, compared with the Si 2p XPS binding energy, observed in the wide scan displayed in appendix, figure A5.2. This is consistent with the core shell structure, suggesting more signal from the surface of the SiO<sub>2</sub> coating is detected, due to the XPS being a surface sensitive technique.

The CdS QDs used for the fabrication of the nano-hybrid satellite material were synthesised in parallel, following a hot injection method detailed by Yu and Peng.<sup>22</sup> In this method surfactant molecules are used to form coordination complexes of precursors, enabling dissolution in organic solvents at high temperatures to form the nanocrystal. The reaction is initiated by the injection of a sulphur precursor into a hot CdO solution of a high boiling solvent. Under these conditions, the CdO and sulphur precursors interact forming a yellow

coloured solution as small nanoclusters begin to form by nucleation, forming bonds between the precursors and displacing the coordinating surfactant ligands from the component atoms.<sup>80</sup> Partially reacted precursors at the surface of the nanocrystal retain one or more ligands, which stabilise the growing cluster. After synthesis, the solutions were collected and purified by flocculation and centrifugation. The QDs were then analysed by UV-Vis spectroscopy (Figure 5. 14) and STEM (Figure 5. 15).

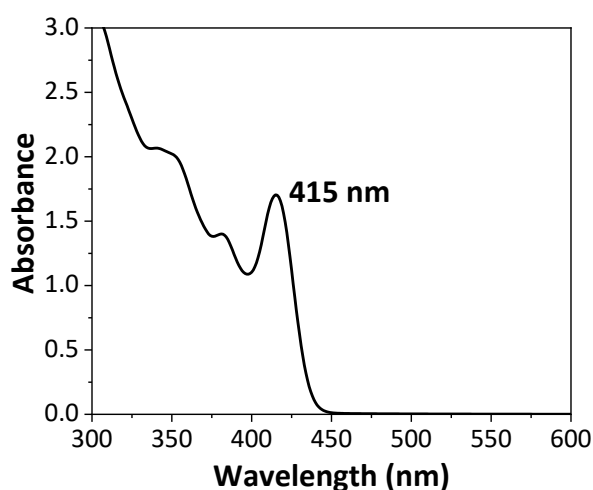


**Figure 5. 14** UV-Vis spectra of CdS QDs in chloroform (CHCl<sub>3</sub>) (20 x dilution vs stock) showing the maximum of excitonic absorption at 415 nm.

The position of the peak ( $\lambda$ ) in the UV-Vis spectroscopy data allowed for determination of the diameter ( $D$ ) (Equation 5. 1) and molar extinction coefficient ( $\epsilon$ ) (Equation 5. 2) of the CdS QDs using empirical equations detailed by Yu and Peng:<sup>81</sup>

$$D = (-6.6521 \times 10^{-8})\lambda^3 + (1.9557 \times 10^{-4})\lambda^2 - (9.5352 \times 10^{-2})\lambda + (13.29)$$

**Equation 5. 1**

$$\epsilon = 21536(D)^{2.3}$$

**Equation 5. 2**

QDs with a maximum of excitonic absorption wavelength of 415 nm and OD 1.7, had a diameter of 3.89 nm, with a concentration of  $2.09 \times 10^{15}$  QDs/ ml. The QDs were then further analysed by STEM (Figure 5. 15) and the average QD diameter of  $3.82 \text{ nm} \pm 0.38 \text{ nm}$  was measured. This value is in agreement with the diameter of the CdS QDs determined from

empirical equation 5.1 above. STEM imaging also revealed the coherent crystallinity of the CdS QDs, with lattice planes extending throughout the entire nanocrystal (Figure 5. 15 B)

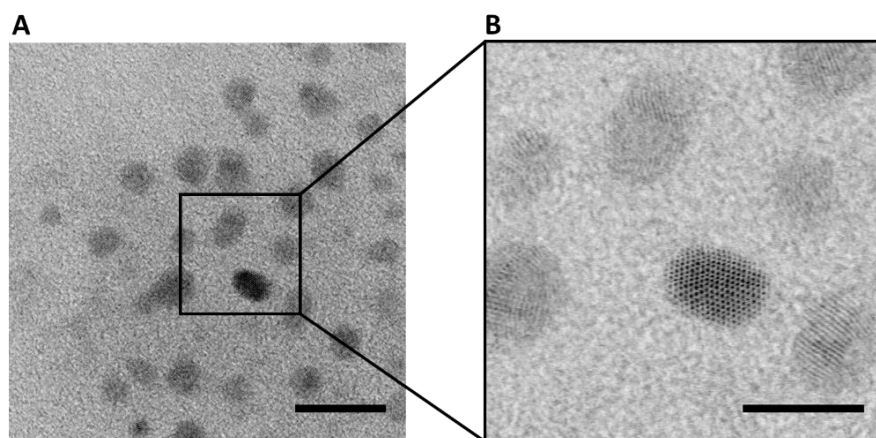


**Figure 5. 15** Representative STEM images of CdS QDs (A) STEM image showing an overview of the QDs (scale bar is 10 nm) (B) Magnified STEM image of selected area (scale bar is 5 nm).

The QDs were subsequently functionalised with 3-mercaptopropionic acid (MPA) and transferred to an aqueous phase by ligand exchange. The thiol group of the MPA strongly binds to the CdS QD, displacing the aliphatic oleic acid ligand and allowing the efficient transfer of the QDs into water. After functionalisation and phase transfer, a red shift in the maximum excitonic absorption wavelength of the QDs was observed (Figure 5. 16), which can be associated with a change in the dielectric constant of the dispersion media. The QDs were then decorated with Pt clusters as co-catalysts via photodeposition in the presence of L-ascorbic acid as a mild reducing agent. No change in the maximum excitonic absorption wavelength was observed (Figure 5. 16 C), which is consistent with literature.<sup>19</sup> Pt-clusters on the QDs act as electron sinks for the charge separation process, allowing for the photocatalytic evolution of hydrogen from water. On the other hand, the MPA functionality not only imparted hydrophilicity to the QDs, but also allowed for coupling with the AgNPs@SiO<sub>2</sub>-NH<sub>2</sub> via the carboxyl group (COOH), through the formation of peptide-like bond to form the nano-hybrid satellite material.

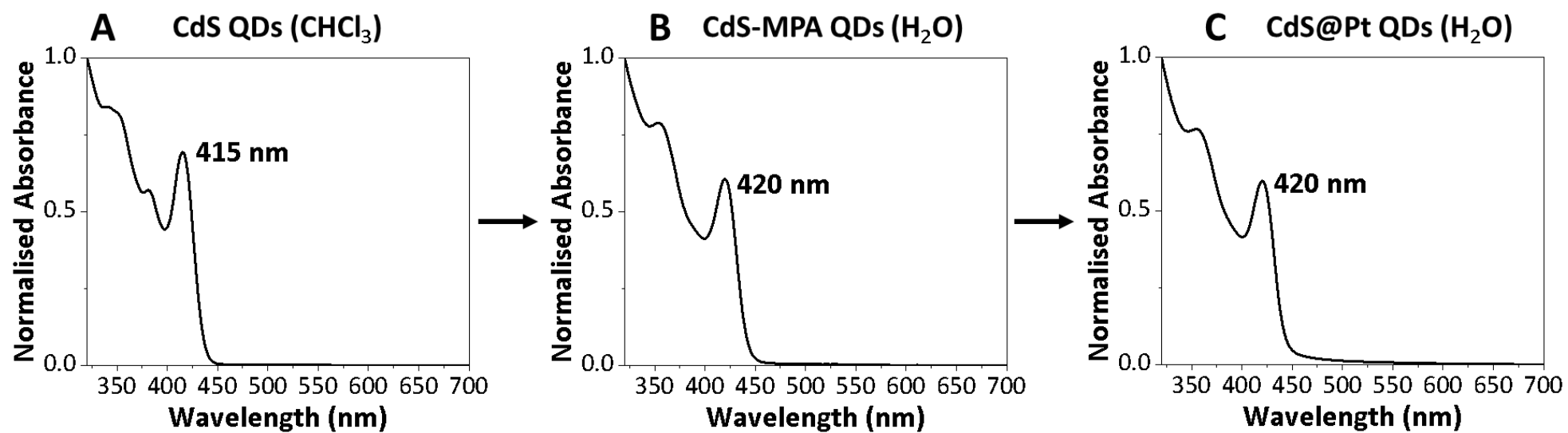
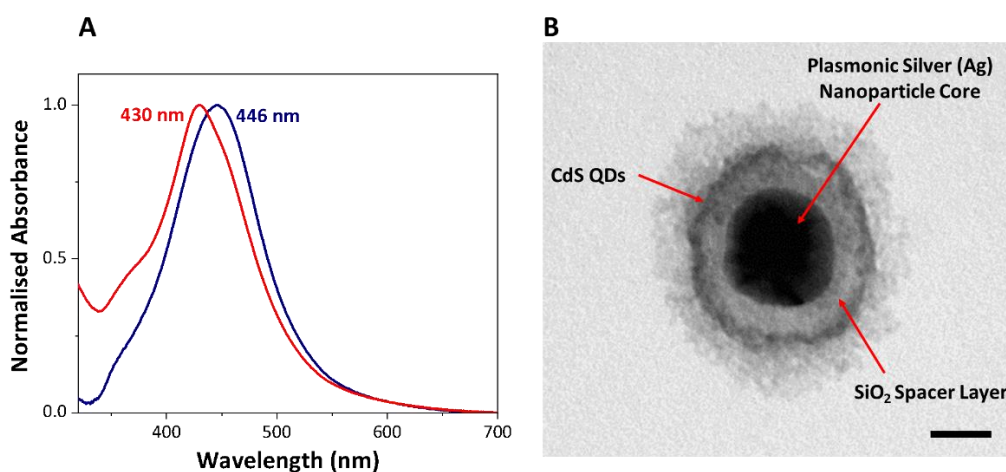


Figure 5. 16 Normalised UV-Vis spectra of CdS QDs before (A) and after phase transfer to  $\text{H}_2\text{O}$  (B) and after decorating the CdS QDs with Pt clusters (C).

After Pt deposition, the CdS QDs were then coupled with the AgNP@SiO<sub>2</sub>-NH<sub>2</sub> via peptide-like coupling of MPA and APTES functional groups to form the nano-hybrid satellite material (Figure 5. 17 B). Peptide coupling agent 4-(4,6-dimethoxy-1,3,5-triazin-2-yl)-4-methylmorpholium chloride (DMTMM) combined with 4-methylmorpholine (NMM) were used to activate the coupling reaction in the presence of a buffer (50 mM 2-(4-morpholinyl)ethanesulphonic acid (MES)), with pH 5.5.<sup>72,73</sup> DMTMM and NMM coupling agents were chosen for this reaction because they have previously been reported to be more efficient in the activation of carboxylic acids compared to other commonly used peptide coupling reagents such as 1-ethyl-3-(3-dimethylaminopropyl)carbodiimide (EDC) and N,N'-dicyclohexylcarbodiimide (DCC).<sup>73</sup> The coupling reaction between the CdS@Pt QDs with the AgNPs@SiO<sub>2</sub>-NH<sub>2</sub> proceeded overnight and the final material was then collected and purified by centrifugation. After fabrication and purification, a blue shift in the UV-Vis spectra was observed (Figure 5. 17 A), which can be attributed to the combination of the QDs and the AgNP@SiO<sub>2</sub> UV-Vis spectra. The nano-hybrid satellite material was then further characterised using several techniques (TEM, STEM, EDS, XPS and Auger spectroscopy) to confirm its morphology and chemical composition.



**Figure 5. 17** (A) Representative normalised UV-Vis spectra of AgNP@SiO<sub>2</sub>-NH<sub>2</sub> (blue) and nano-hybrid satellite material (red), showing blue shift after fabrication of the nano-hybrid satellite material (B) Representative TEM image of the nano-hybrid satellite material after fabrication demonstrating the core shell structure, with plasmonic AgNP core unit coupled with CdS QDs, separated by an SiO<sub>2</sub> dielectric layer (scale bar is 20 nm).

TEM data on the nano-hybrid satellite material (Figure 5. 17 B) reveals the core shell structure, with small dots around the outer SiO<sub>2</sub> shell, suggesting the presence of CdS QD satellite units at the surface of the SiO<sub>2</sub> layer. The satellite structure was further confirmed by high resolution STEM imaging (Figure 5. 18) and EDS mapping (Figure 5. 19). In the STEM imaging (Figure 5. 18), the QDs are observed to be coupled to the AgNP@SiO<sub>2</sub>-NH<sub>2</sub> nanomaterial on the edge of the SiO<sub>2</sub> layer (Figure 5. 18 B), which was further confirmed by the presence of sulphur in the EDS mapping (Figure 5. 19 C). In addition, we observe a variable thickness of the SiO<sub>2</sub> layer around the AgNPs (Figure 5. 17 B and 5. 18 A), suggesting that the SiO<sub>2</sub> coating process is not reproducible and may require further optimisation.

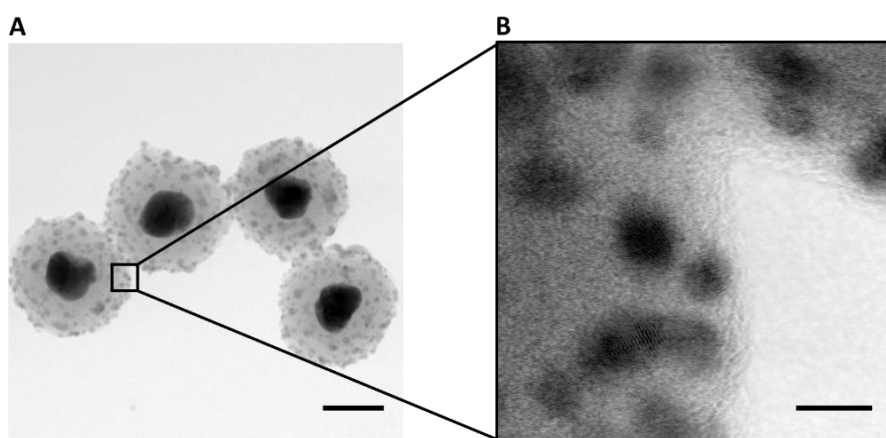


**Figure 5. 18** Representative STEM images of the nano-hybrid satellite material after fabrication (A) STEM image showing an overview of the nano-hybrid satellite materials (scale bar is 50 nm) (B) Magnified STEM image of selected area showing QDs coupled to the AgNPs@SiO<sub>2</sub>-NH<sub>2</sub> (scale bar is 5 nm).

The EDS mapping clearly demonstrates the expected multi-layered core shell nano-hybrid satellite structure, with a AgNP inner core (Figure 5. 19 B), SiO<sub>2</sub> spacer layer (Figure 5. 19 E) and CdS QDs around the SiO<sub>2</sub> layer (Figure 5. 19 C and D). The overlapping of Ag and Cd EDS signals, can be attributed to their characteristic x-ray emissions resulting from different electron transitions in the EDS process, preventing further analysis of the nano-hybrid satellite material via this method (Figure 5. 19 B and D). However, a ring of sulphur around the surface of the SiO<sub>2</sub> layer (Figure 5. 19 C) can be associated with the presence of the CdS QDs. The

presence of Ag and Cd, along with the  $\text{Cd}^{2+}$  oxidation state was also confirmed by XPS and Auger spectroscopy (Figure 5. 20).

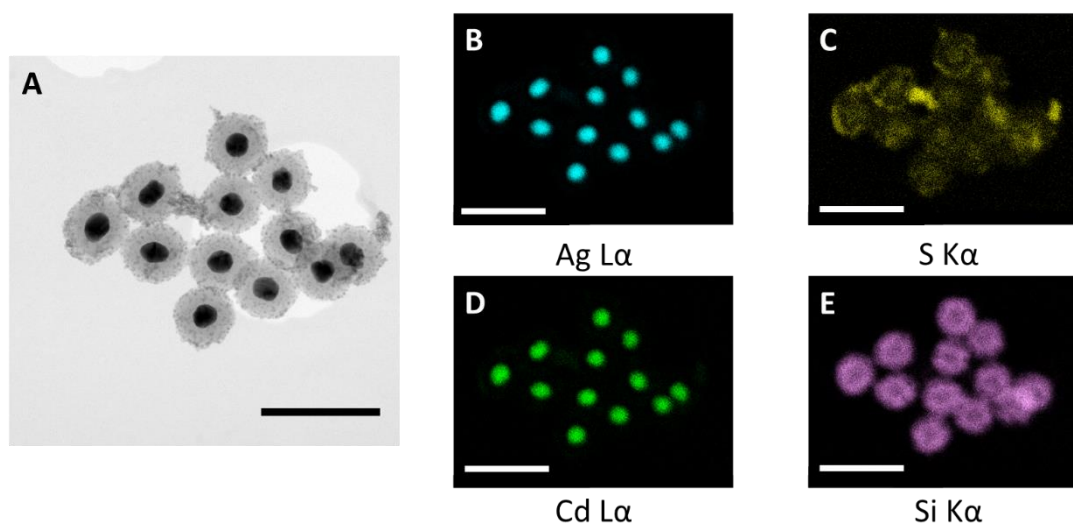


**Figure 5. 19** Representative high resolution STEM image with EDS mapping (scale bars are 200 nm) of the nano-hybrid satellite material after fabrication. (A) STEM image, (B) Ag  $L\alpha$  EDS map, (C) S  $K\alpha$  EDS map, (D) Cd  $L\alpha$  EDS map and (E) Si  $K\alpha$  EDS map.

The presence of metallic silver (Ag) related to the AgNPs was confirmed by the XPS Ag  $3d_{5/2}$  binding energy (368 eV) (Figure 5. 20 A) and the Ag  $M_4N_{45}N_{45}$  Auger peak (356.8 eV) (Figure 5. 20 B), with a measured Auger parameter of 724.8 eV.<sup>82,83</sup> The presence of the CdS QDs along with the  $\text{Cd}^{2+}$  oxidation state was confirmed by the XPS Cd  $3d_{5/2}$  peak binding energy (405.1 eV) (Figure 5. 20 D) and Cd  $M_5N_{45}N_{45}$  Auger peak (374.4 eV) (Figure 5. 20 E), as well as the sulphur 2- oxidation state ( $S2p_{3/2}$ , 161.4 eV) (Figure 5. 20 F).<sup>19,84,85</sup> A peak at 168 eV in the S 2p spectra (Figure 5. 20 F) is also observed, which can be attributed to oxidised sulphur, most likely associated with the presence of the sulfonic acid group of residual MES buffer following the purification process, as this peak has not been observed in other batches of the satellite materials (Figure A5. 4 B).<sup>86</sup> The presence of the Pt co-catalyst was also confirmed by the XPS Pt  $4f_{7/2}$  peak binding energy (72.4 eV) (Figure 5. 20 C).<sup>19</sup>

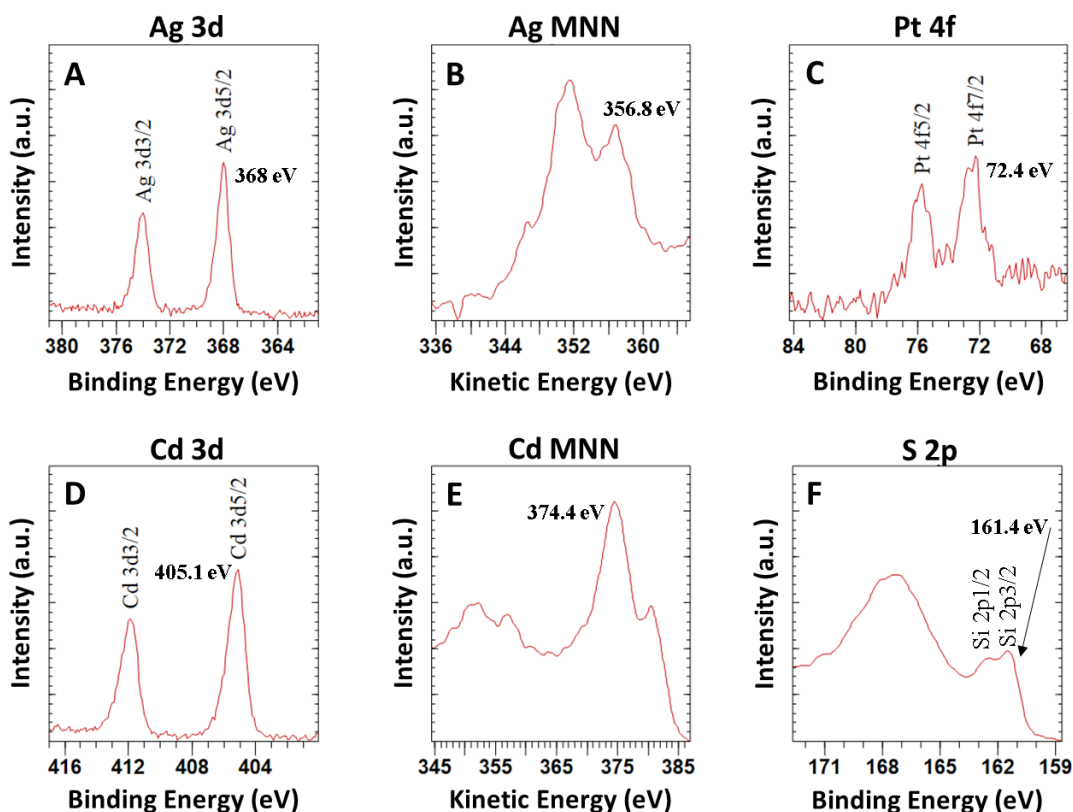


**Figure 5.20** Representative XPS and Auger data of the nano-hybrid satellite material in DI H<sub>2</sub>O drop-cast on a silicon wafer (A) Ag 3d spectra, (B) Ag MNN Auger spectra, (C) Pt 4f spectra, (D) Cd 3d spectra, (E) Cd MNN Auger spectra and (F) S 2p spectra.

After successful fabrication of the desired nano-hybrid satellite material, the experimental work progressed to investigating the stability of these materials under active working conditions.

### 5.3.2 Investigating the Stability of the Nano-Hybrid

#### Satellite Material under Active Working Conditions

Exploring the literature in the field of photocatalysis for the hydrogen evolution from water, it is apparent the lack of systematic understanding of the fundamental principles controlling the stability of nanomaterials under active working conditions. Key parameters involved in the fabrication of these nanomaterials can have a considerable impact on their catalytic function. We investigated here the stability of the nano-hybrid satellite material dispersed in different

aqueous buffers containing different pH buffers and hole scavengers commonly used in the literature.<sup>17–19,24,26,27,74,75</sup> In our initial studies, the morphology of the nano-hybrid satellite material was assessed by TEM under different conditions after 24 hrs (Table A5.1). The morphology of the intermediate AgNP@SiO<sub>2</sub>-NH<sub>2</sub> material and the final nano-hybrid satellite material were first investigated under both basic and acidic conditions. The effect of concentration of both basic and acidic media on the stability of the nano-hybrid satellite material was also investigated. In addition, the morphology of the nano-hybrid satellite material dispersed in mild acidic and neutral conditions was also investigated.

### 5.3.2.1 Basic Conditions

The morphology of the AgNPs@SiO<sub>2</sub>-NH<sub>2</sub> intermediate material dispersed in basic conditions (e.g. in the presence of 20 mM sodium sulphite (Na<sub>2</sub>SO<sub>3</sub>)) displayed in the TEM images (Figure 5. 21 A and B), showed no obvious morphological changes after 24hrs in solution. Conversely, the morphology of the nano-hybrid satellite material dispersed in 20 mM Na<sub>2</sub>SO<sub>3</sub> (Figure 5. 21 C and D) exhibited significant damage at the SiO<sub>2</sub> coating layer, appearing to have a decreased thickness. This suggests the nano-hybrid satellite material is not stable under these basic conditions after 24 hours. The change in morphology also appears to be associated with the presence of the CdS QDs, as no obvious morphological changes were observed for the AgNPs@SiO<sub>2</sub>-NH<sub>2</sub> dispersed under the same conditions.

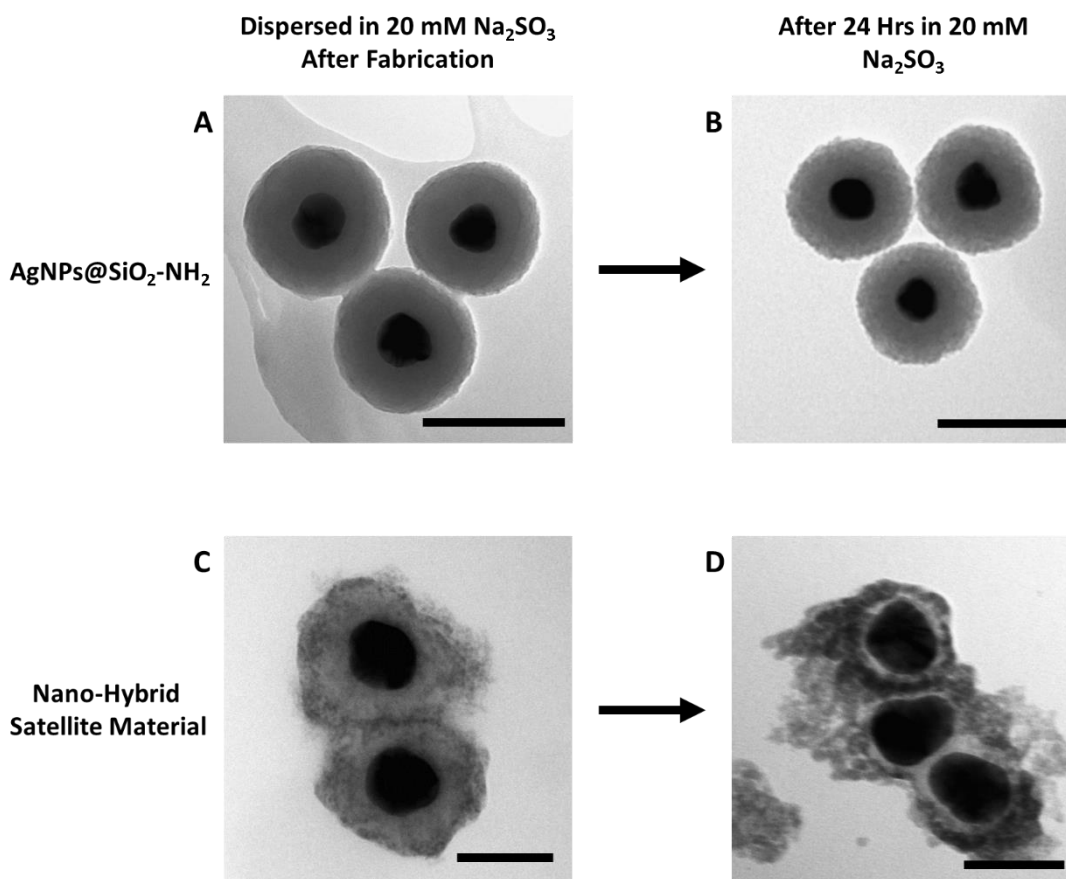


**Figure 5. 21** Representative TEM images of AgNPs@SiO<sub>2</sub>-NH<sub>2</sub> (**A** and **B**) (scale bars are 100 nm) and the nano-hybrid satellite material (scale bars are 50 nm) (**C** and **D**) dispersed in 20 mM Na<sub>2</sub>SO<sub>3</sub>. (**A**) AgNPs@SiO<sub>2</sub>-NH<sub>2</sub> after fabrication (SiO<sub>2</sub> layer thickness 32.7 nm ± 2.05 nm) and (**B**) AgNPs@SiO<sub>2</sub>-NH<sub>2</sub> after 24 hrs (SiO<sub>2</sub> layer thickness 30.73 nm ± 2.4 nm). (**A**) Nano-hybrid satellite material after fabrication (SiO<sub>2</sub> layer thickness 19 nm ± 4.68 nm) and (**B**) Nano-hybrid satellite material after 24 hrs (SiO<sub>2</sub> layer thickness 1.82 nm ± 3.14 nm).

The change in the morphology of the nano-hybrid satellite material also appeared to change when dispersed in other basic medias, such as TEOA (Figure 5. 22) and 3-(cyclohexylamino) propanesulphonic acid buffer (CAPS, pH 10) (see appendix, Figure A5. 5). This suggests that the morphological changes are sensitive to basic conditions and are not strongly dependent of the chemical species of the base. The change in the morphology of the nano-hybrid satellite material appeared to be dependent on concentration of basic media, with a drastic decrease of the SiO<sub>2</sub> layer thickness observed by TEM for the nano-hybrid satellite material dispersed in 1M TEOA after 24 hrs (Figure 5. 22 E and F). While at lower concentrations, such as 0.2 M (Figure 5. 22 C and D) and 20 mM TEOA (Figure 5. 22 A and B), the decrease in the thickness of the SiO<sub>2</sub> layer were less drastic in comparison to 1M TEOA.

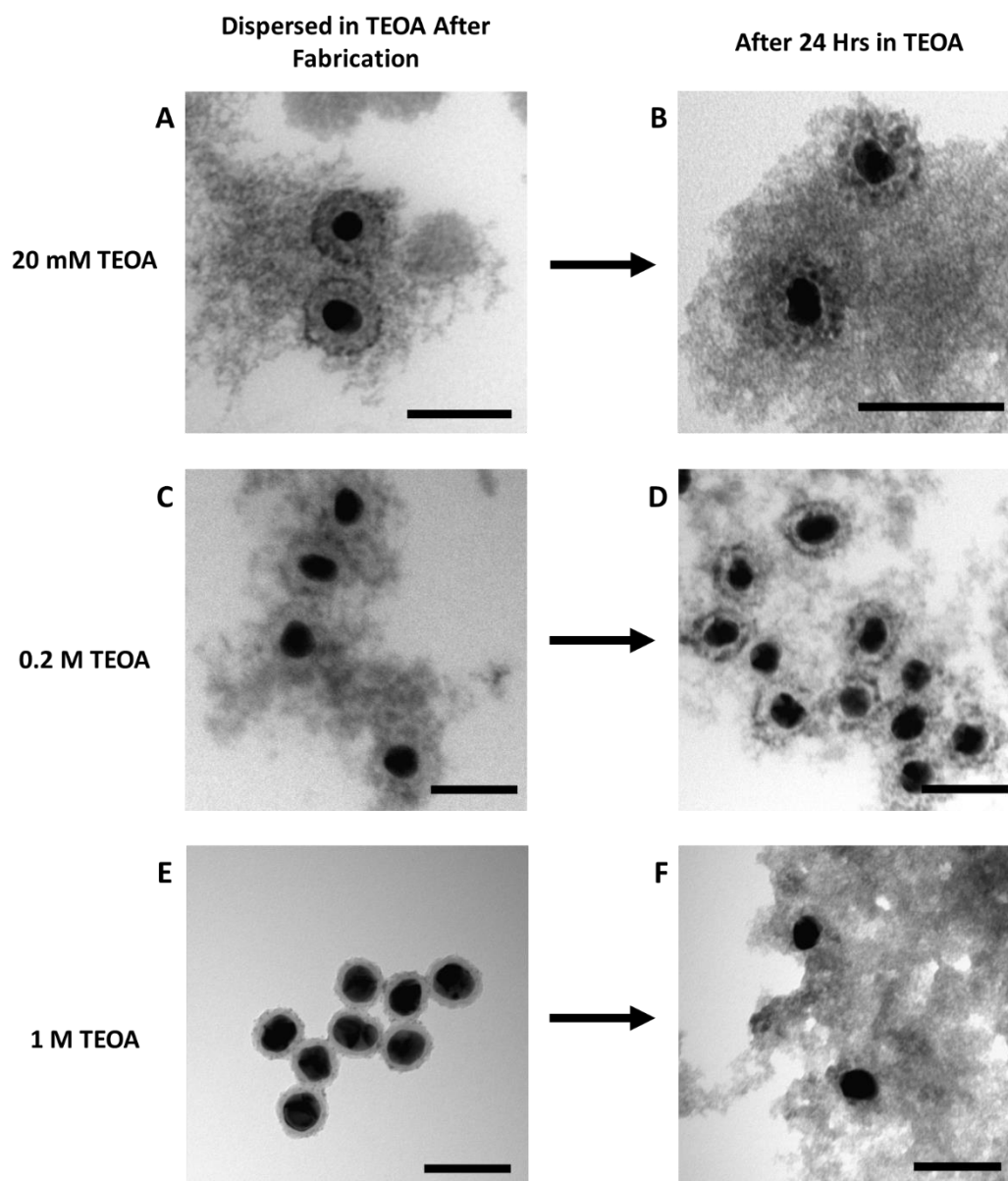


**Figure 5. 22** Representative TEM images of the nano-hybrid satellite material dispersed in TEOA of different concentrations (scale bars are 100 nm).**(A)** 20 mM TEOA after fabrication ( $\text{SiO}_2$  layer thickness  $19.32 \text{ nm} \pm 2.93 \text{ nm}$ ), **(B)** 20 mM TEOA after 24 hrs ( $\text{SiO}_2$  layer thickness  $8.61 \text{ nm} \pm 1.67 \text{ nm}$ ), **(C)** 0.2 M TEOA after fabrication ( $\text{SiO}_2$  layer thickness  $17.77 \text{ nm} \pm 3.66 \text{ nm}$ ), **(D)** 0.2 M TEOA after 24 hrs ( $\text{SiO}_2$  layer thickness  $8.41 \text{ nm} \pm 2.94 \text{ nm}$ ), **(E)** 1 M TEOA after fabrication ( $\text{SiO}_2$  layer thickness  $9.11 \text{ nm} \pm 0.96 \text{ nm}$ ) and **(F)** 1 M TEOA after 24 hrs ( $\text{SiO}_2$  layer thickness  $0.17 \text{ nm} \pm 1.07 \text{ nm}$ ).

### 5.3.2.2 Acidic Conditions

In acidic conditions, (e.g. in the presence of hole scavenger's 0.2 M oxalic acid) after 24 hrs in solution, no obvious morphological changes in the AgNPs@SiO<sub>2</sub>-NH<sub>2</sub> intermediate material were observed (Figure 5. 23 A and B). However, for nano-hybrid satellite material, after 24hrs dispersed in 0.2 M oxalic acid, the material appeared to be 'stripped' from QDs (Figure 5. 23 C and D). While the SiO<sub>2</sub> layer seems to remain intact, there appeared to be a loss in CdS@Pt QDs attached to the surface of the SiO<sub>2</sub> layer of the nano-hybrid satellite material (Figure 5. 23 C and D).

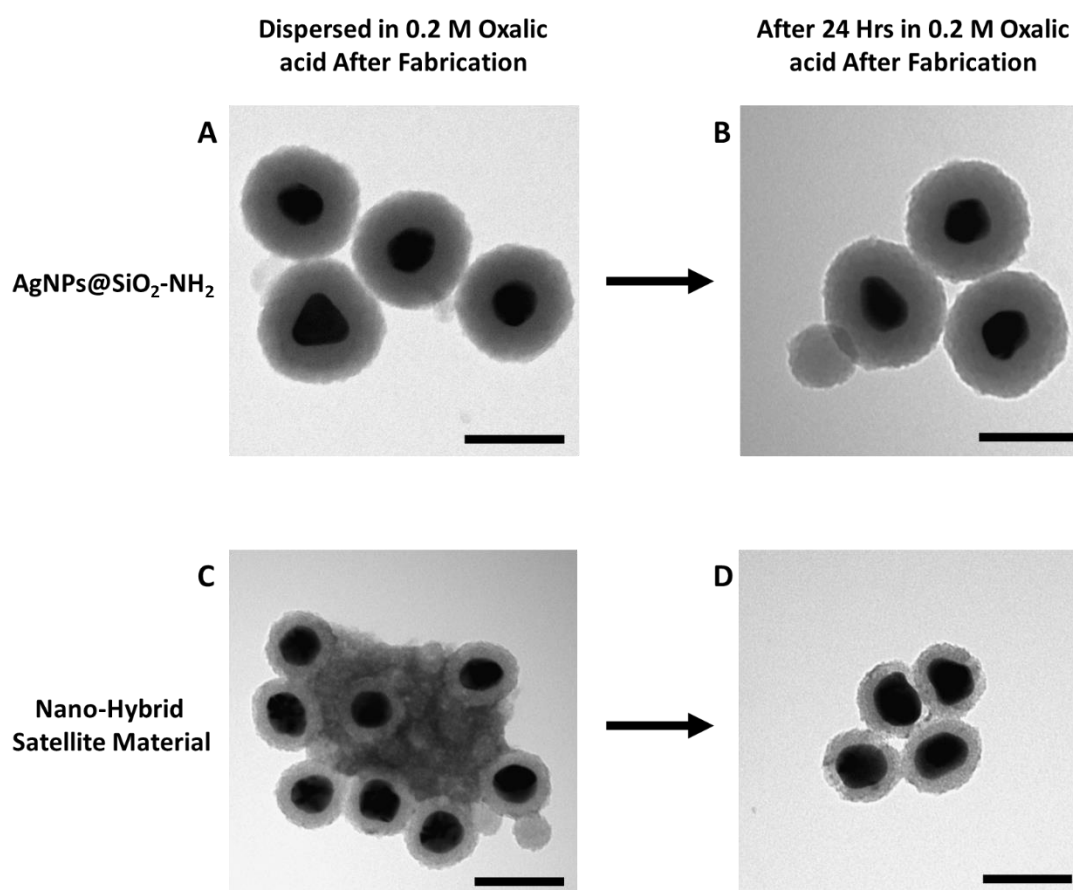


**Figure 5. 23** Representative TEM images of AgNPs@SiO<sub>2</sub>-NH<sub>2</sub> (**A** and **B**) and the nano-hybrid satellite material (**C** and **D**) dispersed in 0.2 M oxalic acid (scale bars are 100 nm). (**A**) AgNPs@SiO<sub>2</sub>-NH<sub>2</sub> after fabrication (SiO<sub>2</sub> layer thickness 36.68 nm ± 1.64 nm) and (**B**) AgNPs@SiO<sub>2</sub>-NH<sub>2</sub> after 24 hrs (SiO<sub>2</sub> layer thickness 37.58 nm ± 2.02 nm). (**A**) Nano-hybrid satellite material after fabrication (SiO<sub>2</sub> layer thickness 17.36 nm ± 1.99 nm) and (**B**) Nano-hybrid satellite material after 24 hrs (SiO<sub>2</sub> layer thickness 19.76 nm ± 5.36 nm).

These morphological changes were consistent when the nano-hybrid satellite material was dispersed in other acidic medias, such as L-ascorbic acid (Figure 5. 24). In addition, these changes also proved to be dependent on the concentration of acidic media. In 0.2 M L-ascorbic acid, the CdS@Pt QDs are completely ‘stripped’ away from the surface of the SiO<sub>2</sub> layer after 24 hrs in solution (Figure 5. 24 C and D). However, in 20 mM ascorbic acid we observe only a fraction of the CdS@Pt QDs ‘stripped’ away from the surface of the SiO<sub>2</sub> layer (Figure 5. 26 A and B).

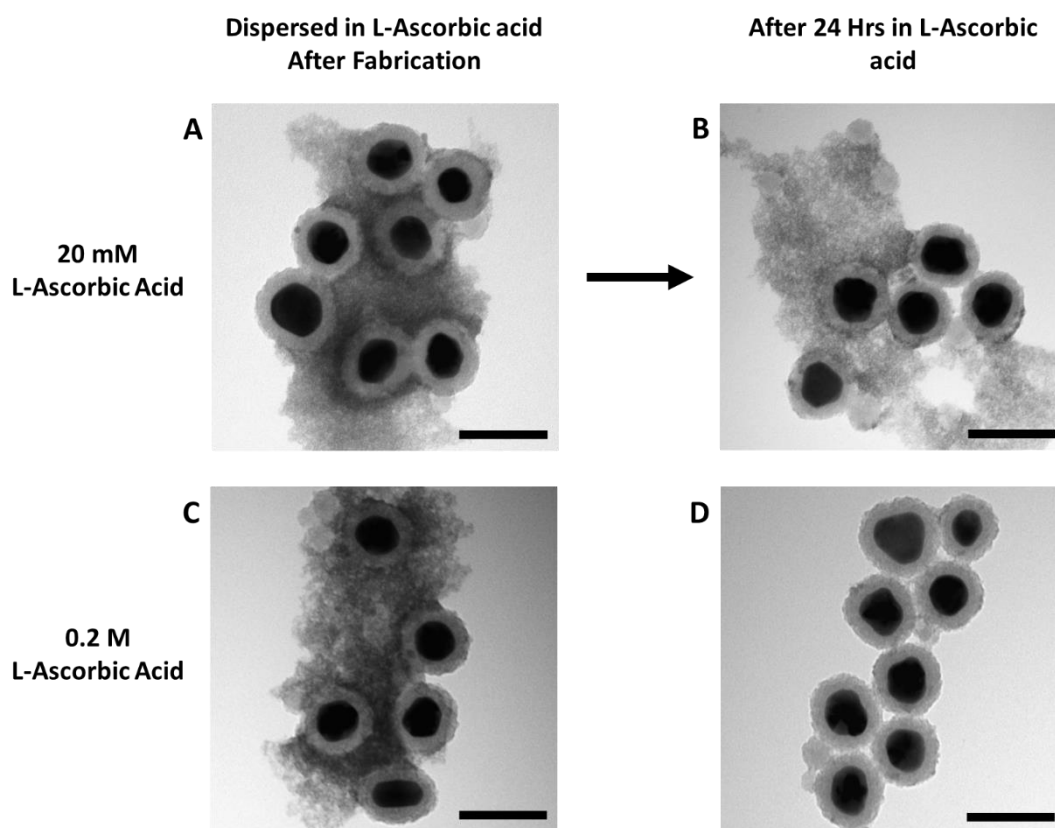


**Figure 5. 24** Representative TEM images of the nano-hybrid satellite material dispersed in L -ascorbic acid of different concentrations (scale bars are 100 nm). (A) 20 mM L-ascorbic acid after fabrication, (SiO<sub>2</sub> layer thickness 18.21 nm ± 1.94 nm) (B) 20 mM L-ascorbic acid after 24 hrs (SiO<sub>2</sub> layer thickness 16.24 nm ± 1.96 nm), (C) 0.2 M L-ascorbic acid after fabrication (SiO<sub>2</sub> layer thickness 16.83 nm ± 1.95 nm) and (D) 0.2 M L-ascorbic acid after 24 hrs (SiO<sub>2</sub> layer thickness 16.56 nm ± 2.19 nm).

### 5.3.2.2 Mildly Acidic and Neutral Conditions

When investigating the morphology of the nano-hybrid satellite material dispersed in mild acidic or neutral conditions after 24 hrs, such as 50 mM MES buffer (pH 5.5) (Figure 5. 25), 50 mM 4-(2-Hydroxyethyl) piperazine-1-ethanesulphonic acid buffer (HEPES, pH 7) (Figure A5. 6) and deionised water (Figure A5 .7), the material appears to be more stable. The QDs remain present at the surface of the SiO<sub>2</sub> layer and the SiO<sub>2</sub> layer thickness remains predominately unchanged.

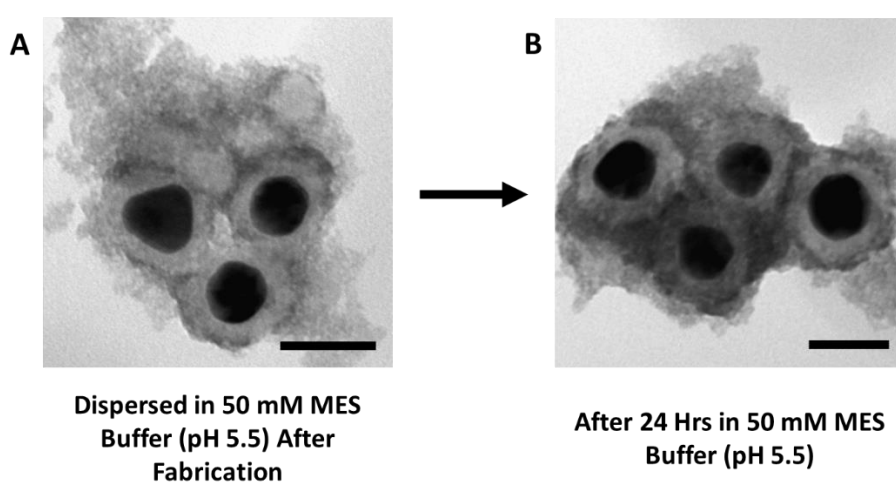


**Figure 5. 25** Representative TEM images of the nano-hybrid satellite material dispersed in 50 mM MES buffer (pH 5.5) (scale bars are 50 nm). (A) After fabrication (SiO<sub>2</sub> layer thickness 12.34 nm ± 2.04 nm) and (B) After 24 hrs (SiO<sub>2</sub> layer thickness 14.29 nm ± 2.15 nm).

This suggests that the morphological changes observed for the nano-hybrid satellite material appear to be strongly pH dependent. To further investigate the mechanism involved in the stability issues of these materials, we combined STEM with EDS mapping, XPS and Auger spectroscopy.

### 5.3.3 Investigating the Mechanism Involved in the Stability of the Nano-Hybrid Satellite Material under Active Working Conditions

Further investigation of the mechanism involved in the degradation of the nano-hybrid satellite material were performed on freshly fabricated materials dispersed in two selected hole scavengers of both basic and acidic pH. 20 mM  $\text{Na}_2\text{SO}_3$  was chosen as the basic hole scavenger and 0.2 M L-ascorbic acid was used as the acidic hole scavenger. After 24 hrs in solution, an aliquot of the samples was collected and purified by centrifugation to remove excess buffer media prior to analysis. The pH of the solutions was also monitored over several days (Figure A5. 8), with no significant change observed. The data from the STEM coupled with EDS mapping, revealed different effects in the chemical composition of the nano-hybrid satellite material, depending on the pH of the dispersion media.

#### 5.3.3.2 STEM and EDS Mapping of the Nano-Hybrid Satellite Material after 24 Hrs Dispersed in Basic Conditions

In the STEM coupled with EDS mapping of the nano-hybrid satellite material dispersed in 20 mM  $\text{Na}_2\text{SO}_3$  for 24 hrs, we observe a decrease in the  $\text{SiO}_2$  layer thickness in some areas (Figure 5. 26 A), suggesting an initial transition stage for the decrease in the thickness of the  $\text{SiO}_2$  layer, as observed in the previous TEM studies (Figure 5. 21). In addition, the sulphur remains predominantly around the outside of the  $\text{SiO}_2$  layer (Figure 5. 26 C), suggesting the CdS@Pt QDs appear to be present.

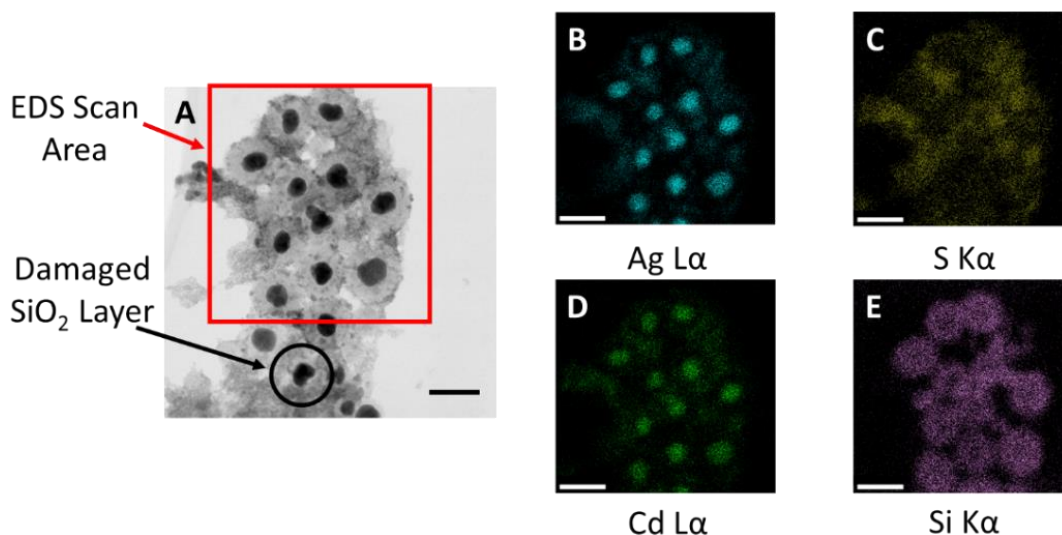


**Figure 5. 26** Representative high resolution STEM image (scale bar is 100 nm) with EDS mapping (scale bars are 100 nm) of the nano-hybrid satellite material after 24 hrs dispersed in 20 mM  $\text{Na}_2\text{SO}_3$ . (A) STEM image, (B) Ag  $L\alpha$  EDS map, (C) S  $K\alpha$  EDS map, (D) Cd  $L\alpha$  EDS map and (E) Si  $K\alpha$  EDS map.

### 5.3.3.2 STEM and EDS Mapping of the Nano-Hybrid Satellite Material after 24 Hrs Dispersed in Acidic Conditions

For the STEM coupled with EDS Mapping data of the nano-hybrid satellite material dispersed in 0.2 M L-ascorbic acid for 24 hrs, we observe a reduction in the amount of QDs surrounding the nanomaterial (Figure 5. 27 A), as observed from the previous TEM studies (Figure 5. 24 C and D), with a leaching of sulphur towards the core of the nanomaterial (Figure 5. 27 C). This suggests the  $\text{SiO}_2$  layer may exhibit some porosity, allowing sulphur to pass to the AgNP core, with the possible formation of oxidised silver, in the form of silver sulphide ( $\text{Ag}_2\text{S}$ ).

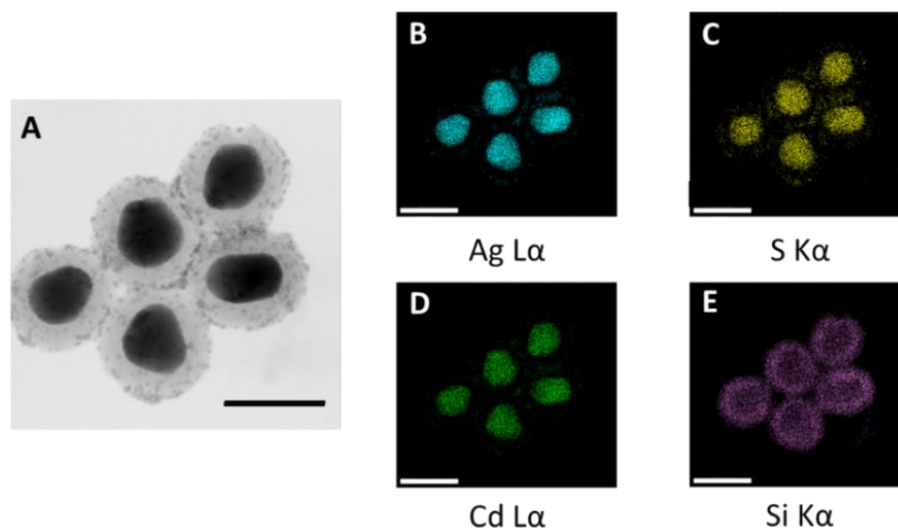


**Figure 5. 27** Representative high resolution STEM image (scale bar is 100 nm) with EDS mapping (scale bars are 100 nm) of the nano-hybrid satellite material after 24 hrs dispersed in 0.2 M L-ascorbic acid. (A) STEM image, (B) Ag L $\alpha$  EDS map, (C) S K $\alpha$  EDS map, (D) Cd L $\alpha$  EDS map and (E) Si K $\alpha$  EDS map.

The nano-hybrid satellite material from the same batch dispersed in deionised water, was also investigated by STEM coupled with EDS mapping for comparison (Figure 5. 28).

### 5.3.3.3 STEM and EDS Mapping of the Nano-Hybrid Satellite

#### Material after 24 Hrs Dispersed in Deionised Water

When deionised water is used as the dispersion media, we observe the thickness of SiO<sub>2</sub> layer of the nano-hybrid satellite material to be stable (Figure 5. 28 A). The presence of CdS@Pt QDs around the surface of the SiO<sub>2</sub> layer is also confirmed, represented by the distribution of sulphur predominately around the outside of the SiO<sub>2</sub> layer in the EDS mapping (Figure 5. 28 C).

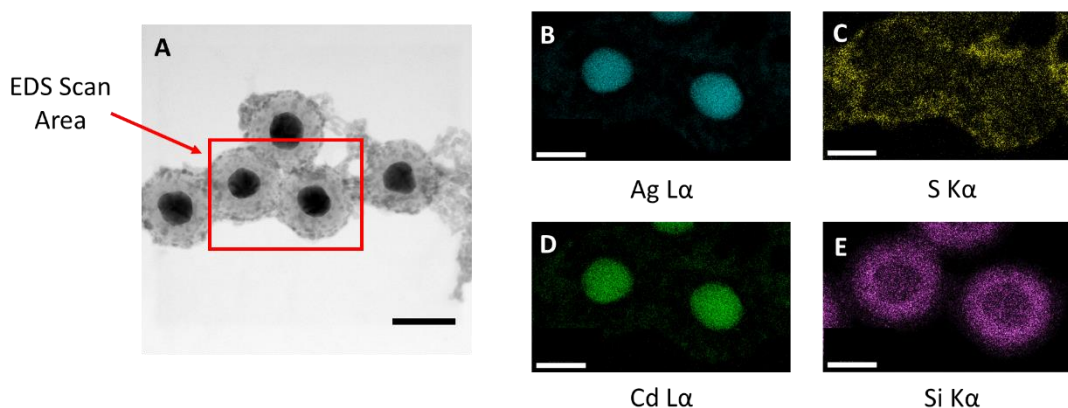


**Figure 5. 28** Representative high resolution STEM image (scale bar is 100 nm) with EDS mapping (scale bars are 50 nm) of the nano-hybrid satellite material after 24 hrs dispersed in deionised H<sub>2</sub>O. (A) STEM image, (B) Ag L $\alpha$  EDS map, (C) S K $\alpha$  EDS map, (D) Cd L $\alpha$  EDS map and (E) Si K $\alpha$  EDS map.

From this data, we can conclude that sulphur migration plays a key role in the morphological changes of the nano-hybrid satellite material, with different effects being observed at different pHs. The role of sulphur in the stability of the nano-hybrid satellite material in these different pH conditions can also be evaluated by XPS and Auger spectroscopy data for the analysis of the silver and cadmium oxidation states in the presence of hole scavengers, 20 mM Na<sub>2</sub>SO<sub>3</sub> and 0.2 M L-ascorbic acid.

#### 5.3.3.4 XPS and Auger Spectroscopy of the Nano-Hybrid Satellite Material after 24 Hrs Dispersed in Basic Conditions

The XPS and Auger spectroscopy data of the nano-hybrid satellite material dispersed in 20mM Na<sub>2</sub>SO<sub>3</sub>, suggest the presence of metallic silver, with an Auger parameter of 724.7 eV, measured from the Ag 3d<sub>5/2</sub> binding energy (367.5 eV) (Figure 5. 29 A) and the Ag M<sub>4</sub>N<sub>45</sub>N<sub>45</sub> Auger peak (357.2 eV) (Figure 5. 29 B).<sup>82,83</sup> Also the Ag 3d peaks are sharp and narrow, as expected for the metallic state of silver.<sup>83</sup> A shift in the Cd 3d<sub>5/2</sub> binding energy (405 eV) (Figure 5. 29 C) and the Cd M<sub>5</sub>N<sub>45</sub>N<sub>45</sub> Auger peak (375.2 eV) (Figure 5. 29 D) is also observed, suggesting a mixture of chemical environments for cadmium in the nano-hybrid satellite material.<sup>84,85</sup>

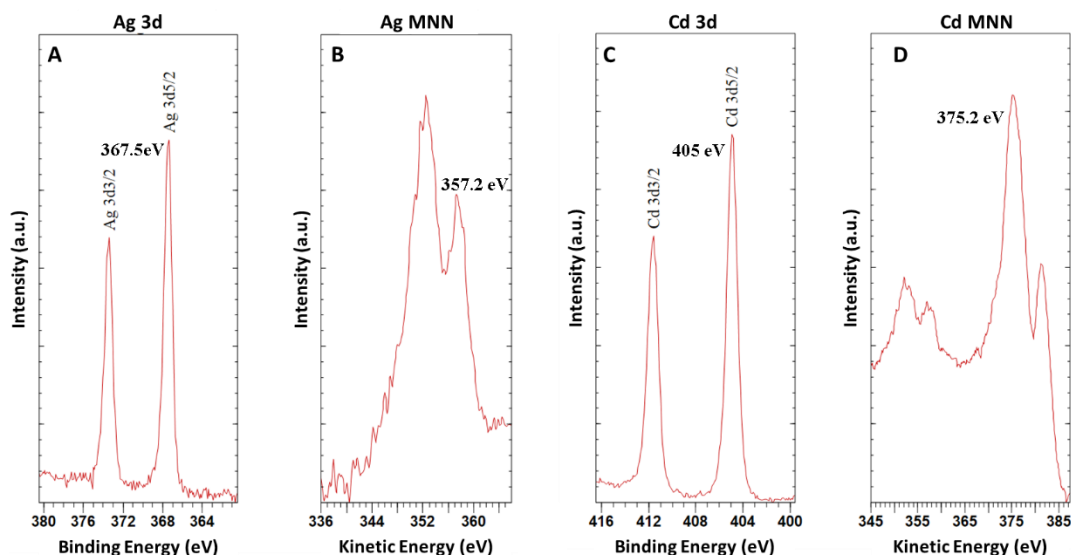


**Figure 5. 29** Representative XPS and Auger data of the nano-hybrid satellite material dispersed in 20 mM Na<sub>2</sub>SO<sub>3</sub> drop-cast on a silicon wafer (**A**) Ag 3d spectra, (**B**) Ag MNN Auger spectra, (**C**) Cd 3d spectra and (**D**) Cd MNN Auger spectra.

### 5.3.3.5 XPS and Auger Spectroscopy of the Nano-Hybrid Satellite

#### Material after 24 Hrs Dispersed in Acidic Conditions

Conversely, the XPS and Auger spectroscopy data for the nano-hybrid satellite material dispersed in 0.2 M L-ascorbic acid, showed a change in the Auger parameter of the silver (723 eV), measured from the Ag 3d<sub>5/2</sub> binding energy (367.4 eV) (Figure 5. 30 A) and the Ag M<sub>4</sub>N<sub>45</sub>N<sub>45</sub> Auger peak (355.6 eV) (Figure 5. 30 B), suggesting the formation of oxidised silver in the nano-hybrid satellite material.<sup>82,83</sup> In addition, we also observe peak broadening in the silver 3d peaks, characteristic of the presence of oxidised silver (Figure 5. 30 A).<sup>83</sup> By combining the EDS mapping data (Figure 5. 27) with the XPS and Auger spectroscopy data (Figure 5. 30), we can hypothesise the formation of silver sulphide (e.g. Ag<sub>2</sub>S) at the surface of the AgNP core. We also observe a shift in the XPS Cd 3d<sub>5/2</sub> binding energy (404.6 eV) (Figure 5. 30 C) and Cd Auger M<sub>5</sub>N<sub>45</sub>N<sub>45</sub> peak (375.5 eV) (Figure 5. 30 D), indicating a mixture of chemical environments for cadmium in the nano-hybrid satellite material.<sup>84,85</sup>

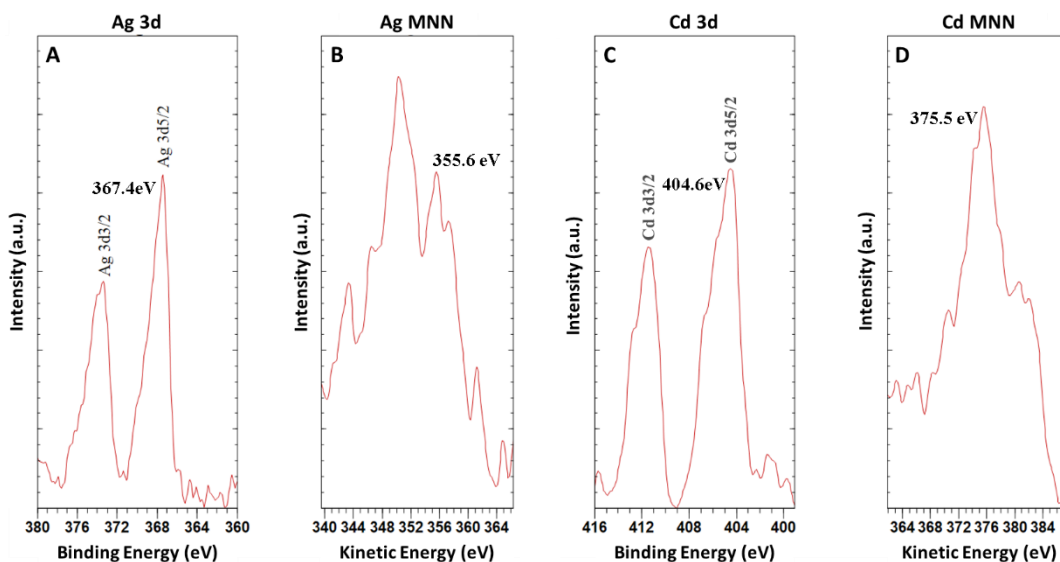


**Figure 5.30** Representative XPS and Auger data of the nano-hybrid satellite material dispersed in 0.2M L-ascorbic acid drop-cast on a silicon wafer (**A**) Ag 3d spectra, (**B**) Ag MNN Auger spectra, (**C**) Cd 3d spectra and (**D**) Cd MNN Auger spectra.

Comparing the data for acid and basic stability tests, we can conclude that under acidic conditions both the AgNP and CdS QDs are affected, with the possibility of sulphide migrating from the CdS QDs to form Ag<sub>2</sub>S, following a mechanism similar to galvanic exchange.<sup>87,88</sup> Under basic conditions, however, the CdS QDs appear to be chemically affected, while the Ag associated with the AgNPs remains in the metallic state. Although, the stability of the of the satellite structure is compromised by the detachment of the SiO<sub>2</sub> layer. Additionally, we must also stress that interpretation of the XPS and Auger data on these systems must be cautious, considering the nano-heterogenous nature of the core-shell satellites, and the short penetration depth of XPS.

These results pose a big challenge for the practical use of these materials and highlights the complexity of the chemistry involved, that to our current knowledge in these systems, has been somewhat overlooked in the literature. Although, these materials appear to be unstable after 24 hrs in solution, we investigated the plasmonic enhancement of these materials towards the photocatalytic production of hydrogen from water, to aid in future developments of these type of systems.

### 5.3.2 Hydrogen Evolution

Due to the unstable nature of the nano-hybrid satellite material observed after 24 hrs dispersed in a hole scavenger solution, the materials were freshly prepared prior to the photocatalytic reactions and stored in deionised water. The nano-hybrid satellite materials were then mixed with 20 mM Na<sub>2</sub>SO<sub>3</sub> as the hole scavenger immediately before carrying out the photocatalytic experiments. Sulphites are the preferred choice of hole scavenger in the photocatalytic systems, particularly with chalcogenide based QDs, as they are very efficient hole acceptors and easily oxidizable, enabling the effective separation of charge carriers and preventing photoanodic corrosion.<sup>18,19</sup> As a result of this, we proceeded with using Na<sub>2</sub>SO<sub>3</sub>, despite the instability of the nano-hybrid satellite material after 24 hrs dispersed in this media. CdS@Pt QDs associated with the same batch of nano-hybrid satellite were also tested for their photocatalytic activity towards the production of hydrogen from water for comparison.

The amount of hydrogen produced during the photocatalytic experiments was measured by the TCD detector of the GC instrument in mol%, which was then subsequently re-calculated to determine the moles of hydrogen (H<sub>2</sub>) produced as follows:

$$\text{Moles } H_2 = \text{Mol\%} \times \left( \frac{\text{Headspace Volume}}{\text{Molar Volume of Ideal gas}} \right)$$

**Equation 5. 3**

Where the volume of the headspace in photocatalytic experiment discussed above is 0.0112 litres and molar volume of ideal gas is 22.4 litres.<sup>89</sup> This data was then used to determine the external quantum efficiency (EQE) of the photocatalytic systems and a turnover number (TON) for the production of hydrogen, based on the concentration of Pt in the photocatalytic reaction solution, assuming all the Pt is deposited on the surface of the QDs (see appendix, section 5.7.2). The concentration of Pt was determined by ICP-OES analysis (Table A5.2).

The EQE for the photocatalytic production of hydrogen was calculated according to literature, from the ratio of 2 x number of hydrogen molecules evolved/ number of incident photons.<sup>19</sup> Due to the potential contribution of the plasmon in the production of hydrogen for the nano-hybrid satellite material, we did not calculate an internal quantum efficiency as it cannot be reliably determined.

To determine an enhancement in the photocatalytic evolution reactions, the external quantum efficiency and the TONs for the nano-hybrid satellite material and CdS@Pt QDs of the same batch were compared. A plasmonic enhancement corresponding to the EQE was calculated by dividing the EQE of the nano-hybrid satellite material by the EQE of the CdS@Pt QDs. The enhancement factor for TONs was calculated following the same approach (Equation 5. 4).

$$\text{Enhancement Factor} = \frac{TON_{\text{Satellite}}}{TON_{\text{CdS@Pt QDs}}}$$

**Equation 5. 4**

Hydrogen evolution experiments proved the photocatalytic activity of both the CdS@Pt QDs and the nano-hybrid satellite material for the production of hydrogen from water. We observed different results from different sample batches (Table 5. 1). In the first set of experiments (batch 1), an enhancement factor of 5 for the EQE of the nano-hybrid satellite material was obtained (Table 5. 1), while in the second experiments (batch 2) a smaller enhancement of 1.17 was obtained (Table 5. 1), suggesting some enhancement effect associated with the properties of the nano-hybrid satellite material. We also observed an extraordinarily low EQE for both the CdS@Pt QDs and the nano-hybrid satellite material, which could be associated with stability issues or low concentrations of Pt at the surface of the QDs. In addition, the EQE only considers the number of incident photons and does not account for the concentration of Pt in the photocatalytic reaction system or the number of QDs, therefore this method is not reliable for determining a true enhancement factor. If we consider the TON of the photocatalytic systems based on the concentration of Pt, we obtain a more accurate depiction

of the plasmonic enhancement for the photocatalytic systems. In batch 1 of experiments, an enhancement factor of 2.94 was obtained (Table 5. 1), while in batch 2 of experiments, there proved to be no enhancement for the nano-hybrid satellite material (Table 5.1), with enhancement factor of 0.7.

The variation in the enhancement factor for different batches could be attributed to the SiO<sub>2</sub> layer thickness. Batch 1 of the nano-hybrid satellite material had an SiO<sub>2</sub> layer thickness of 13.07 nm ± 1.58 nm (Figure 5. 31 A), while in batch 2 the SiO<sub>2</sub> thickness of the nano-hybrid satellite material was 23.30 nm ± 3.26 nm (Figure 5. 31 B). When comparing the hydrogen evolution results for the CdS@Pt QDs (Table 5.1), we also observe an increase in the production of hydrogen with increasing concentration of Pt (Table 5. 1), which is consistent with literature.<sup>69</sup>

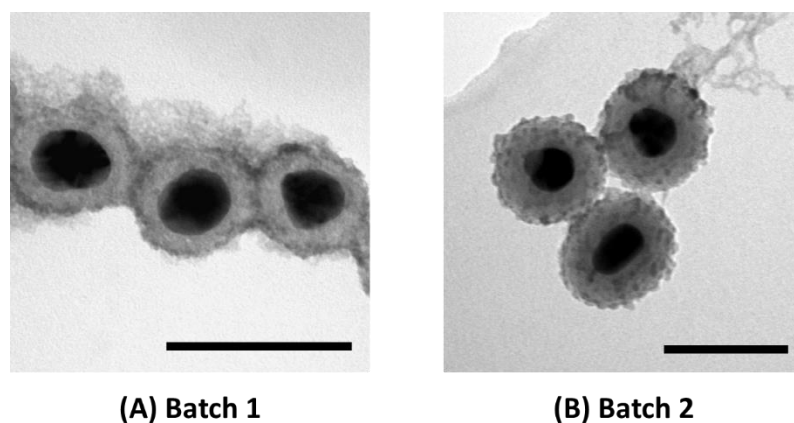


**Figure 5. 31** Representative TEM images of the nano-hybrid satellite materials after fabrication used in the photocatalytic hydrogen evolution reactions. (A) Batch 1 (SiO<sub>2</sub> layer thickness 13.07 nm ± 1.58 nm) and (B) Batch 2 (SiO<sub>2</sub> layer thickness 23.30 nm ± 3.26 nm). (Scale bars are 100 nm).

**Table 5. 1** Photocatalytic H<sub>2</sub> evolution results for batch 1 and 2 of the nano-hybrid satellite material and the CdS@Pt QDs, including the SiO<sub>2</sub> layer thickness for the nano-hybrid satellite materials and concentrations of Pt and CdS QDs in the reaction solution.

H <sub>2</sub> Evolution Sample	SiO <sub>2</sub> Layer Thickness (nm)	Number of CdS QDs in the reaction solution	nmol of Pt in the reaction solution	wt.% Pt/ QD	Total H <sub>2</sub> produced in 4 hrs (μmol)	External Quantum Efficiency (EQE)	EQE Enhancement Factor	TON (μmol H <sub>2</sub> produced/ μmol Pt in the reaction solution)	TON Enhancement Factor
CdS@Pt QDs Batch 1	-	3.54 x 10 <sup>15</sup>	1.03	1.1	10	0.004 %	5.00	9.75 x 10 <sup>3</sup>	2.94
Nano-Hybrid Satellite Batch 1	13.07 ± 1.58	3.08 x 10 <sup>15</sup>	1.74	2.2	50	0.02 %		2.87 x 10 <sup>4</sup>	
CdS@Pt QDs Batch 2	-	1.10 x 10 <sup>15</sup>	2.15	7.7	30	0.012 %	1.17	1.39 x 10 <sup>4</sup>	0.70
Nano-Hybrid Satellite Batch 2	23.30 ± 3.26	1.69 x 10 <sup>15</sup>	3.59	8.3	35	0.014 %		9.75 x 10 <sup>3</sup>	

## 5.4 Conclusions

In this work, we have successfully fabricated a multi-layered core shell nano-hybrid satellite structure by a directed self-assembly using peptide coupling, with dual plasmonic and catalytic properties. The nanomaterial was extensively characterised using several methods, demonstrating a core shell structure with a plasmonic AgNP core, coupled with CdS@Pt QDs, separated by a dielectric SiO<sub>2</sub> spacer layer. The stability of the nano-hybrid satellite material was also rigorously tested under active working conditions of acidic, neutral and basic media, using pH buffers and hole scavengers from literature. The morphology and chemical composition of the nano-hybrid satellite material under these active conditions was investigated using several techniques.

In the TEM and STEM imaging we observed morphological changes in the nano-hybrid satellite material dependent on the pH of the dispersion media. In basic conditions the SiO<sub>2</sub> layer of the nano-hybrid satellite material was depleted over time, with an increase in the depletion rate of the SiO<sub>2</sub> layer dependent on the concentration of the basic media. However, in acidic conditions, the SiO<sub>2</sub> layer of the nano-hybrid satellite material remained intact, but appeared to be 'stripped', with a loss in CdS@Pt QDs attached to the surface of the SiO<sub>2</sub> layer. This also proved to be dependent on the concentration of the acidic media.

These changes were also reflected in the chemical composition of the nano-hybrid satellite material dispersed in basic and acidic conditions. In basic conditions, while silver remained metallic, we observe a small shift in the Cd 3d XPS and Cd M<sub>5</sub>N<sub>45</sub>N<sub>45</sub> Auger peak, suggesting mixed chemical environments for cadmium in the nano-hybrid satellite material. In acidic conditions we observe a change in the oxidation state of silver, with the possible formation of silver sulphide (e.g. Ag<sub>2</sub>S) at the core of the nanomaterial confirmed by EDS mapping. This result suggests that the SiO<sub>2</sub> layer may exhibit some porosity, allowing sulphur to migrate to

the silver AgNP core. A shift in the Cd 3d and Cd  $M_{5}N_{45}N_{45}$  Auger peak was also observed, suggesting mixed chemical environments for cadmium in the nano-hybrid satellite material under acidic conditions. As a result of the stability experiments, we hypothesised that the effects observed can be associated with a mechanism similar to galvanic exchange, correlating the leaching of sulphur from the CdS@Pt QDs, with morphological and chemical changes in the nano-hybrid satellite material. However, the complete mechanism involved is still not well understood, and will be the object of future studies.

Despite the stability issues of nano-hybrid satellite material after 24 hrs, the material also proved to be photoactive towards the photocatalytic evolution of hydrogen from water. The plasmonic enhancement of the nano-hybrid satellite material could be dependent on the thickness of SiO<sub>2</sub> layer between the AgNP and CdS@Pt QDs, however due to stability issues with our nanomaterial, extensive photocatalytic testing on the same batches, precluding a definitive conclusion regarding the mechanism of plasmonic enhancement.

## 5.5 Future Work

In this chapter, we observed an enhancement effect from our nanomaterial in the photocatalytic production of hydrogen from water, however some aspects of the synthetic method and stability issues were determined. To further investigate the plasmonic enhancement of our nanomaterial, we will need to improve the control over the growth of the SiO<sub>2</sub> layer, allowing for a reliable comparison of the hydrogen evolution results, as well as investigating the stability of our nanomaterial with alternative hole scavengers (e.g. methanol).<sup>17,18</sup> In addition to this, optimisation of the Pt photodeposition also needs to be explored.

An alternative coating method, could involve functionalising the surface of the AgNPs with a mercaptosilane molecule prior to the SiO<sub>2</sub> coating process, allowing and improving control over the growth of the SiO<sub>2</sub> layer.<sup>48</sup> Functionalising the surface of the AgNPs prior to the coating process may also lead to an improved stability of the nano-hybrid satellite material. With respect to the stability of the nano-hybrid satellite material we observed a change in the oxidation state and chemical environment of the Ag and Cd under different active working conditions. As a result, we believe the SiO<sub>2</sub> layer may exhibit some porosity, allowing the sulphur to leach through to the core of the nanomaterial. One potential method of investigating the porosity of the SiO<sub>2</sub> layer is Raman pinhole testing.<sup>90</sup> In this method, a known concentration of pyridine is added to both plasmonic nanoparticles and coated plasmonic nanoparticles drop-cast on a substrate (e.g. silicon wafer), which are then analysed using Raman spectroscopy, exploiting the SERs effect.

If the stability of the nano-hybrid satellite material were to be improved, we could also investigate the plasmonic enhancement of AgNPs of different size and shape. The plasmonic effect of gold nanoparticles could also be explored, with the potential of an improved stability under active working conditions. Alternatively, other semi-conducting nanomaterials (e.g.

CdSe) could be explored. This may provide an improved stability with the nano-hybrid satellite material and therefore allow for the consistent testing of the photocatalytic production of hydrogen from water with our nanomaterial. Alternative photocatalysts, such as TiO<sub>2</sub>, may also lead to an enhanced photocatalytic effect in the production of reactive oxygen species, leading this concept to be extended towards antimicrobial applications.

## 5.6 References

- 1 S. Dutta, *J. Ind. Eng. Chem.*, 2014, **20**, 1148–1156.
- 2 F. E. Osterloh, *Chem. Soc. Rev.*, 2013, **42**, 2294–2320.
- 3 M. Ashokkumar, *Int. J. Hydrogen Energy*, 1998, **23**, 427–438.
- 4 N. Zhou, V. López-Puente, Q. Wang, L. Polavarapu, I. Pastoriza-Santos and Q. H. Xu, *RSC Adv.*, 2015, **5**, 29076–29097.
- 5 A. Fujishima and K. Honda, *Nature*, 1972, **238**, 37–38.
- 6 C. Rafanelli, A. Damiani, E. Benedetti, S. De Simone, A. Anav, L. Ciattaglia and I. Di Menno, in *UV Radiation in Global Climate Change*, W. Gao, D. L. Schmoldt and J. R. Slusser, Springer, Heidelberg, 1st Edition, 2010, 73–105.
- 7 J. Zhang, B. Tian, L. Wang, M. Xing and J. Lei, in *Photocatalysis*, J. Zhang, B. Tian, L. Wang, M. Xing and J. Lei, Springer, 1st Edition, 2018, 1–15.
- 8 Y. J. Yuan, D. Chen, Z. T. Yu and Z. G. Zou, *J. Mater. Chem. A*, 2018, **6**, 11606–11630.
- 9 A. Hellman, B. Wang, A. Hellman and B. Wang, *Inorganics*, 2017, **5**, 37.
- 10 A. Kudo and Y. Miseki, *Chem. Soc. Rev.*, 2009, **38**, 253–278.
- 11 S. Kothari, A. Kumar, R. Vyas, R. Ameta and P. B. Punjabi, *J. Braz. Chem. Soc.*, 2009, **20**, 1821–1826.
- 12 W. A. Smith, I. D. Sharp, N. C. Strandwitz and J. Bisquert, *Photoelectrochem. Water Split.*, 2015, **8**, 2851.
- 13 B. A. Pinaud, J. D. Benck, L. C. Seitz, A. J. Forman, Z. Chen, T. G. Deutsch, B. D. James, K. N. Baum, G. N. Baum, S. Ardo, H. Wang, E. Miller and T. F. Jaramillo, *Energy Environ. Sci.*, 2013, **6**, 1983–2002.

- 14 J. D. Blakemore, R. H. Crabtree and G. W. Brudvig, *Chem. Rev.*, 2015, **115**, 12974–13005.
- 15 M. J. Berr, P. Wagner, S. Fischbach, A. Vaneski, J. Schneider, A. S. Sussha, A. L. Rogach, F. Jäckel and J. Feldmann, *Appl. Phys. Lett.*, 2012, **100**, 223903.
- 16 J. Yang, D. Wang, H. Han and C. Li, *Acc. Chem. Res.*, 2013, **46**, 1900–1909.
- 17 M. Wang, S. Shen, L. Li, Z. Tang and J. Yang, *J. Mater. Sci.*, 2017, **52**, 5155–5164.
- 18 J. Schneider and D. W. Bahnemann, *J. Phys. Chem. Lett.*, 2013, **4**, 3479–3483.
- 19 W. Li, G. O’Dowd, T. J. Whittles, D. Hesp, Y. Gründer, V. R. Dhanak and F. Jäckel, *Nanoscale*, 2015, **7**, 16606–16610.
- 20 T. Simon, N. Bouchonville, M. J. Berr, A. Vaneski, A. Adrovic, D. Volbers, R. Wyrwich, M. Döblinger, A. S. Sussha, A. L. Rogach, F. Jäckel, J. K. Stolarczyk and J. Feldmann, *Nat. Mater.*, 2014, **13**, 1–6.
- 21 M. Berr, A. Vaneski, A. S. Sussha, J. Rodríguez-Fernández, M. Döblinger, F. Jäckel, A. L. Rogach and J. Feldmann, *Appl. Phys. Lett.*, 2010, **97**, 93108.
- 22 W. W. Yu and X. Peng, *Angew. Chemie - Int. Ed.*, 2002, **41**, 2368–2371.
- 23 Z. Han, F. Qiu, R. Eisenberg, P. L. Holland and T. D. Krauss, *Science*, 2012, **338**, 1321–1324.
- 24 C. Baslak, E. Aslan, I. H. Patir, M. Kus and M. Ersoz, *Int. J. Hydrogen Energy*, 2016, **41**, 20523–20528.
- 25 J. M. Pietryga, Y.-S. Park, J. Lim, A. F. Fidler, W. K. Bae, S. Brovelli and V. I. Klimov, *Chem. Rev.*, 2016, **116**, 10513–10622.
- 26 A. Das, Z. Han, M. G. Haghghi and R. Eisenberg, *Proc. Natl. Acad. Sci.*, 2013, **110**, 16716–16723.

- 27 C. Gimbert-Suriñach, J. Albero, T. Stoll, J. Fortage, M. N. Collomb, A. Deronzier, E. Palomares and A. Llobet, *J. Am. Chem. Soc.*, 2014, **136**, 7655–7661.
- 28 C. Burda, X. Chen, R. Narayanan and M. A. El-Sayed, *Chem. Rev.*, 2005, **105**, 1025–1102.
- 29 J. Jasieniak, M. Califano and S. E. Watkins, *ACS Nano*, 2011, **5**, 5888–5902.
- 30 M. Grzelczak, J. Vermant, E. M. Furst and L. M. Liz-Marzán, *ACS Nano*, 2010, **4**, 3591–3605.
- 31 Z. Nie, A. Petukhova and E. Kumacheva, *Nat. Nanotechnol.*, 2009, **5**, 15–25.
- 32 M. Grzelczak, J. Vermant, E. M. Furst and L. M. Liz-Marzán, *ACS Nano*, 2010, **4**, 3591–3605.
- 33 K. J. M. Bishop, C. E. Wilmer, S. Soh and B. A. Grzybowski, *Small*, 2009, **5**, 1600–1630.
- 34 L. Scarabelli, A. Sánchez-Iglesias, J. Pérez-Juste and L. M. Liz-Marzán, *J. Phys. Chem. Lett.*, 2015, **6**, 4270–4279.
- 35 W. Hou and S. B. Cronin, *Adv. Funct. Mater.*, 2013, **23**, 1612–1619.
- 36 P. Zhang, T. Wang and J. Gong, *Adv. Mater.*, 2015, **27**, 5328–5342.
- 37 M. Faraday, *Philos. Trans. R. Soc. London*, 1857, **147**, 145–181.
- 38 K. A. Willets and R. P. Van Duyne, *Annu. Rev. Phys. Chem.*, 2006, **58**, 267–297.
- 39 N. G. Bastús, J. Comenge and V. Puentes, *Langmuir*, 2011, **27**, 11098–11105.
- 40 G. Mie, *Ann. Phys.*, 1908, **330**, 377–445.
- 41 L. Scarabelli, M. Grzelczak and L. M. Liz-Marzán, *Chem. Mater.*, 2013, **25**, 4232–4238.
- 42 X. Lu, M. Rycenga, S. E. Skrabalak, B. Wiley and Y. Xia, *Annu. Rev. Phys. Chem.*,

- 2009, **60**, 167–192.
- 43 N. E. Motl, E. Ewusi-Annan, I. T. Sines, L. Jensen and R. E. Schaak, *J. Phys. Chem. C*, 2010, **114**, 19263–19269.
- 44 P. Pallavicini, G. Chirico, M. Collini, G. Dacarro, A. Donà, L. D’Alfonso, A. Falqui, Y. Diaz-Fernandez, S. Freddi, B. Garofalo, A. Genovese, L. Sironi and A. Taglietti, *Chem. Commun.*, 2011, **47**, 1315–1317.
- 45 Q. Zhang, N. Li, J. Goebel, Z. Lu and Y. Yin, *J. Am. Chem. Soc.*, 2011, **133**, 18931–18939.
- 46 N. G. Bastús, F. Merkoçi, J. Piella and V. Puntes, *Chem. Mater.*, 2014, **26**, 2836–2846.
- 47 I. Pastoriza-Santos and L. M. Liz-Marzán, *J. Mater. Chem.*, 2008, **18**, 1724–1737.
- 48 I. Pastoriza-Santos and L. M. Liz-Marzán, in *Nanomaterial Interfaces in Biology*, P. Bergese and K. Hamad-Schifferli, Humana Press, New York 1st Edition, 2013, 75–93.
- 49 P. Mulvaney, *Langmuir*, 2002, **12**, 788–800.
- 50 M. K. Corbierre, J. Beerens and R. B. Lennox, *Chem. Mater.*, 2005, **17**, 5774–5779.
- 51 J. Turkevich, P. C. Stevenson and J. Hillier, *Discuss. Faraday Soc.*, 1951, **11**, 55–75.
- 52 M. Wuihschick, A. Birnbaum, S. Witte, M. Sztucki, U. Vainio, N. Pinna, K. Rademann, F. Emmerling, R. Kraehnert and J. Polte, *ACS Nano*, 2015, **9**, 7052–7071.
- 53 A. Fukuoka, H. Araki, Y. Sakamoto, N. Sugimoto, H. Tsukada, Y. Kumai, Y. Akimoto and M. Ichikawa, *Nano Lett.*, 2002, **2**, 793–795.
- 54 P. C. Lee and D. Meisel, *J. Phys. Chem.*, 1982, **86**, 3391–3395.
- 55 K. Logaranjan, A. J. Raiza, S. C. B. Gopinath, Y. Chen and K. Pandian, *Nanoscale Res. Lett.*, 2016, **11**, 520–529.
- 56 D. Steinigeweg and S. Schlücker, *Chem. Commun.*, 2012, **48**, 8682–8684.

- 57 P. Pallavicini, A. Donà, A. Taglietti, P. Minzioni, M. Patrini, G. Dacarro, G. Chirico, L. Sironi, N. Bloise, L. Visai and L. Scarabelli, *Chem. Commun.*, 2014, **50**, 1969–1971.
- 58 G. Chirico, P. Pallavicini and M. Collini, *Nanomedicine*, 2014, **9**, 1–3.
- 59 H. Yuan, C. G. Khoury, C. M. Wilson, G. A. Grant, A. J. Bennett and T. Vo-Dinh, *Nanomedicine Nanotechnology, Biol. Med.*, 2012, **8**, 1355–1363.
- 60 J. Li, G. Zhan, Y. Yu and L. Zhang, *Nat. Commun.*, 2016, **7**, 11480.
- 61 F. Su, T. Wang, R. Lv, J. Zhang, P. Zhang, J. Lu and J. Gong, *Nanoscale*, 2013, **5**, 9001–9009.
- 62 W. Hou, Z. Liu, P. Pavaskar, W. H. Hung and S. B. Cronin, *J. Catal.*, 2011, **277**, 149–153.
- 63 T. Torimoto, H. Horibe, T. Kameyama, K. I. Okazaki, S. Ikeda, M. Matsumura, A. Ishikawa and H. Ishihara, *J. Phys. Chem. Lett.*, 2011, **2**, 2057–2062.
- 64 C. Gomes Silva, R. Juárez, T. Marino, R. Molinari and H. García, *J. Am. Chem. Soc.*, 2011, **133**, 595–602.
- 65 M. A. Khan, L. Sinatra, M. Oufi, O. M. Bakr and H. Idriss, *Catal. Letters*, 2017, **147**, 811–820.
- 66 K. Matsuda, Y. Ito and Y. Kanemitsu, *Appl. Phys. Lett.*, 2011, **211911**, 3–6.
- 67 A. O. Govorov, J. Lee and N. A. Kotov, *Phys. Rev. B - Condens. Matter Mater. Phys.*, 2007, **76**, 1–16.
- 68 F. F. Schweinberger, M. J. Berr, M. Döblinger, C. Wolff, K. E. Sanwald, A. S. Crampton, C. J. Ridge, F. Jäckel, J. Feldmann, M. Tschurl and U. Heiz, *J. Am. Chem. Soc.*, 2013, **135**, 13262–13265.
- 69 J. Schneider, A. Vaneski, G. R. Pesch, A. S. Susha, W. Yang Teoh and A. L. Rogach, *APL Mater.*, 2014, **2**, 126102.

- 70 M. Lismont, C. A. Páez and L. Dreesen, *J. Colloid Interface Sci.*, 2015, **447**, 40–49.
- 71 W. Stöber, A. Fink and E. Bohn, *J. Colloid Interface Sci.*, 1968, **26**, 62–69.
- 72 S. Rydergren, Uppsala University, 2013.
- 73 P. Farkaš and S. Bystrický, *Carbohydr. Polym.*, 2007, **68**, 187–190.
- 74 Z. R. Tang, B. Han, C. Han and Y. J. Xu, *J. Mater. Chem. A*, 2017, **5**, 2387–2410.
- 75 Á. Kmetykó, K. Mogyorósi, P. Pusztai, T. Radu, Z. Kónya, A. Dombi and K. Hernádi, *Materials (Basel)*, 2014, **7**, 7615–7633.
- 76 K. H. Kim, D. J. Lee, K. M. Cho, S. J. Kim, J. K. Park and H. T. Jung, *Sci. Rep.*, 2015, **5**, 9014.
- 77 S. Agnihotri, S. Mukherji and S. Mukherji, *Nanoscale*, 2013, **5**, 7328–7340.
- 78 M. Ben Haddada, J. Blanchard, S. Casale, J. M. Krafft, A. Vallée, C. Méthivier and S. Boujday, *Gold Bull.*, 2013, **46**, 335–341.
- 79 F. Zhang and M. P. Srinivasan, *Langmuir*, 2004, **20**, 2309–2314.
- 80 C. R. Bullen and P. Mulvaney, *Nano Lett.*, 2004, **4**, 2303–2307.
- 81 W. William Yu, Lianhua Qu, Wenzhuo Guo and Xiaogang Peng, *Chem. Mater.*, 2003, **15**, 2854–2860.
- 82 S. Bera, P. Gangopadhyay, K. G. M. Nair, B. K. Panigrahi and S. V. Narasimhan, *J. Electron Spectros. Relat. Phenomena*, 2006, **152**, 91–95.
- 83 G. I. N. Waterhouse, G. A. Bowmaker and J. B. Metson, *Appl. Surf. Sci.*, 2001, **183**, 191–204.
- 84 M. Marychurch and G. C. Morris, *Surf. Sci.*, 1985, **154**, 251–254.
- 85 S. W. Gaarenstroom and N. Winograd, *J. Chem. Phys.*, 1977, **67**, 3500–3506.
- 86 B. R. C. Vale, R. S. Mourão, J. Bettini, J. C. L. Sousa, J. L. Ferrari, P. Reiss, D. Aldakov

- and M. A. Schiavon, *Sci. Rep.*, 2019, **9**, 8332.
- 87 D. Kriegner, M. Sytnyk, H. Groiss, M. Yarema, W. Grafeneder, P. Walter, A. C. Dippel, M. Meffert, D. Gerthsen, J. Stangl and W. Heiss, *J. Phys. Chem. C*, 2016, **120**, 19848–19855.
- 88 B. D. Anderson and J. B. Tracy, *Nanoscale*, 2014, **6**, 12195–12216.
- 89 D. R. Lide, in *CRC Handbook of Chemistry and Physics*, D. R. Lide, CRC Press, New York, 85th Edition, 2.39.
- 90 J. F. Li, X. D. Tian, S. B. Li, J. R. Anema, Z. L. Yang, Y. Ding, Y. F. Wu, Y. M. Zeng, Q. Z. Chen, B. Ren, Z. L. Wang and Z. Q. Tian, *Nat. Protoc.*, 2013, **8**, 52–65.
- 91 D. R. Lide, in *CRC Handbook of Chemistry and Physics*, D. R. Lide, CRC Press, New York, 85th Edition, 2003, 4.37-4.96.
- 92 P. J. Mohr and B. N. Taylor, in *CRC Handbook of Chemistry and Physics*, D. R. Lide, CRC Press, New York, 85th Edition, 2003, 1.1-1.55.

## 5.7 Appendix

### 5.7.1 Fabrication and Characterisation of Nanomaterials

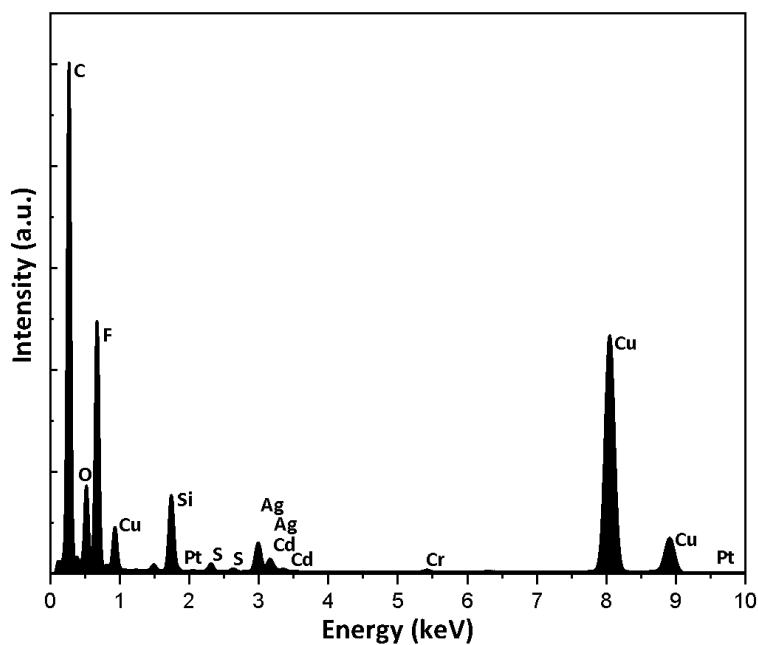


**Figure A5. 1** EDS spectra of the nano-hybrid satellite material after fabrication, used for the EDS mapping.

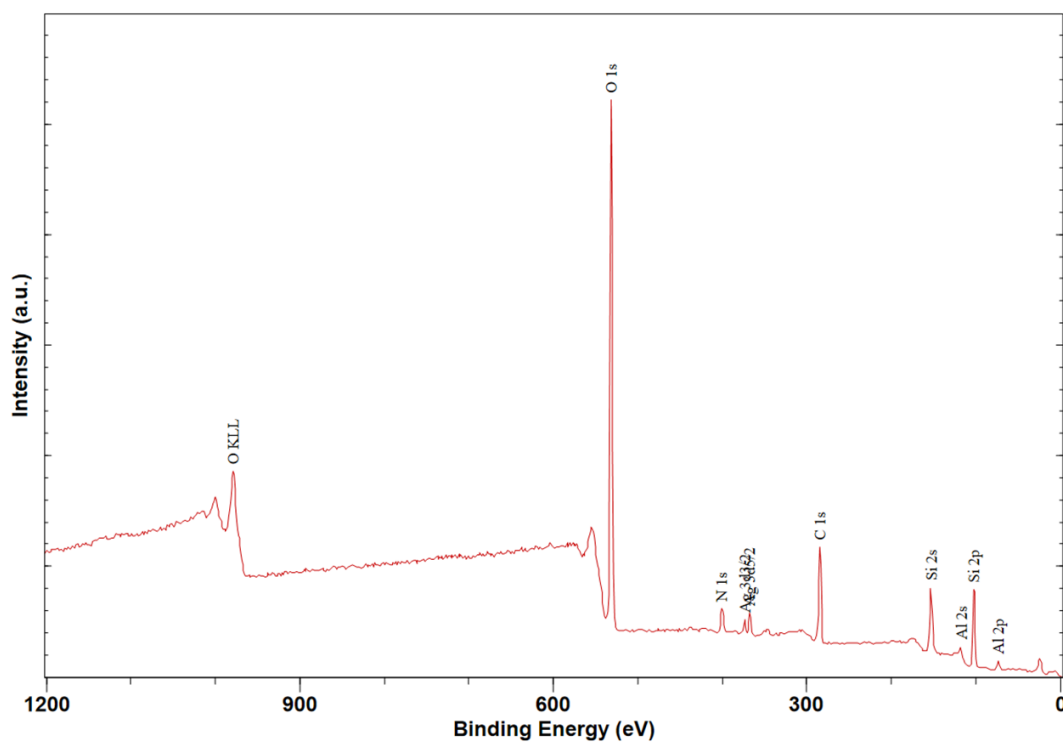


**Figure A5. 2** XPS survey scan of AgNP@SiO<sub>2</sub>-NH<sub>2</sub> drop-cast on an aluminium coated silicon wafer.

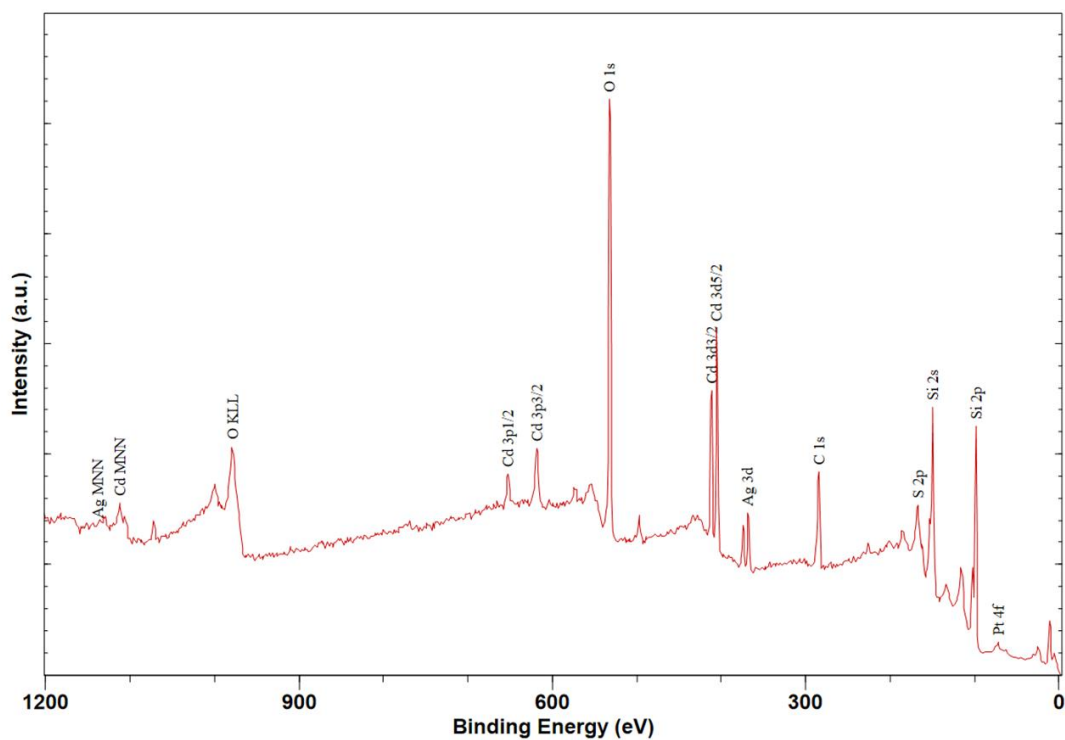


**Figure A5. 3** XPS survey scan of the nano-hybrid satellite material drop-cast on a silicon wafer.

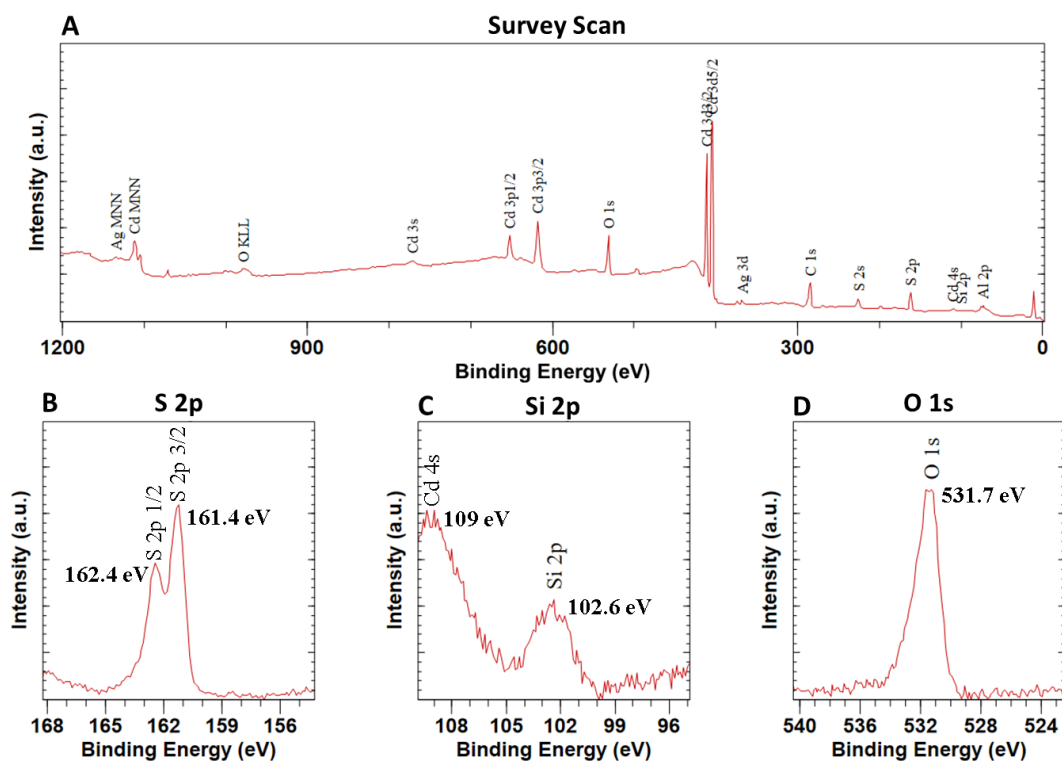


**Figure A5. 4** Representative XPS data of the nano-hybrid satellite material in DI H<sub>2</sub>O drop-cast on an aluminium coated silicon wafer (A) XPS survey scan, (B) S 2p spectra (C) Si 2p spectra (also shows Cd 4s peak) and (D) O 1s spectra.

## 5.7.2 Investigating the Stability of the Nano-Hybrid Satellite Material under Active Working Conditions

### Satellite Material under Active Working Conditions

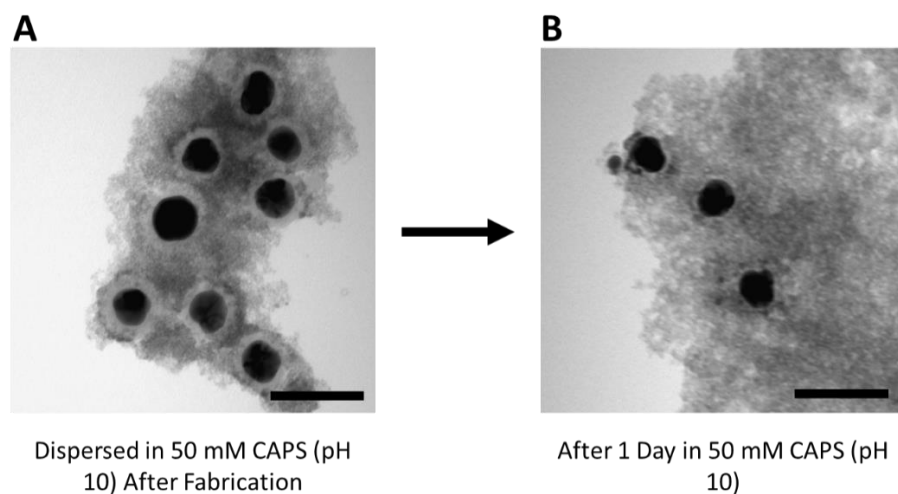


**Figure A5. 5** Representative TEM images of the nano-hybrid satellite material dispersed in 50 mM CAPS (pH 10) (scale bars are 100 nm). (A) After fabrication ( $\text{SiO}_2$  layer thickness  $12.74 \text{ nm} \pm 3.03 \text{ nm}$ ) and (B) After 24 hrs ( $\text{SiO}_2$  layer thickness  $3.04 \text{ nm} \pm 4.04 \text{ nm}$ ).

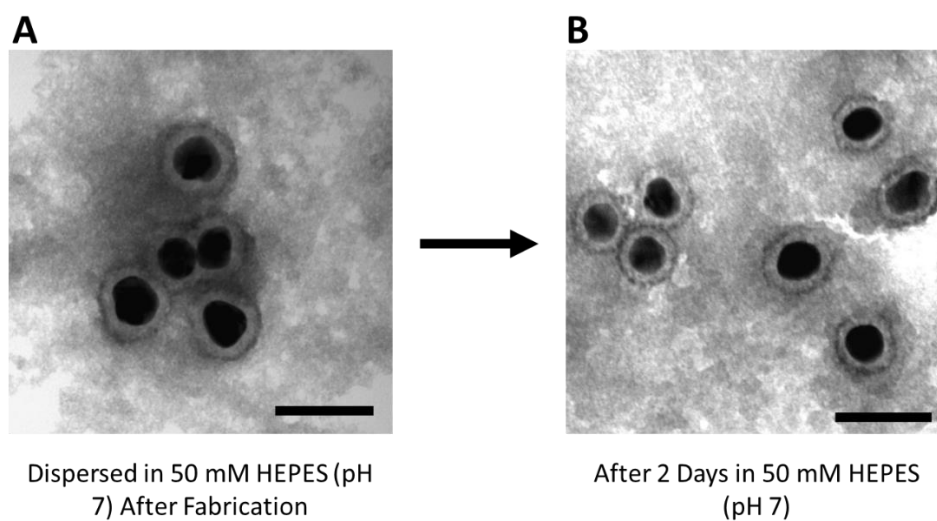


**Figure A5. 6** Representative TEM images of the nano-hybrid satellite material dispersed in 50 mM HEPES buffer (pH 7) (scale bars are 100 nm). (A) After fabrication ( $\text{SiO}_2$  layer thickness  $11.65 \text{ nm} \pm 1.77 \text{ nm}$ ) and (B) After 24 hrs ( $\text{SiO}_2$  layer thickness  $12.3 \text{ nm} \pm 2.18 \text{ nm}$ ).

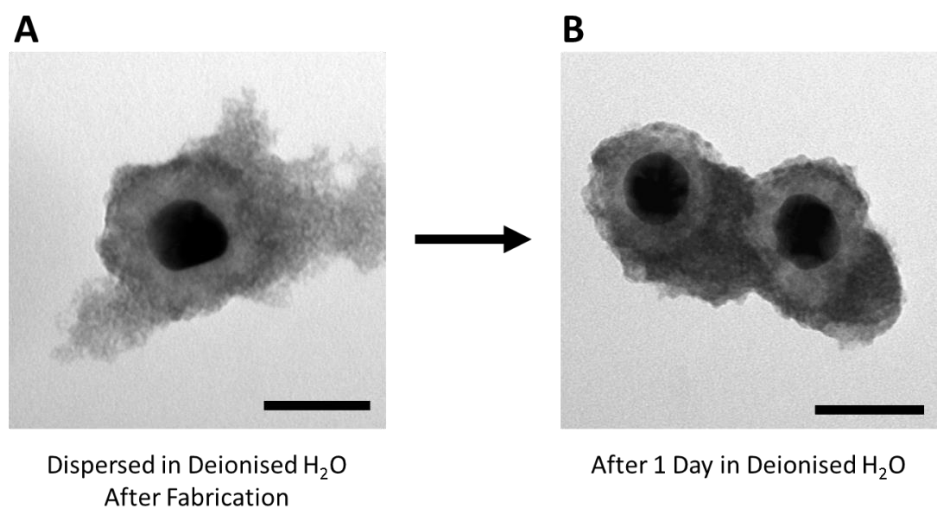


**Figure A5. 7** Representative TEM images of the nano-hybrid satellite material dispersed in DI H<sub>2</sub>O (scale bars are 50 nm). **(A)** After fabrication (SiO<sub>2</sub> layer thickness 13.51 nm ± 2.07 nm) and **(B)** After 24 hrs (SiO<sub>2</sub> layer thickness 12.25 nm ± 1.49 nm).

**Table A5. 1** Summary of the results obtained from the TEM analysis of the nano-hybrid satellite material dispersed in different pH buffers and hole scavengers from literature.

Dispersion Media	Average Thickness of Silica Layer After Fabrication (nm)	Average Thickness of Silica Layer After 24 hrs (nm)	Decrease in Thickness of SiO <sub>2</sub> Layer After 24 Hrs in Solution	CdS QDs Stripped from the Surface of the SiO <sub>2</sub> Layer
Deionised H <sub>2</sub> O	13.51 ± 2.07	12.25 ± 1.49		
☐ 20 mM Na <sub>2</sub> SO <sub>3</sub>	19.00 ± 4.68	1.82 ± 3.14	✓	
☐ ◆ 20 mM TEOA	19.32 ± 2.93	8.61 ± 1.67	✓	
☐ ◆ 0.2 M TEOA	17.77 ± 3.66	8.41 ± 2.94	✓	
☐ ◆ 1 M TEOA	9.11 ± 0.96	0.17 ± 1.07	✓	
☐ ◆ 20 mM L-Ascorbic Acid	18.21 ± 1.94	16.24 ± 1.96		✓
☐ ◆ 0.2 M L-Ascorbic Acid	16.83 ± 1.95	16.56 ± 2.19		✓
☐ 0.2 M Oxalic Acid	17.36 ± 1.99	19.76 ± 5.36		✓
❖ 50 mM MES pH 5.5	12.34 ± 2.04	14.29 ± 2.15		
❖ 50 mM HEPES, pH 7	11.65 ± 1.77	12.3 ± 2.18		
❖ 50 mM CAPS, pH 10	12.74 ± 3.03	3.04 ± 4.04	✓	
<b>Solution Variables:</b>	❖ pH Buffer	☐ Hole Scavenger	◆ Increasing Hole Scavenger Concentration	

### 5.7.3 Investigating the Mechanism Involved in the Stability of the Nano-Hybrid Satellite Materials under Active Working Conditions

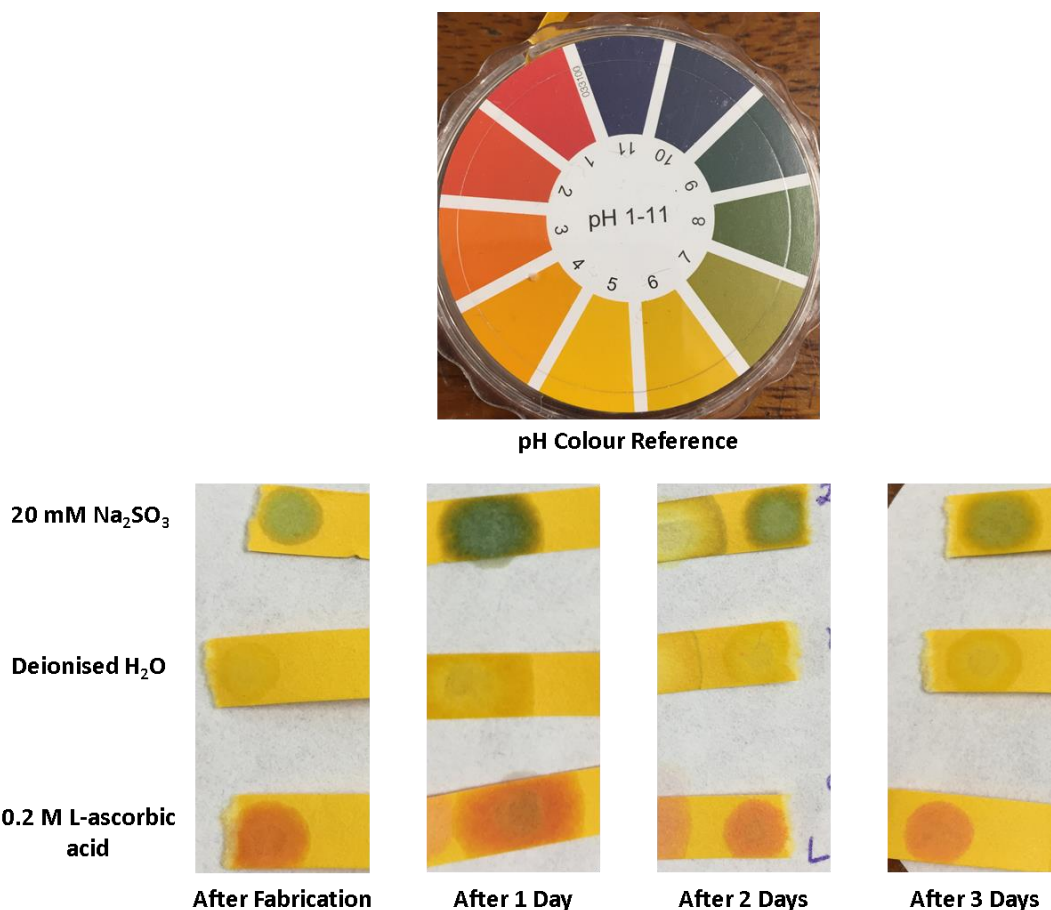
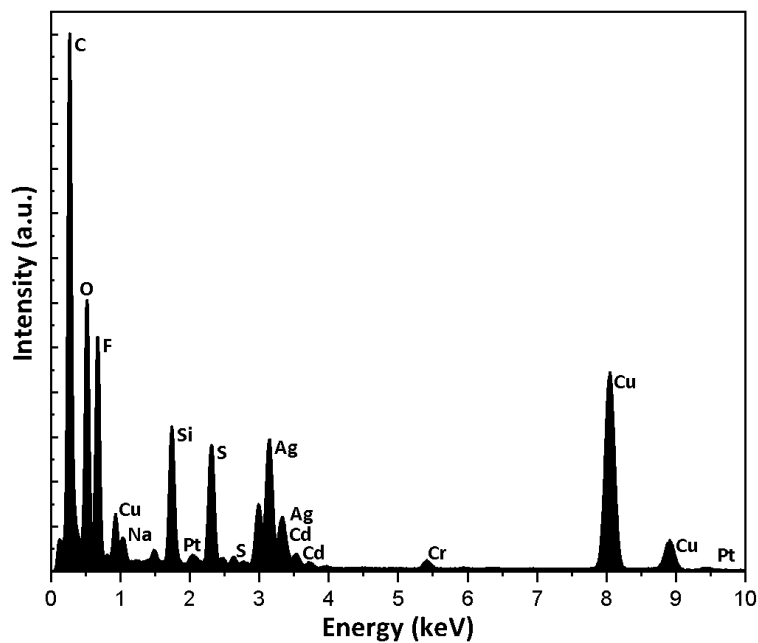
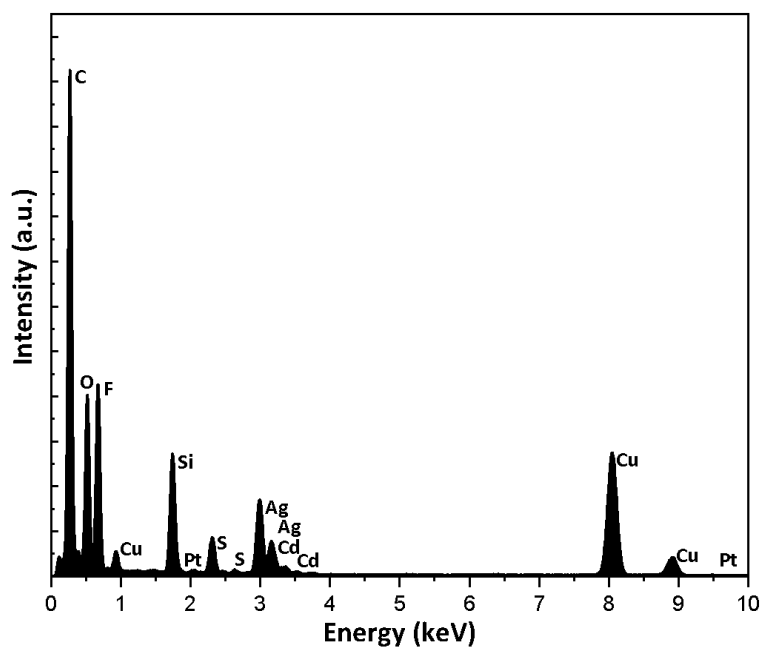


Figure A5. 8 Monitoring the pH of the nano-hybrid satellite material dispersion over 3 days.



**Figure A5. 9** EDS spectra of the nano-hybrid satellite material after 24 hrs dispersed in 20 mM  $\text{Na}_2\text{SO}_3$ , used for the EDS mapping.



**Figure A5. 10** EDS spectra of the nano-hybrid satellite material after 24 hrs dispersed in 0.2 M L-ascorbic acid, used for the EDS mapping.

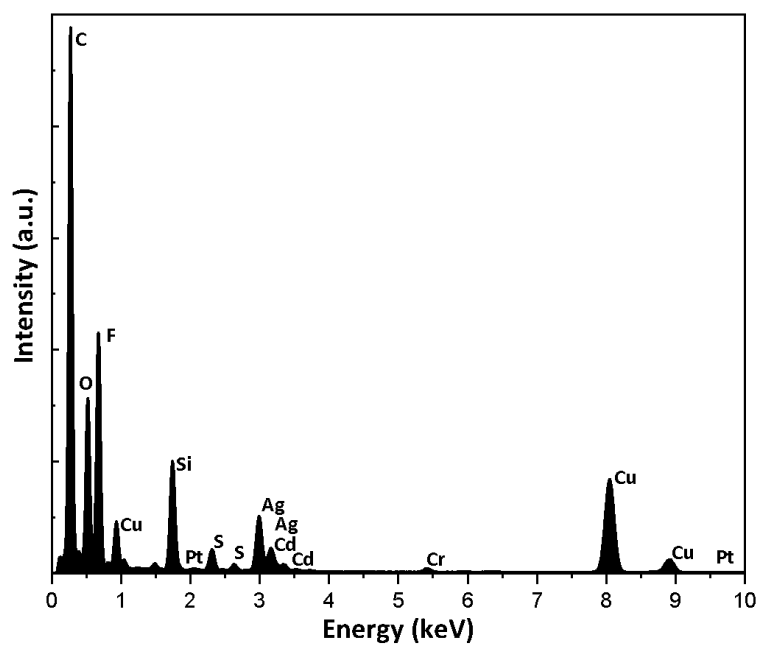


**Figure A5. 11** EDS spectra of the nano-hybrid satellite material after 24 hrs dispersed in DI H<sub>2</sub>O, used for the EDS mapping.

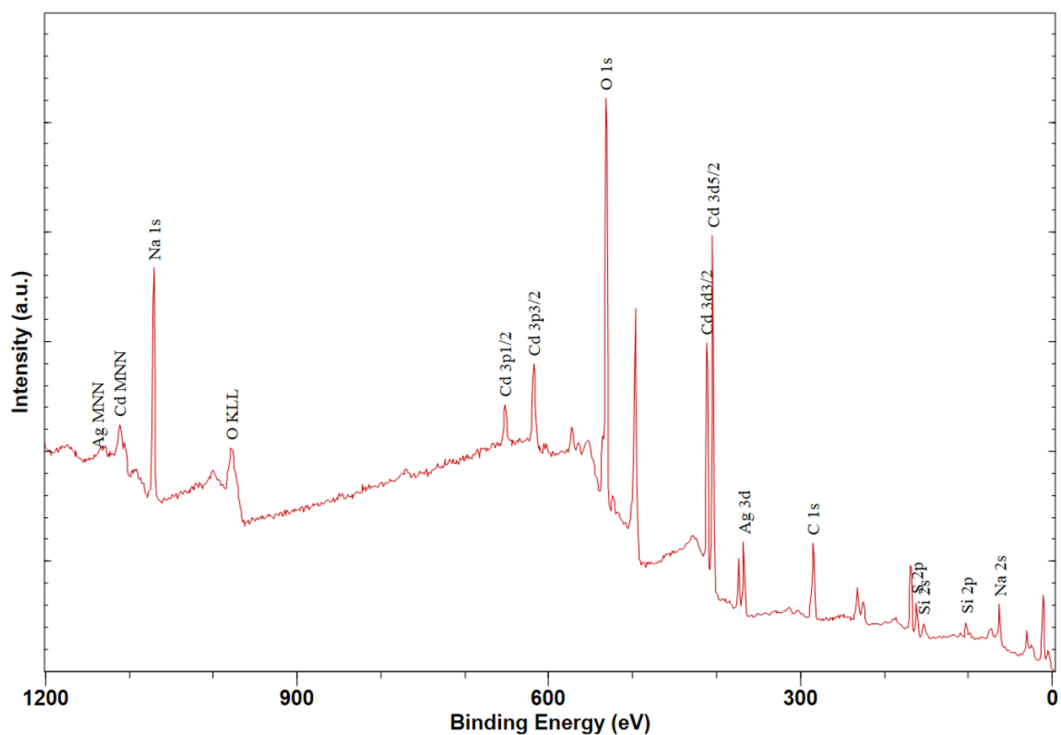


**Figure A5. 12** XPS survey scan of the nano-hybrid satellite material after 24 hrs dispersed in 20 mM Na<sub>2</sub>SO<sub>3</sub> drop-cast on a silicon wafer.

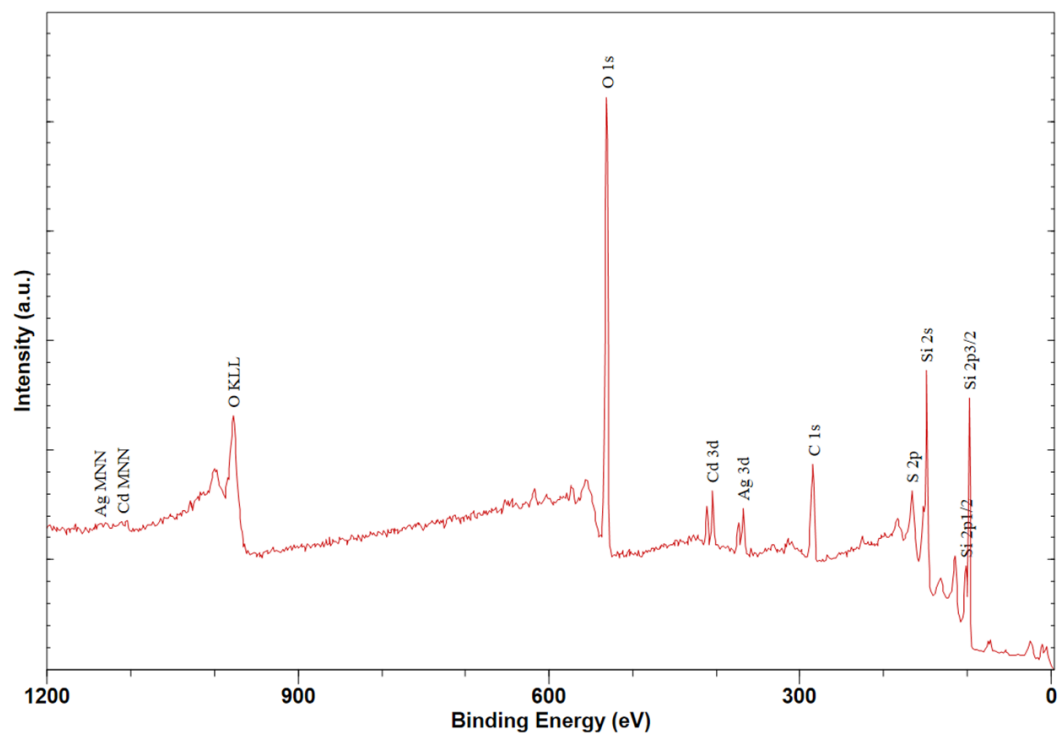


**Figure A5. 13** XPS Survey scan of the nano-hybrid satellite material after 24 hrs dispersed in 0.2 M L-ascorbic acid drop-cast on a silicon wafer.

## 5.7.4 Hydrogen Evolution

### 5.7.4.1 ICP-OES Results

**Table A5. 2** Total concentration of Ag, Cd and Pt in the 7 ml photocatalytic reaction solutions in parts per million (PPM). The values shown are corrected from the dilution (x2) for ICP-OES analysis and the volume of the photocatalytic reaction solution (7 ml) considering 1ppm is equal to  $\mu\text{g ml}^{-1}$ .

<b>H<sub>2</sub> Evolution Sample</b>	<b>Concentration of Ag (PPM)</b>	<b>Concentration of Cd (PPM)</b>	<b>Concentration of Pt (PPM)</b>
CdS@Pt QDs Batch 1	--	17.61	0.20
Nano-Hybrid Satellite Batch 1	0.33	15.33	0.34
CdS@Pt QDs Batch 2	--	5.46	0.42
Nano-Hybrid Satellite Batch 2	0.84	8.40	0.70

After measuring the concentration of Cd and Pt in the reaction solutions, these results were then used for calculating the concentration of CdS QDs and the wt.% of Pt per CdS QD in the reaction solutions. This was assuming that all of the Cd present are components of the CdS QDs and all of the Pt is deposited on the surface of the CdS QDs.

### 5.7.4.2 Calculating the Number of QDs in the Reaction Solutions

To calculate the number of CdS QDs in the photocatalytic reaction solutions, the volume (V) of a single CdS QD was first determined by equation A5. 1, assuming all QDs in the reaction solutions are homogenous in size.

$$V = \frac{4}{3}\pi r^3$$

**Equation A5. 1**

Where r is the radius of a QD in cm (nm multiplied by  $1 \times 10^7$ ). The mass (m) of a QD was then calculated following equation A5. 2.

$$m = \frac{V}{\rho}$$

**Equation A5. 2**

Where  $\rho$  is the density of CdS, which is  $4.83 \text{ g ml}^{-1}$ .<sup>91</sup> The % weight of Cd in CdS is 77.8 %, given by dividing the atomic mass of Cd ( $112.41 \text{ g mol}^{-1}$ )<sup>92</sup> by the molar mass of CdS ( $208.46 \text{ g mol}^{-1}$ ),<sup>91</sup> which is then used to determine the mass of Cd in a CdS QD.

$$\text{Mass of Cd in QD} = 77.8\% \times \text{Mass of Cds QD}$$

**Equation A5. 3**

The number of QDs in the photocatalytic reaction solution (sol) is then calculated as follows:

$$\text{No. QDs in Reaction Sol} = \frac{\text{ICP Conc Cd}}{\text{Mass of Cd in a CdS QD}}$$

**Equation A5. 4**

Where ICP Conc Cd is the total concentration of Cd in the photocatalytic reaction solutions taken directly from table A5. 1.

### 5.7.4.3 Calculating the Concentration of Pt in the Reaction Solutions

The concentrations displayed in table A5.1 have been corrected from the dilution (x2) for ICP-OES analysis and the volume of reaction solution (7 ml) considering 1 ppm is equal to  $\mu\text{g ml}^{-1}$ . The values displayed in table A5.1 are therefore the total concentrations of the respective elements in the 7 ml photocatalytic reaction solutions. As a result, the calculation for the concentration in terms of nmols of Pt in the reaction solutions, begins as follows:

$$M = \left( \frac{\text{ICP Conc Pt}}{7} \right) / \text{Atomic Mass Pt}$$

**Equation A5. 5**

Where M is the molar concentration and the atomic mass of Pt is  $195.08 \text{ g mol}^{-1}$ .<sup>92</sup> This is then converted to nanomolar (nM) and subsequently re-calculated to obtain the nmols of Pt in the reaction solutions, where 1 M Pt is equal to  $195.08 \text{ g L}^{-1}$ .<sup>92</sup> Therefore, in the 7 ml photocatalytic reaction solution:

$$\text{nmols Pt Reaction Solution} = \left( \frac{\text{nM}}{1000} \right) \times 7$$

**Equation A5. 6**

### 5.7.4.4 Calculating the Weight % of Pt per CdS QD

The weight % (wt.%) of Pt per CdS QD can be calculated from the details discussed above. The mass of QDs in the reaction solutions is first calculated from the calculated mass of a CdS QD and multiplying this by the number of CdS QDs in the photocatalytic reaction solutions. The wt.% of Pt for each QD is then calculated as follows:

$$\text{wt}\% = \left( \frac{\text{Mass of Pt in Reaction Sol}}{\text{Mass of QDs in Reaction Sol}} \right) \times 100$$

#### 5.7.4.5 Calculating Turnover Numbers for the Pt in the Hydrogen Evolution Reactions

The concentration of Pt in the photocatalytic reaction solutions (Table 5.1) was first converted into  $\mu\text{mol}$  (nmol multiplied by  $1 \times 10^3$ ). The turnover number (TON) for the concentration of hydrogen ( $\text{H}_2$ ) produced per  $\mu\text{mol}$  of Pt during the 4 hr photocatalytic reactions was then calculated as follows:

$$TON = \frac{\mu\text{mol } H_2}{\mu\text{mol } Pt}$$